2011

Correlating Microstructural Development And Failure Mechanisms To Photo Stimulated Luminescence Spectroscopy And Electrochemical Impedance Spectroscopy In Thermal Barrier Coatings

Balaji Jayaraj
University of Central Florida

CORRELATING MICROSTRUCTURAL DEVELOPMENT AND FAILURE MECHANISMS TO PHOTO STIMULATED LUMINESCENCE SPECTROSCOPY & ELECTROCHEMICAL IMPEDANCE SPECTROSCOPY IN THERMAL BARRIER COATINGS

by

BALAJI JAYARAJ
B.E. Sri Ramakrishna Engineering College, 1999
M.S. University of Central Florida, 2003

A dissertation submitted in partial fulfillment of the requirements
for the degree of Doctor of Philosophy
in the Department of Mechanical, Materials and Aerospace Engineering
in the College of Engineering and Computer Science
at the University of Central Florida
Orlando, Florida.

Spring Term
2011

Major Professor: Yong-Ho Sohn

ABSTRACT

Thermal barrier coatings (TBCs) are widely used for thermal protection of hot section components in turbines for propulsion and power generation. Applications of TBCs based on a clearer understanding of failure mechanisms can help increase the performance and life-cycle cost of advanced gas turbine engines. Development and refinement of robust non-destructive evaluation techniques can also enhance the reliability, availability and maintainability of hot section components in gas turbines engines.

In this work, degradation of TBCs was non-destructively examined by photostimulated luminescence spectroscopy (PSLS) and electrochemical impedance spectroscopy (EIS) as a function of furnace thermal cycling carried out in air with 10-minute heat-up, 0.67, 9.6 and 49.6 -hour dwell duration at 1121°C (2050°F), and 10-minute forced-air quench. TBCs examined in this study consisted of either electron beam physical vapor deposited and air plasma sprayed yttria-stabilized zirconia (YSZ) on a variety of bond coat / superalloy substrates including bond coats of NiCoCrAlY and (Ni,Pt)Al, and superalloys of CMSX-4, Rene'N5, Haynes 230 and MAR-M-509. Detailed microstructural characterization by scanning electron microscopy and energy dispersive spectroscopy was carried out to document the degradation and failure characteristics of TBC failure, and correlate results of PSLS and EIS.

Mechanisms of microstructural damage initiation and progression varied as a function of TBC architecture and thermal cycling dwell time, and included undulation of the interface between the thermally grown oxide (TGO) and bond coats, internal oxidation of the bond coats, and formation of Ni/Co-rich TGO. These microstructural observations were correlated to the evolution in compressive residual stress in the TGO scale determined by PSLS shift. Correlations

include stress-relief and corresponding luminescence shift towards stress-free luminescence (i.e. ν = 14402 cm^{-1} and ν = 14432 cm^{-1}) associated with subcritical cracking of the TGO scale and stress-relaxation associated with gradual shift in the luminescence towards stress-free luminescence (i.e. ν = 14402 cm^{-1} and ν =14432 cm^{-1}) is related to the undulation of TGO/bondcoat interface (e.g., rumpling and ratcheting).

Microstructural changes in TBCs such as YSZ sintering, TGO growth, and subcritical damages within the YSZ and TGO scale were also correlated to the changes in electrochemical resistance and capacitance of the YSZ and TGO, respectively. With thermal exposure the YSZ/TGO resistance and capacitance increased and decreased as result of sintering and TGO growth. With progressive thermal cycling damages in the TGO was related to the TGO capacitance showing a continuous increase and at failure TGO capacitance abruptly increased with the exposure of bondcoat. Further correlations among the microstructural development, PSLS and EIS are documented and discussed, particularly as a function of dwell time used during furnace thermal cycling test, with due respect for changes in failure characteristics and mechanisms for various types of TBCs.

ACKNOWLEDGMENTS

I am indebted to my advisor, Dr. Yong-ho Sohn for his support, guidance, thoughtful discussions and patience. Dr. Sohn did play an integral part for my success in my career and in future for many more thoughtful discussions to come. I sincerely thank Dr. Vimal Desai for his continuous support, suggestions, encouragement and help.

I would like to extend my gratitude to my dissertation committee members: Dr. Linan An, Dr. Helge Heinrich, Dr. Jayanta Kapat, Dr. Seetha Raghavan and Dr. Carlos Koeneke for their valuable suggestions and thoughtful discussions.

I would like to acknowledge the financial support that funded my Ph.D. research from Department of Energy (DOE) through University Turbine Systems Research (UTSR) program.

I would like to extend my thanks to my friends Rashmi Ranjan Mohanty, Barbara Franke, Abby Elliot, Sankar Laxman, Srinivas Vishweshwaraiah, Prabhakar Mohan, Emmanuel Perez, Chip O Toole, David Miranda, Chris Petroak, Jing Liu, Jai-won Byeon, Travis Patterson and Catalina Uribe Restrepo.

Finally, I would like to thank my wife Aruna, who always has supported and continuously encouraged me to make my wish come true. I have no words to express my appreciation for her love, understanding and belief in me. In addition, I would like to dedicate this thesis to my mother Surya and late father Jayaraj who are happy for me for making this significant accomplishment.

Last but not the least I would like to extend my gratitude to my fellow AMPAC staffs Kirk Scammon who has helped me in training all characterization equipments and Karen Glidewell, Kari Styles and Waheda for all the paper work required for completion of this degree.

TABLE OF CONTENTS

LIST OF FIGURES

LIST OF TABLES

1 INTRODUCTION

Modern industrial processes require operation of machines in very harsh environments that consist of high temperature (near melting thresholds of various alloys), steep temperature gradients, high pressure, enormous stresses on individual components, oxidation, corrosion and ingestion of particulate matter (e.g., erosion and impact damage). The machines subjected to the harsh environments include gas turbines, both land and aero derivatives, steam turbines, petroleum refineries and nuclear reactors critical for power and transportation sectors. Typically modern gas turbines can see operating temperatures as high as 1350°C (3000°F) in hot turbine section with internally cooled parts. To withstand these operating temperatures, a ceramic coating was proposed by NASA, and developed extensively over the last 50 years. This multilayered ceramic coating system is referred as thermal barrier coatings (TBCs). [1]

TBCs have been extensively used in past/recent years for thermal protection of hot section components in turbines for power/aero applications. [2] TBCs allow an increase in thermodynamic efficiency of a gas turbine by allowing higher operating temperatures and reduced cooling air requirements. In general a TBC consists of thermally insulating ceramic topcoat (typically ZrO_2-7~8 wt% Y_2O_3, known as the YSZ), a thermally grown oxide (TGO) scale, an oxidation resistant metallic bondcoat (MCrAlY or Pt-modified NiAl), and a superalloy substrate (Ni-Co based). Microstructure of typical TBC systems are presented in Figure 1. Until now, YSZ is the choice of chemistry for ceramic layer and is deposited either by air plasma spray [3] (APS) or electron beam physical vapor deposition (EB-PVD) [4]. Bondcoats are deposited by air plasma spray (APS), low-pressure/vacuum plasma spray (LPPS/VPS) [5], high velocity oxygen fuel (HVOF) [6,7] for a MCrAlY (M=Ni and/ or Co) bondcoat and a combination of

electro-plating and chemical vapor deposition (CVD) in case of Pt-modified NiAl bondcoat. This bondcoat is also known as (Ni,Pt)Al.

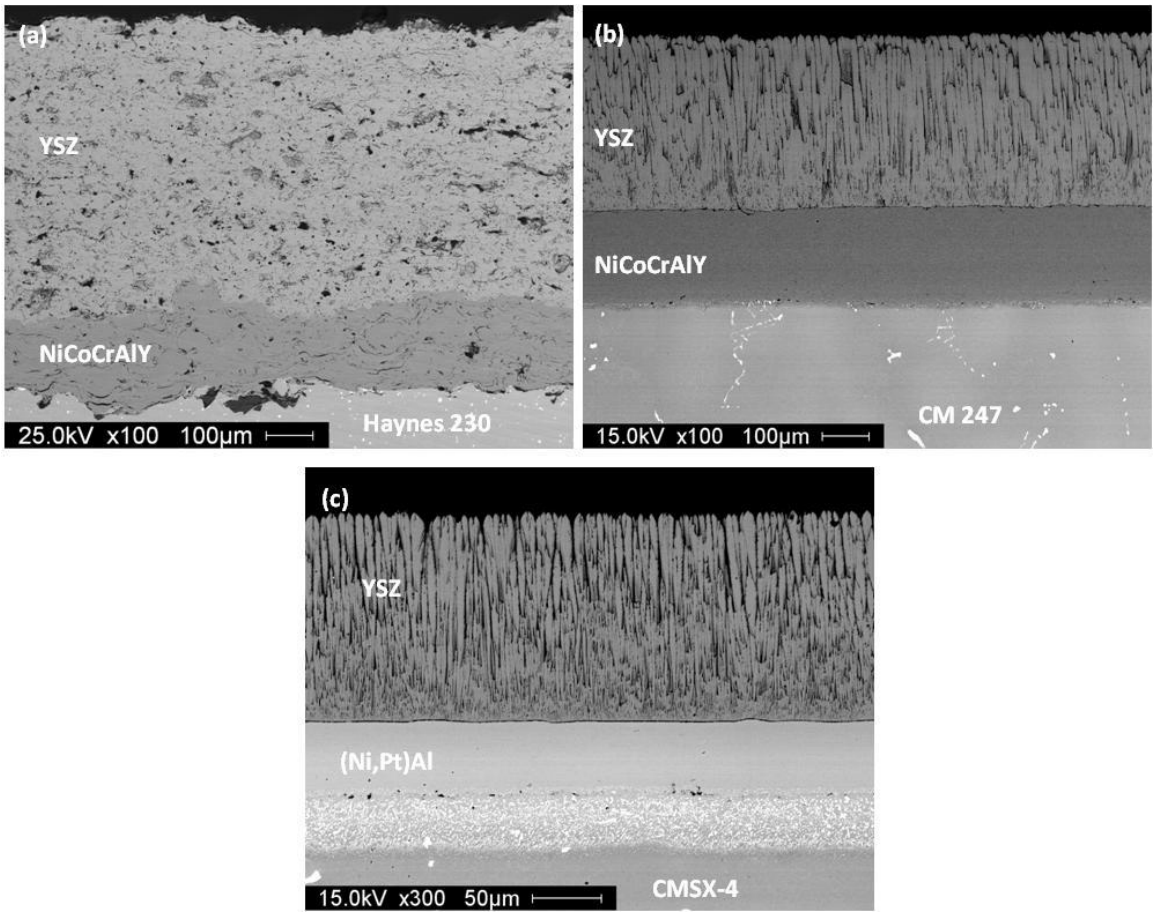

Figure 1 Backscatter electron images of TBCs (a) APS TBC on APS (Ni,Co)CrAlY bondcoat (b) APS TBC on (Ni,Co)CrAlY bondcoat and (c) EB-PVD YSZ on (Ni, Pt) Al bondcoat.

During engine operation these coatings are exposed to severe/harsh environmental conditions such as centrifugal stresses, hot corrosion, fatigue and creep. Typical skin temperature around the bondcoat to topcoat interface is around 700-900 °C based on the location in a gas turbine. In order to survive these conditions TBC material (topcoat) should have the following properties: (1) high melting point (2) low density (3) high surface emissivity (4) high thermal shock resistance (5) low vapor pressure (6) resistance to oxidation (7) low thermal conductivity

(8) high coefficient to thermal expansion (9) resistance to gaseous and particulate emission. Yttria stabilized with zirconia meets these properties and has been the choice of material for TBCs for over 5 decades. The topcoat is permeable to oxygen which occurs in abundance during engine operation and hence there is a need of intermediate layer referred as bondcoat (50-150 μm), is applied between ceramic layer and substrate. This bondcoat should also protect the base material from corrosion that occurs due to the combustion products of the gas turbine. Bondcoat acts as an aluminum reservoir, oxidizes and forms thermally grown oxide (TGO) at the interface between the bondcoat and topcoat during high temperature exposure. Formation of TGO is inevitable but the bondcoat is engineered to form α-Al_2O_3 and its growth rate is slow, uniform and relatively defect free. [8]

With continuous operation of gas turbine (typically for a year 8000 hours for IGT/20,000 hrs for aero engines) at operating temperatures around 1100-1300 °C (based on engine type) bondcoat continuously oxidizes and forms α-Al_2O_3 with other oxides such as Cr_2O_3/NiO. [9, 10] Compressive growth stresses are generated with continuous formation of α-Al_2O_3 and this stress is estimated to be <1 GPa. [11] At room temperature upon cooling, thermal expansion mismatch between the TGO and bondcoat leads to additional compressive stress in the TGO up to 6 GPa. [12, 13, 14] The large magnitude of compressive stress within the TGO scale provides the necessary strain energy for microscopic imperfections that develops into microcracks, and consequently failure of coatings at or near the vicinity of the TGO. This particular type of failure is common in EB-PVD TBCs.

The alumina scale formed during oxidation of bondcoat exhibits polymorphic phase transformation at early stages of oxidation. Initially γ, θ- Al_2O_3 forms on the bondcoat surface and subsequent phase transformation to α-Al_2O_3 also alters residual stress in the TGO scale from

volumetric constraint and nucleation of sub-critical cracks, eventually leading to the spallation of coating at TGO interface.[15] In case of APS TBCs, the delamination is often observed at the YSZ coating due to thermally activated processes such as oxidation, sintering, diffusion and creep. [16] The phase transformation and the TGO growth may not play a significant role in APS TBCs compared to EB-PVD TBCs.

Final TBC failure is generally observed with the spallation of ceramic layer and exposure of the metallic bondcoat under beneath. This can be catastrophic since the metallic components are exposed to temperature close to its melting in advanced gas turbines. Therefore, there is a need for non-destructive inspection/evaluation (NDE) techniques that can monitor the integrity of TBC system, and detect early damages in the TGO beneath the YSZ, either in-situ at high temperature or during service at room temperature. In this study photostimulated luminescence spectroscopy (PLS) and electrochemical impedance spectroscopy (EIS) technique were employed to monitor the TBC health with respect to furnace thermal cycling. Correlation of NDE parameters and microstructural degradation in the light of TBC failure was established in this study.

PL pioneered by Clarke et al. [17,18,19,20,21] and refined by Sohn, Gell, Jordan et al. [22, 23, 24] has the capability of being an NDE technique for EB-PVD TBCs. This technique was demonstrated by Sohn *et* al. [25] for evaluation of compressive residual stress on land derivative blades with intact TBC. This technique can provide information regarding the following factors with TBC failure: (1) residual stress within the α- Al_2O_3 scale; (2) polymorphic phase transformation of Al_2O_3 scale; and (3) formation of other oxides in the TGO scale [26] PL has been restricted to EB-PVD TBCs, since PL cannot be applied to APS TBCs without impregnating APS YSZ coatings with other medium [27] whose effect on the TBC lifetime has

not been investigated. In APS TBCs, relevant signals (e.g., incident beam and luminescence) are attenuated significantly due to the presence of defects geometrically oriented parallel to the TGO/bondcoat interface.

In the field of corrosion sciences EIS, is a well known technique to detect corrosion underneath the paint surfaces. [28] This technique was first employed to examine TBCs by Desai *et* al. [29] results whose results demonstrated a good potential to provide information on the following factors associated with TBC failure [30]: (1) Thickness of TGO scale; (2) Adhesion integrity of TGO/bondcoat and YSZ/TGO interfaces; (3) Microstructure, thickness, sintering and cracking in YSZ.

In this study, PSLS and EIS have been concurrently employed as NDE techniques in indentifying the damage accumulation due to continuous furnace cyclic oxidation of APS and EB-PVD TBCs. The furnace cyclic oxidation was performed using CM Rapid Temp Furnace for TBC specimens using cycles of 1-, 10- and 50-hour. Each thermal cycle consisted of 10-min ramp, and 10-min cooling with different dwell time of 0.67 hours, 9.8 hours and 49.8 hours. Four different types of TBCs were investigated in this study: two types of EB-PVD and two types of APS. The EB-PVD types include as-coated and grit blasted (Ni,Pt)Al bondcoats on single crystal substrates namely CMSX-4 and Rene-N5, respectively. The APS TBCs include APS and LPPS MCrAlY bondcoat on Haynes 230 and MAR-M-509, respectively, former being a Ni-base and later being a Co-base alloy. Microstructural analyses of TBCs were carried out using X-ray diffraction (XRD), scanning electron microscopy (SEM) equipped with X-ray energy dispersive spectroscopy (XEDS). Summarized in Table 1 are the primary NDE and microstructural analysis techniques employed in this study to examine the critical materials phenomena associated with TBC failure.

Table 1: Primary NDE and microstructural analysis techniques employed in this study to examine the critical materials phenomena associated with TBC failure.

Main factors Associated with TBC Failure	Potential NDE Technique	Microstructural Analysis
Thickness/Growth of TGO	EIS	SEM, EDS
Polymorphic Transformation of Al_2O_3 in TGO	PSLS	-
Residual Stress in α-Al2O3 TGO	PSLS	-
Formation of Ni/Co Rich TGO		SEM, EDS
Sintering of YSZ	EIS	SEM
Phase Transformation of YSZ	XRD	
Adhesion Integrity of TGO/Bondcoat Interface and YSZ/TGO Interface	PSLS, EIS	SEM

The main objective of this study was to indentify the damage initiation/accumulation due to continuous furnace cyclic oxidation of APS and EB-PVD TBCs by NDE techniques, namely PSLS and EIS, and microstructural analyses, so that microstructural degradation of TBCs can be correlated to the NDE parameters with respect to TBC failure mechanisms. This objective was achieved with the following goals and associated tasks.

1. Determine furnace thermal cyclic lifetime for four (two types of EB-PVD and two types of APS) different types of commercial production TBCs.
2. Evaluate and examine four (two types of EB-PVD and two types of APS) different types of commercial production TBCs as a function of thermal cyclic oxidation concurrently by PSLS and EIS:
    a. Measurement and analyses of PSLS for documenting the evolution in phase transformations and compressive residual stress, including stress-relief (e.g., spallation) in the α-Al_2O_3 scale within the TGO as a function of furnace thermal cycling.

b. Measurement and analyses of electrochemical impedance for documenting the evolution in sintering, micro-cracking, TGO growth as a function of furnace thermal cycling.

3. Extensive microstructural analyses of four (two types of EB-PVD and two types of APS) different types of commercial production TBCs as a function of thermal cyclic oxidation using SEM equipped with XEDS.
4. Establish correlations among selected NDE parameters, microstructural degradation/development, and failure mechanisms for EB-PVD and APS TBCs.

2 LITERATURE REVIEW

2.1 Thermal Barrier Coatings

Industrial gas turbines, both land base and aero engines, are dependent on TBCs for a greater efficiency achieved with higher operating temperatures. Superalloys used in these engines offer the structural integrity to hot components and the operating temperatures exceeding 1300 °C which is pushing the limits of superalloys.[31] This was all made successful in applying a thin protective layer called thermal barrier coatings. These coatings have evolved for 50 years and successfully helped in increasing the engine performance with increasing firing temperatures. Technology for development of TBCs encompasses different chemistry, processing techniques, physical appearance, and TBCs are applied on hot components primarily for thermal protection. In this section, the processing and advancement of TBCs are introduced.

2.1.1 Selection of materials for Thermal barrier coatings

Design of TBCs depend on material selection, which endures very tough environment namely, corrosion and oxidation resistance. Table 2 lists some design requirements that are mandatory for TBCs. The requirements for metallic bondcoat are similar to that stand alone metallic coating or overlay coatings which is oxidation resistance and capable of acting as an aluminum reservoir. At operating temperatures, the bondcoat should form a protective α-Al_2O_3 scale with good scale adherence. The primary objective of TBCs is to provide thermal insulation to hot components at operating conditions and the magnitude of temperature reduction is inversely proportional to thermal conductivity. In an typical engine (aero/land) environment the

turbine inlet temperature are in excess of 1649°C (3000°F) and all the hot components along the gas flow should endure/survive in this environment without melting. In addition TBCs should have good oxidation resistance and a thermal expansion coefficient closer to that of bondcoat superalloy.

Table 2. Typical design requirements for thermal barrier coatings.

Metallurgical Property	Criteria	Rationale
Melting Point	High	Operating at high temperatures
Thermal conductivity	Low	Thermal conductivity inversely proportional to temperature reduction
Thermal expansion co-efficient	High	co-efficient of thermal expansion should be as close in magnitude to superalloy substrate and bondcoat
Stability	Stable Phase	Phase transformation will be structurally detrimental
Oxidation resistance	High	High operating temperatures result in highly oxidizing environment
Corrosion resistance	Moderate to high (depend on Cr^{3+} concentration)	Operating environment to be corrosive
Strain Tolerance/Fracture Toughness	High	Cyclic conditions imposes large strain ranges

2.1.2 Ceramic Topcoat Chemistry

Zirconia based ceramics have been utilized as a choice of chemistry for thermal barrier coatings.[32] According to Figure 2 pure zirconia undergoes polymorphic phase transformation from monoclinic to tetragonal at 1170°C , from tetragonal to cubic at about 2370°C and with melting temperature at 2690°C during heating and cooling. Figure 3 shows the crystallographic structure of the cubic, tetragonal and monoclinic phases. The tetragonal to monoclinic phase transformation results in 3-5% volume increase from cooling zirconia from a high temperature. This volumetric transformation can result in cracking, crumbling and loss of structural integrity.

Alloying zirconia with rare earth oxides such as CaO, MgO, Y_2O_3, Sc_2O_3, In_2O_3 and CeO_2 inhibits the phase transformation, and stabilizes high temperature phase resulting in elimination of volume change. Yttria stabilized zirconia (YSZ) is a choice of material for many high temperature applications.

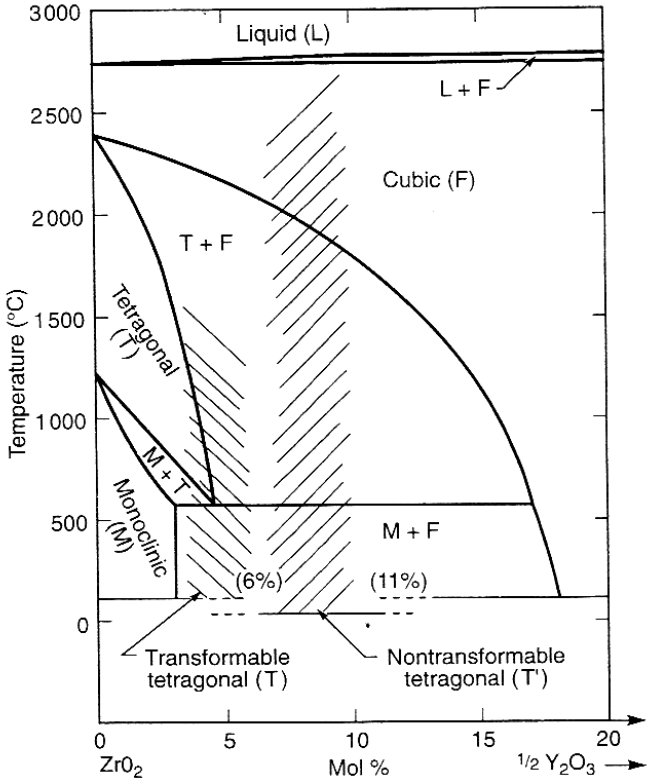

Figure 2. Phase diagram of ZrO_2-Y_2O_3 system. [33]

From the binary phase diagram, a mixture of 2-3 mol% Y_2O_3 with zirconia solid solution sintered at 1400-1600°C and cooled at appropriate rate will not yield the equilibrium monoclinic and cubic phase but a metastable phase will be retained. [34] This phase is referred as the tetragonal zirconia polycrystalline (TZP) phase, and to distinguish this phase from the other systems and phases formed, it is referred as ytttia-tetragonal polycrystalline (Y-TZP) phase.

Similarly, a 4-5mol% Y_2O_3 in zirconia solid solution heated at 2200-2400° or above cubic phase region and rapidly quenched will yield a metastable tetragonal (t') phase. This phase is referred as partially stabilized zirconia (Y-PSZ or PSZ) and has properties different to Y-TZP phase. The t' phase has higher yttria content than that allowed by the phase diagram (e.g., higher that t-phase).

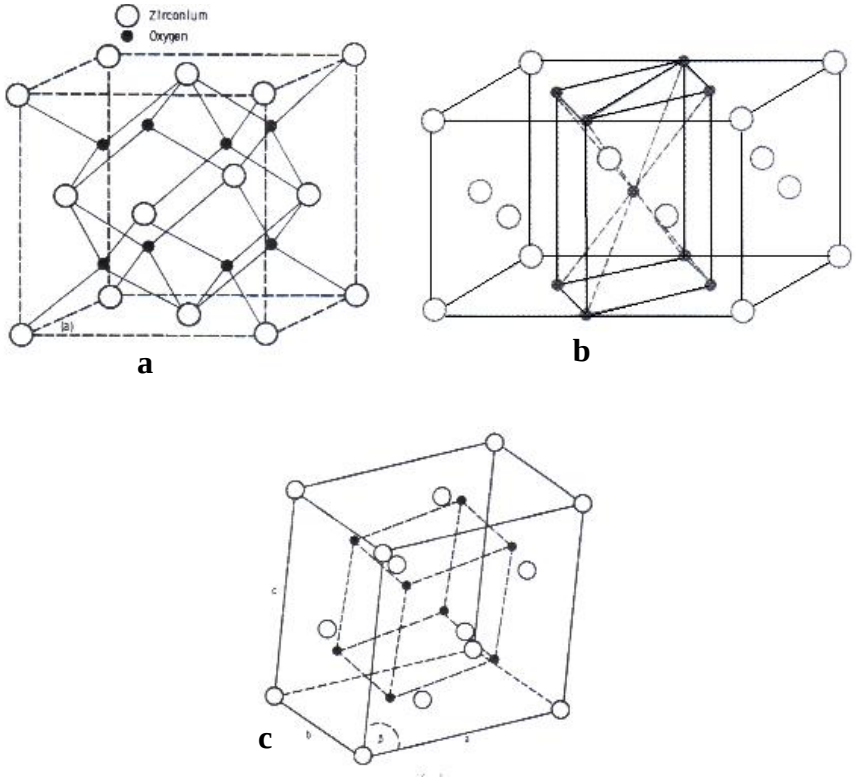

Figure 3. Crystallographic structure of (a) cubic (b) tetragonal (c) cubic ZrO_2.

The TZP (t) zirconias exhibit very high strength (1 GPa) and high fracture toughness greater than $15Mpa\sqrt{m}$ and they are considered as one of the strongest ceramics. Because of their high fracture toughness there is a wide interest in TZP for extrusion dies, cutting instruments, machine tools, wear parts in engines and machinery. The t-phase undergoes phase transformation under high stress (e.g., crack tip) and transforms to m-ZrO_2 phase. In contrast the t' phase does not transform under mechanical stress and so called non-transformable tetragonal

phase. The transformations occurring in t and t' phases are largely accepted by ceramists: (1) the transformation of cubic to tetragonal phase is diffusion controlled (2) the rapidly quenched t' phase is formed by diffusionless transformations, and is characterized by anti-phase boundaries (APBs) which result in reduction in symmetry during the phase transformation and (3) the t-m transformation toughening process is Martensitic with the grain size and Y_2O_3 content being the primary factors determining the martensitic start (M_s) temperature transformation.[31]

The amount and choice of oxides determines the high temperature performance of TBCs. Magnesia and yttria are choice of ceramics used as stabilizers for zirconia, where magnesia finds its application on hot components in the combustion side whereas yttria finds itself in the hot components of turbine section. As determined from burner rig experiments by Stecura et.al., [35,36,37] maximum thermal cycle lifetime is provided by the t' partially stabilized zirconia within narrow range about 6-8w%. This is shown in Figure 4. The t' phase in the YSZ can be deposited by processes capable of adding enough energy to raw materials to melt, evaporate or chemically fragment to dimensions that can be deposited with adequate cohesive and adhesive strength. One kind of process that can deliver high energy based on phenomenon of plasma.

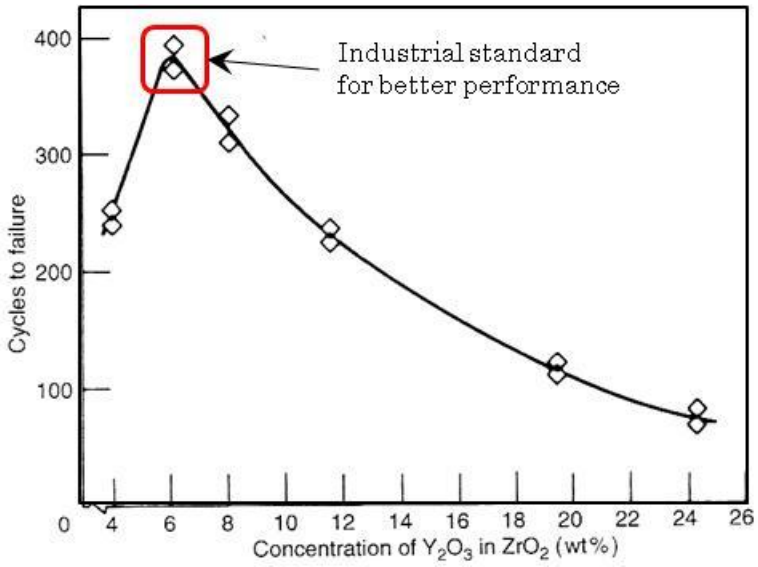

Figure 4. Effect of yttria content on thermal cyclic life of YSZ thermal barrier coatings. [35]

2.1.3 Air plasma sprayed TBCs

In this process, a plasma plume melts the coating feedstock, which is in the form of powders, and deposits on the coating surface. [38, 39] The plasma is created in a plasma gun, and a schematic representation of the plasma gun is shown in Figure 5. This process is performed at atmospheric condition so it is referred as air plasma spray or atmospheric plasma spray coating. A DC potential is struck between a tungsten anode and tungsten cathode, plasma is generated using a mixture of argon plus hydrogen or hydrogen plus nitrogen. Typical plasma temperatures are in the range of 6000-12000° C. The powder is fed internally or externally using a carrier gas (argon) into the plasma plume where the plasma drives the particle onto to a target with a velocity of 200-600m/s. The injection velocity of powder particle is critical because plasma behaves as a viscous fluid. The particle sizes can vary according to the application of coating but, in general, they are around 40-100 μm, and the standoff distance for coating is around 10-50 cm.

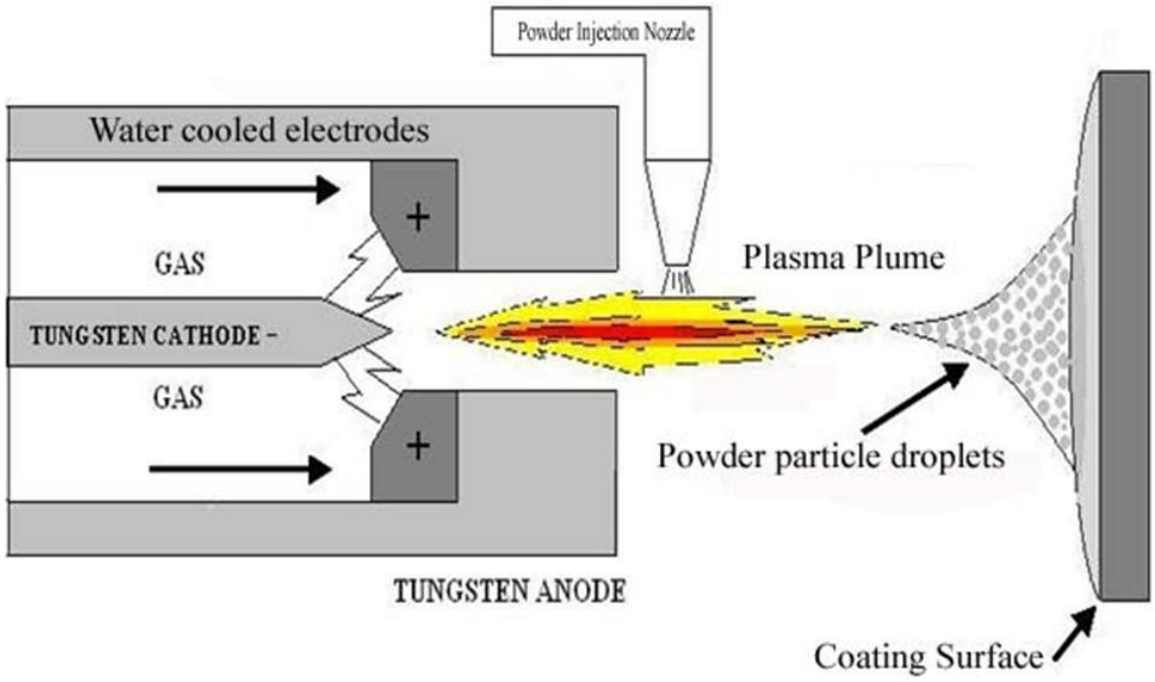

Figure 5. A schematic illustration of air plasma spray process.

The resulting microstructure of APS TBCs is shown in Figure 6. From the process and cross-section it is understood that the ceramic topcoat adheres to the bondcoat by means of mechanical interlocking. Therefore for APS coating, bondcoat surface roughness is critical for better adhesion. Also from Figure 6, we observe that the MCrAlY coating can be deposited by APS technique. This particular type of bondcoat commonly employed in combustion coating hardware. The ceramic layer contains 10-15 % volume porosity, which is critical for lower thermal conductivity. Effect of density/porosity can influence the thermal cycle life of TBCs as shown in Figure 7 .

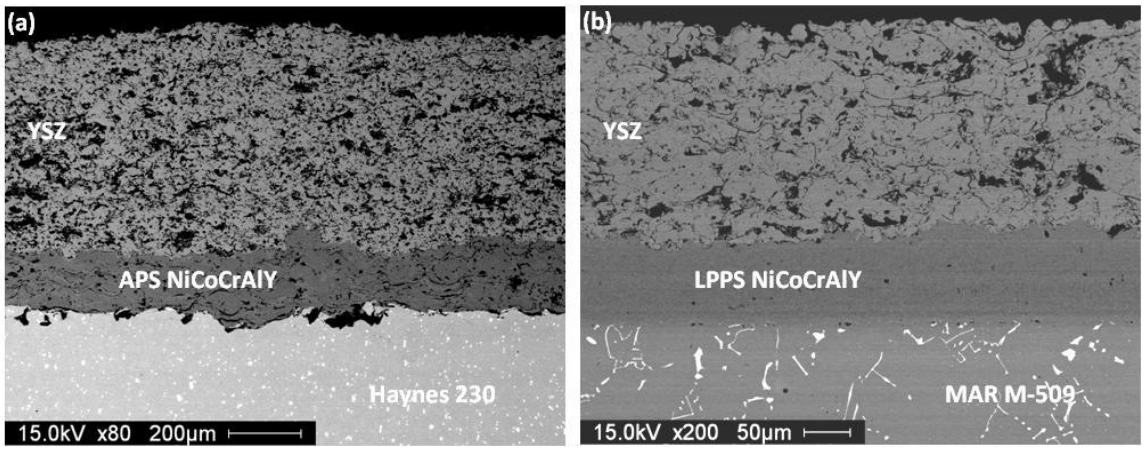

Figure 6. Typical cross-sectional microstructure of APS ceramic coating on (a) APS bondcoat (b) LPPS bondcoat.

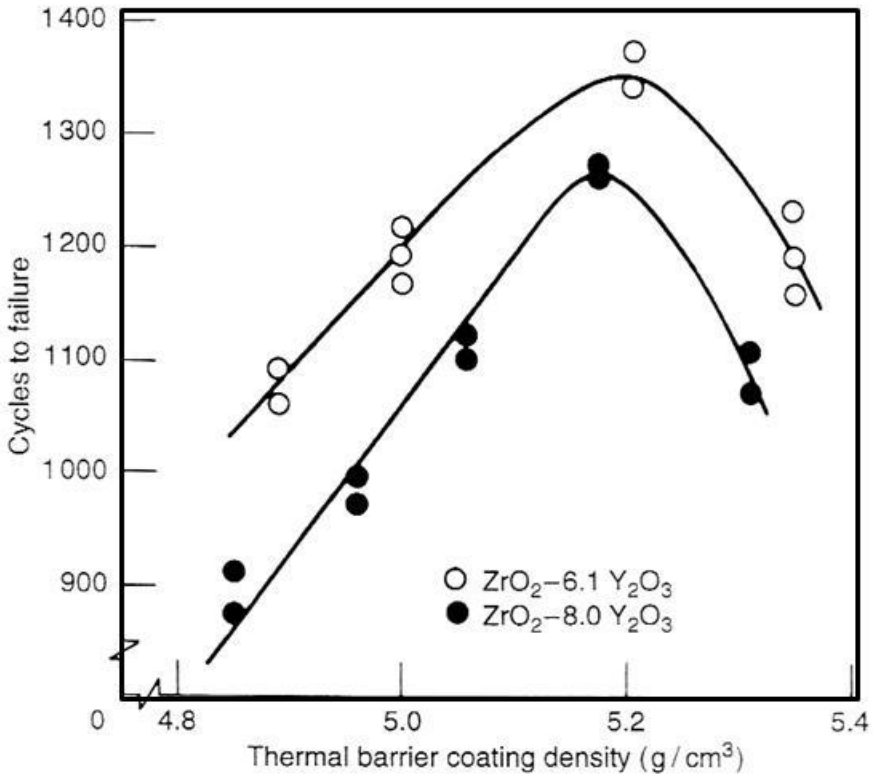

Figure 7. Effect of the ZrO_2 layer density on the thermal cycle life of ZrO_2-Y_2O_3 thermal barrier coatings.[35]

Reproducibility of APS coatings is an ongoing problem in the coating industry. One of the problems identified by Rigney et al. [40] is YSZ starting powders, and was demonstrated using 5 different processes; (1) spray drying (2) spray drying and sintering (3) sintering and

crushing (4) casting and crushing and (5) casting, crushing and fusing. The thermal cycle life was found to vary from 40-100 hours at 1093°C. It was concluded that critical factors were particle size and uniformity, chemical homogeneity, and method of manufacturing. From these results, no direct correlation could be made between the cyclic life and phase constituents, except that the shortest-lived coatings had the most monoclinic phase and longest coating had least tetragonal phase.

2.1.4 Electron beam physical vapor deposited (EB-PVD) TBCs

This process is a modification of high-rate vapor deposition used in metallic coatings for depositing ceramic layer of TBCs. [4,41] The basic principle of EB-PVD process consists of heating the raw materials (YSZ ingot) with the focused high-energy electron beam. This energy melts and vaporizes the ingot, the part to be coated is held over the pool. The vapor deposits on to the part and solidifies, which results in columnar growth of the YSZ. Columnar grains as shown by the microstructure in Figure 8 accommodate the strain by free expansion (or contraction) of columns into the gaps within the coating, which results in negligible stress buildup. [41] Also during initial coating deposition, thin layer (< 2μm) of dense ZrO_2 is formed to promote chemical bonding between the ZrO_2 and bondcoat, but if it becomes too thick (> 2μm), it may sustain and transmit compressive stresses sufficient to cause cracking within the outer ZrO_2 coating.

Other advantage of this type of coating is bondcoat surface roughness for ceramic deposition is not as critical as APS ceramic topcoat deposition. Bondcoats for EB-PVD TBCs are normally of MCrAlY or (Ni,Pt)Al type. For good adhesion, the bondcoat surface should be

smooth or preferably polished [42], in contrast to plasma-sprayed TBCs, which require a rough bondcoat.

Despite the aerodynamic efficiency and higher durability, EBPVD TBCs in general have (1) higher costs and process time for (2) higher thermal conductivity by a factor of 2 as compare to plasma sprayed TBCs. [43]

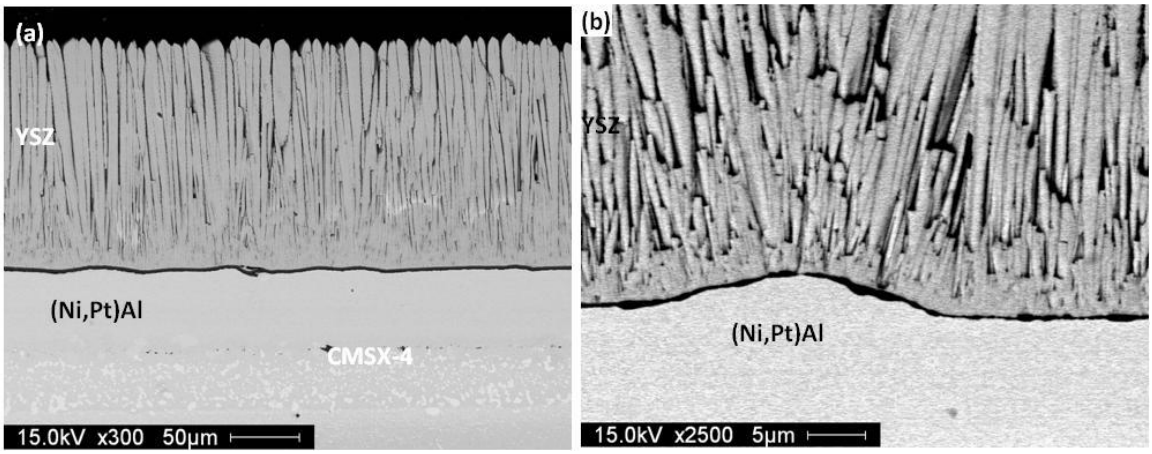

Figure 8. Cross-sectional microstructure of EB-PVD TBCs on (Ni,Pt)Al bondcoat and CMSX-4 substrate.

2.2 Bondcoats

Superalloys which provide the structural integrity to gas turbine are generally developed with optimized structural properties such as tensile, creep and fatigue strength. These properties are maintained and achieved to some extent at the expense of environmental resistance. The environmental resistance (corrosion/oxidation) therefore has to be provided by the metallic coatings. [44] These coatings do not carry any load but differ in microstructure and chemistry to provide good oxidation and corrosion protection. The following requirements listed in Table 3 play multiple roles in protecting the hot components of a gas turbine.

Table 3. Requirements of bondcoat for reliable and durable TBCs. [45, 46]

Property	Underlying principle
Oxidation/Corrosion resistance	Must form a protective surface scale (Al_2O_3/Cr_2O_3) of uniform thickness and be thermodynamically stable Slow growth rate of protective surface scale Adherent surface scale High concentration of scale former
Stability	No undesired phase transformation within the coating Low diffusion rate across interface at service temperatures Compositional stability across the interface Minimal brittle phase formation
Adhesion	Must adhere to the coating substrate Thermal expansion should be close to substrate properties avoiding thermal stress Minimal growth stresses Optimized surface condition
Structural Properties	Should be able to withstand creep, fatigue and impact loading of surface without failure

As discussed earlier the chemical composition of the bondcoat can consist of Ni,Co, Al, Cr, Al, Pt, Ta, Si, Y etc. Each individual element play a significant role in TBC lifetime and its corrosion/oxidation behavior. The advantages and disadvantages of these elements with respect to the engine environment are highlighted in Table 4.

Table 4. Elemental Constituents of metallic/overlay coatings, their functions and effects.[46]

Elements	Role	Detrimental Aspects
Ni	Major constituent of coating/substrate in solid solution. Provides strength.	Reacts with sulfur causing degradation of coating system
Co	Major constituent of coating/substrate in solid solution. Provides strength.	Reacts with sulfur causing degradation of coating system
Al	Primary element in providing oxidation resistance	Large concentrations lowers melting point
Cr	Constituent of coating/substrate alloy. Contributes to hot corrosion resistance and oxidation resistance up to 816°C	Lowers Creep strength
Ta	Hot corrosion and strength are enhanced	
Si	Enhances oxidation and type II (<850° C) hot corrosion	Increase in silicon concentration leads to formation of brittle phases
Hf, Y, Y2O3 and reactive elements	Improves adherence of alumina and chromia scales	Large amounts are detrimental
Pt	Improves oxidation and hot corrosion resistance	

2.2.1 Air plasma sprayed Bondcoats

The basic principle for application of air plasma sprayed bondcoat is same as application of air plasma sprayed ceramic layer. A schematic of the plasma gun is shown in Figure 5. MCrAlY powder is injected in the powder injection nozzle and deposited on to the coating substrate. [47, 48] The resulting bondcoat has superior surface roughness in the range of 5-13 μm. The cross-sectional microstructure of APS bondcoat compared to VPS bondcoat thermal barrier coating is shown in Figure 9. This type of metallic bondcoat results in high oxide content due to in flight oxidation of molten particles. This could result in reduced capability to protect substrate from oxidation and corrosion resistance. The in flight/process related oxidation can be eliminated in "inert gas shrouded" plasma spray. In the shrouded plasma spray, inert gas is injected

surrounding the plasma plume to create a sheath. This sheath limits access of air to the molten particles.

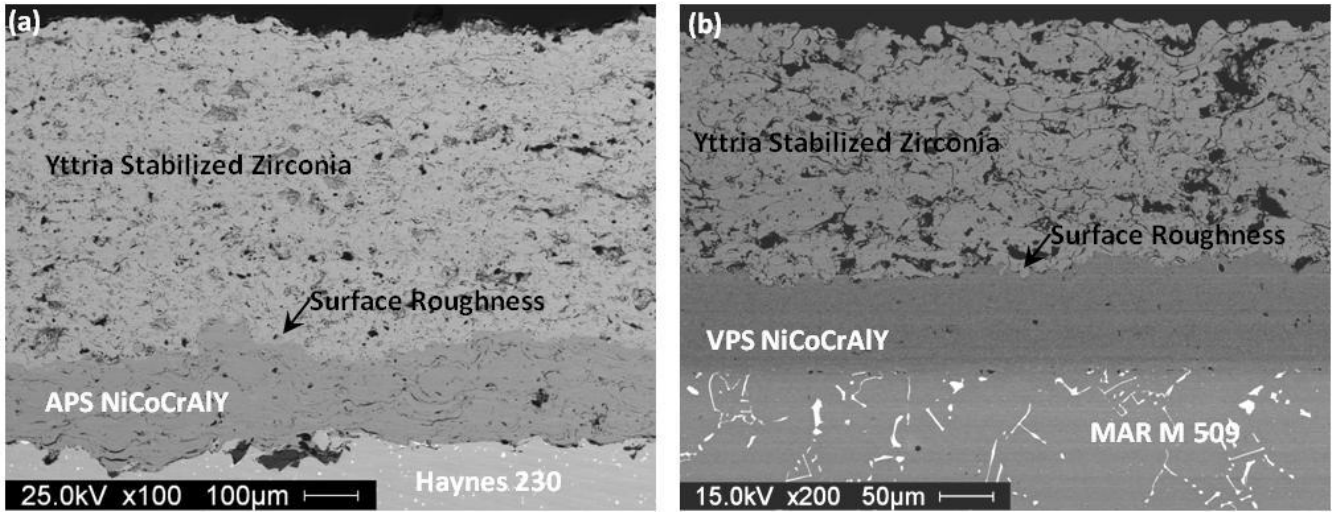

Figure 9. Cross-sectional microstructure and bondcoat surface roughness comparison (a) APS bondcoat on APS topcoat (b) LPPS bondcoat on APS topcoat.

2.2.2 Low pressure plasma spray or Vacuum plasma spray (LPPS/VPS) Bondcoats

This process was designed by Muehlberger, 1998 [5,49] to eliminate oxidation during deposition of metallic coating. In this process the part and gun are enclosed in a vacuum chamber which is pumped down and back filled with argon at a chamber pressure of 30-60 torr. This system also offers flexibility in preheating and cleaning the part after grit blasting (coating surface preparation) by the process of reverse transferred arc prior to the initiation of coating deposition. A schematic representation of the LPPS system is shown in Figure 10. The cross-sectional microstructure of typical LPPS bondcoats is shown in Figure 11. Advantages of this type of coating are as follows:

- Negligible in-flight oxidation of molten metal droplets during their transit in air.

- Compositional flexibility with high deposition rates can be achieved through liquid droplet transfer.
- Intermetallics can be sprayed using this process. [50]

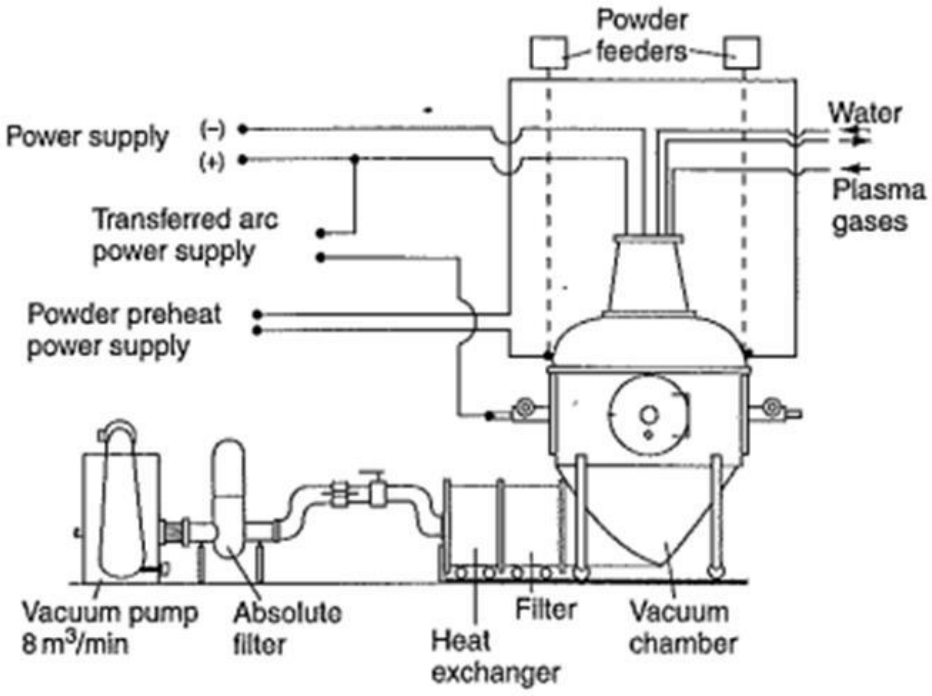

Figure 10. A schematic illustration of LPPS/VPS coating system.

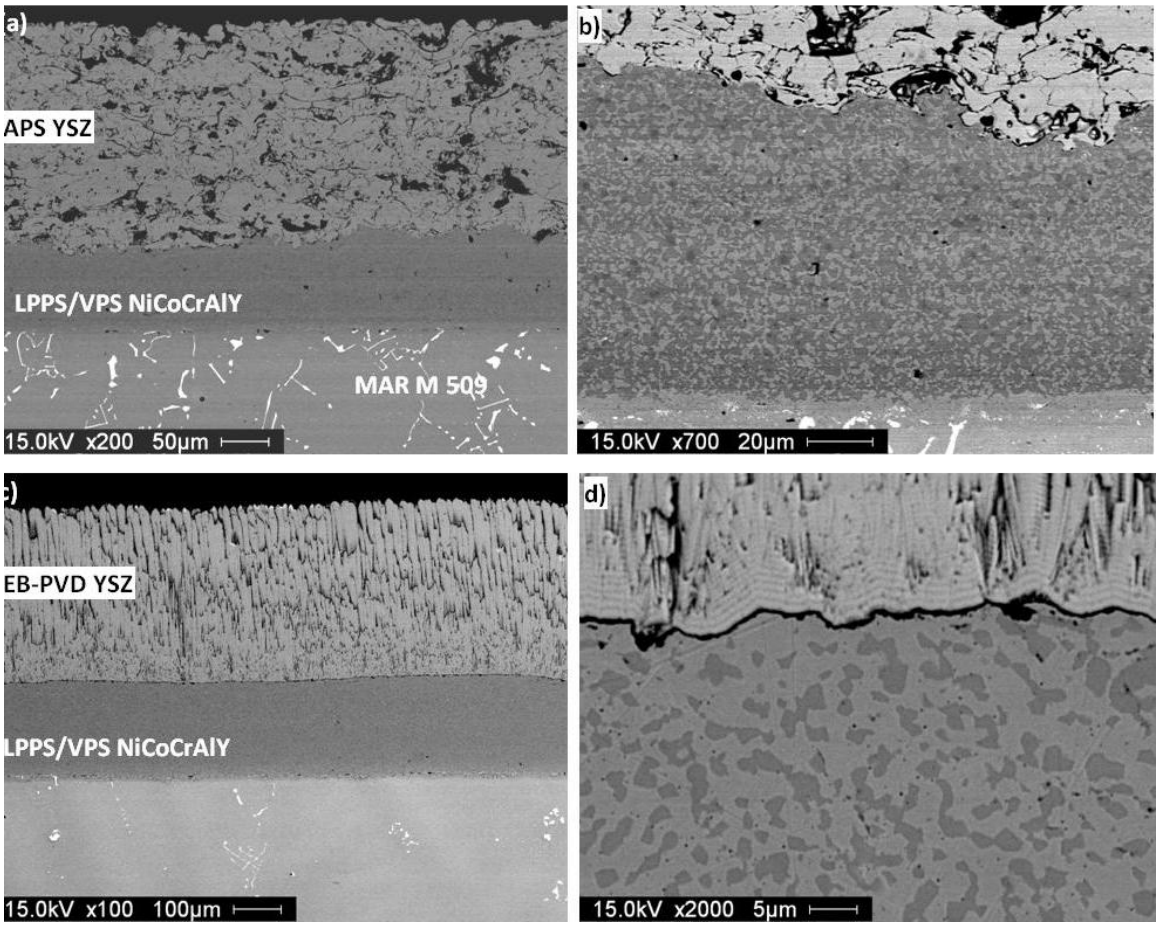

Figure 11. Cross-sectional microstructure of LPPS bondcoat (a,b) APS ceramic topcoat (c,d) EB-PVD YSZ coatings.

2.2.3 Diffusion coatings [51,52]

There are various ways to achieve these types of coatings as illustrated in Figure 12. In general, the process can be summarized as:

- Generation of Al, Cr or Si containing vapors
- Transport of vapors to the coating/component surface
- Vapor reacts with the substrate followed by associated diffusion process

- Diffusion heat treatment/ stabilization heat treatment necessary to achieve desired microstructure, composition and restoration of base metal properties.

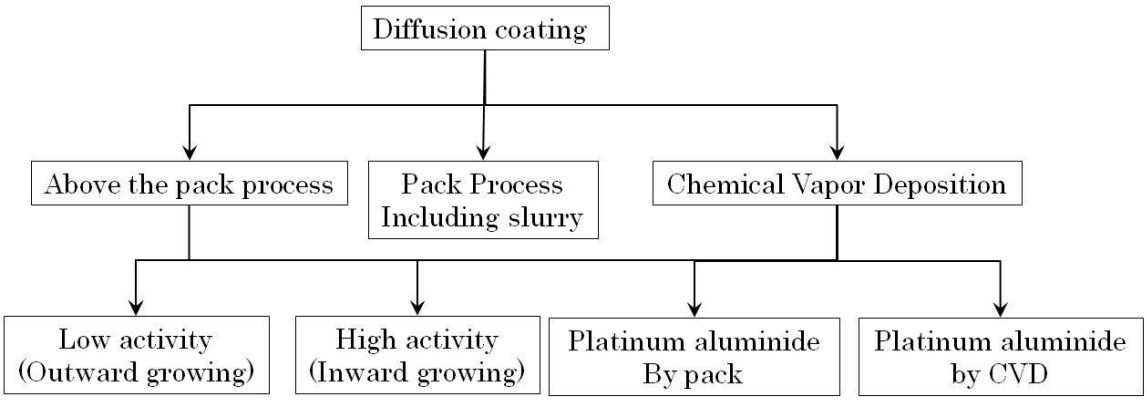

Figure 12. Different types of diffusion aluminide coating processes.

2.2.3.1 Chemical Vapor Deposition Process

This process utilizes halide vapor such as $AlCl_3$, created in external generator by passing HCl or Cl_2 gas over aluminum pellets at temperatures about 300° C. The parts to be coated are fixed inside a retort in CVD furnace which is held at 1000-1100°C. One of the major advantages of CVD process is the part that needs to undergo additional heat treatments. This can be achieved in the same chamber. The above process is typically used to produce nickel aluminide coatings.

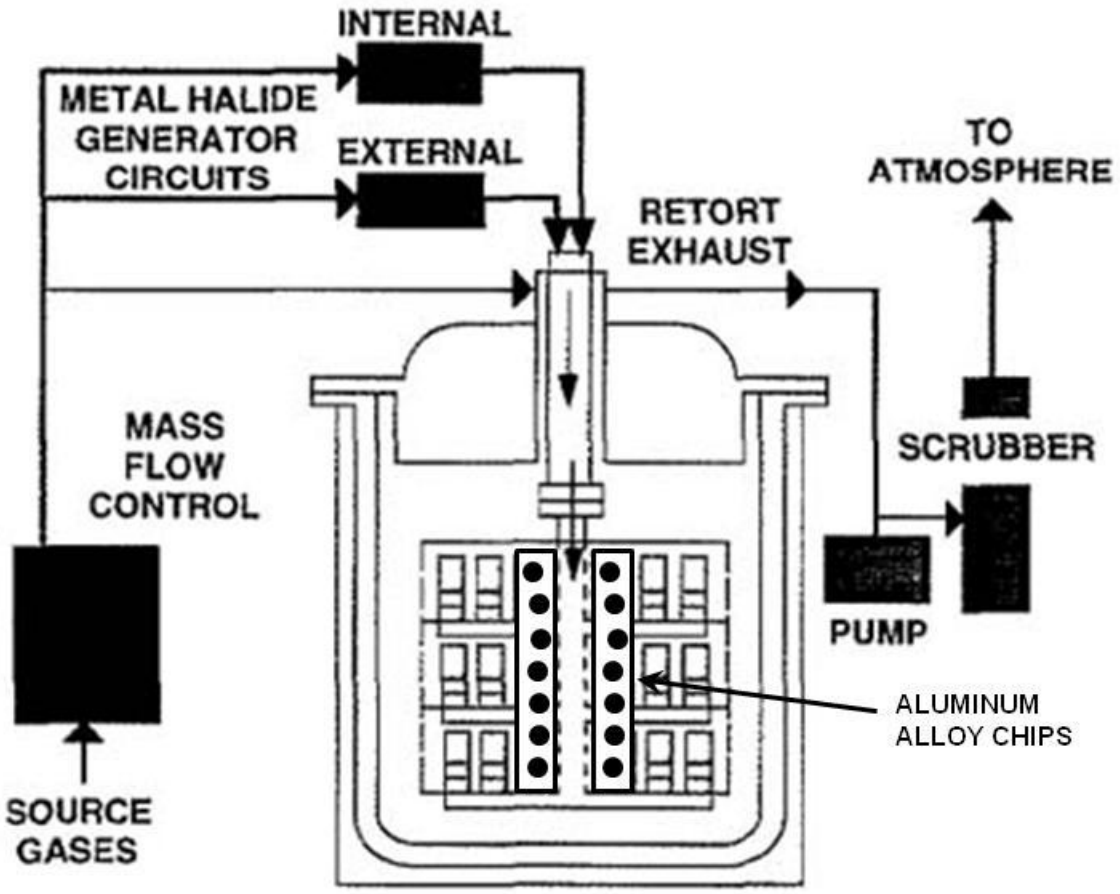

Figure 13. Chemical vapor deposition chamber for high- activity aluminide coating. [53]

In case of (Ni,Pt)Al coatings the first step is electro plating or physical vapor deposition of thin layer of Pt (2-10 μm) followed by diffusion heat treatment (vacuum or inert atmosphere 950-1000°C for few hours). This is done for enhancing the Pt adhesion to the base metal coating surface. After this process the coating substrate is subsequently aluminided by pack or CVD processes. This process yields a better oxidation resistance coating where the bondcoat primarily forms pure α-Al_2O_3 scale. [53] Cross-sectional microstructure of EB-PVD TBCs with (Ni,Pt)Al bondcoats is shown in Figure 14 .

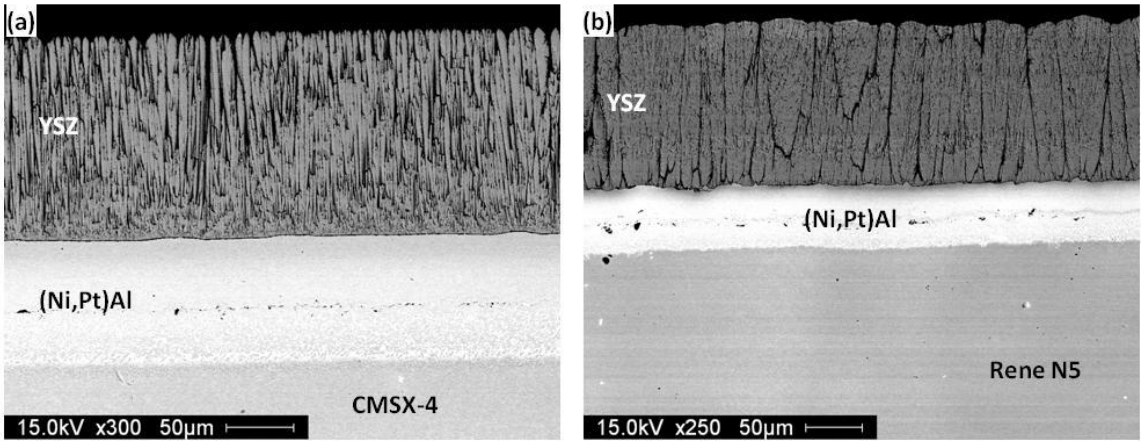

Figure 14. Cross-sectional microstructure of diffusion aluminide (Ni,Pt)Al bondcoat of EB-PVD TBCs on different superalloy substrates.

2.2.4 High velocity oxygen fuel (HVOF) Bondcoats

This is a novel technique derived from D-Gun™ process and recently has a gained an application in deposition of MCrAlY coatings. This process yields microstructure similar to that of LPPS/VPS process but with better cost-effectiveness. The basic principle of this process starts with an ignition of combustible mixture of fuel and oxygen under high pressure in the combustion chamber to create a continuous flame. The combustion product exits the nozzle at supersonic velocity (close to Mach 4) with associated "shock diamonds". Coating material in the form of powder is injected into the flame axially or radially. The heated powders are carried in the expanded jet of gas, which on impact on the substrate plastically deform, cool and solidify. [5, 6] A schematic of HVOF system is shown in Figure 15. This particular process is successfully used to deposit wear-resistant coatings such as WC/Co and Cr_3C_2/NiCr. The microstructure of HVOF- sprayed coatings is characterized by low porosity (<2%), low oxide content (<2%) and clean coating substrate interface. MCrAlY coatings deposited by this method yields similar or equivalent quality to that obtained by LPPS as shown in Figure 16 .

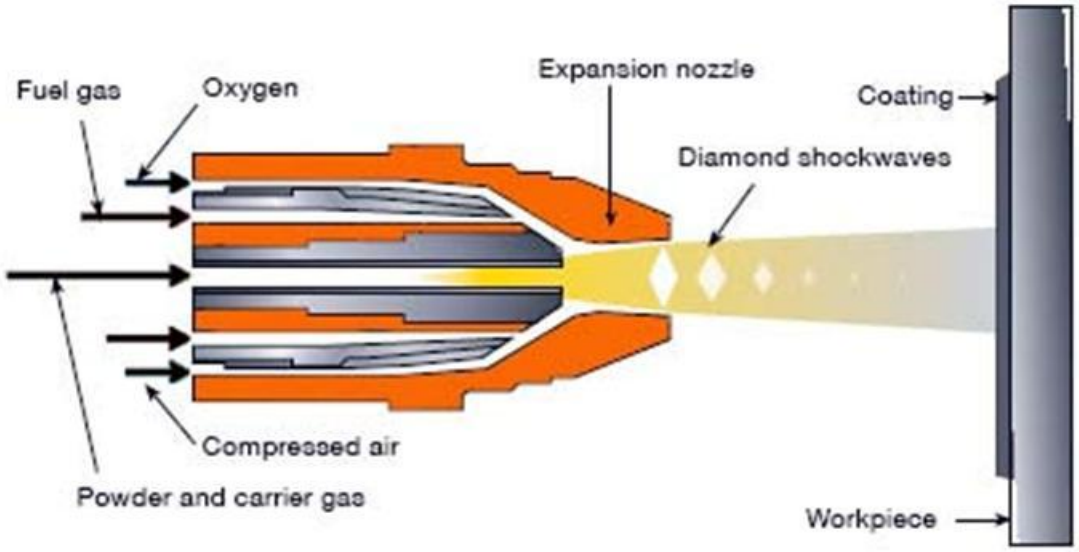

Figure 15. A schematic of HVOF cross-section.

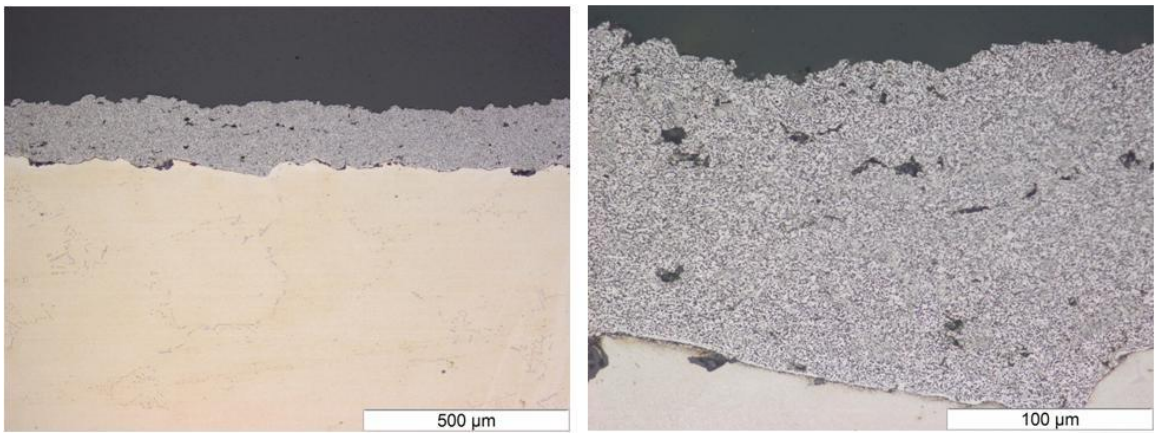

Figure 16. Typical cross-sectional microstructure of HVOF coatings.

2.3 Failure Mechanism in Thermal Barrier Coatings

Continued service exposure of hot section components result in incremental damage, which accumulates with time and cycles. Thermal cycling alone plays a significant role in coating spallation along with mechanical and chemical processes. The growth of the TGO as a consequence of bondcoat oxidation during engine operation is the most important phenomenon responsible for the spallation failure of TBCs. Edge and buckle driven delamination compete as mechanisms for final TBC failure. For this final failure to occur, there needs to be an initiation of crack. For the two types of the TBCs, namely APS and EB-PVD, the failure mechanisms can be different.

2.3.1 Failure mechanism of plasma sprayed TBCs

Plasma sprayed TBCs fail by spallation of the ceramic coating. The driving force for the spallation is the combination of cyclic thermal strain due to CTE mismatch, continued oxidation due to the TGO growth and sintering in ceramic layer. The failure is observed at the vicinity of the TGO but within the ceramic coating.

2.3.1.1 Failure at the bondcoat/TGO interface

In plasma, sprayed TBCs bondcoat surface roughness is undulated/rough for initial mechanical interlocking. At the undulated surface with the formation of the TGO during high temperature exposure, two out of plane stresses are encountered by the TGO. These are tensile and compressive stresses at the crest and troughs, respectively. With prolonged thermal exposure

and continuous growth of the TGO, the out-of-plane tensile stress increases, this causes cracking at the TGO/ bondcoat interface at crest as shown in Figure 17. [54]

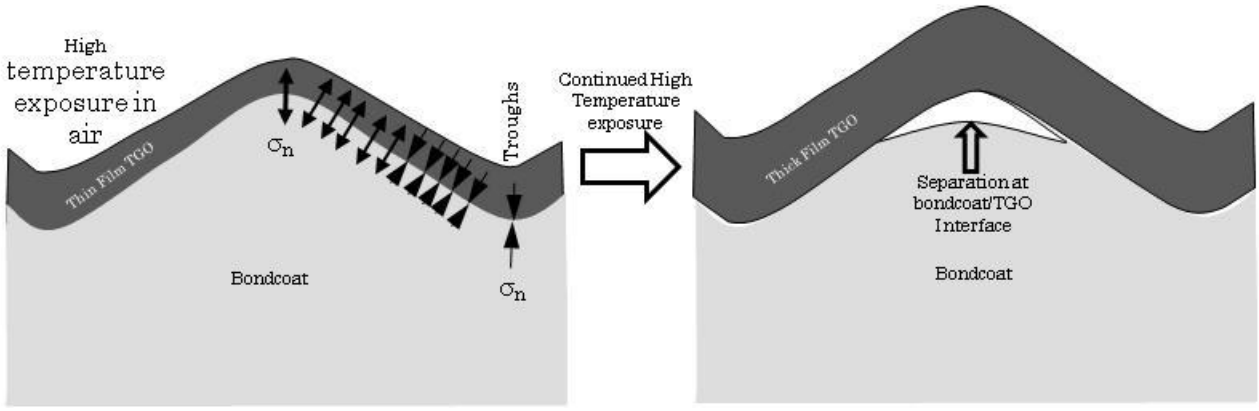

Figure 17. Schematic representations of local separation at the TGO/bondcoat interface caused by residual stress across the interface as a result of film being under compression.

2.3.1.2 Failure at the TGO/ Topcoat Interface and Within TBCs

This particular type of coating delamination is commonly reported for the plasma sprayed TBCs. This type of failure is from out plane stress due to the TGO growth as discussed previously along with thermal expansion mismatch within the topcoat due to sintering. The magnitude of stress from thermal expansion mismatch is an order of magnitude lower than the residual stresses within the TGO. This is because not only sintering takes place but also micro cracking because of topcoat sintering. This porous and cracked ceramic topcoat is much more compliant than the TGO, and it has a relatively lower thermal expansion coefficient mismatch with the bondcoat. Because of the highly undulating nature of the metal/ceramic interface, out-of-plane stress results in the vicinity of the TGO/topcoat interface: tension at the crests and compression at the troughs. Therefore, the compressive stress at the troughs and the tensile stress at the crest result in the fracture of the TBCs at the TGO/ topcoat interface at the crests. The

cracking occurs within the highly brittle topcoat in the vicinity of the crest as shown in Figure 18. Many initiation sites are needed for large scale buckling to happen. [55]

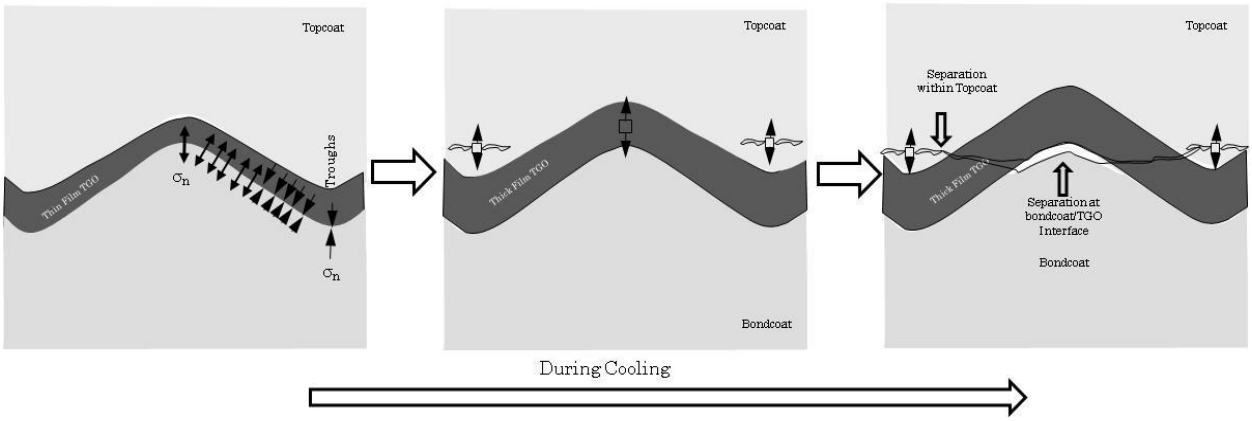

Figure 18. Progressive crack initiation in the topcoat due CTE mismatch and out of plane tensile stresses in the TGO driving a crack within the YSZ and at the TGO/bondcoat interface.

2.3.2 Failure mechanism of EB-PVD TBCs

Similar to APS TBCs, residual stresses in ceramic coating as well as within the TGO play important roles in dictating the failure of EB-PVD TBCs. The residual stresses in the strain tolerant columnar ceramic structure of EB-PVD TBCs would be significantly lower than that within the TGO; hence the failure is seldom concentrated within the ceramic for EB-PVD TBCs. [56]

2.3.2.1 Rumpling/Ratcheting of Bondcoat

This particular type of failure is commonly observed in diffusion aluminide systems with EB-PVD ceramic layer. [57, 58, 59] This failure occurs on the surface defects such as grain boundary ridges associated with CVD process as shown in Figure 19. During high temperature exposure preferential oxidation occurs at these grain boundary and cavities. With the

presence of these ridges the stress field is modified into out-of plane tensile stress at the peak of ridges and in-plane tensile stress at the shoulders of ridges at room temperature. [60] The magnitudes of these stresses were calculated to be 2 GPa, and can cause crack in the TGO near the ridges and shoulders of the ratchet allowing further accelerated oxidation of bondcoat at the grain boundary as schematically illustrated in Figure 20.

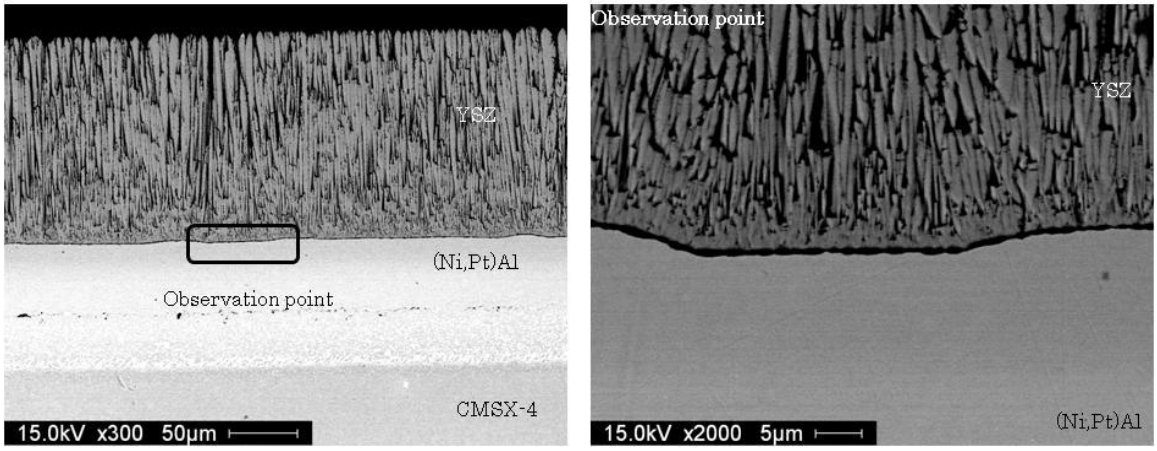

Figure 19. Grain boundary ridges observed in this study on as-coated diffusion aluminide bondcoat on EB-PVD TBCs.

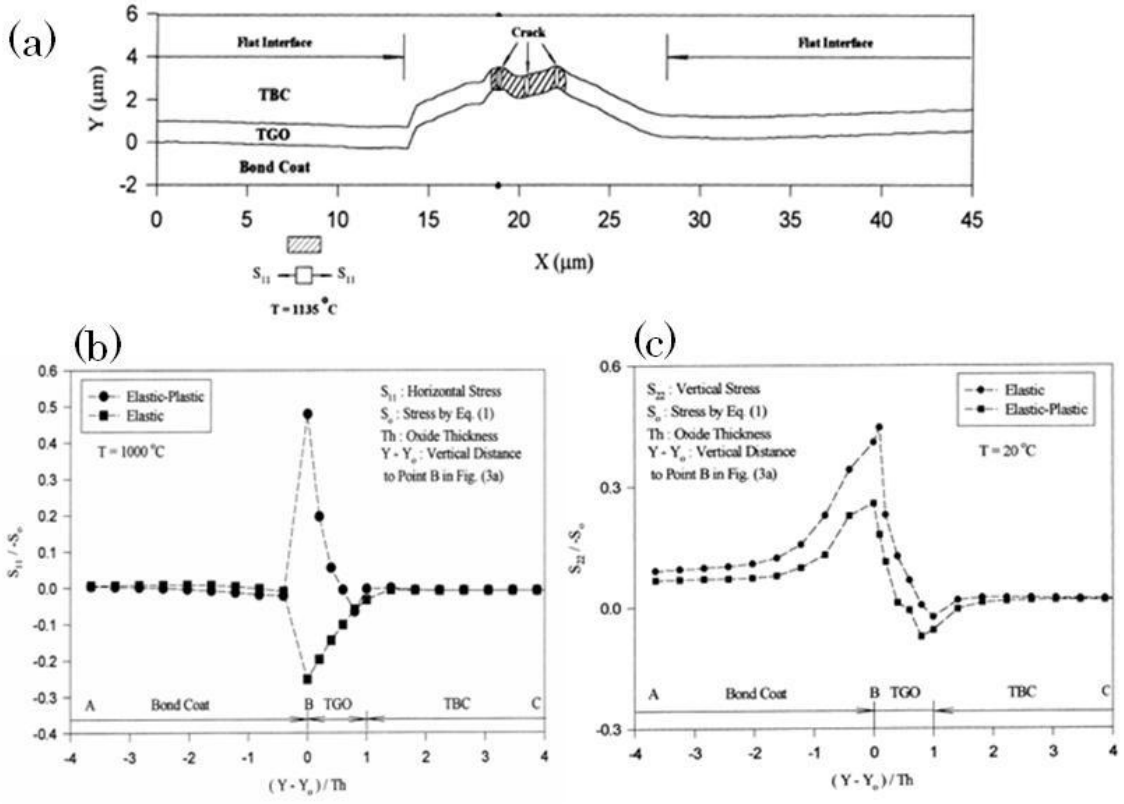

Figure 20. Finite element simulation model results for bondcoat ridge defects (a) simulation mesh geometry (b) horizontal stress at the ridge and (c) vertical stress along the ridge. [60]

The rumpling-driven failure is commonly observed in both diffusion aluminide and MCrAlY bondcoat on EB-PVD systems as shown in Figure 21. The cause for rumpling is from cyclic oxidation that produces a concurrent plastic deformation of bondcoat together with the adherent oxide scale. This phenomenon is generally known to arise from thermal expansion mismatch [61] between the oxide scale and the bondcoat on which oxide scale forms at high temperature or due to oxide scale cracking and spallation. [62, 63]

Rumpling was also observed during isothermal oxidation in vacuum and reported by Panat et al.[65] They found that in the absence of TBCs, critical wavelength for bondcoat

rumpling is not affected by initial surface preparation but is related thermal expansion mismatch stresses between the developing the TGO and the bondcoat. [64, 65]

In case of MCrAlY, rumpling can be observed at early stages and progressively increases in amplitude and contribute to ceramic coating spallation by the increasing the in-plane and out-of plane tensile stress in the TGO. [66] This phenomena was reported to cause no apparent damage to MCrAlY/ TGO interface but damages were observed within the non-compliant YSZ [67]

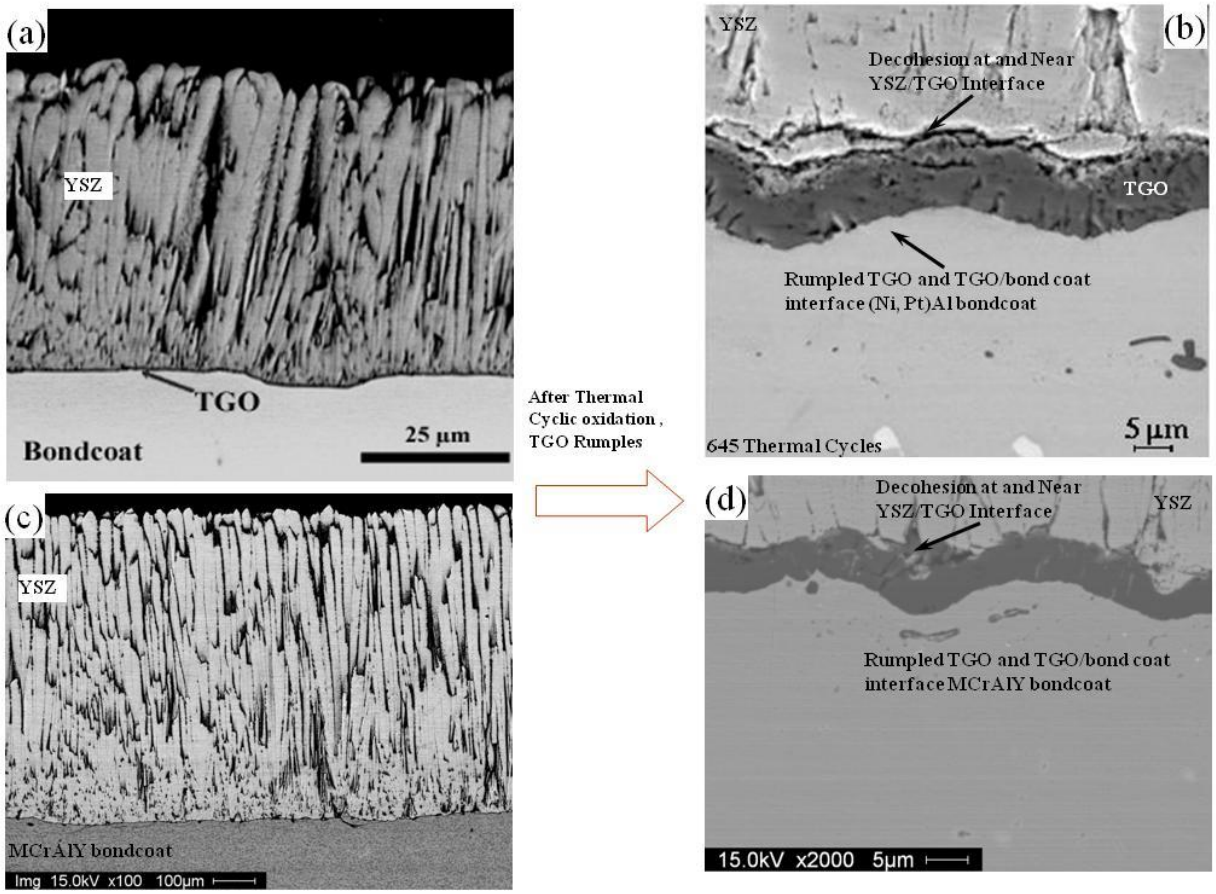

Figure 21. Rumpling observed on different bondcoat systems for EB-PVD thermal barrier coatings. [68,69]

2.3.3 Final Failure Modes

For a gas turbine to function reliably and durably, understanding the final coating failure together with initial damage assessment is critical. It is understood that the TGO plays an important role in coating spallation and final separation occurs at or near the TGO interfaces, and is preceded by a sequence of events that cause buckling and/or edge delamination. The failure mechanisms as well as reliability vary for different types of TBCs, further complicated by application parameters, surface treatments, and thermal exposure. Final failure initiates as an interface separation that grows by thermomechanical fatigue, accompanied by thickening of the TGO, and involves edge delamination and/or buckling with a link up of the TGO/bondcoat interface with the preexisting defects. A schematic of edge and buckling final failure is presented in Figure 22.

"Buckling" by definition occurs when a structure (subjected usually to compression) undergoes visibly large displacements, transverse to the load. This phenomenon is commonly observed in EB-PVD samples, and is the separation of the TGO from the bondcoat over a large area. Buckle propagation is motivated by the strain energy density in the TGO and resisted by the fracture toughness of the TGO/BC interface. The extent of propagation before failure depends on the relative toughness of the TGO and the interface. [70]

Another scenario for a final failure mode occurs when the ceramic coating suppresses the buckling of the TGO. This could happen if there are sufficient voids within the TGO, separating it from the ceramic coating for an area of critical size; it has been proposed that the required critical flaw size should be close to that for the TGO alone.[71] When buckling is suppressed other competing mechanism that can be observed is the edge delamination. Edge-delamination is

probable when the in-plane moduli of the thick topcoat are moderately high, caused by the large elastic strain energy, which develops during cooling. [72]

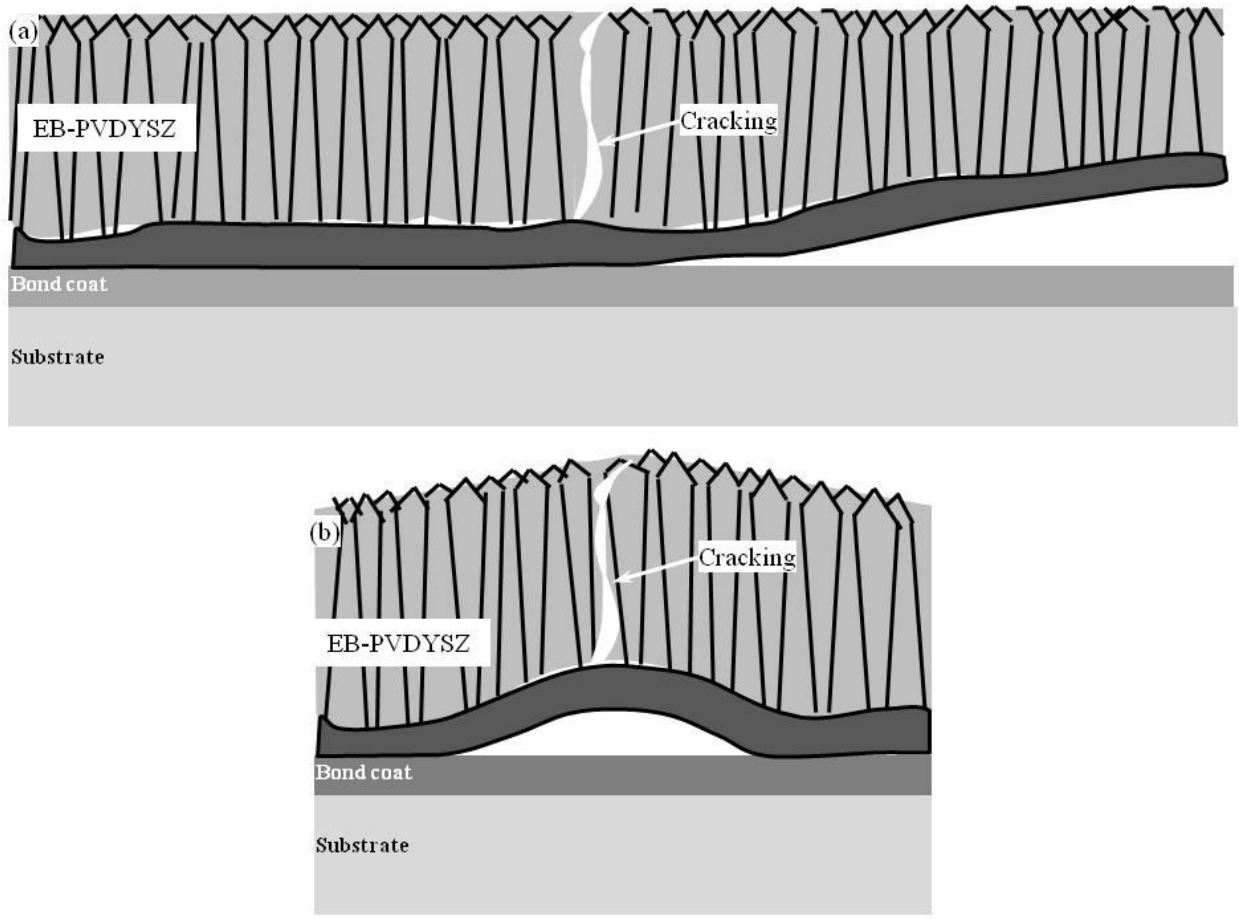

Figure 22. Schematics of (a) edge delamination (b) buckling observed in TBCs.

2.4 Photostimulated Luminescence Spectroscopy

This technique was developed based on Raman spectroscopy principle, and it relies on inelastic scattering, or Raman scattering, of monochromatic light, usually from a laser in the visible, near infrared, or near ultraviolet range. The laser interacts with molecular vibrations, phonons or other excitations in the system, resulting in the energy of the laser photons being shifted up or down. The shift in energy gives information about the phonon modes in the system. [73]

As explained earlier there is a need for NDE technique that can monitor health and damages in TBCs which occurs with time and temperature. Piezospectroscopy was applied to α-Al_2O_3 to measure residual stresses by Grabner in the 1970's. [74] Later, photostimulated luminescence (PL) spectroscopy was developed as a nondestructive inspection technique for the assessment of residual stresses and phase constituents within the TGO scale buried under the YSZ topcoat in TBCs by Clarke et al. [17-21]

PL is an optical method that probes Cr^{3+} dopants incorporated into the Al_2O_3. A schematic diagram is shown Figure 23. The source of excitation is a laser beam with a wavelength of 514 nm, which is chosen to penetrate through the EB-PVD YSZ, and yet be within the optical absorption band of the Cr-doped Al_2O_3. The reflected fluorescence signal is recorded. In the case of stress-free α-Al_2O_3, two distinct peaks appear, which are allowed by the crystallographic symmetry of the Cr^{3+} site in the α-Al_2O_3 crystals, corresponding to the R_1 and R_2 fluorescence doublets shown by the dashed line in Figure 24. For a stress free α-Al_2O_3 these doublets occur near frequencies of 14402 and 14432 cm^{-1}. Under any applied and/or residual stress, the frequency of the Cr^{3+} luminescence shifts systematically (solid line in Figure 24) $\Delta\nu$,

so called piezospectroscopic effect. The frequency shift can be calibrated, and the resulting applied and/or residual stress value in the α-Al_2O_3 scale can be determined based on the relation:

$$\Delta\nu_{stress} = \Pi_{ij}\,\sigma_{ij}^{c} = \Pi_{ij}\,a_{ki}\,a_{lj}\,\sigma \qquad [1]$$

where Π_{ij} is the ij-th component of the piezospectroscopic tensor and σ_{ij}^{c} is the stress state in the crystallographic basis of the host crystal. In a general coordinate system, the stress state, σ_{ij}, is related to σ_{ij}^{c} by the transformation matrix a_{ij}.

When the α-Al_2O_3 is untextured and polycrystalline with small grain size (i.e., smaller than the probing volume), the frequency shift is proportional to the trace of the stress tensor, namely,

$$\Delta\bar{\nu} = \frac{1}{3}\Pi_{ii}\,\sigma_{jj} \qquad [2]$$

If the distribution of grains in the TGO is assumed to be randomly oriented, the frequency shift when TGO is under biaxial stress would be:

$$\Delta\bar{\upsilon} = \frac{2}{3}\Pi_{ii}\,\bar{\sigma} \qquad [3]$$

By measuring the frequency shifts for stress-free and polycrystalline α-Al_2O_3, the biaxial stress can be directly obtained by inverting Eq. (3). The numerical value for piezospectroscopic tensor, Π_{ii}, for R_2 luminescence is 7.61 cm^{-1}/GPa. [75]

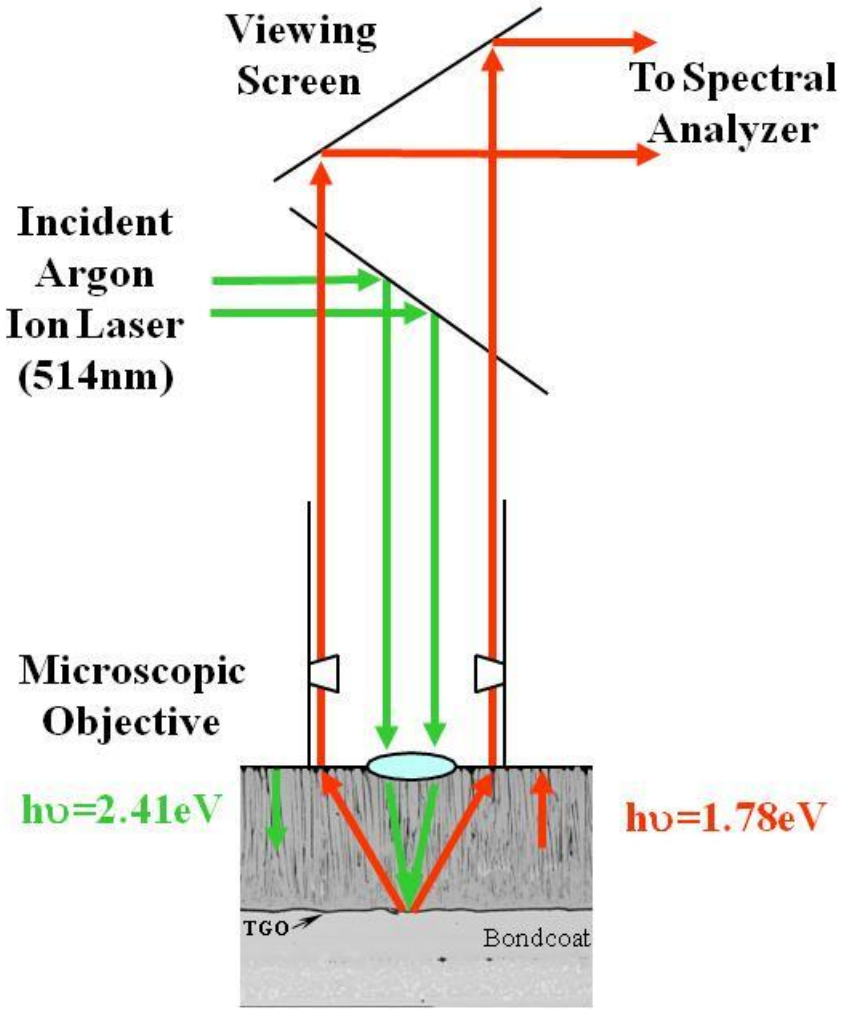

Figure 23: A schematic illustration of photo-stimulated luminescence spectroscopy technique.

Other factors influencing the frequency shift and shape of the luminescence are temperature, and concentration of Cr^{3+} and other impurity ions. Assuming that these contributions are uncorrelated, their net effect on the frequency shift is simply additive:

$$\Delta\nu = \Delta\nu_{stress} + \Delta\nu_{temp.} + \Delta\nu_{conc} \qquad [4]$$

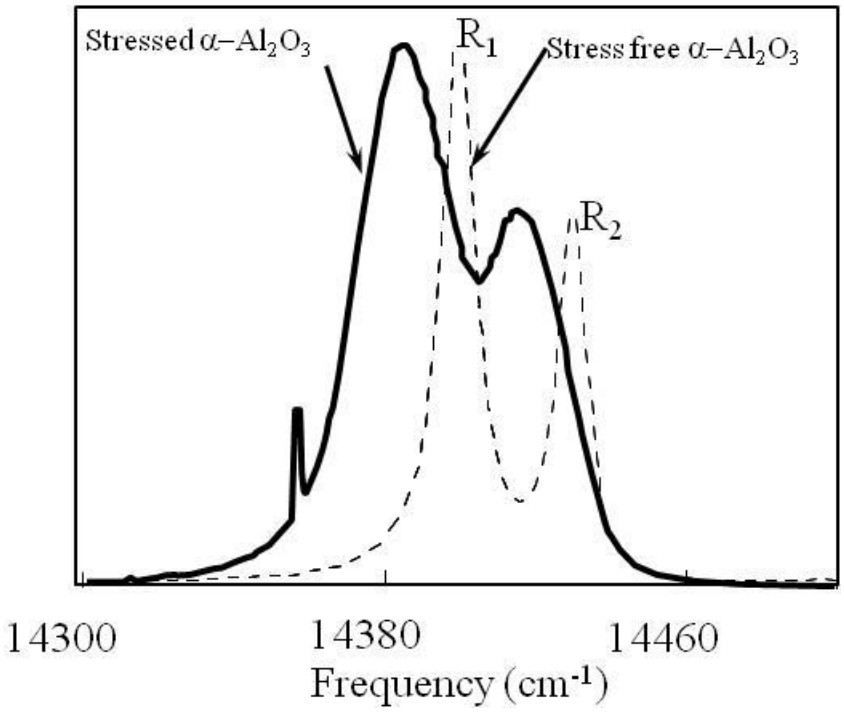

Figure 24: Typical PL spectra from comparing stressed (e.g., compression) and stress free α-Al_2O_3 scale.

The temperature-induced fluorescence shift is described using a scalar factor, β:

$$\Delta\nu_{temp} = \beta(T)\, T \qquad [5]$$

In Eq.[5] the temperature dependence factor β is found to be empirically insignificant. During spectrum acquisition, temperature can be monitored and kept constant.

Another factor affecting frequency shift is Cr^{3+} concentration and is been established previously.

$$\Delta\nu_{conc.} = 0.99 C_m \qquad [6]$$

where C_m is the concentration of chromium in weight percent. When the Cr^{3+} is uniformly distributed across the sample (i.e., isomorphous Al_2O_3-Cr_2O_3 at high temperature), only the temperature and stress variations need to be accounted for. The effect of doping ions addition to

Cr^{3+} (e.g., Fe, Ti, Ni, or Y) has been investigated recently by Clarke *et al* [76] who found that the ions that are soluble in α-Al_2O_3 will cause systematic changes in the luminescence frequency and intensity, whereas those ions that are insoluble have no effect on the R-line luminescence.

PL not only can determine the residual stresses within the α-Al_2O_3 scale, but also can identify polymorphs of transient Al_2O_3 within the TGO scale. Figure 25 shows, respectively, the N, Q, and G-luminescence arising from a significant Cr_2O_3 concentration in the TGO, the presence of metastable θ-Al_2O_3 which is characterized by a doublet at approximately 14575 and 14645 cm^{-1}, and γ-Al_2O_3 at about 14360 cm^{-1} within the TGO. [69]

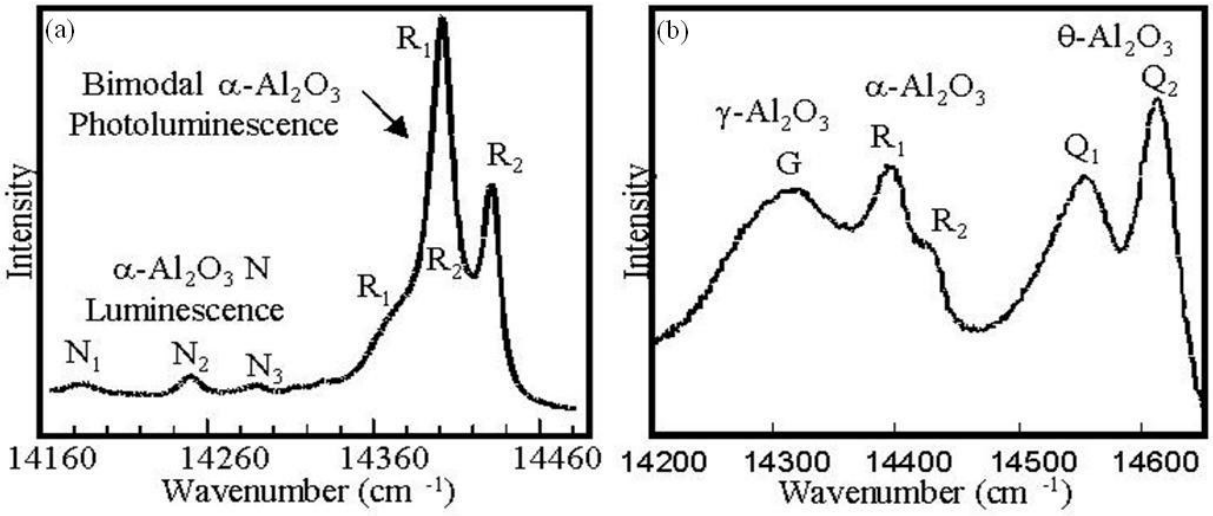

Figure 25: (a) N-type luminescence arising from the presence of significant Cr_2O_3 in α-Al_2O_3 scale; (b) Luminescence from γ, α and θ-Al_2O_3 labeled G, R_1-R_2 and Q_1-Q_2, respectively.

2.5 Impedance Spectroscopy

Electrochemical impedance spectroscopy (EIS) has been extensively used in the field of aqueous corrosion, and as an analytical technique for other applications which include ceramics and semiconductors. When an ac signal voltage (V) is applied to a material, the ratio of applied voltage over current (V\I), known as the impedance (Z) can be measured. This impedance varies with respect to the voltage as a function of frequency in materials that are considered as insulators. The frequency variation is a function of interfaces that develop when a potential is applied, which relates to physical and chemical characteristics of materials. If the frequency is varied over a range with applied voltage and the results are analyzed based on the impedance, it is possible to assess the physical nature of material and chemical activity at the interface.

The basic principle which governs EIS is applying a very small amplitude signals without significantly disturbing the properties of the material itself. This is an advantage over other NDE techniques. To make an EIS measurement, a small amplitude signal, usually a voltage between 5 to 50 mV, is applied to a specimen over a range of frequencies (0.001 Hz to 100,000 Hz). The EIS instrument records the real (resistance) and imaginary (capacitance/inductance) components of the impedance response of the system. The impedance response is then plotted usually plotted as Bode or Nyquist plots and examined with an ac equivalent circuit consisting of elements (resistor, capacitor, inductor etc), which would have behaved in a manner similar to the system being investigated.

The numerical value of electrical circuit elements and variation in those values can then be correlated to physical parameters such as porosity and thickness in the case of coatings.

The advantages of electrochemical impedance measurement over other techniques include:

- Rapid acquisition of data (often within minutes)
- Accurate, repeatable measurements
- Non-destructive
- Highly adaptable to a wide variety of different applications.

2.5.1 Electrochemical impedance spectroscopy theory

In corrosion systems, EIS is a well developed analytical technique to monitor the corrosion rates based on impedance. An electrical element, resistor is defined as the element that impedes the flow of current (I) when a voltage (V) is applied, and the value of resistance (R) can be defined for dc signal using ohm's law as:

$$R = \frac{V}{I} \tag{7}$$

when a dc potential (V) is applied across the circuit the resulting current (I) can be measured by connecting an ammeter in series with the circuit, and the resistance (R) can be computed.

For ac signal, the analogous equation is:

$$Z = \frac{V}{I} \tag{8}$$

where Z is defined as the impedance. Figure 26 shows a typical plot of a voltage (V) sine wave applied across a given circuit and the resultant ac current waveform. Electrochemical impedance response is normally measured using a small excitation signal. In a linear system, the current response to a sinusoidal potential will be a sinusoidal at the same frequency, but shifted in phase.

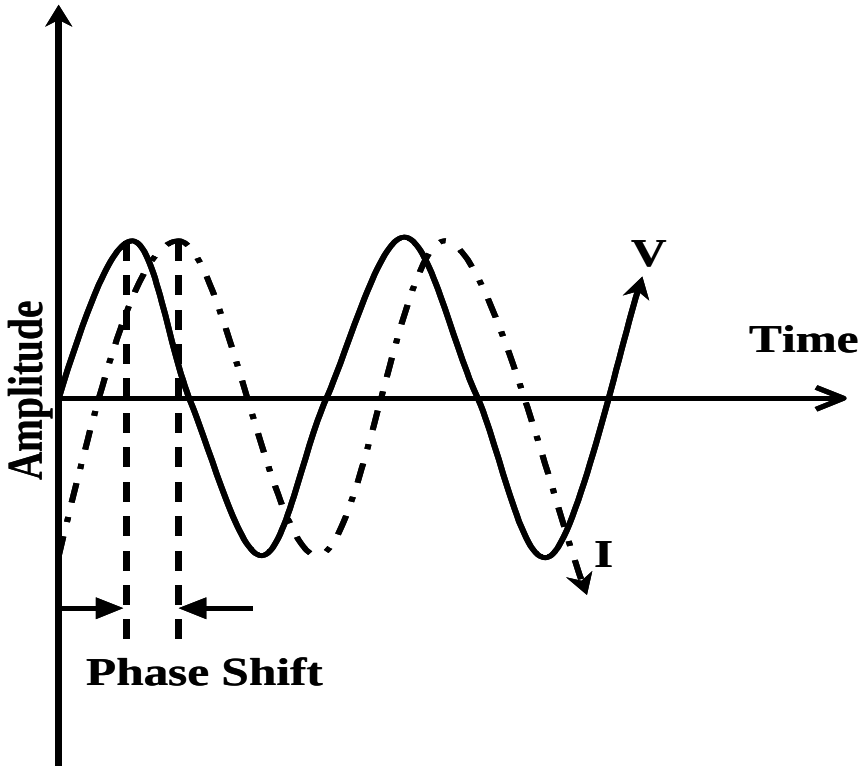

Figure 26: AC waveforms for an applied potential and the resulting current.

The impedance of the AC waveform can be represented in form of vector for characterization. This can be represented in terms of its amplitude and phase characteristics or as real and imaginary part of complex numbers. Equation (2) can be rewritten in vector form as:

$$\vec{Z} = \frac{\vec{V}}{\vec{I}} \tag{9}$$

where the ac voltage ($\vec{V}$) can be expressed as a complex number:

$$\vec{V} = \vec{V}^{*} + j\vec{V}^{**} \tag{10}$$

The superscripts * and ** correspond to real and imaginary component of a vector. The resulting current ($\vec{I}$) can also be represented as a complex number:

$$\vec{I} = \vec{I}^{*} + j\,\vec{I}^{**} \tag{11}$$

The resulting vector expression for ac impedance *(* $\vec{Z}$ *)* is :

$$\vec{Z} = \vec{Z}^{*} + j\,\vec{Z}^{**} \tag{12}$$

on the same coordinates axes as the current and voltage vectors.

The magnitude of the impedance can be expressed as:

$$|Z| = \sqrt{\left(Z^{*}\right)^{2} + \left(Z^{**}\right)^{2}} \tag{13}$$

and the phase angle (ϕ) can be defined as:

$$\phi = \arctan\left(\frac{Z^{**}}{Z^{*}}\right) \tag{14}$$

2.5.2 Electrical circuit elements

In general an equivalent electrical circuit is commonly constructed to analyze EIS data, which would provide response similar to that of the material system under investigation. This equivalent circuit consists of electrical elements such as resistors, capacitors, and inductors. Table 5 shows the circuit elements and the impedance response of the components. The parameters listed in Table 5 such as C and L are defined as the capacitance and inductance. The impedance of a resistor is independent of frequency, and has only a real component. Because

there is no imaginary impedance, the current through the resistor is always in phase with the voltage.

Table 5: Common electrical elements and their impedance expression.

Component	Current vs Voltage	Impedance
Resistor	V=IR	Z=R
Inductor	E=L di/dt	Z=jωL
Capacitor	I= C dE/dt	Z=1/jωC

The impedance (Z) of the capacitor (C) has no real component. Its imaginary component is a function of frequency, where $\omega = 2\pi f$ (where ω, is angular frequency and f is the frequency). A capacitor's impedance decreases as the frequency is increased. The current through a capacitor has a phase shift of –90 degrees with respect to the voltage, with current leading the voltage. Since the impedance of the capacitor varies inversely with the frequency $Z = (j\omega C)^{-1}$ at high frequencies, a capacitor acts as a short circuit: its impedance approaches zero. At low frequencies, a capacitor acts as an open circuit, and the impedance approaches infinity.

The impedance versus frequency behavior for an inductor is opposite to that of a capacitor. Inductors have only imaginary impedance component, and the current through the inductor is always 90 degrees out of phase with respect to the voltage. As the frequency increases, the impedance of an inductor increases. It acts as a short circuit (i.e., zero impedance) at infinitely low frequencies and as infinite impedance at very high frequencies. Inductors generally represents absorption phenomena at the interface of the material.

2.5.3 Serial and parallel combinations of circuit elements

The total impedance (Z_{eq}) of the system can be modeled using a circuit, which consists of a combination of simple elements such as resistors, capacitors, and inductors. The impedance values of the individual components can be combined according to some simple rules governing the system impedance for circuit elements both in parallel and series combinations. For linear impedance elements in series, we can calculate the equivalent impedance can be calculated as:

$$Z_{eq} = Z_1 + Z_2 + Z_3 \tag{15}$$

where Z_1, Z_2, Z_3 are the impedance of the elements (resistor or capacitor or inductor). For linear impedance elements in parallel, we can calculate the equivalent impedance can be expressed as:

$$\frac{1}{Z_{eq}} = \frac{1}{Z_1} + \frac{1}{Z_2} + \frac{1}{Z_3} \tag{16}$$

2.5.4 Data representation

Equations (2) and (3) can be expressed in complex number as:

$$\begin{aligned} V(t) &= V_0 \cos(\omega t) \\ I(t) &= I_0 \cos(\omega t - \phi) \end{aligned} \tag{17}$$

Where V (t) is the potential at time t, V_0 is the amplitude of the signal, and ω is the angular frequency. Similarly I (t) is the current at time t, I_0 is the amplitude of the current, and ϕ the difference between the current and voltage vector. The relationship between the angular frequency and frequency f (Hz) is$\omega = 2\pi$.

Therefore Eq. (9) can be rewritten as:

$$Z = \frac{V(t)}{I(t)} = \frac{V_0 \cos(\omega t)}{I_0 \cos(\omega t - \phi)} = Z_0 \frac{\cos(\omega t)}{\cos(\omega t - \phi)} \tag{18}$$

Using Euler's Expression:

$$\exp(j\phi) = \cos\phi + j\sin\phi \tag{19}$$

It is possible to express the impedance as a complex function. The potential is then described as:

$$V(t) = V_0 \exp(j\omega t) \tag{20}$$

The current is expressed as:

$$I(t) = I_0 \exp(j\omega t - j\phi) \tag{21}$$

The impedance is then represented as a complex number:

$$Z(\omega) = \frac{V}{I} = Z_0 \exp(j\phi) = Z_0(\cos\phi + j\sin\phi) \tag{22}$$

Impedance response is plotted as nyquist or bode plot. Nyquist plots are made by plotting total the impedance Z (ω) of a circuit as imaginary part of the impedance (Z^{**}) on the y-axis, and the real part of the impedance (Z^{*}) on the x-axis. The inadequacy of a Nyquist plot is that from a data point on the plot one cannot obtain the frequency that was used to record that point. Impedance of the same circuit can also be plotted as the absolute magnitude of the impedance $|Z|$ and the phase angle ϕ on the y-axis using the log frequency on the x-axis called the Bode plot. In this plot one can obtain the frequency that was used to record that point.

2.5.5 Plot Analysis

In EIS data is recorded as impedance or phase angle plot. The impedance plot has real component (resistance) and imaginary component (capacitance) of the system. From the impedance spectrum, a circuit model can be derived with various elements. Simulation of the impedance response is performed based on the assigned numerical values to all the circuit elements, and the values are interpolated. In an electrochemical cell, slow electrode kinetics, slow preceding chemical reactions, and diffusion can all impede electron or ionic flow (in an electrochemical system, flow of current through an electrolyte is accomplished by ions), and can be considered analogous to the resistors, capacitors, and inductors that impede the flow of electrons in an ac circuit. Thus, an electrochemical system consisting of a series of the above mentioned reactions could be represented or simulated by an ac equivalent circuit consisting of a series of elements such as resistors, capacitors and inductors. The EIS of a system can be separated into impedances contributed by each of the elements based on frequency range. Each of the elements represents one of the particular processes and thereby the corresponding impedance of the elements represents a physical parameter or a chemical/ electrochemical process.

For example, in a Nyquist plot, a pure resistance, R, is a single point on the, Z^*, axis and in a Bode plot, it is a straight line parallel to the log f axis at a height of the R-value. The straight line indicates that the impedance is independent of frequency and has no reactive component. The phase angle (θ) is zero at all frequencies. Similarly for a Nyquist plot, shape of a pure capacitance, C, is a vertical line at $Z^*=0$, indicating that the resistive component, Z^*, is zero, and that the reactive component, Z^{**}, is inversely related to the frequency, f. In the Bode plot, shape

for this capacitor is a straight line with a slope of –1 on a log $|Z|$ axis, indicating that $|Z|$ is inversely related to the frequency f and the value of θ is –90° at all frequencies.

Resistors and capacitors give a characteristic shape in both Nyquist and Bode plots when combined to form simple systems. The equivalent circuit elements not only allow calculation of their individual values but also how they change with exposure/degradation indicating how they interact with each other elucidating the evolution of defects. For example, the resistor and capacitor in series combination shown in Figure 27, gives a different plot shape as shown in Figure 28.

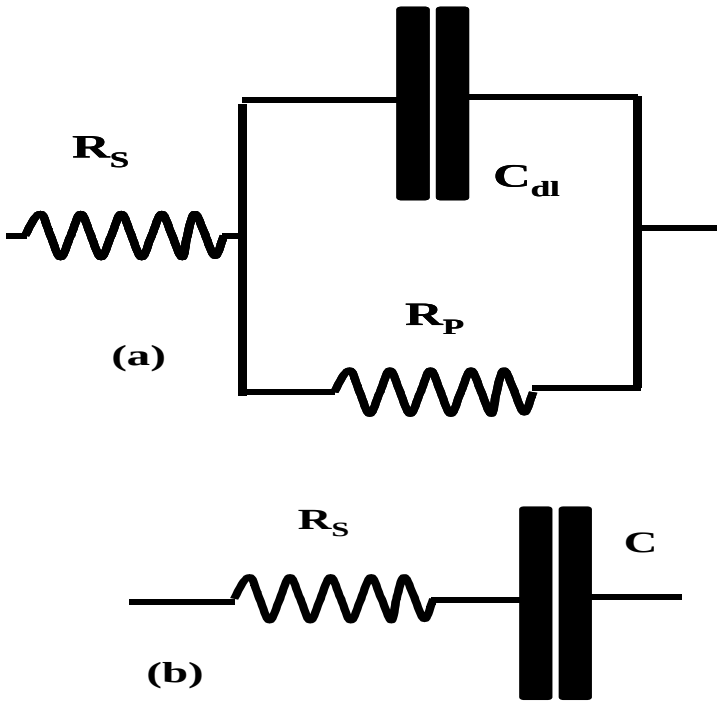

Figure 27. AC equivalent circuits (a) A polarization resistance, R_P and capacitance, C_{dl}, with the solution resistance, R_S in series (b) A solution resistance, R and capacitance, C in series.

A metal covered with an undamaged coating generally has very high impedance and can be represented as a resistor and capacitor in series. The model includes a resistor, R_S (solution resistance through the electrolyte) and a capacitor representing the coating. The nyquist plot for this circuit is shown in Figure 28. The value of the capacitance cannot be determined from the nyquist plot. The capacitance value can only be determined by curve fitting or by examination of the data points. The solution resistance can be obtained from the intercept of the curve with the real axis. The maximum limit in the impedance for most of the EIS measurement is close to 10^{10} Ω. The Bode plot for the same circuit is shown in Figure 29. From this plot one also gets the solution resistance, but it does not appear because the impedance of the coating is higher than the solution resistance.

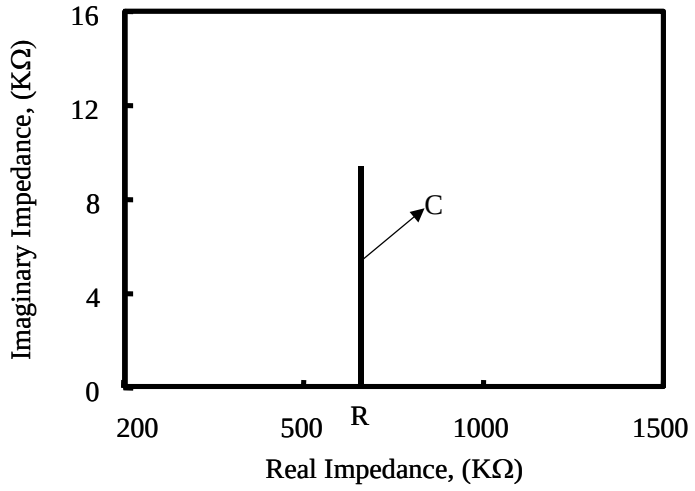

Figure 28: Nyquist plot for a circuit consisting of a solution resistance, R_S and capacitance, C in series.

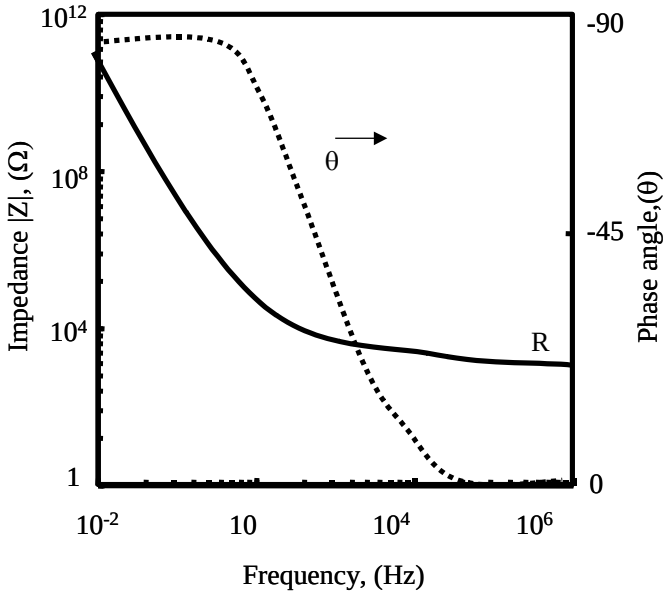

Figure 29: Bode and impedance plots for a series solution resistor, R and capacitor, C.

The Randles circuit shown in Figure 30 models the electrochemical impedance of an interface and fits many simple electrochemical systems. At the interface between an electrode and electrolyte, a double layer is established as shown in Figure 31 in which negatively charged ions line up at the electrode surface. Positively charged ions then line up in response to maintain the electro-neutrality, but are separated from the anions due to their sheath of hydration. This double layer acts, as a capacitor C_{dl} in parallel with the polarization resistance (R_P) due to the charge transfer reaction. The ionically conducting electrolyte impedes the transfer of charge (ions) and, acts as a resistor, R_S in series with the C_{dl} and R_P. This simple Randles circuit is a starting point for other more complex models.

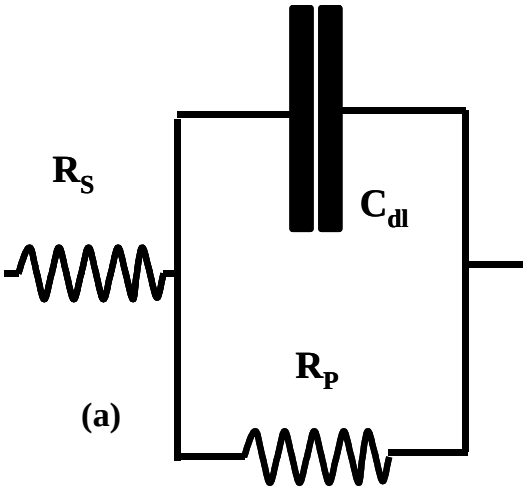

Figure 30: Randles circuit representing a simple electrochemical cell.

A characteristic Nyquist plot for the Randles circuit is presented in Figure 32. The plot is always a semicircle. In the Nyquist plot, the high frequency response lies to the left followed by lower frequency to the right. The solution resistance (R_S) can be found by reading the real axis value at the high frequency intercept. This is the intercept near the origin of the plot. The real axis value at the other (low frequency) intercept is the sum of the polarization resistance and the solution resistance (R_P+R_S). The diameter of the semicircle therefore equals to the polarization resistance (R_p). Figure 33 is the Bode plot for the same circuit. The solution resistance, and R_P+R_S can be read on the vertical axis depicting $|Z|$. The phase angle in this Randles circuit does not reach 90° as it would for pure capacitive impedance. The phase angle would approach 90° if the values for R_s and R_p were more widely separated.

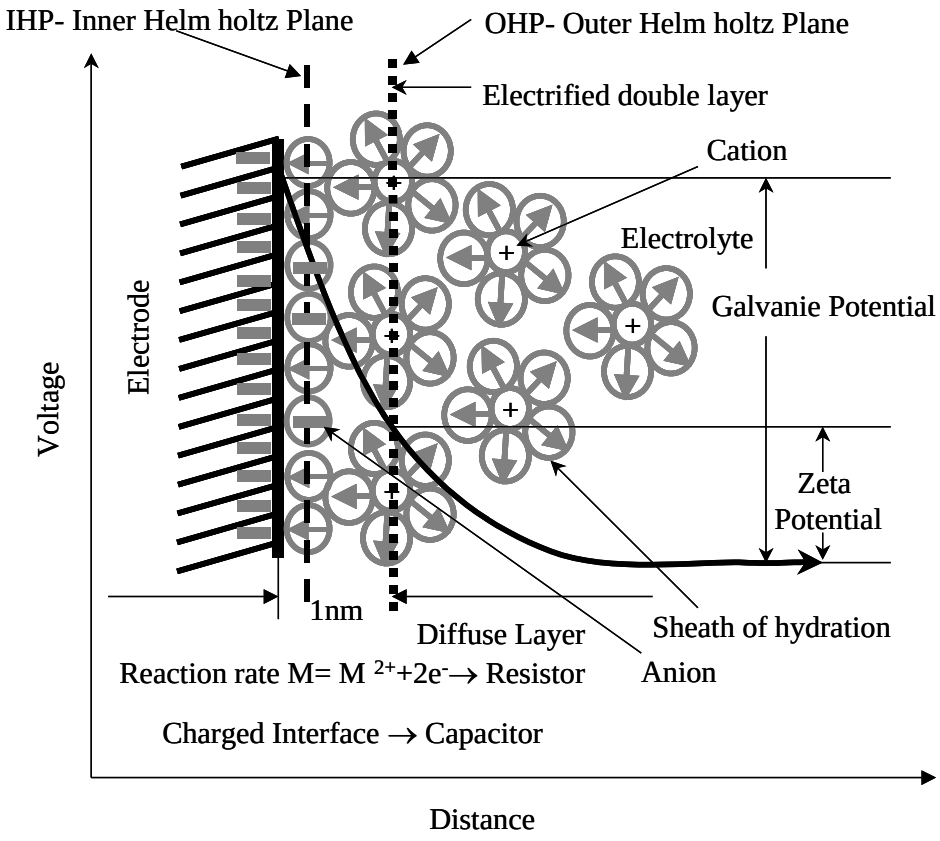

Figure 31. Double layer at the interface between the electrode and the electrolyte.

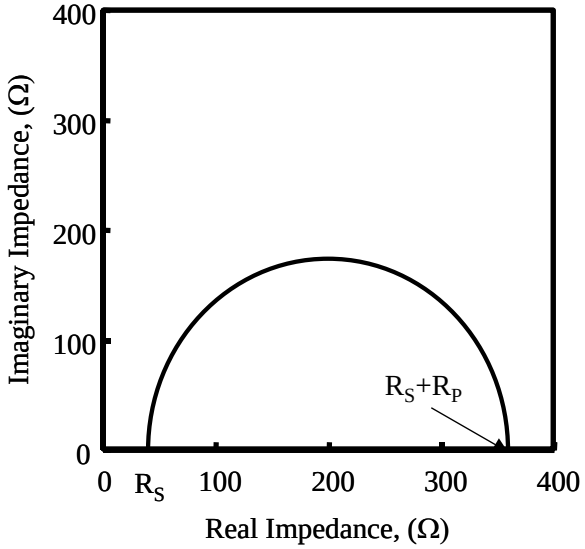

Figure 32: Nyquist plot for a Randles circuit.

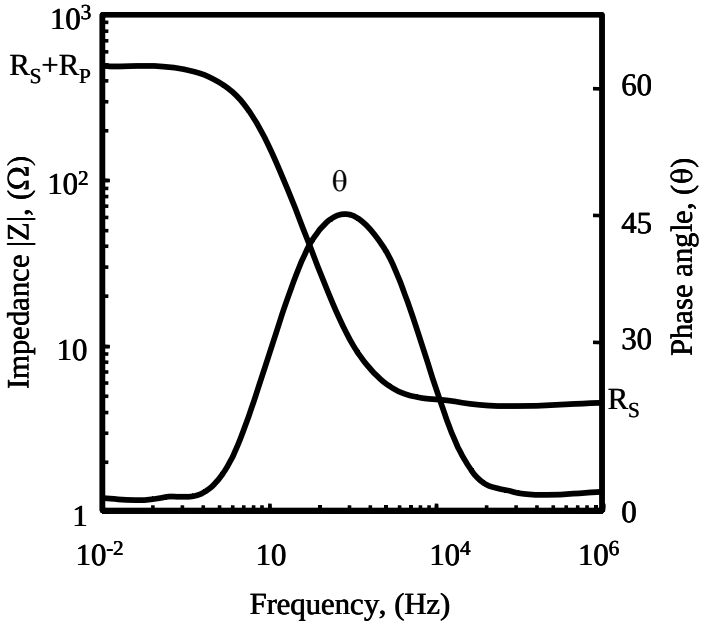

Figure 33. Bode plot for a Randles circuit.

The most successful application of EIS is for evaluating coated metals. Walter [77] reported one of the typical EIS spectra for coated metal as shown in Figure 34. The circuit model, as shown in Figure 34, was used to describe the electrochemical process. The resistance, R_P, was interpreted as the pore resistance due to the electrolyte penetrating through pores within the coated paint film. The film capacitance, C_C, was interpreted as the capacitance of the electrical capacitor consisting of the metal and electrolyte, or simply as the capacitance of the intact film. Therefore, two semicircles, which present the relaxation processes of the film capacitor and double layer, appear in the Nyquist plot in Figure 34(b). The other parameters shown in Figure 34 have the same meaning as shown in Figure 30.

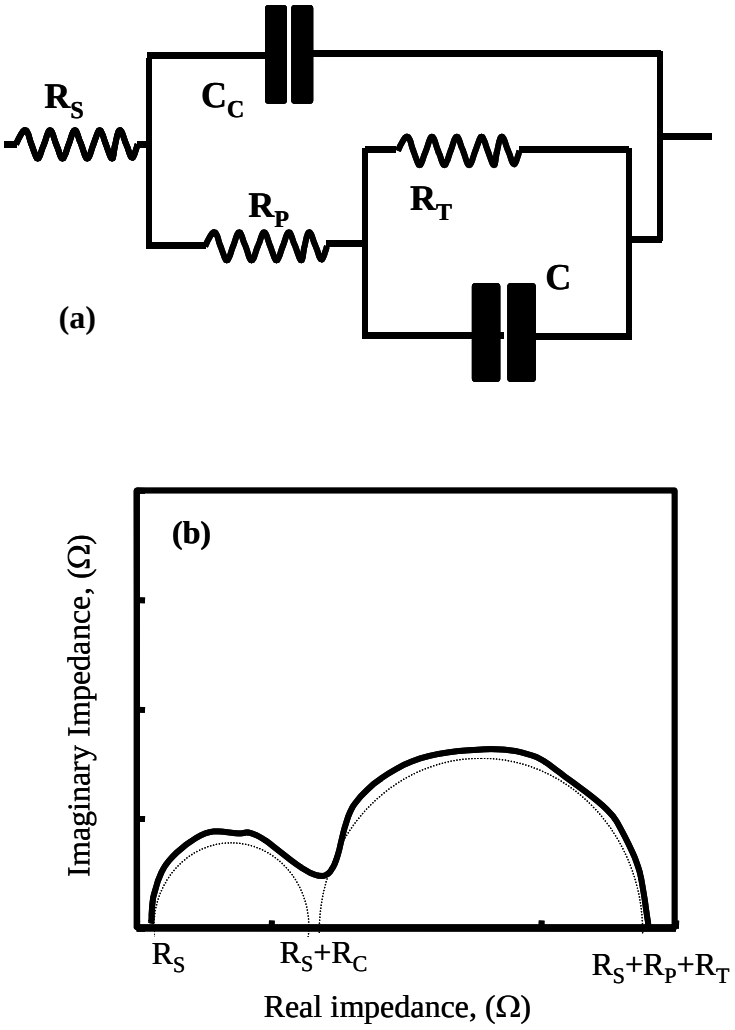

Figure 34: Typical (a) Equivalent circuit model for coated metal/solution interface. R_S, solution resistance; R_T, charge transfer resistance; C, Faradaic capacitance of metal; R_P, pore resistance; C_C, capacitance of intact film. (b) The Nyquist plot with two distinct semicircles.

The corresponding Bode plot is shown in Figure 35. From this plot one can see two-phase angle maxima, one at the higher frequency domain usually containing paint film information, and one at lower frequency domain, containing the substrate information. The Bode phase plot shows phase angle reaching towards zero at corresponding low and high frequencies. Representing the resistive behavior of R_S and R_S+R_T. This phase angle rise towards maximum value, at intermediate frequencies, corresponds to the capacitive behavior(C).

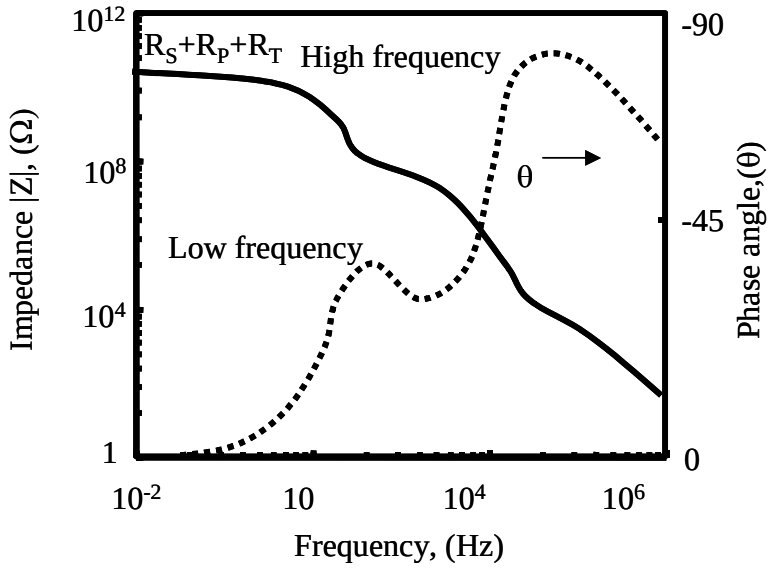

Figure 35. A typical Bode plot for painted metal/solution interface in the absence of diffusion.

In many cases the equivalent circuit shown in Figure 34 will not be adequate as a model for the painted metal/solution interface. One modification takes into account diffusion processes within pores in the paint film and is modeled by the inclusion of Warburg or pseudo-impedance, Z_ω, placed in series with R_P. Z_ω is defined as:

$$Z_\omega = \sigma\omega^{-1/2}(1-j) \tag{23}$$

The substrate double layer capacitance, C_{dl}, may or may not appear in parallel with R_P+ Z_ω. Nyquist and Bode plots, corresponding to the equivalent electrical circuit shown in Figure 36 and are presented in Figure 37. In this model, R_S is the resistance of the electrolyte, R_C and C_C are the resistance and capacitance of the coating, R_P is the polarization resistance, which is inversely proportional to the corrosion rate, C_{dl} is the double layer capacitance at the electrode-electrolyte interface, and Z_ω is an impedance due to the diffusion of reactants to the surface of the electrode.

During the life of the coating, the equivalent circuit model no longer remains the same and changes. This change is dependent on processes such as moisture penetration, onset of corrosion and break up of coating. When a coating is new and effective, R_P, R_C, C_{dl} and Z_ω are not present and the model is similar to that shown in Figure 34(a). As the moisture penetrates the coating, R_C must be considered. When the corrosion starts, R_P and C_{dl} become operable. When the corrosion rate becomes high Z_ω is present. If the pores in the coating clog over time, the corrosion rate decreases and Z_ω needs to be considered, but if the coating breaks up, R_C, C_C and Z_ω become inoperable and the system acts like a bare metal. Further analysis and mathematics behind the Warburg impedance can be found elsewhere. [78]

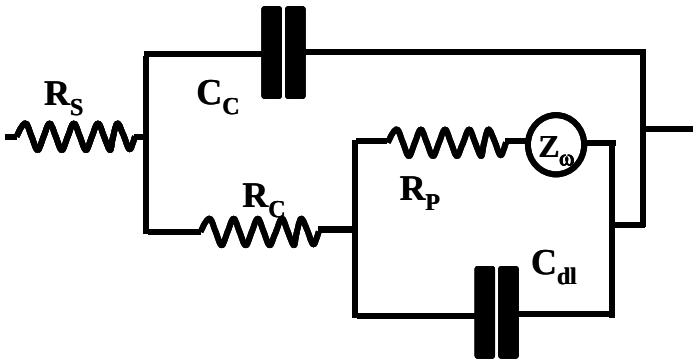

Figure 36. Equivalent circuit model in the presence of diffusion for a painted metal/solution interface.

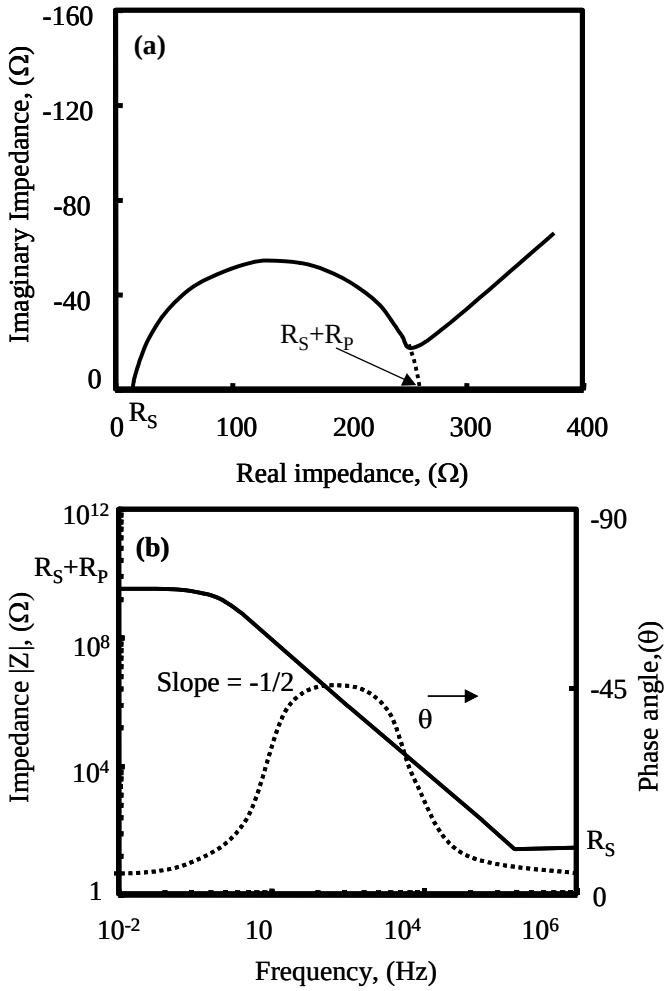

Figure 37.Typical (a) Nyquist (b) Bode plot for painted metal/solution interface in the presence of diffusion.

It is generally easy to imagine what might correspond to a resistance or a capacitance in an equivalent circuit model of an electrochemical cell. It is much harder to explain the presence of an inductor. The Nyquist plot of a common Randles cell (representing a simple slow electron transfer) shows a semicircle in the first quadrant as shown in Figure 32, the Nyquist plot for circuits involving inductors show impedances below the x-axis, generally in the fourth quadrant as shown in Figure 38.

The effect of inductance is often seen at the highest frequencies as shown in Figure 38. The impedance of an inductor increases with frequency, while that of a capacitor decreases. High frequency inductive behavior has several possible causes. Some batteries, formed by rolling a thin anode-electrolyte-cathode "sandwich" into a compact cylinder, may show these effects. These "stray" inductances are generally only a few micro Henry (uHy). Instrumental artifacts can also cause high frequency inductive behavior, notably capacitance associated with the current measuring resistor. Many potentiostat manufacturers have already made corrections for this effect in their EIS software.

A Nyquist plot, similar to that shown in Figure 39(a), is occasionally seen in the impedance literature. The most quoted explanation for this low frequency inductive behavior is an adsorption process at the electrode surface. Although the two arcs appear to be semicircles, they are often distorted near the rightmost extreme in Z*. The point of maximum Z* often occurs above the x-axis, in the first quadrant, not on the x-axis as shown in Figure 39 . The segment shown identifies the region of low frequency inductive behavior. An equivalent circuit that might fit this data is shown in Figure 39(b).

Depending on the relative magnitudes of the time constants R_2C and $L/(R_2+R_3)$, the "diameter" of the inductive loop in the Nyquist plot, may be anywhere from zero to R_3. The position of the "middle frequency" x-axis intercept (indicated by the "X") is as small as R_1+R_2 [when $L/R_3<<R_2C$] or as large as $(R_1+R_2+R_3)$ when $/R_3>>(R_2+R_3)$ C.

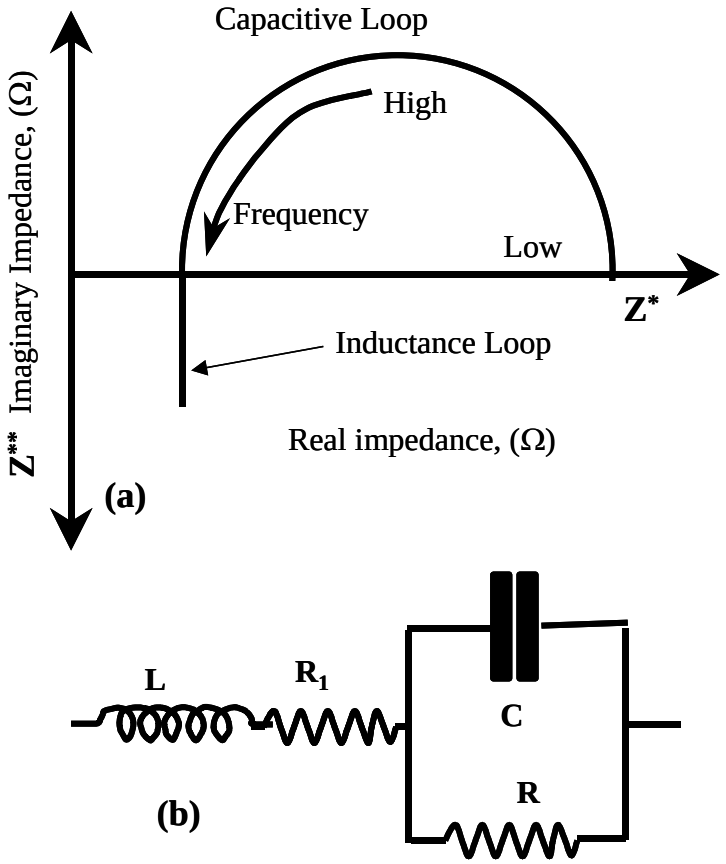

Figure 38 A typical (a) nyquist plot showing high frequency inductive behavior (b) and equivalent circuit model in the presence of high frequency inductive loop.

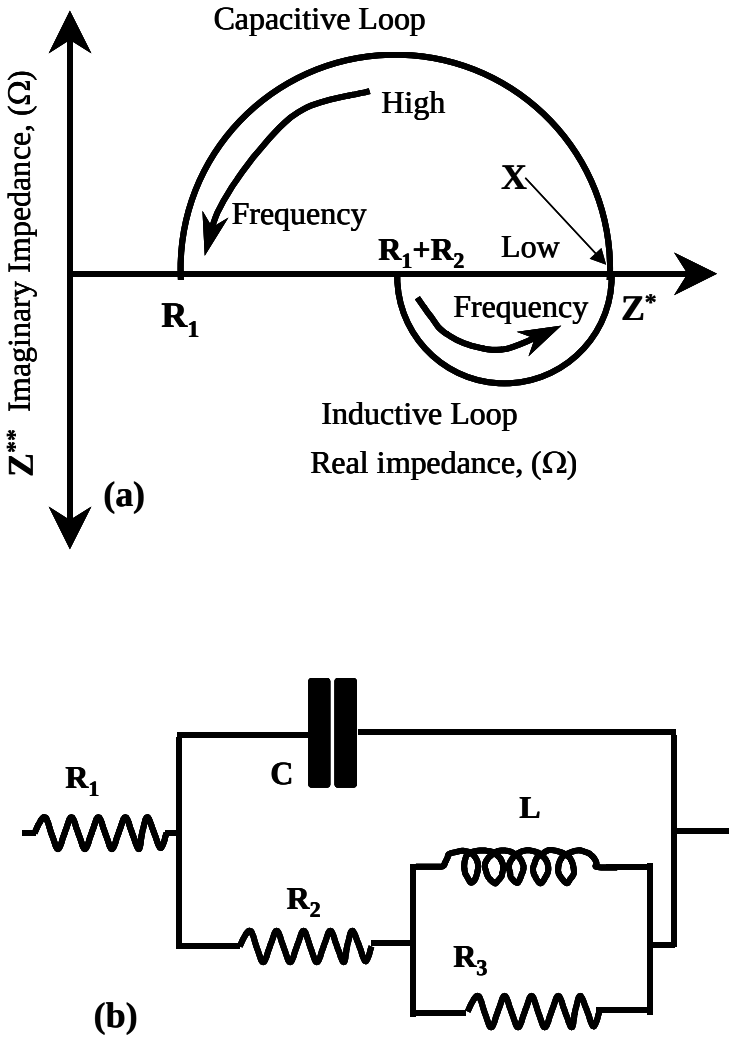

Figure 39 (a) a typical nyquist plot showing low frequency inductive behavior and (b) an equivalent circuit that might fit this data.

2.5.6 Constant phase elements (CPE)

A perfectly smooth homogenous electrode can be represented by an equivalent circuit made up of an electrolyte resistance (R_S) in series with the double layer capacitor C_{dl} and the polarization resistance (R_P) in parallel to C_{dl} as shown in Figure 30.

The constant phase element (CPE) is a non-intuitive circuit element that was discovered (or invented) while looking at the response of real-world systems. In some systems where the Nyquist plot was expected to be a semicircle with the center on the x-axis, the observed plot was indeed the arc of a circle, but with the center some distance below the x-axis.

These depressed semicircles have been explained by a number of phenomena, depending on the nature of the system being investigated. However, the common trend among these explanations is that some property of the system is not homogeneous or that there is some distribution (dispersion) of the value of some physical property of the system. Therefore in the case of YSZ monoliths and APS TBCs (exposed and as received), a CPE is used rather than an ideal capacitor in the ac equivalent circuits where the depression of the semicircle is seen. [79-85]

Generally, CPE is used if the material under investigation cannot be regarded as homogenous. Common examples of homogenous materials are: the surface of a bare solid metal, [79,80] coated metals, [81,82] solid electrolytes, [83] dielectrics, [84] and semiconductors. [85] The use of CPE is more suitable to describe the behavior of a non-ideal capacitor, which contains various phases as dielectric materials. In this study YSZ monolith and APS TBCs are considered, which are usually inhomogeneous in a physical sense because of the geometric defects such as surface roughness. These geometric defects, give rise to frequency dispersion due to non-uniform distribution in the current density. [86,87] Over a fairly wide range of frequencies such effects may be described with the empirical concept of a Constant Phase Element. The impedance of the CPE is given by:

$$Z_{CPE}(j\omega) = A^{-1}(j\omega)^{-n} \tag{24}$$

where *A* is a constant that is independent of frequency, ω is angular frequency, $j = \sqrt{-1}$, and n is an exponential index, which represents a dispersion of relaxation frequency. When n=1, the CPE represents an ideal capacitor, when n=0, CPE acts as a pure resistor.

In their text**,** MacDonald, *et. al*. [88] point out that even though a particular theory may not give exactly CPE behavior, very often CPE behavior will fit experimental data so well that the deviations are totally masked by experimental noise and uncertainties. This is increasingly true as the complexity of a circuit model grows. In short, a CPE can act as a useful modeling element, even if the true nature of the system is unknown.

3 EXPERIMENTAL

3.1 Specimen Description of Thermal Barrier Coatings

Four TBC systems, identified in Table 6 as type I through IV, were supplied from industrial partners. Each type of TBC consisted of 20 specimens with geometrical specification (25.4 mm in diameter and 3.2 mm in thickness) schematically illustrated in Figure 40. Table 6, shows the samples investigated in this study consisted of different types of bondcoat namely (Ni,Pt)Al and NiCoCrAlY, different types of ceramic coating plasma deposition EB-PVD and APS, on different superalloy substrates. The chemical compositions of the superalloys are presented in Table 7. The two types of EB-PVD TBCs did receive different processing techniques for the bondcoat namely type-III bondcoat was as-deposited CVD coating compared to type-IV coating that was grit blasted using a proprietary grit blasting technique. In the case of APS TBCs, type I coating had a shrouded APS bondcoat and type-II coating had a LPPS/VPS bondcoat. Also type-I and type-II coating are conventional cast superalloy compared to type-III and type-IV which are single crystal alloys. EIS response with respect to 1-hour thermal cycling for Type-II TBCs was studied previously. [89] In this study, the EIS response is used as a reference to compare type-I TBCs but the impedance responses were collected at different cyclic responses. Type-II coating substrate was a Co-base superalloy compared to other coatings which had Ni-base superalloy as the substrate.

Table 6. Specifications for four types of commercially produced thermal barrier coating systems employed in this study.

TBC System	7YSZ Deposition and Thickness	Bondcoat Type and Thickness	Superalloy Substrate	Notes
I	APS; 600 μm	NiCoCrAlY; 175 μm	Haynes 230	-
II	APS; 200 μm	NiCoCrAlY; 100 μm	MAR-M-509	-
III	EB-PVD; 145 μm	(Ni,Pt)Al; 50 μm	CMSX-4	As-Coated Bondcoat
IV	EB-PVD; 140 μm	(Ni,Pt)Al; 35 μm	Rene'N5	Grit-Blasted Bondcoat

Table 7. Chemical composition of the superalloy substrates used in this study on which the bondcoat and ceramic coating are deposited.

Substrate Material	Elemental Composition in wt%											
	Ni	Co	Cr	Ta	W	Al	Re	Ti	Mo	Fe	Hf	Notes
CMSX-4™	-bal-	9.0	6.5	6.5	6.0	5.6	3.0	1.0	0.6	-	0.1	Single crystal
ReneN-5™	-bal-	7.5	7.0	6.5	5.0	6.2	3.0	0.0	1.5	-	0.15	Single crystal
Haynes 230™	-bal-	5.0	22.0	-	14.0	0.3	-	-	2.0	3.0	-	0.5%Mn,0.4 %Si, 0.1%C, 0.2%La,0.015%B
MAR-M-509™	10.0	-bal-	23.4	3.5	7.0	-	-	0.2	-	-	-	0.5% Zr, 0.6%C

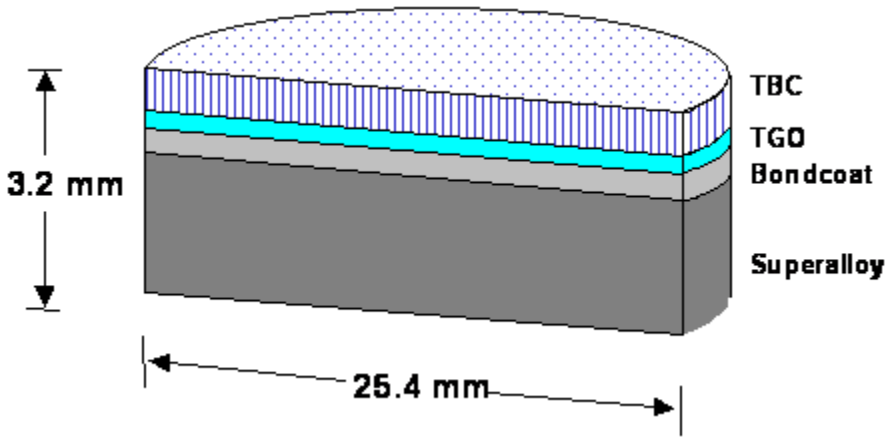

Figure 40. Specimen geometry for thermal barrier coatings employed in this study.

3.2 Furnace Thermal Cycling Test

Thermal cyclic oxidation for each type of TBC has been carried out using CM™ Rapid Temperature furnace with vertical cycling package as shown Figure 41. Each cycle consists of 10-minute heat-up to 1121°C (2050°F), 0.67, 9.6 or 49.6-hour hold at 1121°C, and 10-minute forced-air quench. Temperature of the specimen stage (20 cm by 20 cm) has been monitored by S-type thermocouples attached to a YSZ disk (25.4 mm in diameter and 3 mm in thickness). In between thermal cycles the samples were rotated inside the furnace to make sure the uniformity in temperature exposure.

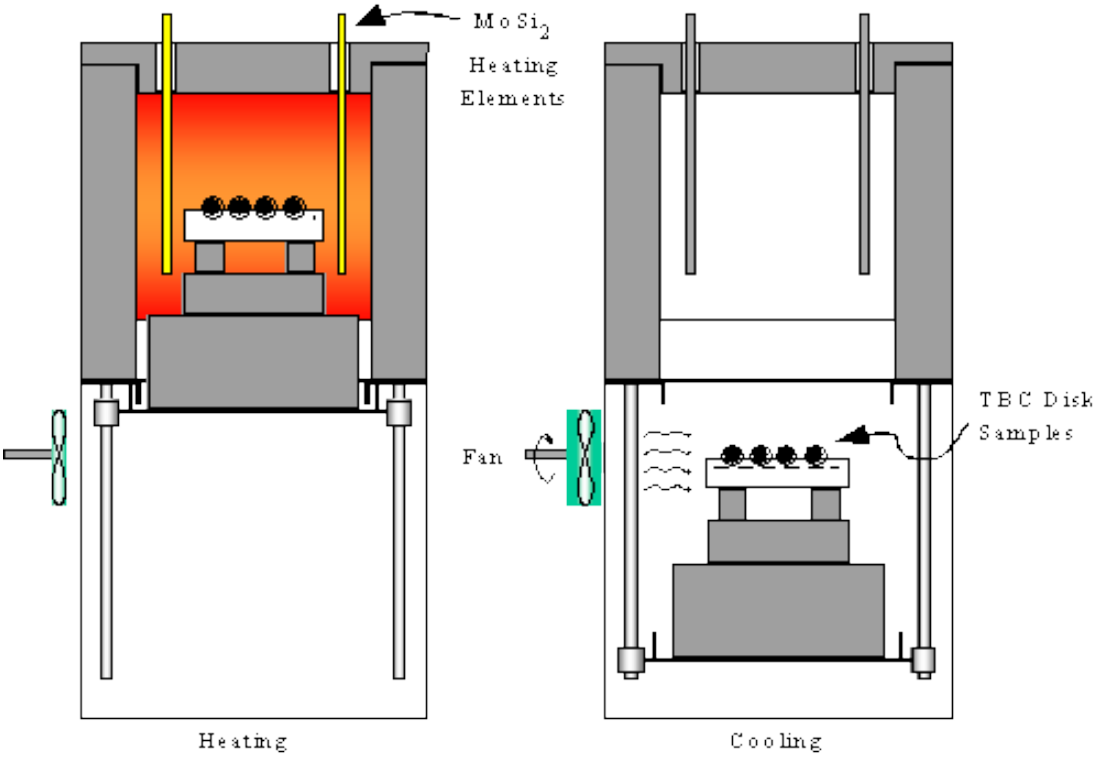

Figure 41. A schematic diagram of the CM™ Rapid Temperature cyclic oxidation furnace during (a) high temperature oxidation and (b) cooling.

3.3 PSLS and EIS Measurements

For 20 specimens of each TBC type, thermal cyclic oxidation testing has been carried out using the matrix given in Table 8. At specified thermal cycles, TBCs were visually inspected, photographed and examined by PSLS and EIS. Selected TBC specimens after specific thermal cycles have been also employed for microstructural analysis according to Table 8. Thermal cycling of TBC was stopped at failure. Failure is defined visually as 20-30% delamination or spallation of ceramic coating.

Table 8. Matrix of the thermal cyclic oxidation test for each type of TBCs.

Number of TBCs*	Type of Oxidation Test	NDE by PSLS and EIS (cycles)	Microstructural Analysis (% lifetime)
1	N.A.	0	0
9	1 hour	0,1,5,10-Failure#	10, 50, 80 and Failure (5 spc.)
5	10 hour	0,1,2,3,4,…Failure#	30, 80, Failure (3 specimens)
5	50 hour	0,1,2,3,4,…Failure#	50 and Failure (3 specimens)

Every 20 cycles until failure.

3.3.1 Photostimulated luminescence spectroscopy (PSLS)

For performing the NDE inspection using PSLS, a Renishaw™, System 1000B Ramanscope™ (Renishaw™, Gloucestershire, UK) equipped with a Leica™ DM/LM optical microscope shown in Figure 42 was used. The luminescence data acquisition points for two types of EB-PVD samples are shown in Figure 43. A non-linear least-square curve-fitting routine for a mix of Lorentzian and Gaussian functions was employed for curve fitting routine on collected luminescence from α-Al_2O_3, based on the parameters set by Clarke *et al.* [90] The

parameters employed are as follows: (1) the distance between the peaks R_1 and R_2 should satisfy 29 cm^{-1} $<R_2-R_1<35$ cm^{-1} and (2) integrated intensity ratio R_2 to R_1 should be 50% $< I_{R2}/I_{R1} <$ 70%.

Aforementioned, the luminescence from α-Al_2O_3 shown in Figure 24 can exhibit bimodal luminescence. The PSLS spectra was monitored closely at every thermal cycle and in case of emerging stress free luminescence the data acquisition points were concentrated for that region including the standard measurements shown in Figure 43. In such cases for curve fitting this type of spectra requires a third set of R_1-R_2 peaks near the stress-free value R_2=14432 cm^{-1}.

Figure 42. Renishaw TM 1000B Raman Microscope used for performing PSLS measurements in this study.

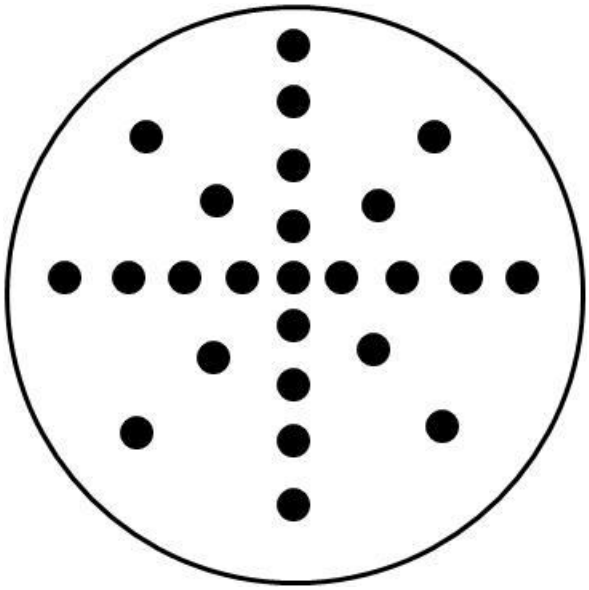

Figure 43. Inspection points for PSLS measurements on EB-PVD TBC specimens investigated in this study.

3.3.2 Electrochemical impedance spectroscopy (EIS)

EIS was performed using a three electrode EG&G Princeton Applied Research™ and IM6e BAS ZAHNER™ frequency response analyzer as schematically illustrated in Figure 44. The electrolyte used in this study was 0.01M (molar) potassium Ferri/Ferro cyanide $\{(K_3Fe(CN)_6/K_4Fe(CN)_6{\cdot}3H_2O)\}$. This was a choice of electrolyte because of its highly reversible (redox) electrochemical exchange current density and non-interference with the system. The electrodes, namely reference and counter electrodes are a standard calomel electrode and a platinum mesh with a large area compared to the working electrode (TBCs).

Data acquisition time for each measurement with TBC as working electrode, platinum as counter electrode and calomel electrode as reference electrode ranged from few seconds to minutes. This allowed to stabilize the open circuit potential to a constant value, i.e., complete penetration of the electrolyte through open pores of TBCs. AC amplitude of 10mV was applied

over the frequency range of 10m-1MHz with the constant, circular working/probe diameter of 1 cm. Sufficient care was taken to remove air-bubbles prior to EIS measurements due to inherent porosity in topcoat ceramic microstructure. For statistical confidence, a minimum of 2 measurements was carried out for each specimen.

The system response was recorded as Bode plot or Nyquist plot. The effectiveness of this technique lies in the correct interpretation of the EIS data represented by Nyquist and/or Bode plot, which is accomplished by generating an ac equivalent circuit. This electrical circuit can be modeled by parameters, such as resistors, capacitors, and inductors. The change in the elemental values can be related to the type, characteristics, and the kinetics of the electrochemical process. Using a non-linear curve fitting analysis, the system response is simulated using the ac electrical circuit, and the values are compared.

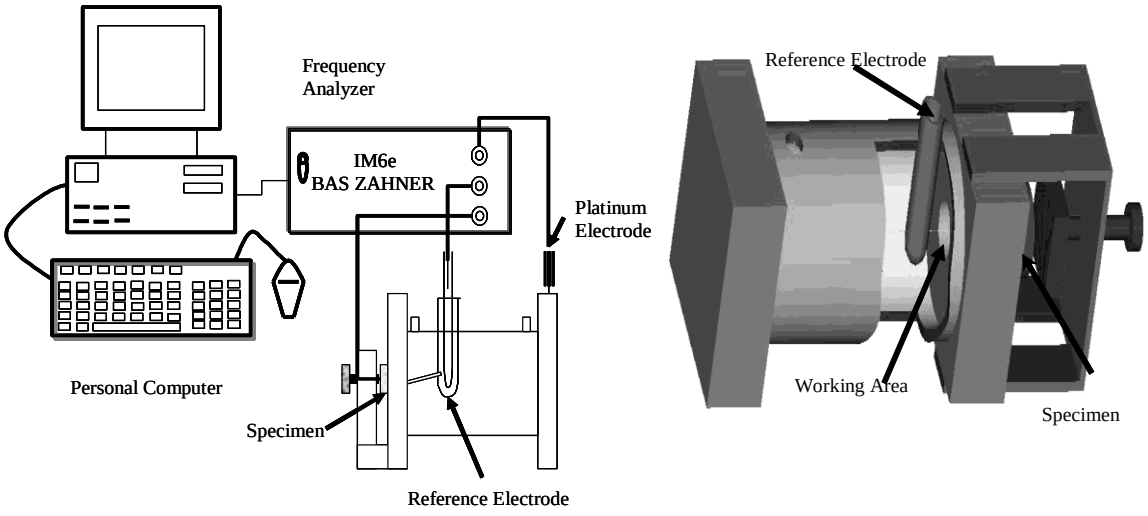

Figure 44. A schematic diagram of a typical set-up for electrochemical impedance spectroscopy.

3.4 EIS models for Thermally Cycled Sampels

In general TBCs have a multilayer structure; ac equivalent circuit models are designed in this study to establish a relationship between the morphological/physical properties and the electrical parameters in the equivalent circuit. The electrical parameters used in the EIS circuit are listed in Table 9. This complex EIS model was derived from previous work performed by Jayaraj *et al* [91,92] where TBCs were simulated with standalone YSZ containing open pores and nickel aluminides after cyclic oxidation. The EIS model now combines both the YSZ with open pores and nickel aluminides.

Table 9. Abbreviations used in the Ac equivalent circuit for EIS models.

Parameters	Description
R_S	Solution resistance between the reference electrode and the topcoat surface
R_{YSZ}	The resistance of the ceramic topcoat
C_{YSZ}	The capacitance of the ceramic topcoat
R_{PORE}	The resistance of the pore (summation of the defects in the ceramic topcoat)
C_{PORE}	The capacitance of the pore (summation of the defects in the ceramic topcoat)
R_T	The transmission resistance of the double layer at the interface between the ceramic topcoat and the metallic bondcoat
C_T	The capacitance of the double layer at the interface between the ceramic topcoat and the metallic bondcoat
R_{TGO}	The resistance of the thermally grown oxide
C_{TGO}	The capacitance of the thermally grown oxide

3.4.1 Air Plasma Sprayed TBCs EIS Models

The as-sprayed TBC specimens consist of ceramic topcoat with intersplat porosity, micro-cracking, bondcoat and superalloy substrate. Based on each individual layers, the electrical impedance in EIS measurement will be attributed to the electrolyte resistance, topcoat thickness, inherent porosity within topcoat and topcoat/bondcoat interfaces. In as-sprayed condition for APS TBCs, thermally grown oxide scale is not observed at the bondcoat to topcoat

interface and hence the electrical resistance due to the oxide scale is ignored in circuit model. The ac equivalent circuit is presented in Figure 45. For air plasma TBCs constant phase elements were employed instead of pure capacitance to accommodate any non-uniform charge distribution that may arise due to surface/interface roughness.

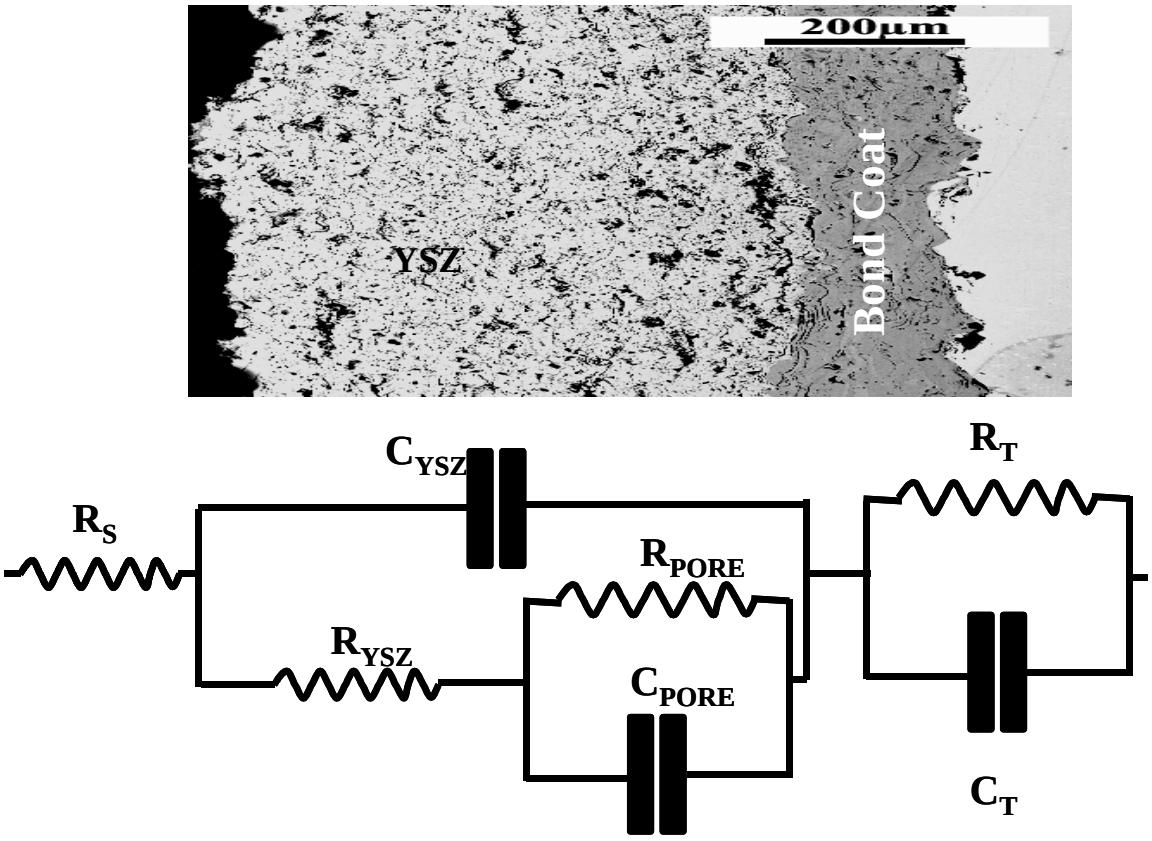

Figure 45. A model of an EIS ac-equivalent circuit for APS TBCs without the TGO.

3.4.2 Air Plasma Sprayed TBCs EIS Models after thermal cyclic exposure

The ac equivalent circuit for APS TBCs, after exposure is different from that of as-coated ones because of the bondcoat oxidation that result in the formation of uniform and continuous TGO. The impedance of TGO cannot be neglected in the EIS measurement system. Thus, an ac equivalent circuit for the post-exposed TBC is modeled as shown in Figure 46. This circuit

establishes the relationship between the post-exposed morphological/physical properties of TBC containing the TGO with EIS electrical parameters.

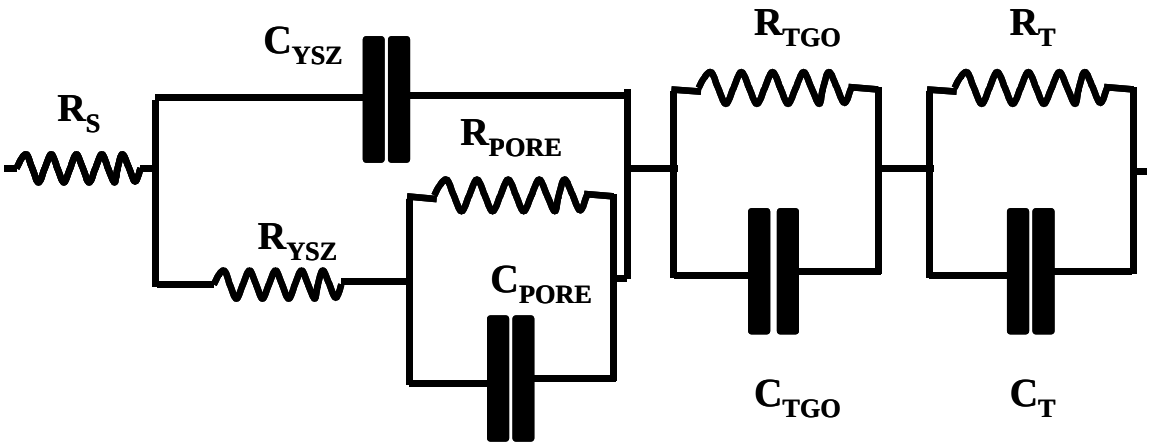

Figure 46. EIS AC equivalent circuit model for thermally exposed APS TBCs with TGO.

3.4.3 Electron Beam Physical Vapor Deposited EIS models

The as-coated TBCs consist of a ceramic topcoat with porosity, bondcoat and substrate. In addition, the as-coated EB-PVD TBCs have a very thin and uniformly developed TGO. As a result, the electrical impedance in EIS measurement will be attributed to the electrolyte resistance (conductivity of the electrolyte), ceramic topcoat (thickness), porosity in the topcoat, TGO and the interface between the TGO and bondcoat. A model employed in this study is presented in Figure 47. In this circuit for EB-PVD TBCs, an ideal capacitor is used rather than a CPE. This is because of the relatively smooth surface of the YSZ as well as the interface between the TGO and bondcoat.

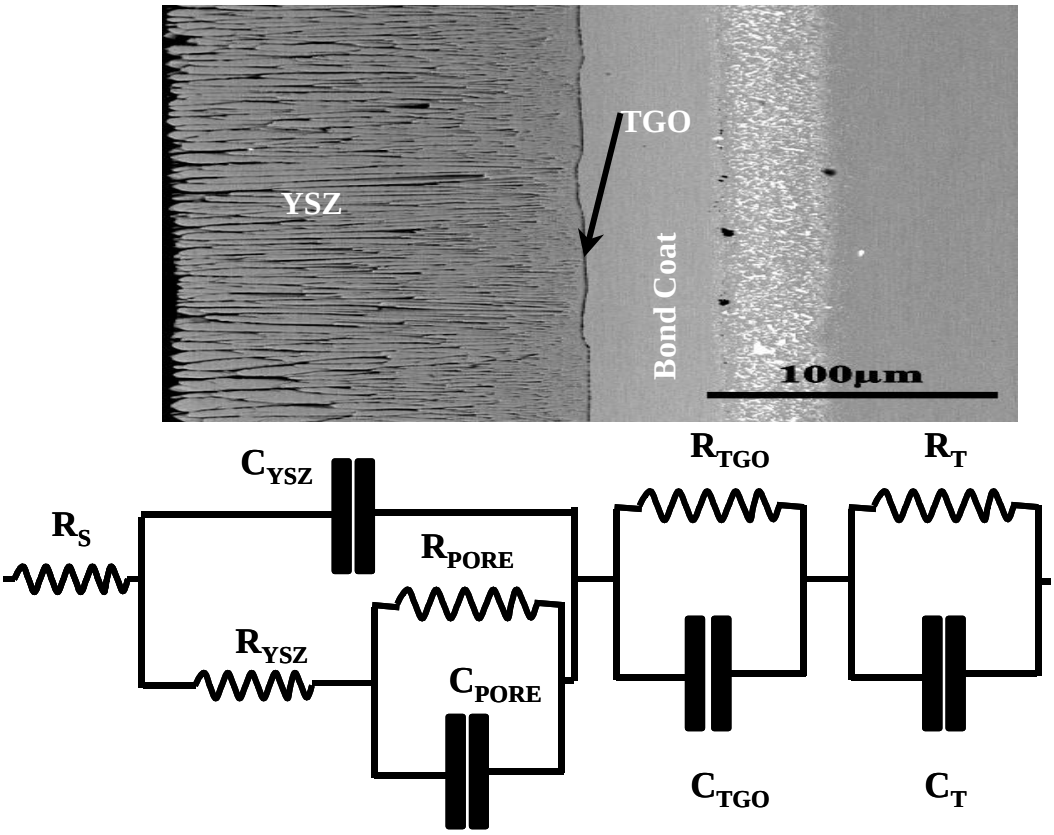

Figure 47. A typical microstructure of as-coated EB-PVD TBCs and the corresponding AC equivalent circuit employed for electrochemical impedance spectroscopy.

3.5 Microstructural Characterization

Before and after thermal cyclic oxidation, selected specimens of TBCs were employed for the microstructural and failure analysis as presented in Table 8. Development of microstructural features and failure characteristics of TBCs have been examined by SEM/EDS as a function of thermal cycles. Specimens used for microstructural characterization were mounted using Buehler® epoxy and sectioned using Buehler® Isomet low speed saw. This is done to avoid damages associated with mechanical sectioning. Then the samples were ground and

polished down to 0.5 μm diamond paste using Stuers™ Rotopol. After carbon coating, they were examined with SEM equipped with EDS.

4 RESULTS

4.1 Microstructural assessment of As-coated Specimens

The as-coated specimens from industrial partners were initially used for NDE evaluation and after that carefully prepared for microstructural analysis as described in the experimental section to avoid any mechanical damages.

4.1.1 As-coated APS TBCs

Figure 48 represents typical backscatter electron micrograph of as-received type I (600μm-thick) and type II (200μm-thick) APS TBCs. Specimens confirmed to the specification described in Table 6. From SEM, no significant TGO scale was observed in the as-received APS TBCs as shown in Figure 48. However, a difference in the microstructure of APS YSZ was observed. Type I APS TBC did not exhibit typical splat morphology while Type-II TBC did exhibit as seen in Figure 49. The microstructural difference is correlated to the NDE results by EIS a distinctive difference in pore capacitance C_P for these two specimens is reported. This difference in microstructure of the APS 7YSZ coatings is presented in Figure 49 with higher magnification backscatter electron micrographs.

In the as-coated type I TBC specimen, extensive presence of voids between the YSZ and NiCoCrAlY bondcoat interface was observed as presented in Figure 50. The TGO consisted of agglomerated α-Al_2O_3 particles ~100 nm in size. Figure 50 also shows that the microstructure of type I APS YSZ coating does not have the typical columnar grains within splats and splat boundaries. At localized regions where the TGO has fully developed, atomic level bonding was

observed at the YSZ/TGO and TGO/bondcoat interfaces as presented in Figure 50. This is common for APS bondcoat showing an intermediate oxide scale at the interface because of in-flight oxidation of NiCoCrAlY particles. These microstructural observations indicate that the integrity of type I APS TBCs, at least in as-coated condition, may be maintained significantly by "mechanical interlocking" with some adhesion by "chemical bonding."

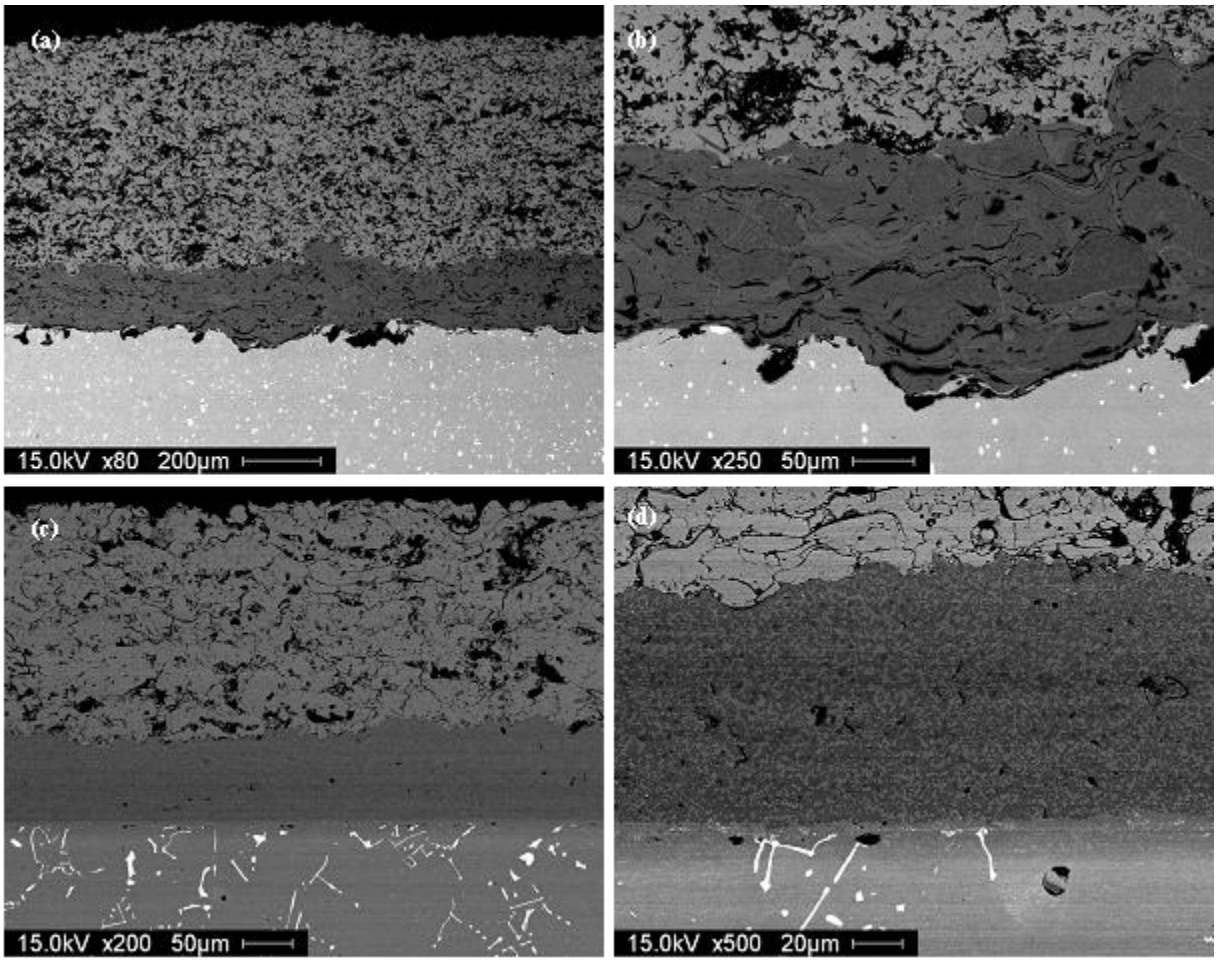

Figure 48. Typical backscatter electron micrographs of (a,b) type I and (c,d) type II APS TBCs specimens.

In the as-coated type II TBC sample, interfacial void between the YSZ and NiCoCrAlY bondcoat was largely filled with carbon (presumably from mounting epoxy) as seen in Figure 50. Also, the TGO was not observed because the bondcoat was sprayed by LPPS. The splat

boundary and micro-cracking within the ceramic coating was more prominent in this type of TBCs.

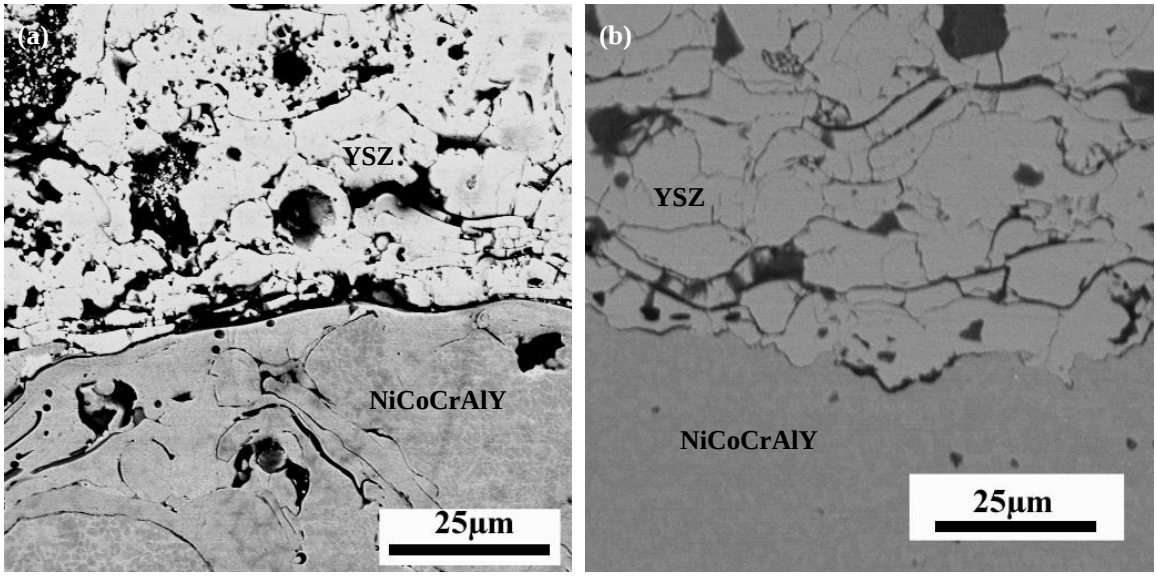

Figure 49. High magnification backscatter electron micrographs of (a) type I and (b) type II APS TBCs specimens.

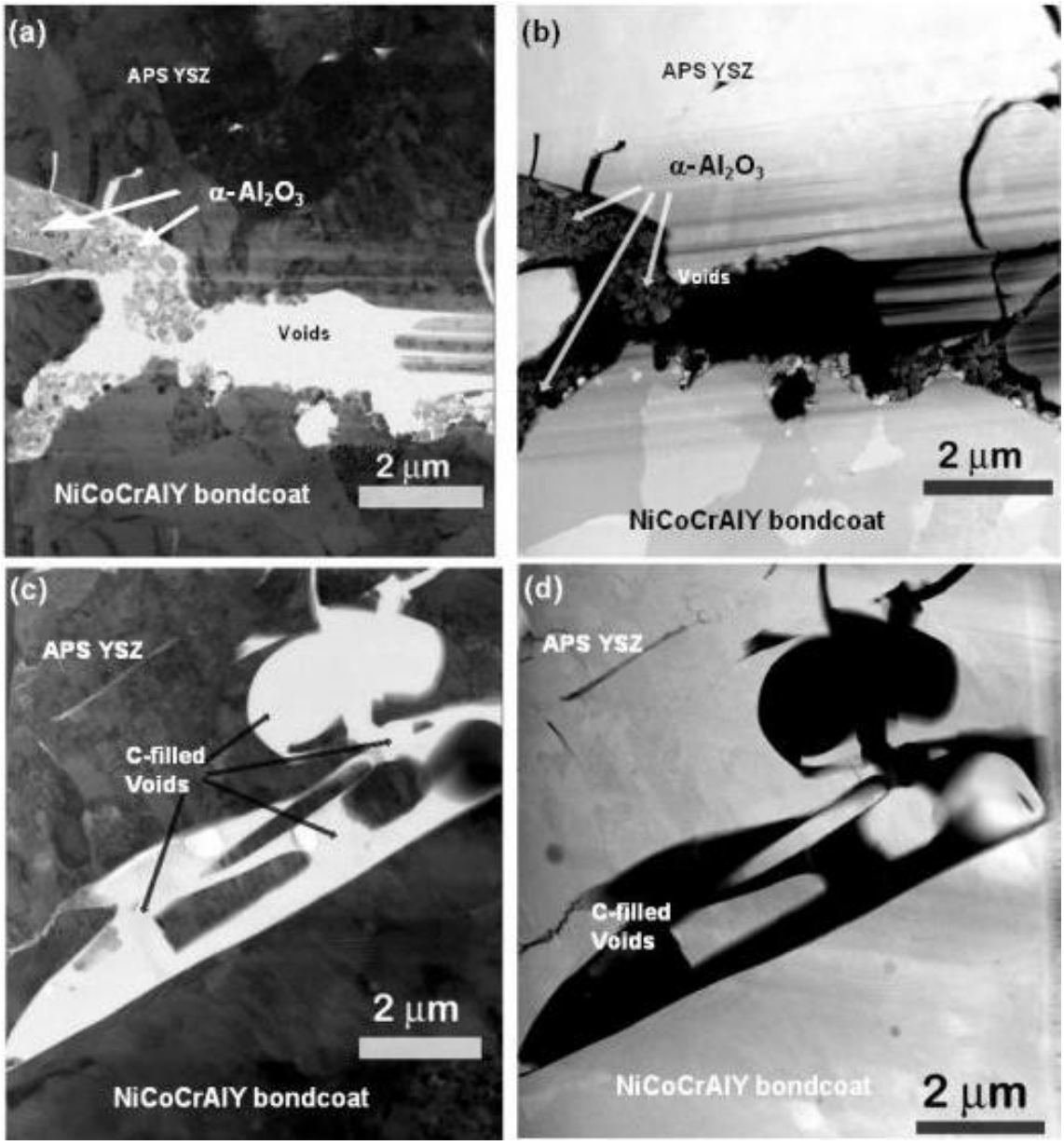

Figure 50. Type- I (a) Bright field and (b) HAADF micrograph of as-received type I APS TBC exhibiting extensive presence of voids, and TGO that consists of agglomerated α-Al_2O_3 particles (~100nm in size). Type –II (c) Bright field and (d) HAADF image of as-coated APS TBC exhibiting extensive presence of carbon-filled voids, absence of TGO and conventional columnar YSZ grains within splats.[93]

4.1.1.1 As-coated EB-PVD TBCs

Figure 51 presents backscatter electron micrographs of the as-coated type III and IV EB-PVD TBCs. The specimens conformed to the specification described in Table 6. Type III and IV EB-PVD YSZ coatings exhibited strain-tolerant columnar microstructure. For these TBCs, a thin TGO layer was observed in the as-received condition as presented in Figure 52. The thin TGO observed at the interface for Type-III and Type-IV has different morphology presumably due to the surface processing condition before the deposition of YSZ. Comparing two types of EB-PVD samples, it can be observed from Figure 51(b) and (d), bondcoat did exhibit smooth and irregular interface, respectively. The smooth as-processed CVD bondcoat showed ridges associated with the bondcoat grain boundaries whereas the grit blasted surface had a few Al_2O_3 grit embedded on the surface due to grit blast.

A detailed analysis reported elsewhere on the same type of TBCs [93] on microstructure was conducted by site-specific observation on specimen using HR-STEM. In the as-coated type III TBC, a continuous TGO layer was observed along with patches of "mixed-oxide" layer as seen in Figure 53. Regions in the TGO with "mixed-oxide" were always thicker (~0.5μm) than those consisting of continuous α-Al_2O_3 layer (~0.1μm) as presented by Figure 53.

Relative to type III TBCs, the microstructure of type IV EB-PVD TBC specimen presented in Figure 51 exhibited many distinctive features including (1) larger inter-columnar voids, (2) more feathery YSZ columns, (3) thinner Al_2O_3 TGO without a "mixed-oxide" layer, (4) large residual α-Al_2O_3 particles from grit blasting, and (5) smaller β-(Ni,Pt)Al grains. A bright field and high angle annular dark field electron micrographs showing the residuals from grit-blasting are presented in Figure 54.

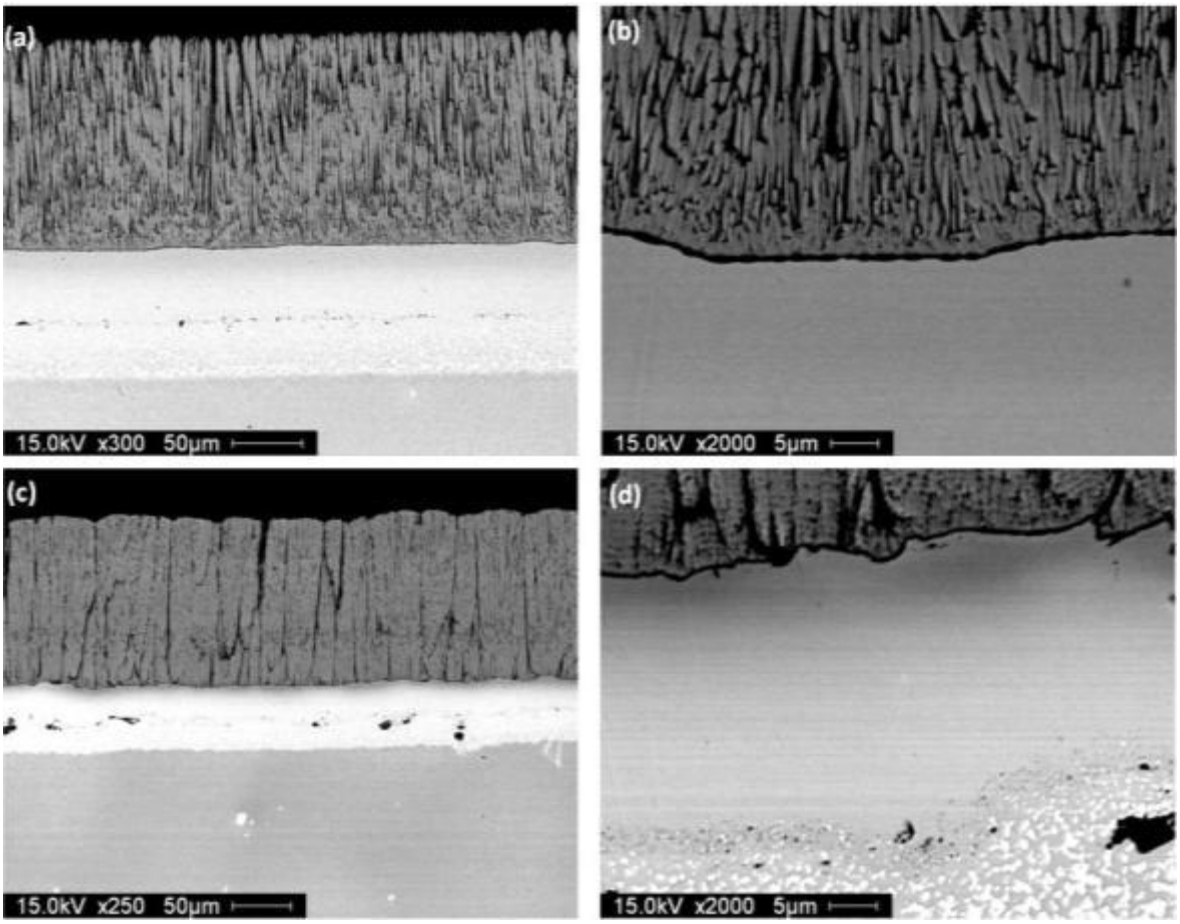

Figure 51. Typical backscatter electron micrographs of EB-PVD TBCs specimens with different surface processing techniques (a,b) type III with as-coated (Ni,Pt)Al bondcoat (c,d) type IV with grit-blasted (Ni,Pt)Al bondcoat.

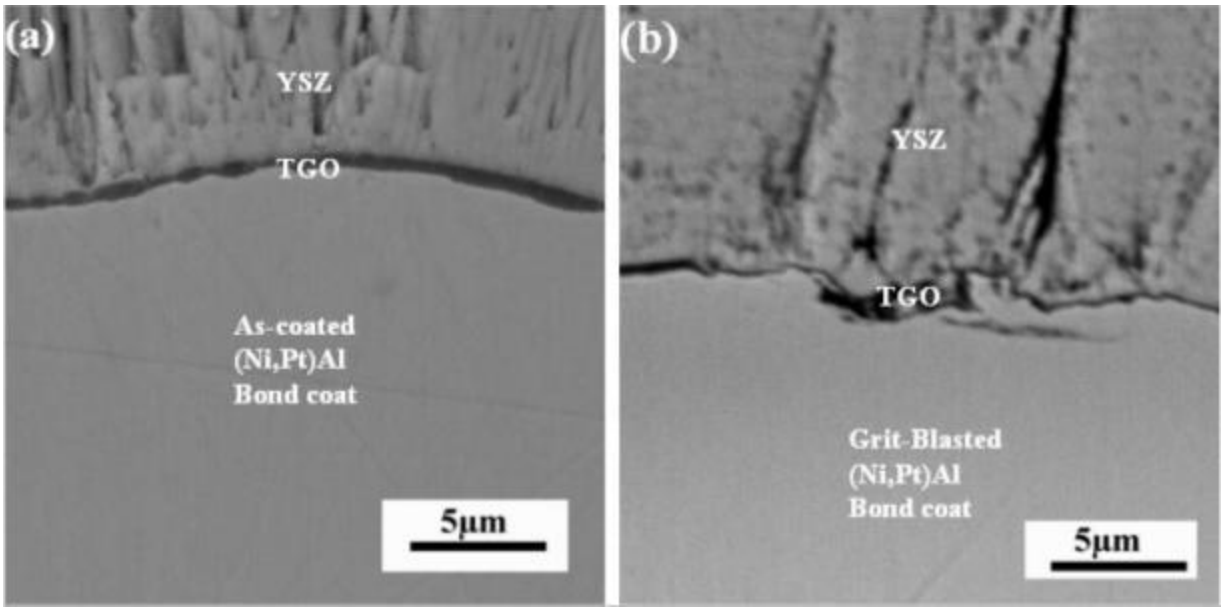

Figure 52. High magnification backscatter electron micrographs of EB-PVD TBCs (a) type III as-coated (Ni,Pt)Al bondcoat (b) type IV grit blasted (Ni,Pt)Al bondcoat specimens.

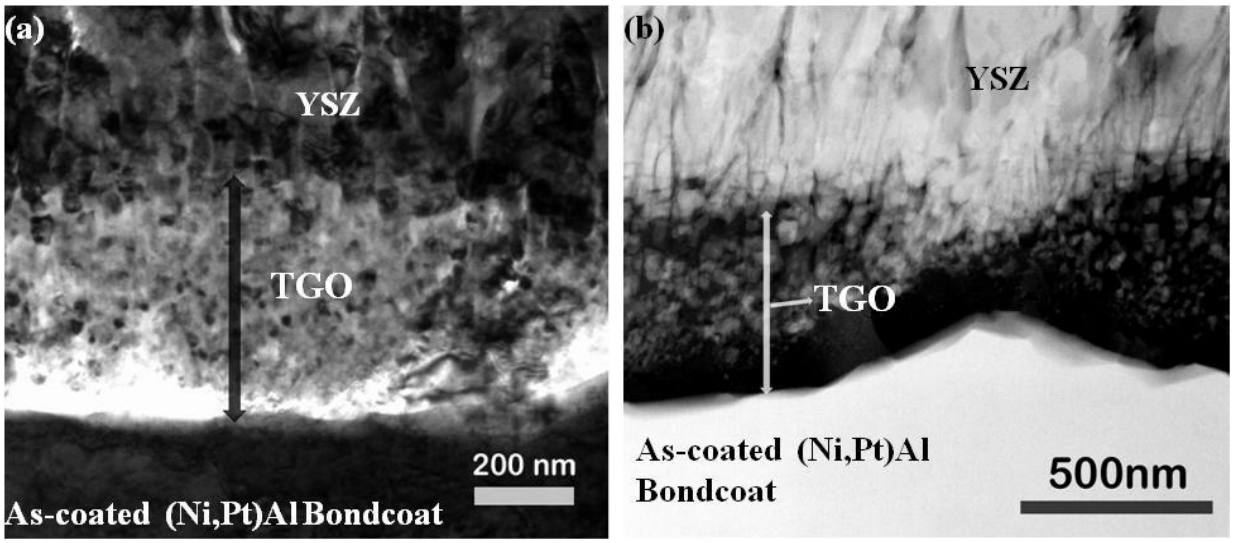

Figure 53. Presence of other oxides, and mixed oxides is apparent within the interface (a) Bright field and (b) HAADF images of as-received type III EB-PVD TBCs with as-coated (Ni,Pt)Al bondcoat.

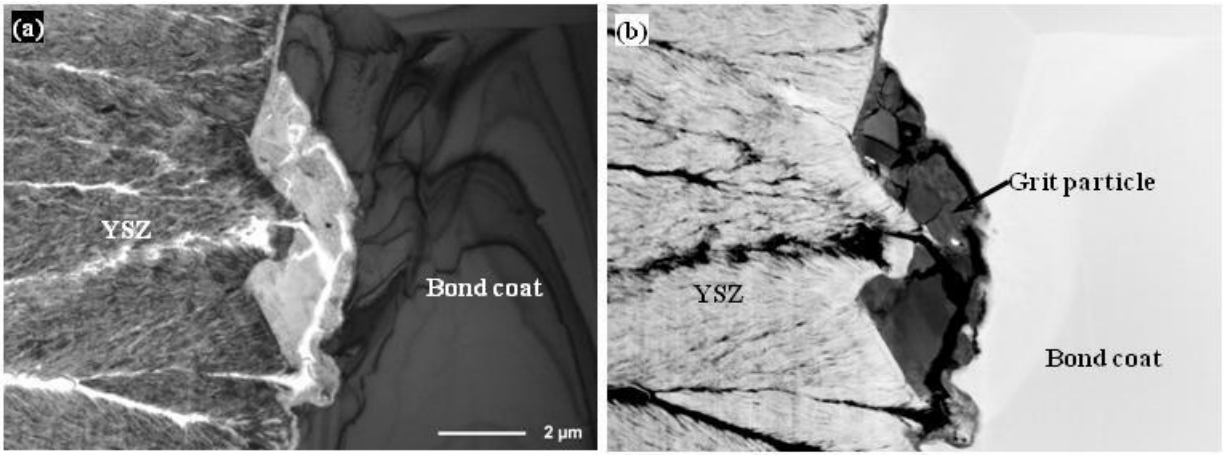

Figure 54. (a) Bright field and (b) HAADF images of as-received type IV EB-PVD TBCs with grit-blasted (Ni,Pt)Al bondcoat. Presence of large residual α-Al_2O_3 particles from grit blasting was frequently observed.

4.2 Furnace thermal Cyclic Lifetime

TBC lifetime was determined using CM™ Rapid Temperature furnace for 1, 10 and 50-hour thermal cycling at 1121°C (2050°F) using 5, 3 and 2 specimens, respectively for each dwell time. Each cycle consisted of 10-minute heat-up, 40-minute, 9.8 hours and 49.8 hours dwells at 1121°C and 10-minute forced air-quench. The TBC lifetimes are reported in Table 10 and Figure 55. Independent of the dwell time at 1121°C (2050°F), the lifetime of type I TBCs was the highest followed by types III and IV. The total cyclic dwell time before failure for the four different types of TBCs is also presented in Figure 56.

Table 10. Specifications and thermal cycling lifetime for four types of TBCs investigated in this study.

TBC System	7YSZ Deposition and Thickness	Bondcoat and Thickness	Superalloy Substrate	Dwell Time (Hrs) at 1121°C (2050°F)	Number of Specimens Tested	TBC Lifetime and Standard Deviation (#)
I	APS 600 μm	NiCoCrAlY 175 μm	Haynes 230	0.67 9.8 49.8	5 3 2	527 (20) 113 (1) 39 (0.7)
II	APS 200 μm	NiCoCrAlY 100 μm	MAR-M-509	0.67 9.8 49.8	8 1 1	286 (76) 18 (0) 8 (0)
III	EB-PVD 145 μm	As-Coated (Ni,Pt)Al 50 μm	CMSX-4	0.67 9.8 49.8	6 4 2	406 (22) 55 (3) 12 (1.5)
IV	EB-PVD 140 μm	Grit-Blasted (Ni,Pt)Al 35 μm	Rene'N5	0.67 9.8 49.8	6 3 2	360 (39) 42 (2) 9.5 (0.7)

From the furnace cyclic lifetime for all four types of TBCs, 10%, 50% and 70% lifetime was calculated as presented in Table 11. Similar calculation of lifetime at 30% and 80% for the four types of TBCs was carried out for 10-hour and 50% for 50-hour thermal cycling as reported in Table 11. Furnace thermal cycling was carried out up to these cycles and TBC samples were examined for the microstructural evolution as functions of thermal cycling.

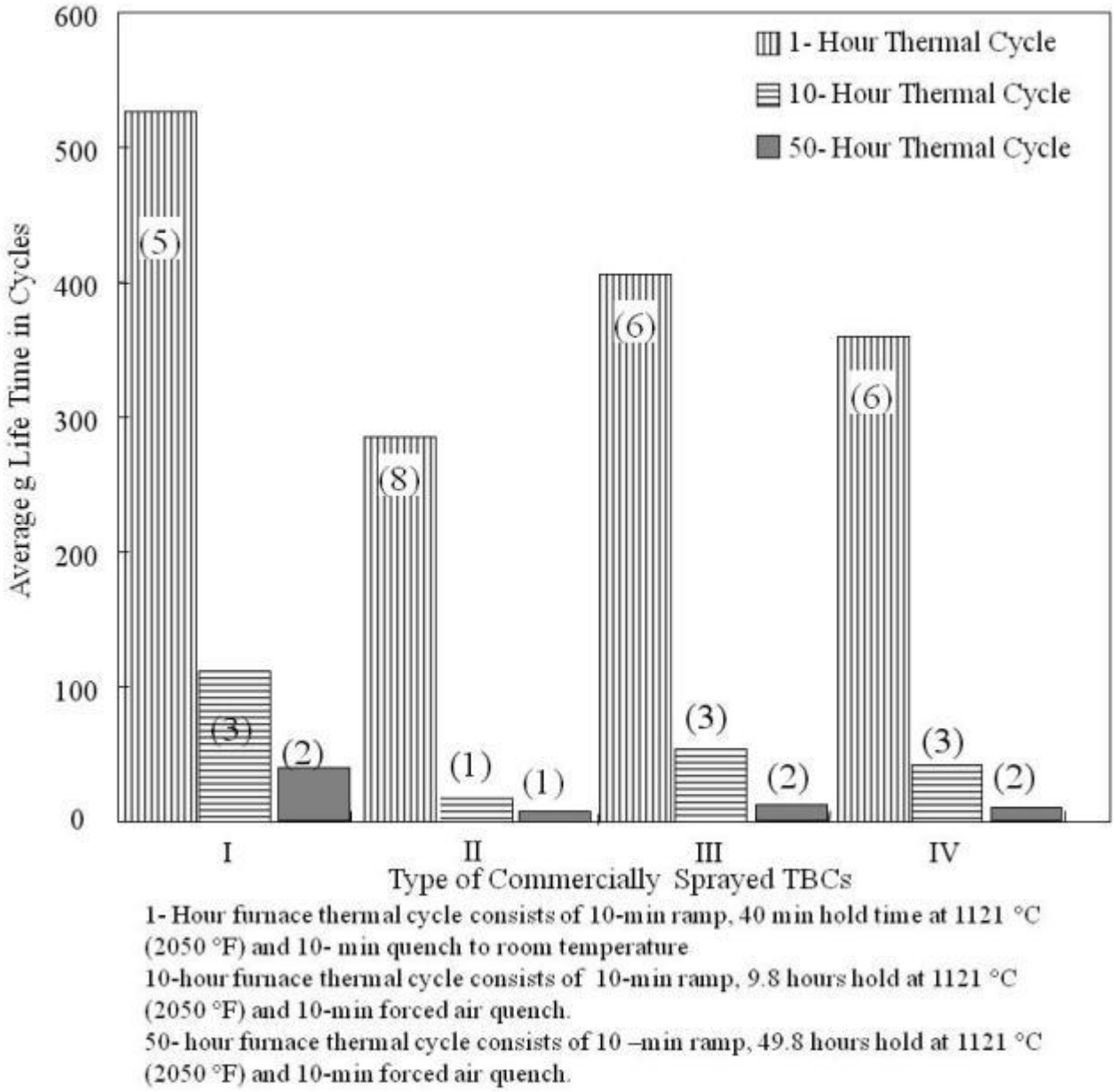

Figure 55. Furnace cyclic lifetime assessed from thermal cycling at 1121°C for four-types of TBCs. Values in parenthesis represent the number of specimen employed to determine the lifetime using 1, 10 and 50 –hour thermal cycling

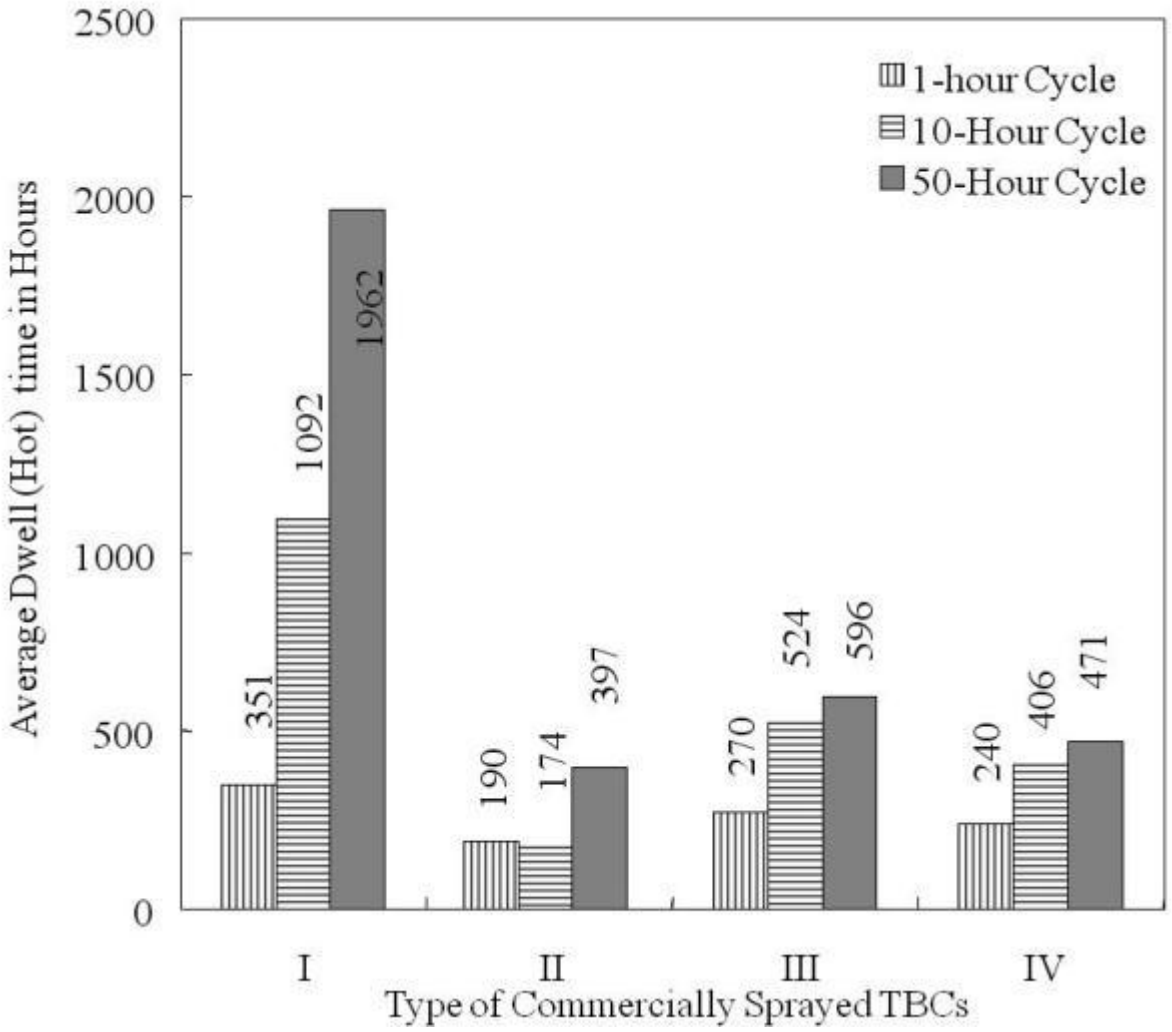

Figure 56. Dwell time life during thermal cycling at 1121°C for four-types of TBCs tested using 1, 10 and 50 –hour thermal cycling.

Table 11. Thermal cyclic lifetime for TBCs and specimens employed for microstructural analysis.

TBC System	TBC Lifetime and Standard Deviation (#)	1-Hour Thermal Cycling			10-Hour Thermal Cycling		50-Hour Thermal Cycling
		10% Lifetime	50% Lifetime	70% Lifetime	30% Lifetime	80% Lifetime	50% Lifetime
I	527 (20) 113 (1) 39 (0.7)	50	260	360	35	90	20
II	286 (76) 18 (0) 8 (0)	30	140	200	5	15	4
III	406 (22) 55 (3) 12 (1.5)	45	200	280	20	45	6
IV	360 (39) 42 (2) 9.5 (0.7)	35	180	250	15	35	4

4.3 Visual Observation of APS TBC Spallation

4.3.1 1-Hour Furnace Thermal Cycling

Figure 57 shows the typical fracture surface after the YSZ coating spalled for type-I APS TBCs with APS NiCoCrAlY bondcoat. From the fracture surface of the YSZ, two distinctive contrast features, namely black and white, are observed. The black region is the TGO and the white region is the YSZ. A similar interpretation can be made on the bondcoat surface after spallation shown in Figure 57(b). From this evidence, it is clear that the coating failure for this particular type of TBCs during 1-hour thermal cycling occurred at the YSZ/TGO interface within the YSZ.

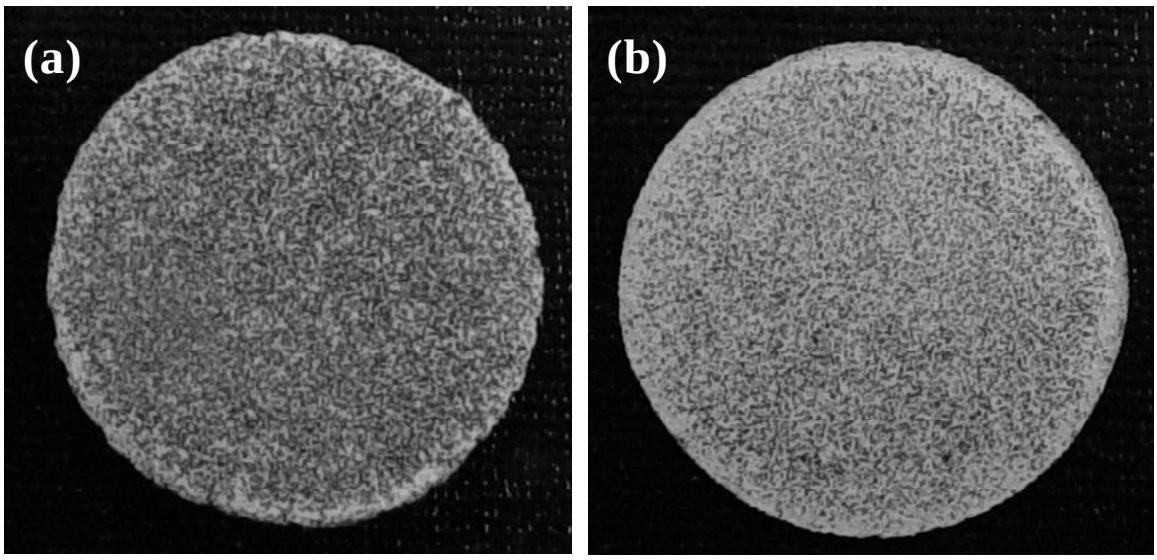

Figure 57. Macro photographs illustrating failure mode of type I APS TBCs with APS NiCoCrAlY bondcoat with average lifetime of 527 cycles: (a) bottom surface of the spalled YSZ coating and (b) top surface of the bondcoat after the YSZ spallation.

A similar observation and explanation can be given to the type-II APS TBCs examined in this study with LPPS NiCoCrAlY bondcoat shown in Figure 58. Initial fracture occurred by edge delamination shown in Figure 58(b). A detailed analysis was carried out in later section 4.8.1 .

Figure 58. Macro photographs illustrating failure mode of type II APS TBCs with NiCoCrAlY bondcoat with average lifetime of 286 cycles: (a) top surface of bondcoat after YSZ spallation that (b) occurred with initial damage at the edge of the button.

4.3.2 10-Hour Furnace Thermal Cycling

Figure 59 and Figure 60 show visual observation of fracture surface for type-I and type-II APS TBCs after 10-hour thermal cycling. Comparing the fracture surface to 1-hour thermal cycling, 10-hour thermal cycling showed same gray scale visually/macroscopically: where the fracture occurred at the YSZ/TGO interface and within the YSZ. Detailed investigation on cross-sectional fractography was performed and later reported in the section 4.8.2.

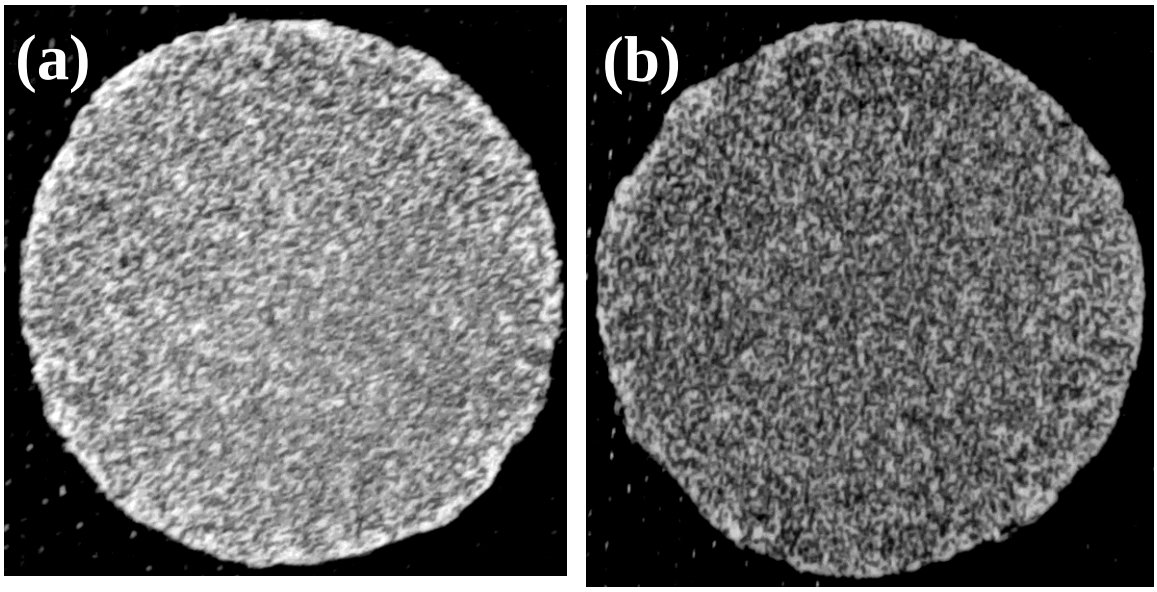

Figure 59. Macro photographs illustrating failure mode of type I APS TBCs with APS NiCoCrAlY bondcoat with average lifetime of 113 cycles: (a) bottom surface of spalled the YSZ coating and (b) top surface of bondcoat after the YSZ spallation.

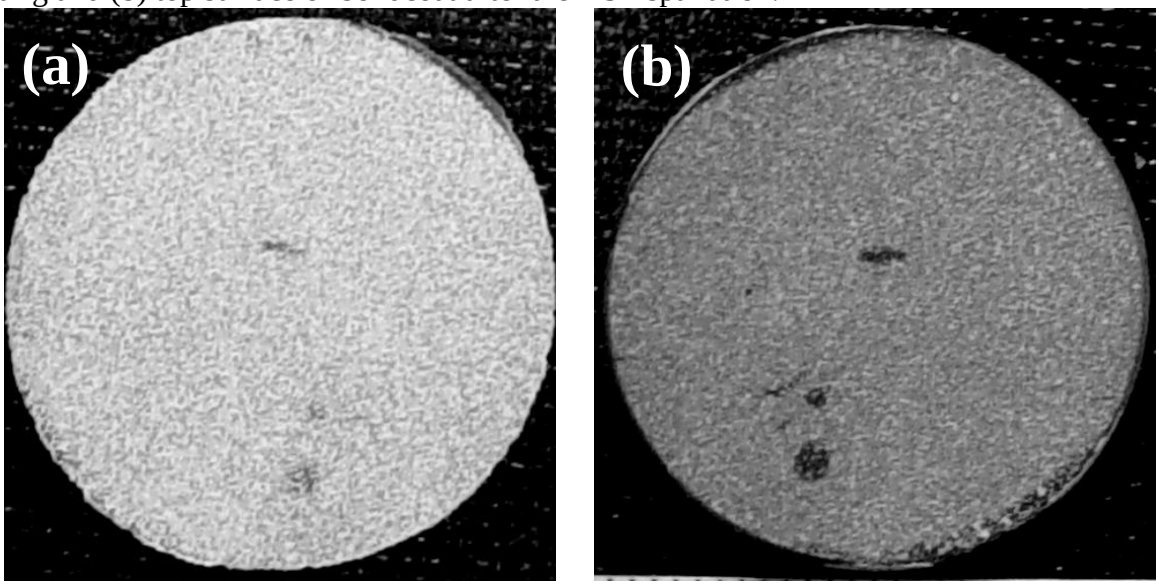

Figure 60. Macro photographs illustrating failure mode of type II APS TBCs with NiCoCrAlY bondcoat with average lifetime of 18 cycles: (a) bottom surface of the YSZ after spallation of the coating from the bondcoat (b) top surface of bondcoat after the YSZ spallation.

4.3.3 50-Hour Furnace Thermal Cycling

Figure 61 and Figure 62 show macroscopic fracture of type-I and type-II APS coatings after 50-hour thermal cycling. In comparing to 1 and 10-hour thermal cycling, there is no striking difference. A minor difference is the bondcoat surface after coating separation. It showed more gray scale content compared to 1-hour and 10-hour thermal cycles after failure. The fracture path for APS TBCs regardless of the bondcoat type remained at the YSZ/TGO interface within the YSZ. The micro constituents of the fracture surface will be reported in section 4.8.3.

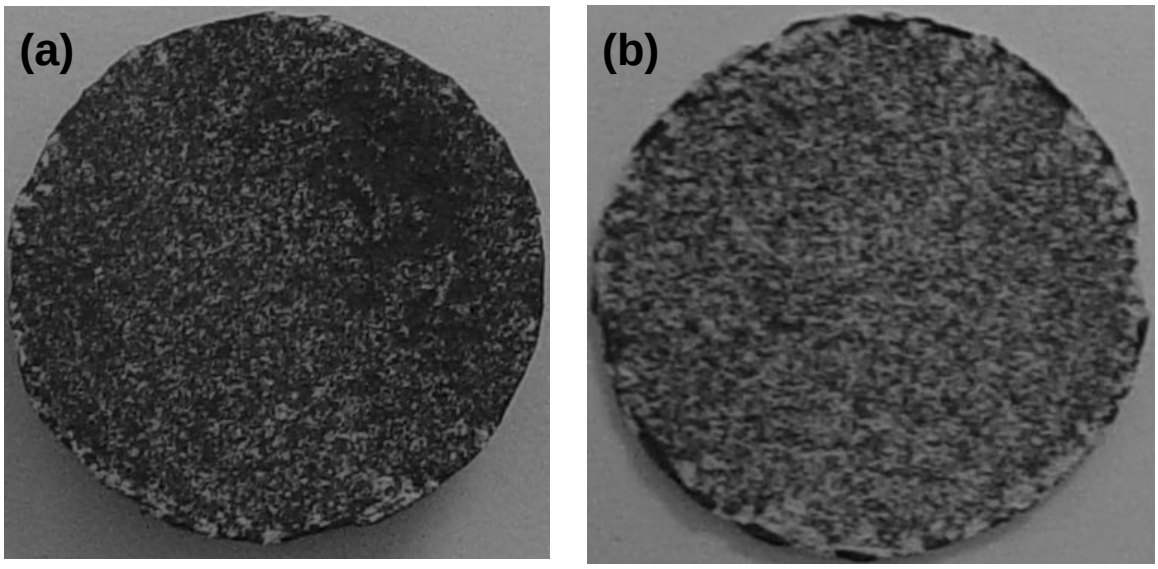

Figure 61. Macro photographs illustrating failure mode of type I APS TBCs with APS NiCoCrAlY bondcoat with average lifetime of 39 cycles: (a) top surface of bondcoat after the YSZ spallation and (b) bottom surface of the YSZ after spallation.

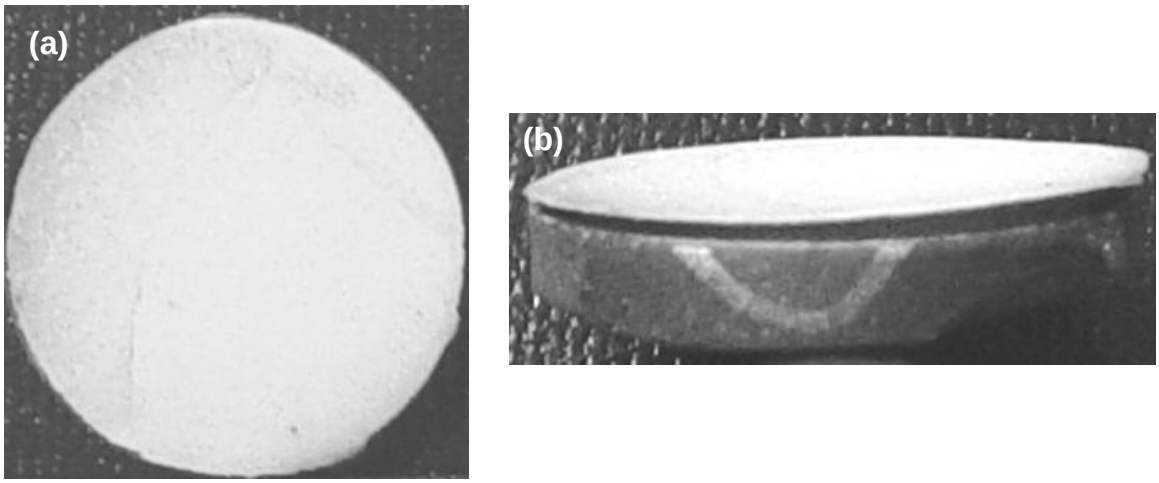

Figure 62. Macro photographs illustrating failure mode of type II APS TBCs with VPS NiCoCrAlY bondcoat with average lifetime of 8 cycles: (a, b) top surface of delaminated YSZ and (c) A front view of the delamination of YSZ coating.

4.4 Visual Observation of EB-PVD TBC Spallation

4.4.1 1- Hour Furnace Thermal Cycling

For the as-coated type-III EB-PVD TBCs with (Ni,Pt)Al bondcoat, visual observation of fracture surface is shown in Figure 63. It is evident that the YSZ coating fractured into multiple fragments at failure. Visual observation shows black and light gray regions on the surface. The light contrast areas from the bondcoat surface are from regions where there is YSZ still attached to the bondcoat and grey areas are region where TGO is still present on the bondcoat surface. The fracture occurred at the YSZ/TGO interface. For grit blasted (Ni, Pt) Al type-IV EB-PVD TBCs visual observation of fracture surface is shown in Figure 64. From Figure 64(a) it can be observed that the YSZ coating buckled in certain regions at failure as pointed by arrows. Detailed investigation of the fracture surface for type-III and type-IV coating will be discussed later in section 4.9.1.

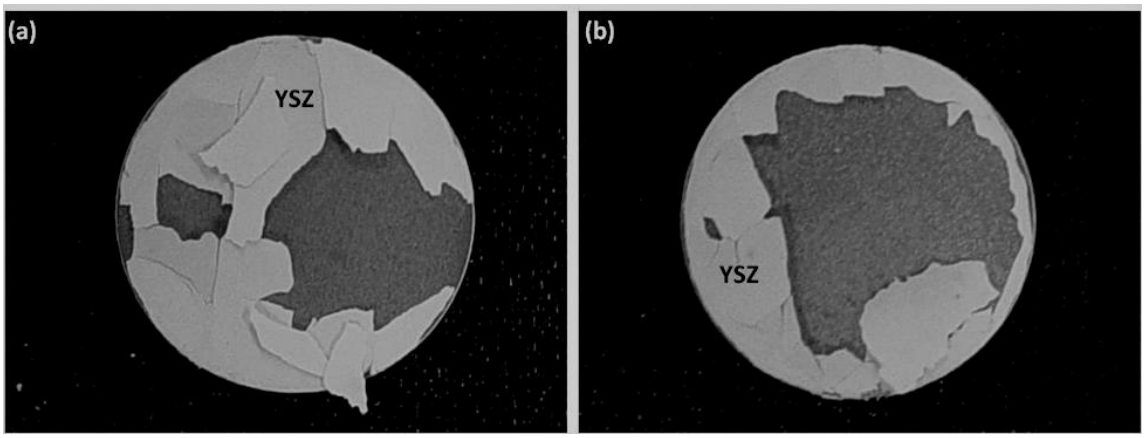

Figure 63. (a,b) Macro photographs illustrating failure mode of type III EB-PVD TBCs with as-coated (Ni,Pt)Al bondcoat with average lifetime of 418 cycles.

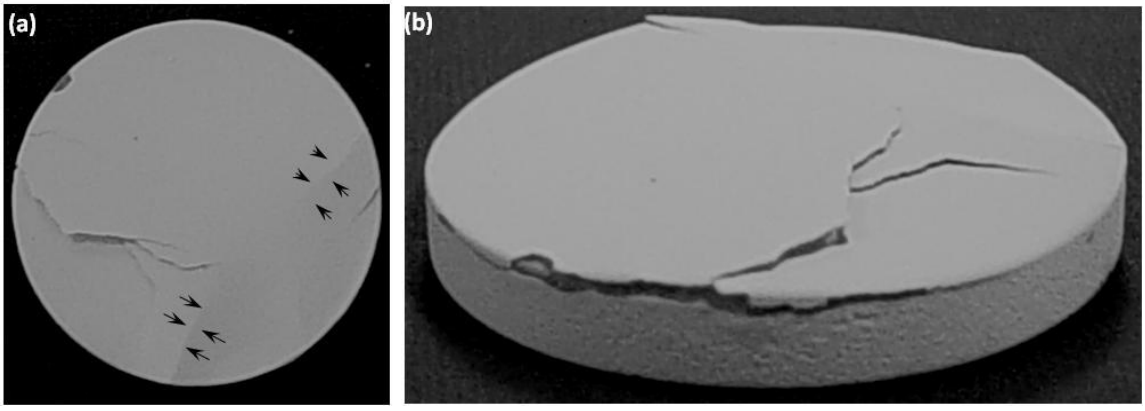

Figure 64. Macro photographs illustrating failure mode of type IV EB-PVD TBCs with grit-blasted bondcoat with average lifetime of 362 cycles: (a) top surface of buckled YSZ and (b) disintegration of the YSZ coating afterwards.

4.4.2 10-Hour Furnace Thermal Cycling

Visual observation of fracture surface from type-II EB-PVD with as-coated (Ni,Pt)Al bondcoat is shown in Figure 65. The macroscopic fracture surface is different compared to the 1-hour fracture surface shown in Figure 63. The bondcoat surface area shows lighter gray scale and more shiny surface compared to 1-hour thermal cycling. The lighter gray scale corresponds to

the TGO and shiny surface to the bondcoat surface. From this observation it can concluded that the fracture path is at the TGO/bondcoat interface.

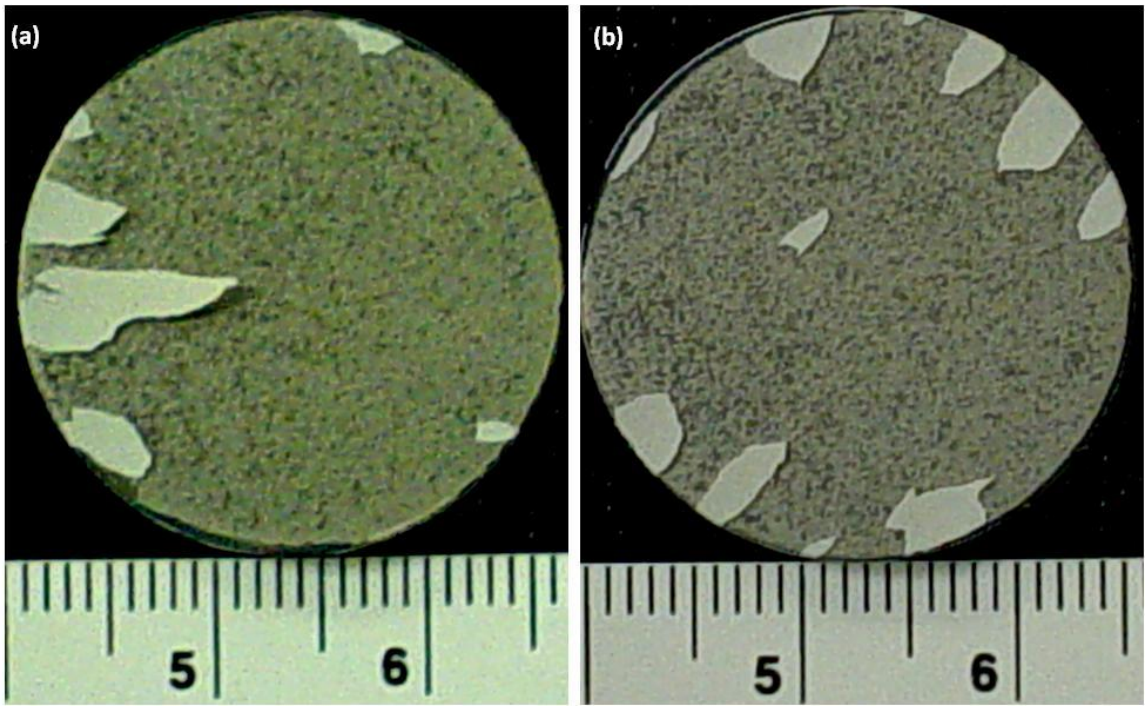

Figure 65. (a,b) Macro photographs of bondcoat surface illustrating failure mode of type III EB-PVD TBCs with as-coated (Ni,Pt)Al bondcoat with average lifetime of 55 cycles.

Fracture surface of type-IV EB-PVD TBCs with grit blasted (Ni,Pt)Al bondcoat is shown in Figure 66. The ceramic topcoat YSZ, showed localized regions of large scale buckling along with areas of intact YSZ. This could be a precursor to the final failure of YSZ into fragments with an additional thermal cycle. A higher magnification on the buckled region shows cracks running through the YSZ as seen on Figure 66(b,d). A detailed microstructural characterization was carried on both types of EB-PVD TBCs after 10-hour thermal cycle is discussed later in the section 4.9.2.

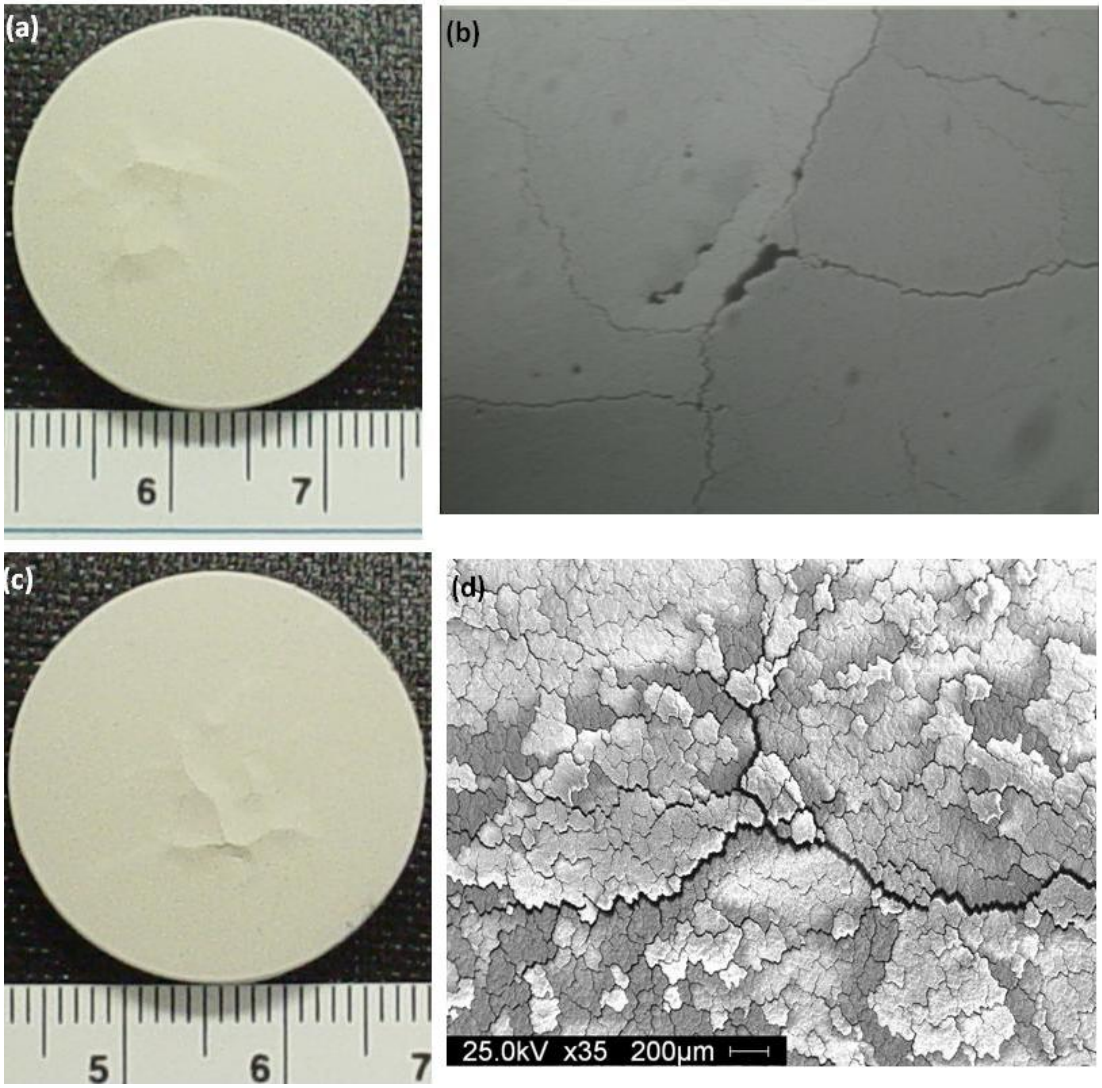

Figure 66. Macro photographs illustrating failure mode of type IV EB-PVD TBCs with grit-blasted bondcoat with average lifetime of 42 cycles: (a, c) top surface of buckled YSZ and (b,d) A magnified view of the buckling in the YSZ coating.

4.4.3 50-Hour Furnace Thermal Cycling

Visual observation of fracture surface for type-III EB-PVD TBCs with as-coated (Ni,Pt)Al bondcoat is shown in Figure 67. From macroscopic observation, the TGO appear in gray contrast and the bondcoat surface appears in light contrast (shiny surface). For these TBCs, fracture occurred at the TGO/bondcoat interface based on the gray scale. A detailed investigation will be presented in section 4.9.3 for this type of TBCs. This particular type of surface is often a result of large scale buckling of the YSZ, and commonly observed in isothermal oxidation not in thermal cyclic oxidation.

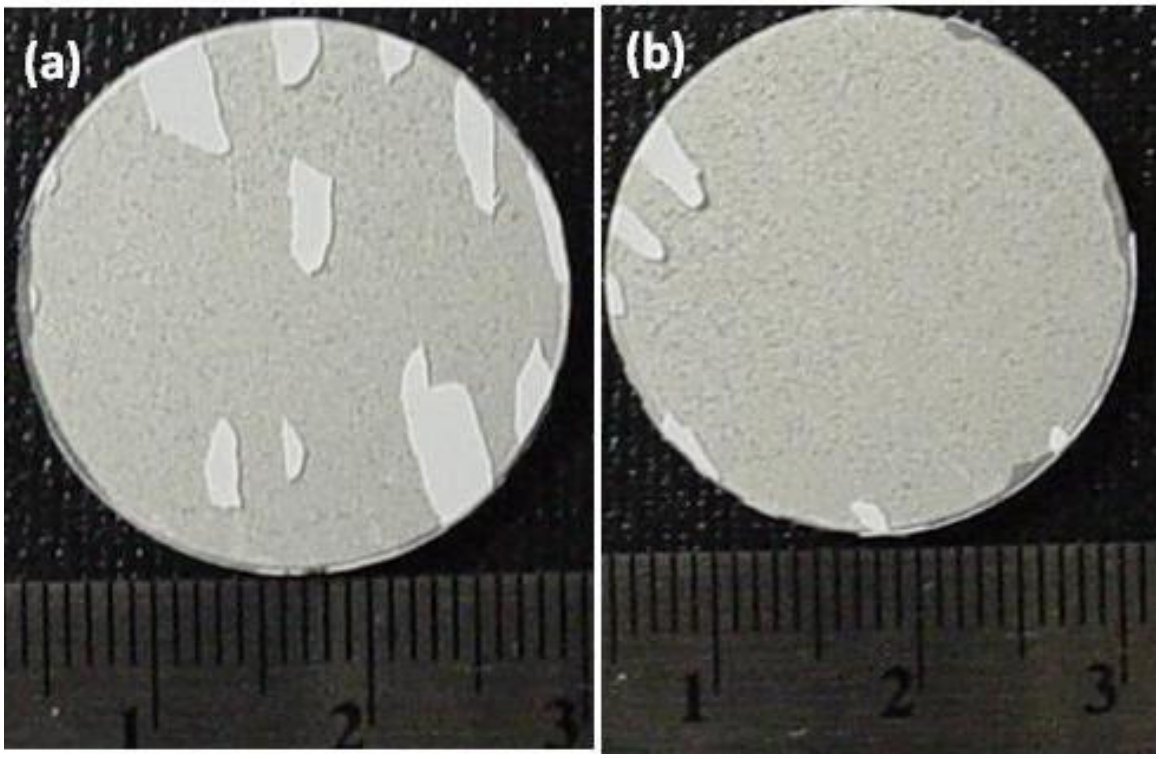

Figure 67. Macro photographs illustrating failure mode of type III EB-PVD TBCs with as-coated (Ni,Pt)Al bondcoat with average lifetime of 12 cycles. Large scale buckling is observed in both samples after 50-hour thermal cycling.

Figure 68 shows the macrograph of type-IV EB-PVD TBCs with grit-blasted (Ni,Pt)Al bondcoat. These samples also failed by large scale buckling comparing. The micro-constituents and the difference of the fracture surface will be discussed later in the section 4.9.3.

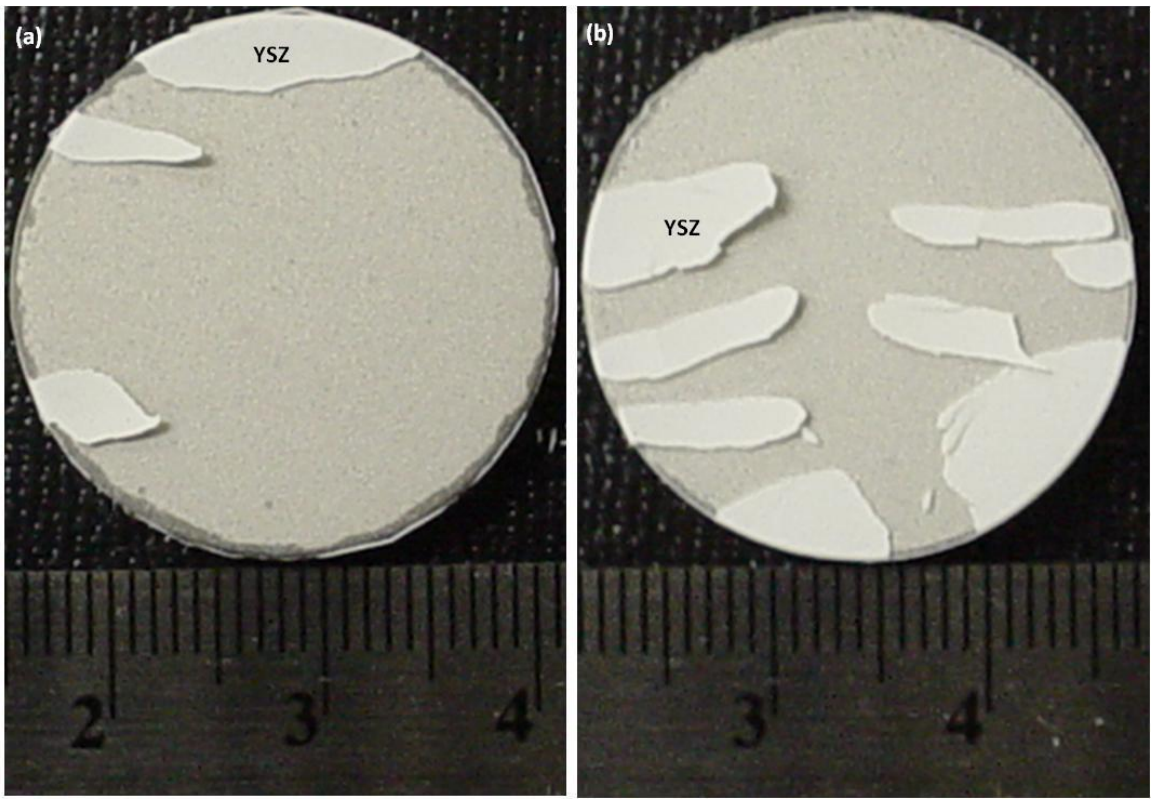

Figure 68. Macro photographs illustrating failure mode of type IV EB-PVD TBCs with grit-blasted (Ni,Pt)Al bondcoat with average lifetime of 9 cycles. Large scale buckling was observed in both samples after 50-hour thermal cycling.

4.5 PSLS of EB-PVD TBCs

4.5.1 As-coated EB-PVD Thermal Barrier Coatings

PSLS data was collected for type III, as-coated EB-PVD TBCs with (Ni,Pt)Al bondcoat. Typical measurement points are shown in Figure 43 for all 20 specimens. For this particular type of EB-PVD TBCs, luminescence from polymorphs of Al_2O_3 namely α,γ and θ was observed. In as-coated condition, the relative luminescence from each sample is shown in Figure 70. The luminescence from α-Al_2O_3 was significant compared to the θ and γ-Al_2O_3. The values reported in Figure 70 do not quantitatively correspond to amount (e.g., volume fraction). Figure 71 and Figure 72 present the shift in the position of R_2 luminescence $\overline{\Delta\upsilon}$ based on measurements for type III TBCs. In all cases, bimodal (i.e., two sets of R'_1 and R'_2) luminescence corresponding to higher (~5 GPa) and lower (~3.5 GPa) compressive residual stress in the α-Al_2O_3 was observed based on a non-linear least square curve fitting analysis.

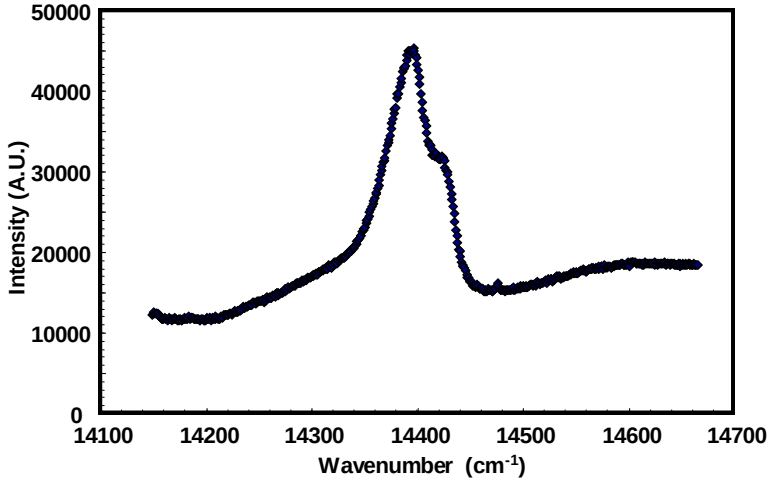

Figure 69. Typical photostimulated luminescence spectrum from as-received type III EB-PVD TBCs with as-coated (Ni,Pt)Al bondcoat.

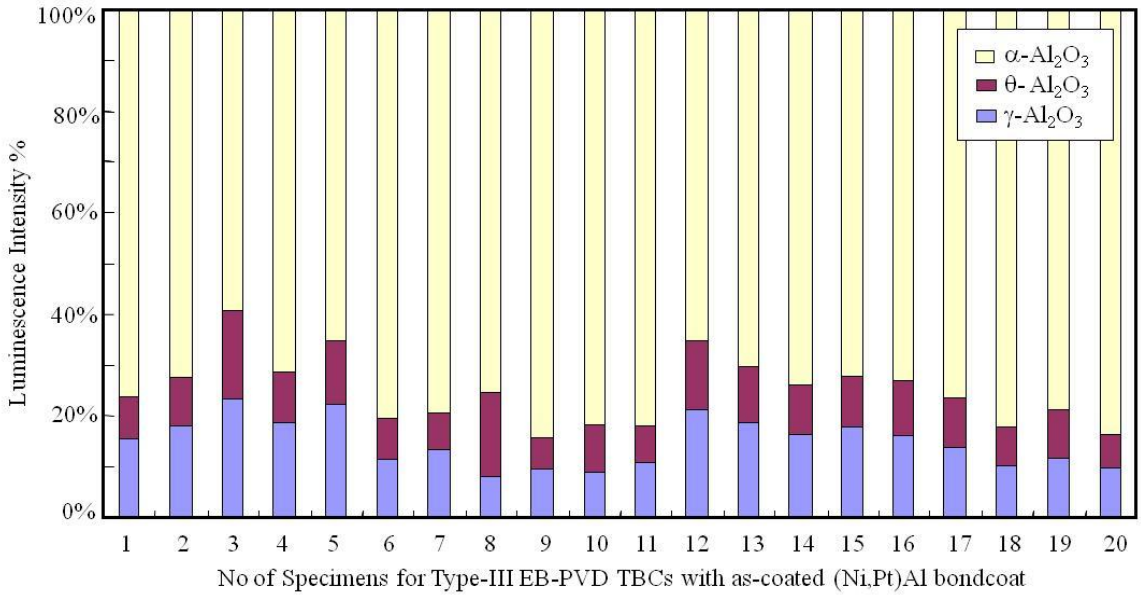

Figure 70. Relative luminescence intensity from α-, γ- and θ-Al_2O_3 in the TGO for as-coated type III TBCs with as-coated (Ni,Pt)Al bondcoat.

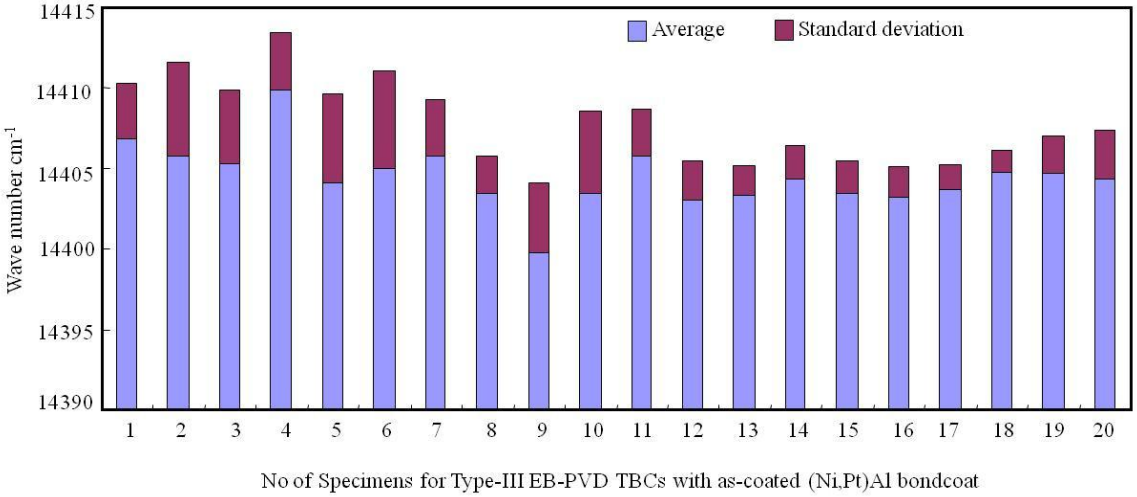

Figure 71. Relative shift in the R_2 luminescence recorded for the specimens analyzed for type-III as-coated (Ni,Pt)Al bondcoat with CMSX-4 substrate.

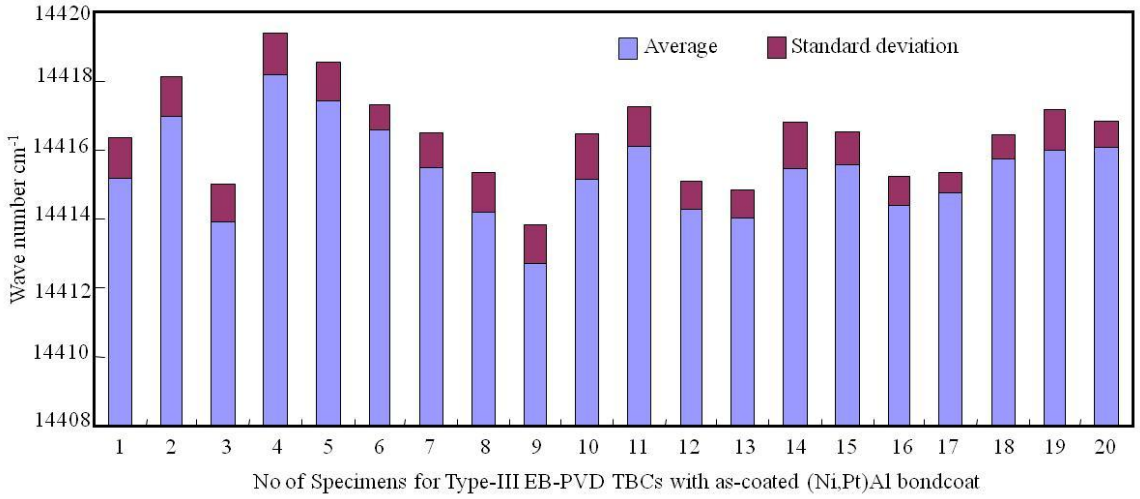

Figure 72. Relative shift in the R_2, luminescence recorded for the specimens analyzed for type-III as-coated (Ni,Pt)Al bondcoat with CMSX-4 substrate.

PSLS was collected for 20 specimens of type IV, as-coated EB-PVD TBCs with grit-blasted (Ni,Pt)Al bondcoat. For all 20 specimens with luminescence, 30 spots measurements were carried out. Clear and distinguishable luminescence from α-, γ- and θ-Al_2O_3 was observed in all spectra for 16 specimens as presented in Figure 73(a). The remaining four specimens exhibited luminescence with low signal-to-noise ratio as presented in Figure 73(b). Relative luminescence intensity from α-, γ- and θ-Al_2O_3 polymorphs is presented in Figure 74. In general, 60~70% of luminescence intensity was from the α-Al_2O_3 while 30~40% of luminescence intensity was from γ- and θ-Al_2O_3 for as-coated type IV TBCs. These values do not correspond to the actual volume fraction of Al_2O_3 polymorphs. Relative to type III TBCs with as-coated (Ni,Pt)Al bondcoat, a slightly stronger γ-Al_2O_3 luminescence than θ-Al_2O_3 was observed.

Figure 75 and Figure 76 represent the shift in the position of R_2 luminescence $\overline{\Delta\upsilon}$ determined based on 30 spot measurements for as-coated type IV TBCs. In all cases, bimodal (i.e., two sets of R_1 and R_2) luminescence corresponding to higher (~6 GPa) and lower (~1 GPa)

compressive residual stress in the α-Al_2O_3 was observed based on a non-linear least square curve fitting analysis.

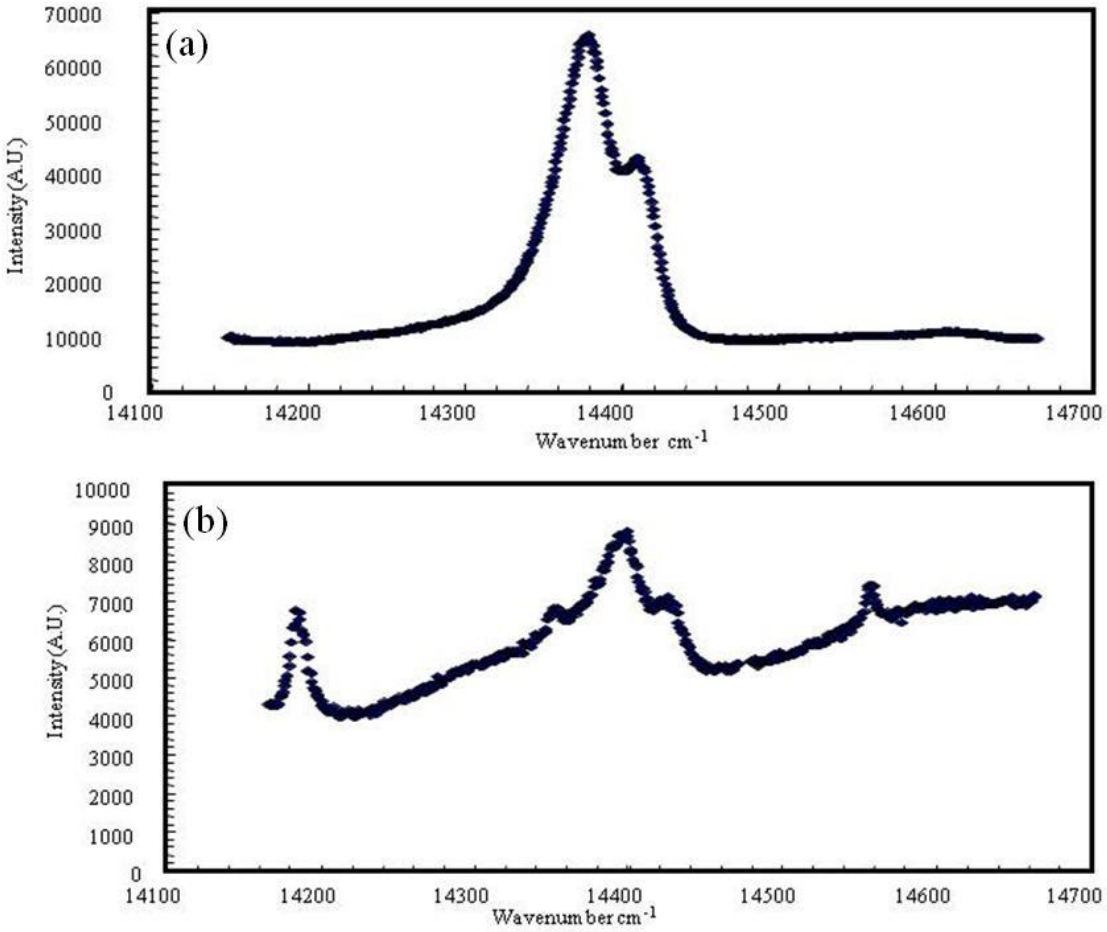

Figure 73. Typical photostimulated luminescence spectrum from as-received type IV EB-PVD TBCs with grit-blasted (Ni,Pt)Al bondcoat: (a) 16 specimens with strong luminescence and (4) the remaining 4 specimens with low signal-to-noise ratio.

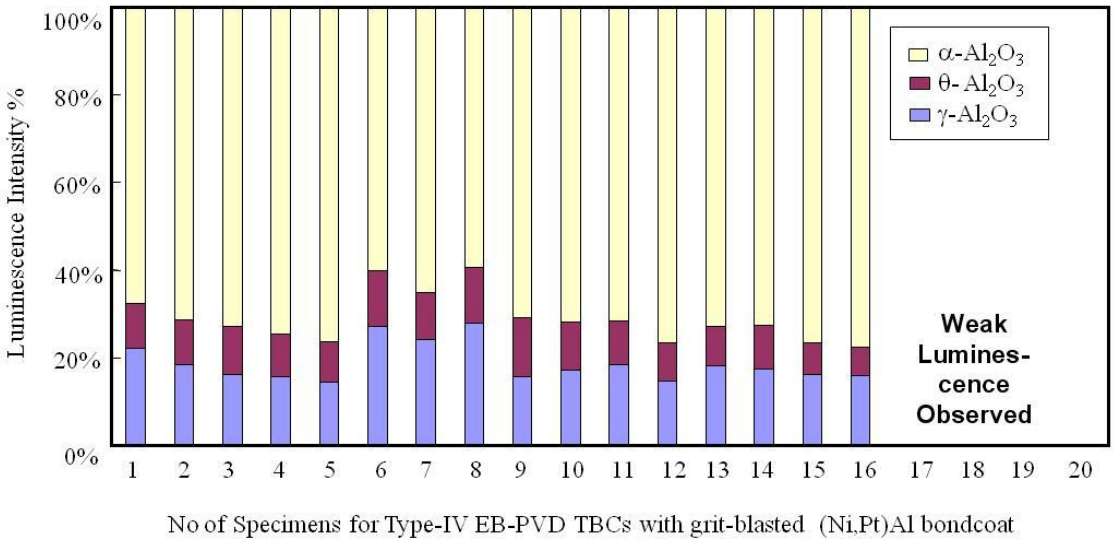

Figure 74. Relative luminescence intensity from the α-, γ- and θ-Al_2O_3 in the TGO for as-coated type IV TBCs with grit-blasted (Ni,Pt)Al bondcoat.

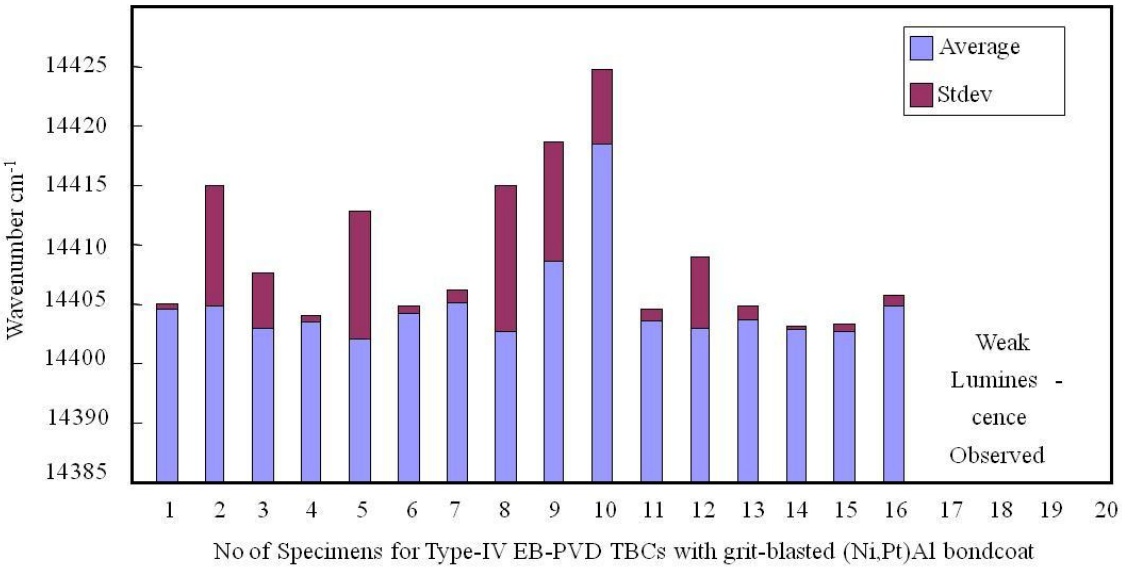

Figure 75. Relative shift in the R_2 luminescence recorded for the specimens analyzed for type-IV grit-blasted (Ni,Pt)Al bondcoat with Rene N5 substrate.

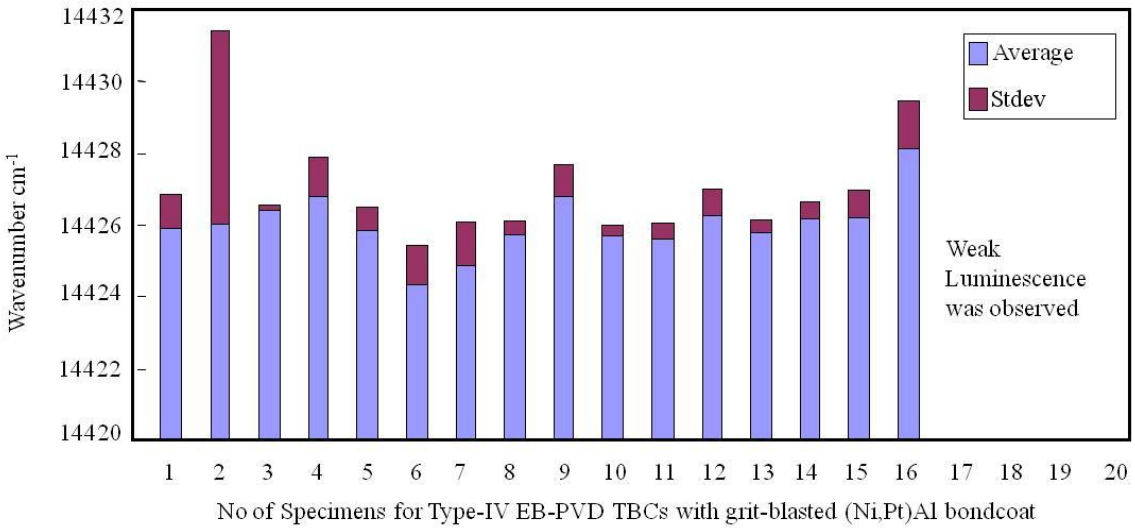

Figure 76. Relative shift in the $R_{2'}$ luminescence recorded for the specimens analyzed for type-IV grit-blasted (Ni,Pt)Al bondcoat with Rene N5 substrate.

4.5.2 1-Hour Furnace Thermal Cycling

Figure 77 represents typical luminescence evolution observed for type III TBCs as a function of 1-hour thermal cycling. The lifetime for 1-hour thermal cycles was 406 ± 22 cycles. After 400 cycles, more than half of 20-randomly-selected measurement indicated a third luminescence peak which can be seen in Figure 77. A similar type of response was obtained for the same type of TBCs and the results were published previously. [94] A bimodal luminescence (i.e., two sets of R_1-R_2 luminescence) was observed until 50% of furnace thermal cycle life time for this type III TBCs. However, a tri-mode luminescence emerged starting from approximately 50% lifetime, and a third set of R''_1-R''_2 luminescence emerged.

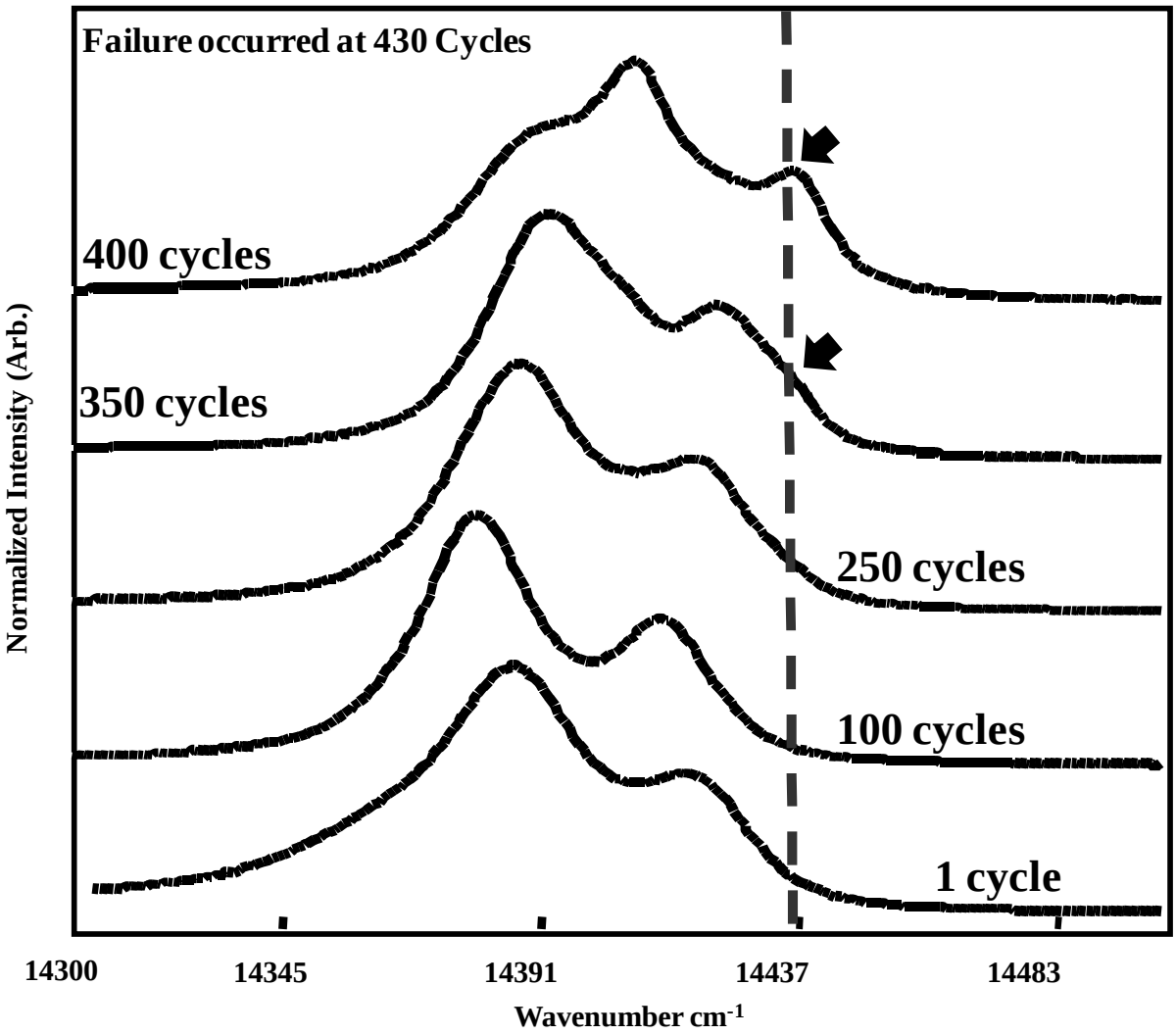

Figure 77. Typical photostimulated luminescence spectra as a function of 1-hour thermal cycling for type III EB-PVD TBCs with as-coated (Ni,Pt)Al bondcoats. TBC spallation has occurred at 430 cycles and luminescence from stress-relieved TGO scale (marked by dotted vertical line and arrows) was observed starting 350 cycles by examining the derivatives of the spectra.

The evolution of relative luminescence intensity obtained up to 50% and 70% of lifetime for the type III TBCs is presented in Figure 78 and Figure 79, respectively. In these Figures, R_2, R_2', and R_2" refer to tri-mode luminescence of higher, lower and no shifts, respectively, where the emergence of "no-shift" luminescence may be related to the stress-relief associated with damage within the TGO. The compressive residual stress within the TGO as a function of 1-hour

thermal cycling for type III EB-PVD TBCs with (Ni, Pt) Al bondcoats are presented in Figure 80 and Figure 81.

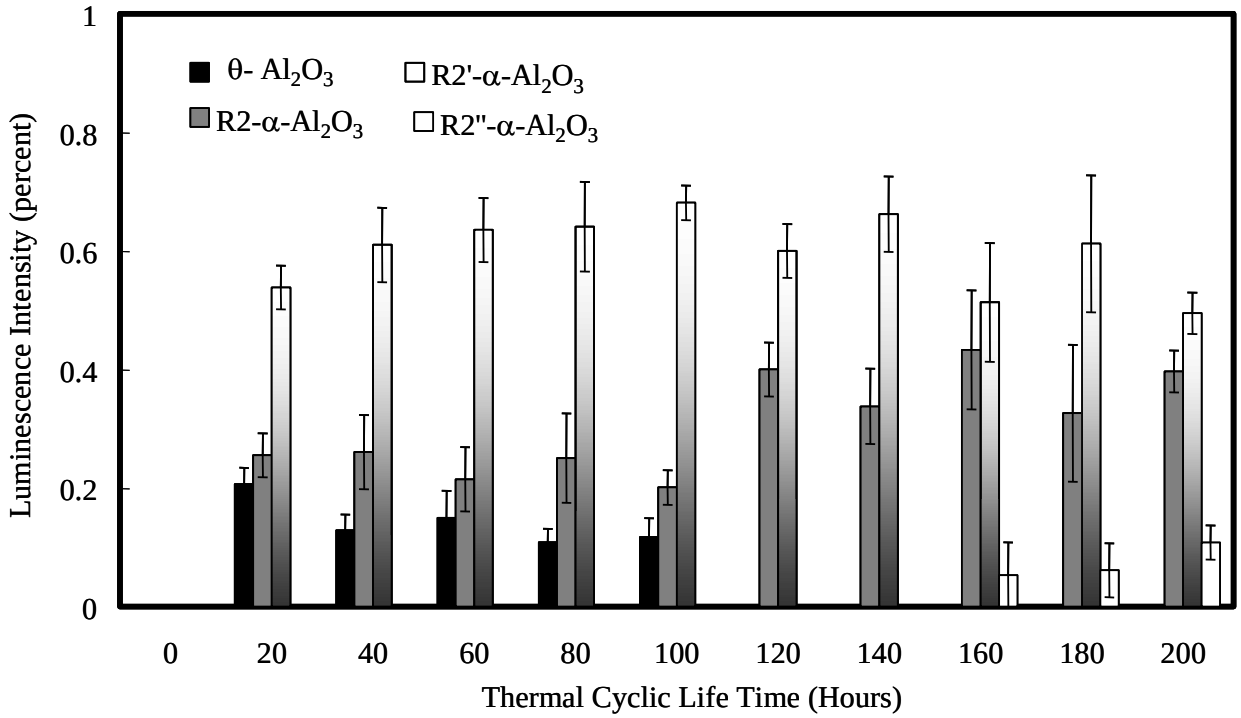

Figure 78. Relative luminescence intensity from θ and α (R_2, R'_2 & R''_2) in the TGO developed on type-III TBCs with as-coated (Ni,Pt)Al bondcoat, thermally cycled until 50% of its lifetime.

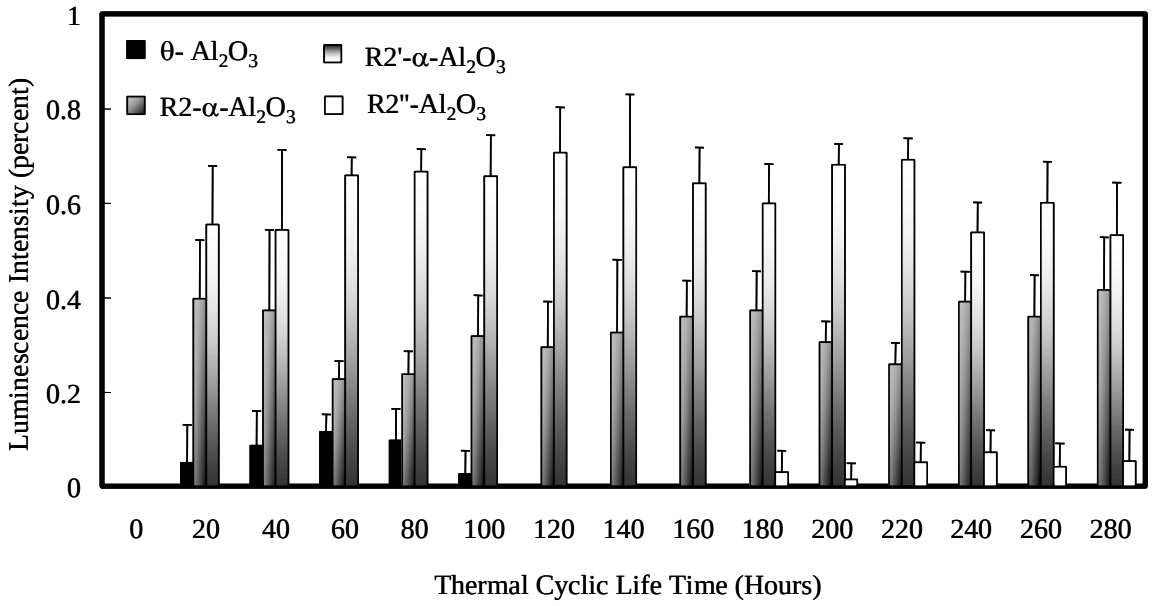

Figure 79. Relative luminescence intensity from θ and α (R_2, R'_2 & R''_2) in the TGO developed on type-III TBCs with as-coated (Ni,Pt)Al bondcoat, thermally cycled until 70% of its lifetime.

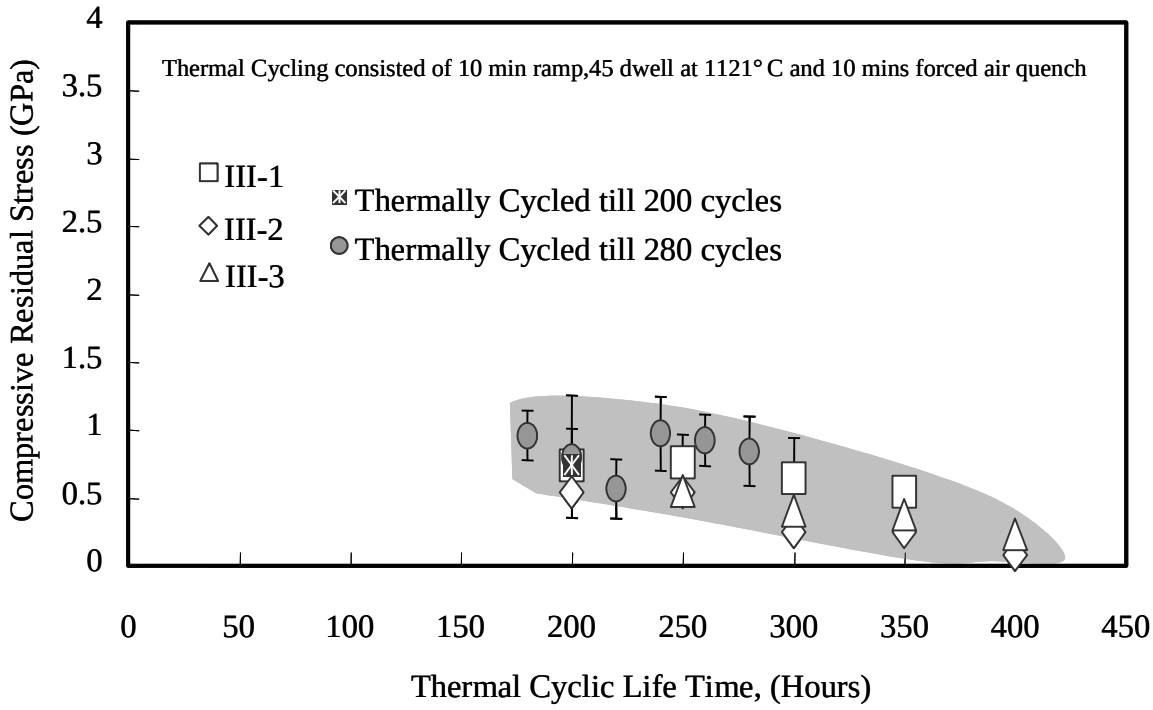

Figure 80. Compressive residual stress within the TGO as a function of 1-hour thermal cycling for type III EB-PVD TBCs with (Ni,Pt)Al bondcoats. Values of compressive residual stress were calculated from the emerging luminescence with minimum shift in the tri-modal luminescence.

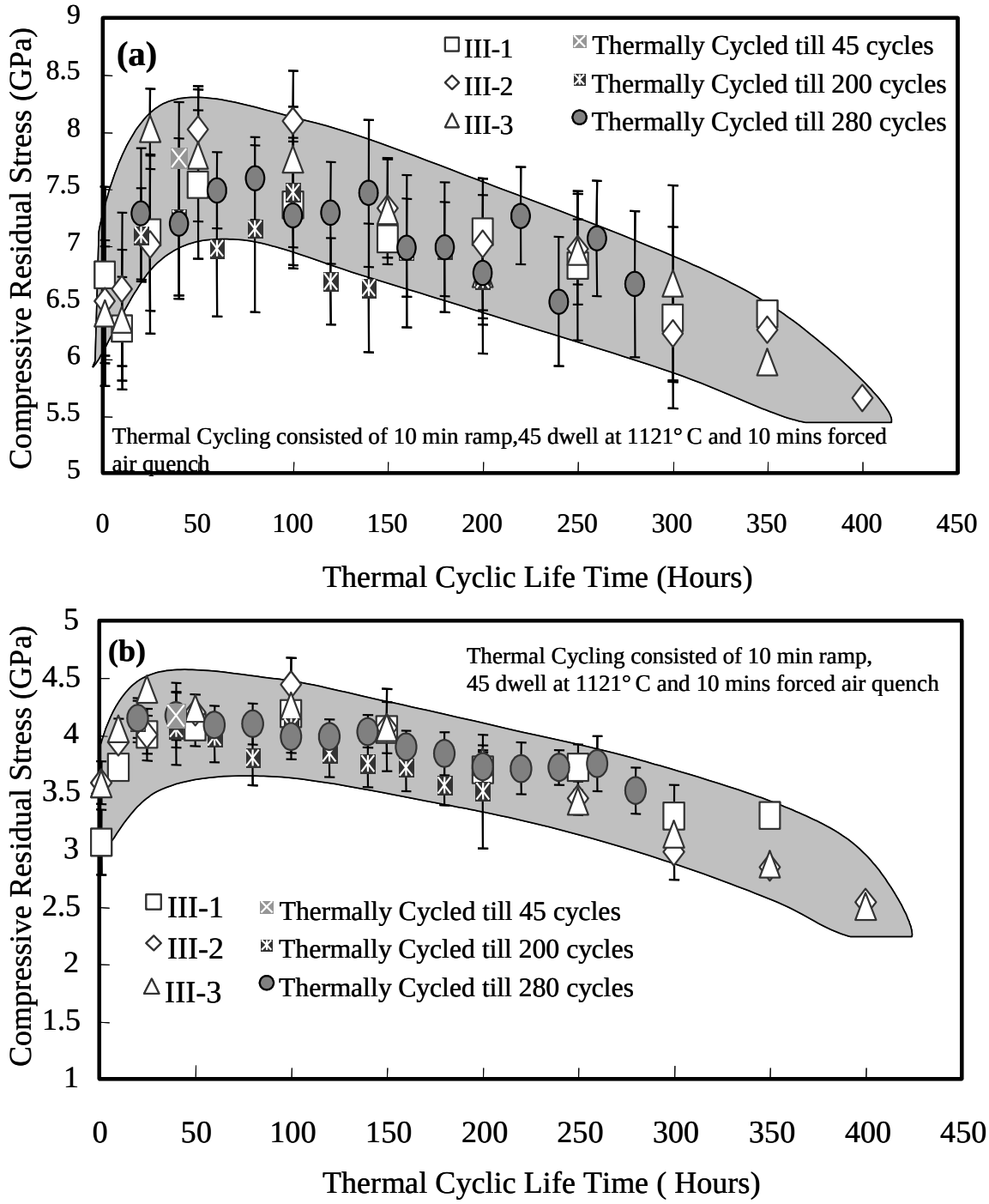

Figure 81. Compressive residual stress within the TGO as a function of 1-hour thermal cycling for type III EB-PVD TBCs with as-coated (Ni,Pt)Al bondcoats. Values of compressive residual stress were calculated from the (a) higher shift luminescence and (b) lower shift luminescence from the bimodal luminescence.

Typical photostimulated luminescence spectra from type IV EB-PVD TBCs with grit-blasted (Ni,Pt)Al bondcoat are presented in Figure 82 as a function of 1-hour thermal cycling. The average lifetime from 1-hour thermal cycles was 360 ± 39 cycles. There is a gradual shift in the luminescence towards stress free luminescence before the actual failure at 350 cycles. The compressive residual stress determined based on luminescence shift showed an initial increase, a gradual decrease after 50 cycles and a complete stress-relief after 300 cycles as shown in Figure 83. Both higher and lower stresses arising from the bimodal luminescence exhibited an initial increase, and a gradual and significant decrease before the final spallation. While the initial increase may be due to initially under-developed TGO scale, gradual changes in the luminescence frequency are significant, and can serve to assess life-remain for type IV TBCs. This decrease may be related to undulation of TGO-bondcoat interface and related damages that occurred during the 1-hour thermal cycling.

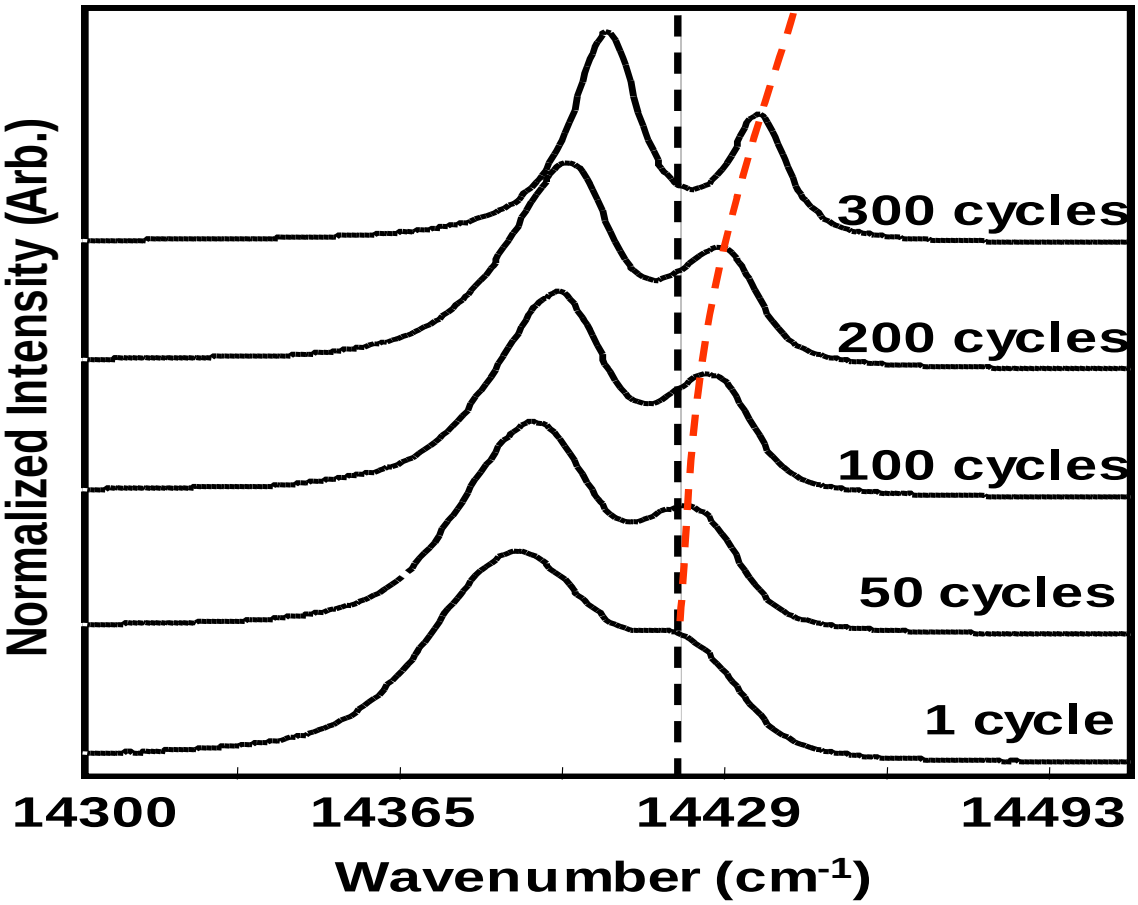

Figure 82. Typical photostimulated luminescence spectra as a function of 1-hour thermal cycling for type IV EB-PVD TBCs with grit blasted (Ni,Pt)Al bondcoats with TBC lifetime 360±39 cycles and luminescence from stress-relieved TGO scale (marked by dotted vertical line) was observed starting as early as 10% lifetime by examining the derivatives of the spectra.

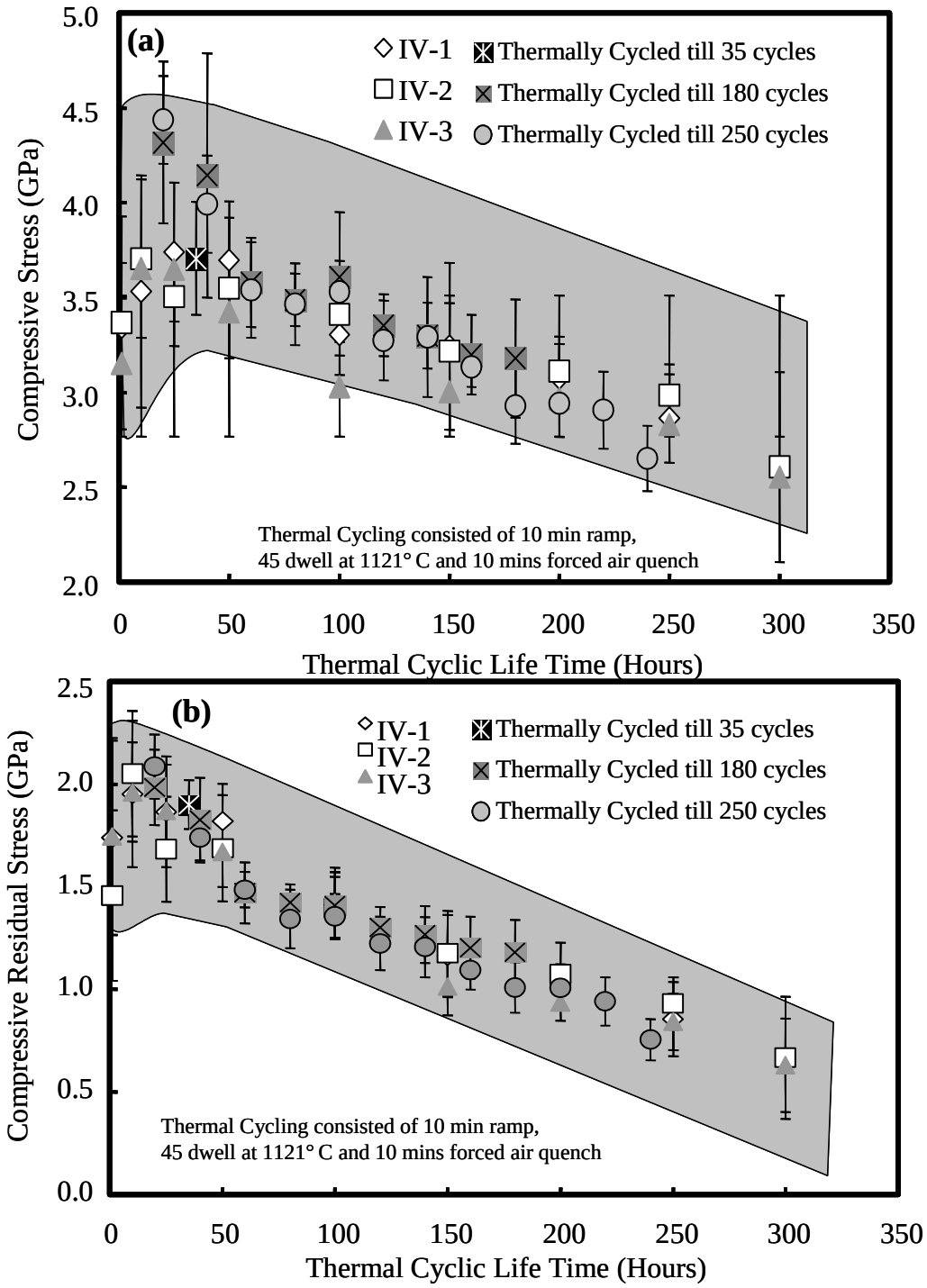

Figure 83. Compressive residual stress within the TGO as a function of 1-hour thermal cycling for type IV EB-PVD TBCs with grit-blasted (Ni,Pt)Al bondcoats. Values of compressive residual stress were calculated from bimodal luminescence corresponding to (a) higher and (b) lower shifts in luminescence.

4.5.3 10-Hour Furnace Thermal Cycling

Thermal cyclic lifetime for type-III EB-PVD TBCs was 55±3 cycles. Evolution of typical luminescence response with thermal cycling is shown in Figure 84. The evolution and detection of stress-relief in the TGO scale for type-III TBCs can be quantified by taking the second derivatives ($d^2c/d\upsilon^2$) of luminescence spectrum at υ=14432 for R_2 luminescence. As shown in Figure 85, the luminescence spectrum with $d^2c/d\upsilon^2$ =0 at $\upsilon \cong$ 14432 ± 3 were observed. Observation of stress free luminescence was observed prior to coating spallation in this type similar to 1-hour thermal cycling. The stress free luminescence would be related to the sub-critical damages and stress relief in the TGO scale. For type-III TBCs with as-coated (Ni,Pt)Al bondcoat, the luminescence shift associated with the stress relief of the TGO scale was observed even for 10-hour cycle as function of thermal cycling as shown in Figure 86. These spectrums were deconvoluted based on the bimodal luminescence (i.e., two sets of R_1-R_2 luminescence) until 60% lifetime. After 60% lifetime, a third set of R_1-R_2 luminescence emerged, which was clearly related to the stress free luminescence of the α-Al_2O_3 that arises due to the stress-relief within the TGO scale. The compressive residual stress within the TGO scale for 10-hour thermal cycling, and 30% lifetime of type-III TBCs is shown in Figure 86.

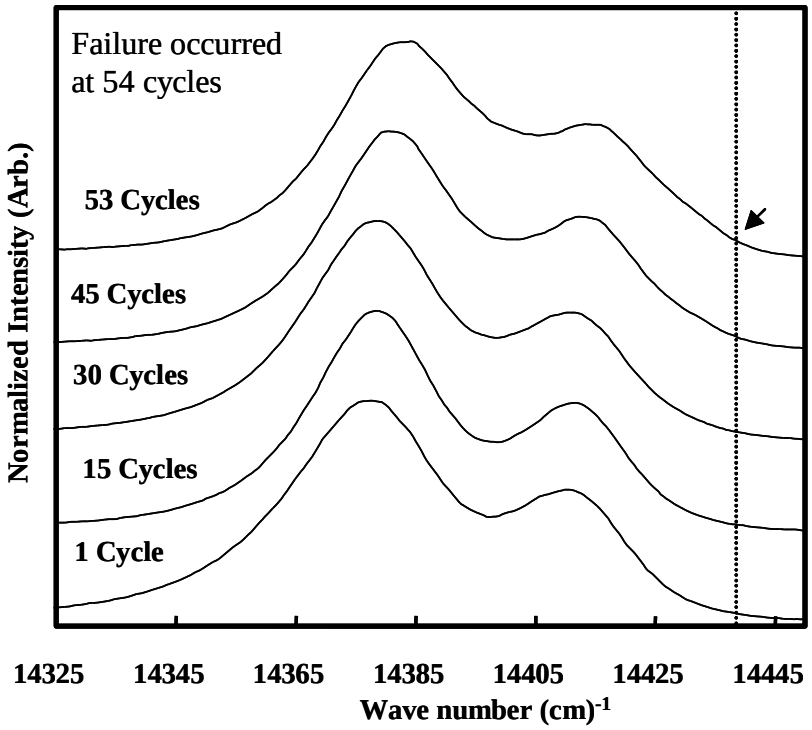

Figure 84.Typical photostimulated luminescence spectra from the stress-relieved TGO scale (marked by dotted vertical line and arrows) was observed as a function of 10-hour thermal cycling for type III EB-PVD TBCs with as-coated (Ni,Pt)Al bondcoats. TBC spallation has occurred after 54 cycles.

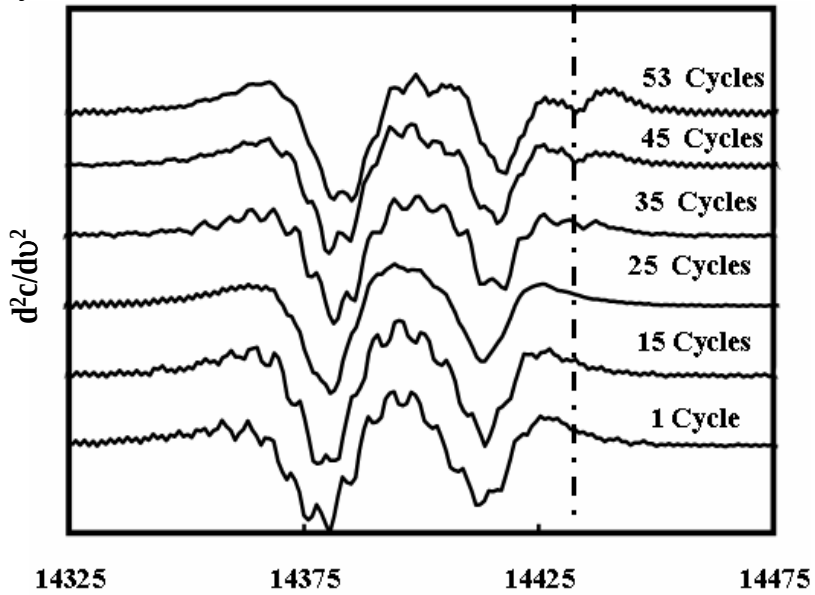

Figure 85. Typical derivatives of luminescence spectrum associated with stress-relieved luminescence frequency at $\upsilon \cong 14432 \pm 3$ for R_2 after 10-hour thermal cycling.

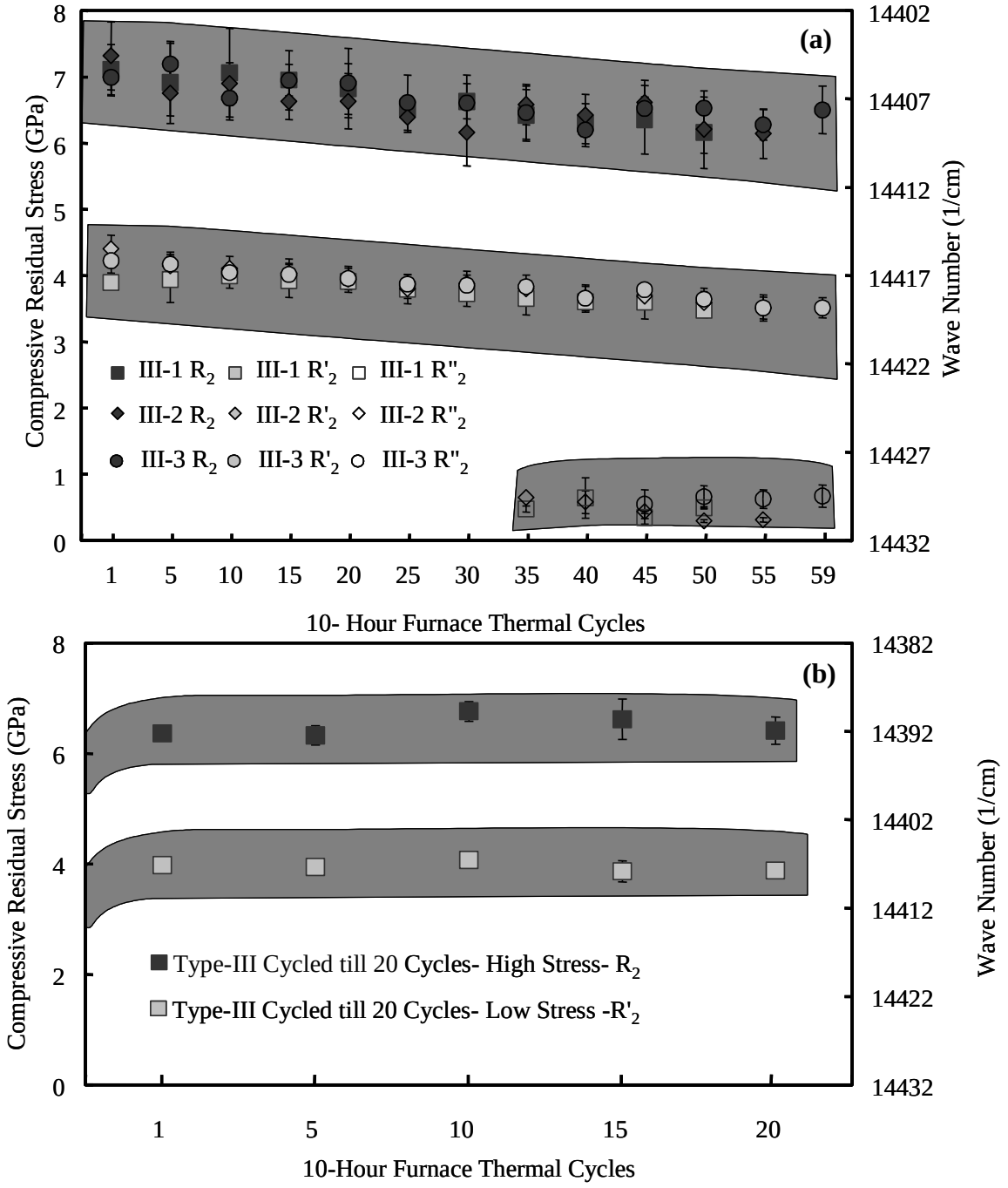

Figure 86. Compressive residual stress within the TGO scale were calculated from bimodal and tri-mode luminescence as a function of 10-hour thermal cycling for type-III TBCs with as-coated (Ni,Pt)Al bondcoat (a) Values of compressive residual with thermal cycling (b) compressive residual stress after 30% life time of TBCs.

10-hour furnace thermal cycle lifetime for type-IV grit-blasted EB-PVD TBCs was 42±2 cycles. Typical luminescence spectra from type-IV TBCs with grit-blasted (Ni,Pt)Al bondcoat are presented in Figure 87. When compared to type-IV TBCs examined during 1-hour thermal cycling, a gradual shift towards stress free luminescence was not observed for these TBCs during 10-hour thermal cycling. The compressive residual stress within the TGO scale as a function of 10-hour thermal cycling, including up to 30% and 80% is presented in Figure 88. An initial increase in the magnitude of compressive residual stress was observed presumably due to the initial TGO development with oxidation. However, the magnitude of the compressive residual stress in the TGO scale remained relatively constant as a function of 10-hour thermal cycling. This type of behavior may be specific for TBC type, and in particular, type of thermal cycling (e.g., dwell time at high temperature).

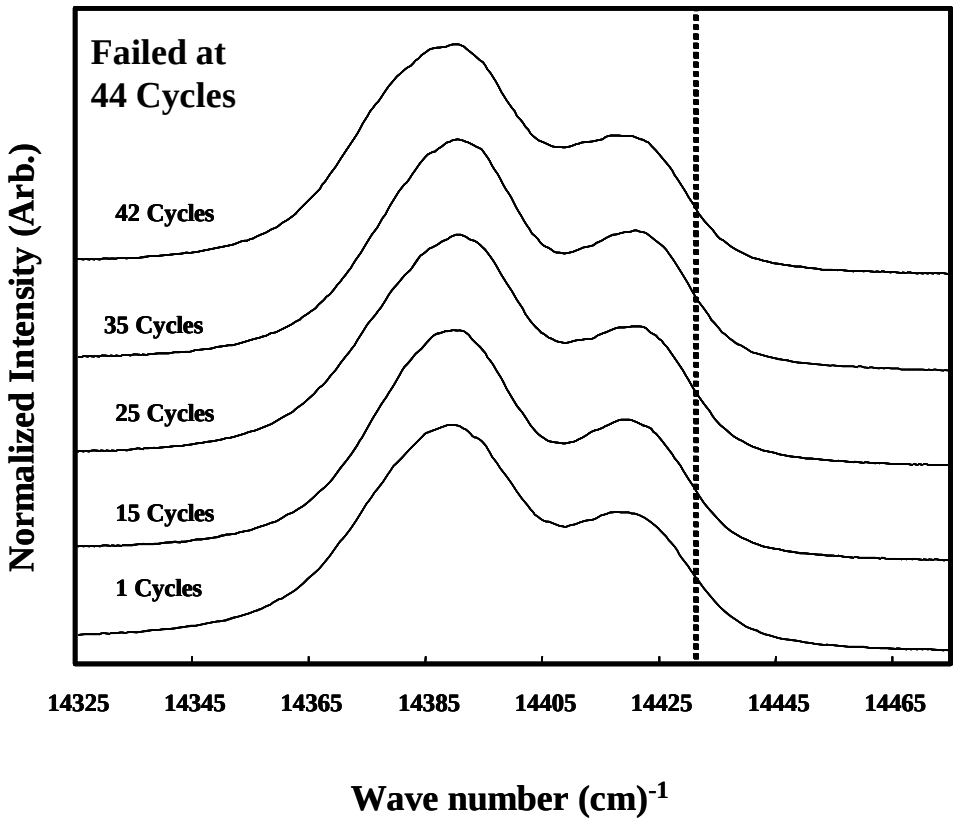

Figure 87. Typical luminescence spectrum observed as a function of 10-hour thermal cycling for type-IV TBCs with grit blasted (Ni, Pt)Al bondcoat. TBC spallation occurred after 44 cycles and there is no changes in the luminescence shifting towards stress free as observed using 1-hour thermal cycling.

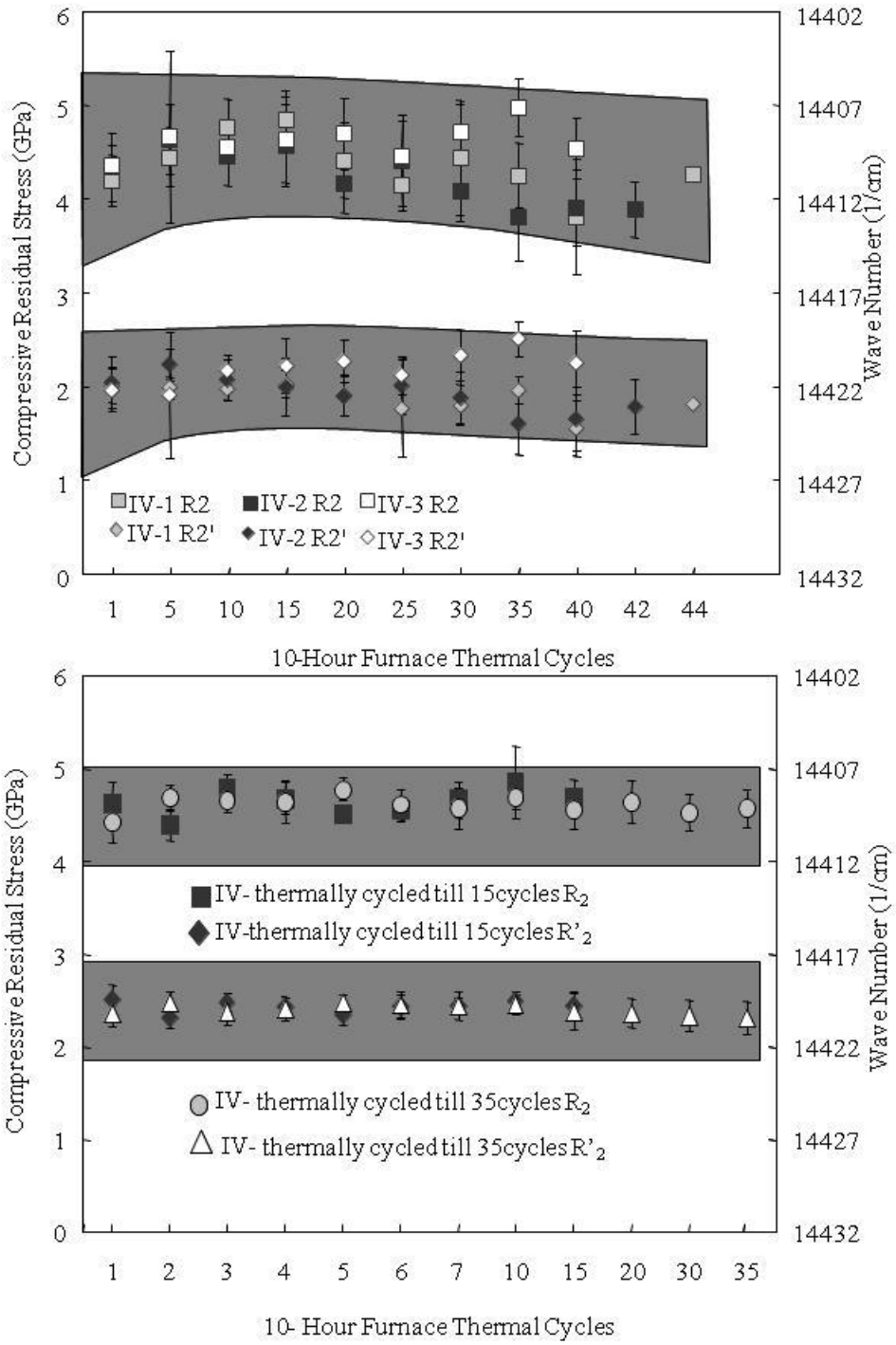

Figure 88. Compressive residual stress within the TGO as a function of 10-hour thermal cycling for type-IV TBCs with grit-blasted (Ni, Pt)Al bondcoat. The values of compressive residual stress were calculated from bi-modal luminescence corresponding to higher and lower shifts in luminescence (a) as a function of 10-hour thermal cycles and (b) 30% and 80 % life time as a function of 10-hour thermal cyclic life time.

4.5.4 50- Hour Furnace Thermal Cycling

Furnace thermal cyclic lifetime for type-III TBCs with as-coated (Ni,Pt)Al bondcoat was 12±1.5 cycles. The value of compressive residual stress for type-III TBCs is shown in the Figure 89. The evolution of relative intensities obtained up to failure for type-III TBCs is presented in Figure 90. Where R_2 and R_2' refer to bi-modal luminescence of the higher and lower shift in luminescence. There was no emergence of stress-free luminescence that was detected previously in 1 and 10 hour thermal cycles.

Furnace thermal cyclic lifetime for 50-hour thermal cycles for type-IV EB-PVD TBCs was 9.5±0.7 cycles. The evolution in compressive residual stress in the TGO scale is presented in Figure 91. Both high and low stresses increased initially and remained constant until failure. The compressive residual stress remained constant with an initial increase in the early stages presumably due to the development of the TGO. This trend was similar to type-IV TBCs tested using 10-hour thermal cycles.

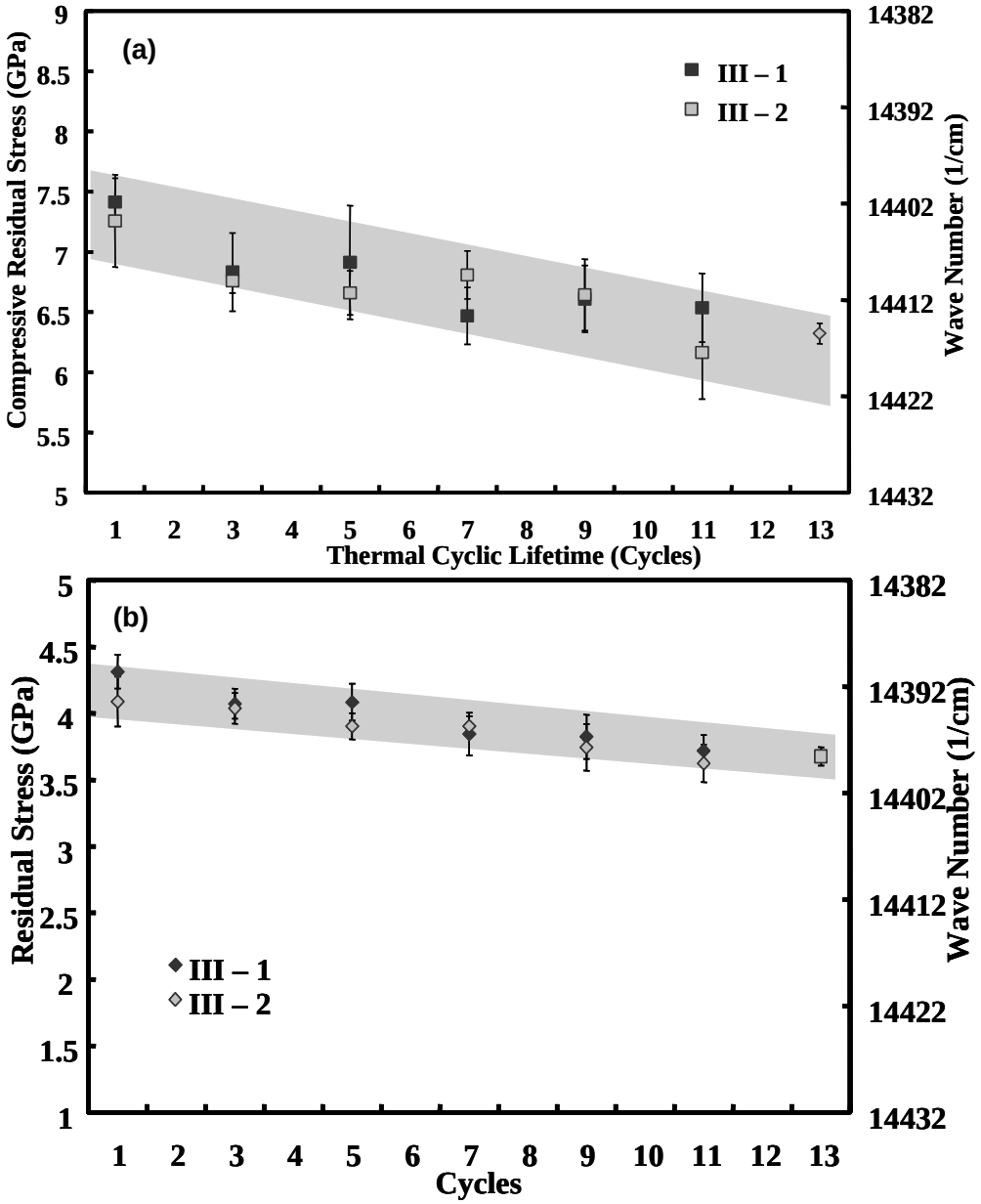

Figure 89. Compressive residual stress within TGO as a function of 50-hour thermal cycling for type-III TBCs with as-coated (Ni,Pt)Al bondcoat. Values of compressive residual stress were calculated from bimodal luminescence corresponding to (a) high and (b) low compressive stress.

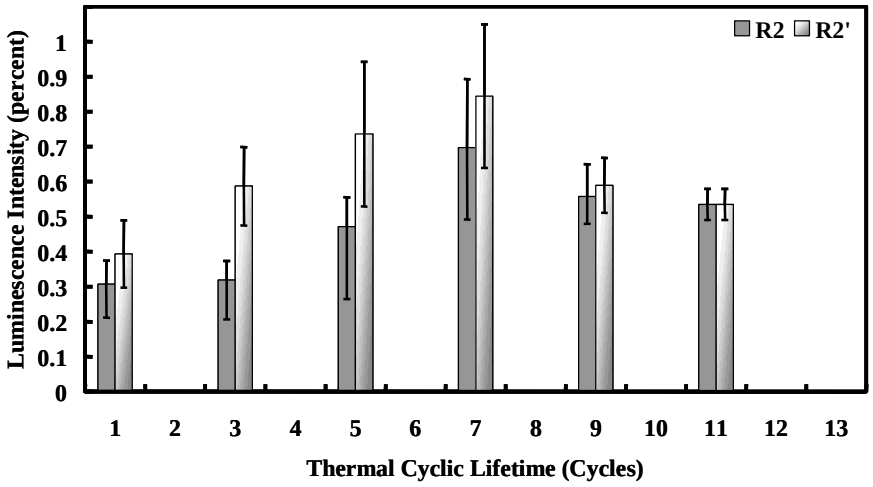

Figure 90. Relative luminescence intensity from R_2, R'_2 in the TGO of type-III TBCs with as-coated (Ni,Pt)Al bondcoat thermally cycled using 50-hour dwell time.

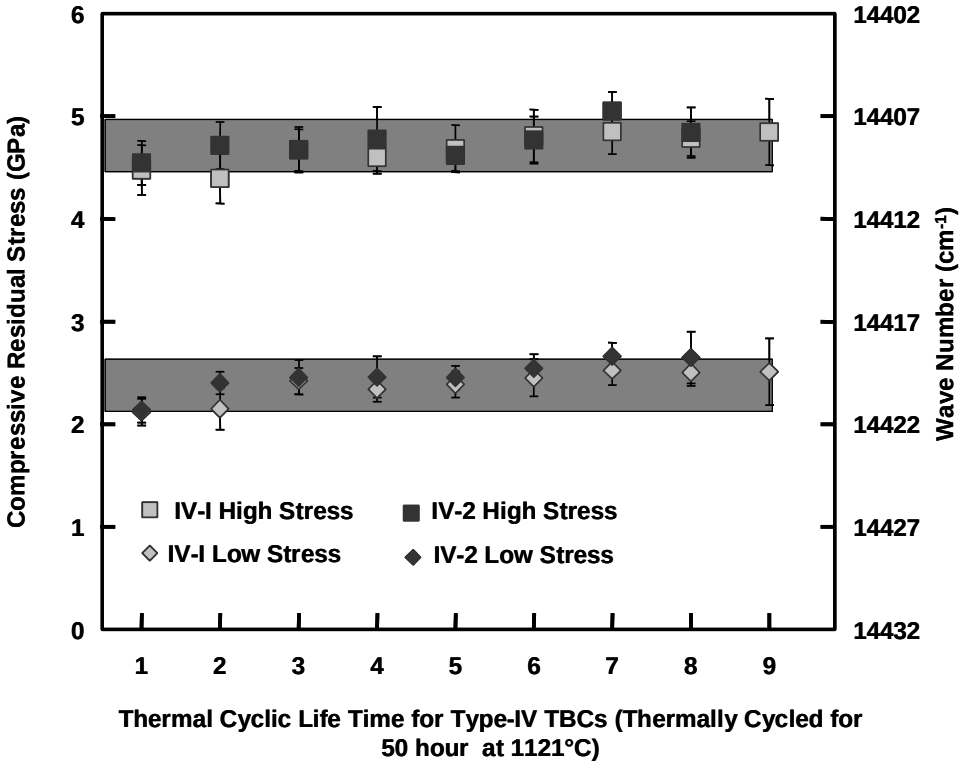

Figure 91. Compressive residual stress within the TGO as a function of 50-hour thermal cycling for type-IV TBCs with grit blasted (Ni,Pt)Al bondcoat. Values of compressive residual stress were calculated from bimodal luminescence.

4.6 EIS OF APS TBCS as a function thermal Cycling

4.6.1 Impedance response during 1-hour thermal Cycling for APS TBCs

For type I APS TBCs, EIS measurement was carried out 3 times for specimens at 10%, 50% and 70% of thermal cyclic lifetime. The variation in the impedance and phase angle plot with respect to the thermal cycling is shown in Figure 92 and Figure 93, respectively. Aforementioned, the impedance response from the TGO cannot be neglected because of the bondcoat oxidation resulting in the formation of uniform and continuous TGO. So the impedance response from TGO has to be added to the ac equivalent circuit. The values of resistance and capacitance of various TBC constituents, calculated based on the ac-equivalent circuit are presented in Table 12. The equivalent circuit for the APS system fits the impedance response using non-linear least square analysis with $\leq 5\%$ error.

The impedance plot presented in Figure 92 shows that the impedance response of the TBCs increases initially during thermal cycling and then decreases with further thermal cycling corresponding to 50% of its lifetime. The individual electrical parameters response with thermal cycling representing each layer of APS TBCs is shown in Figure 94 through Figure 97. The R_{YSZ} and R_{TGO} increased initially due to sintering of the YSZ topcoat and growth of TGO scale with high temperature exposure, respectively. The decrease in R_{YSZ} and R_{TGO} relate to the sub-critical damages that initiate in the topcoat (micro-cracking) and within the TGO scale with thermal cycling. The C_{YSZ} did not change significantly with thermal cycling and C_{TGO} decreased with thermal cycling until failure.

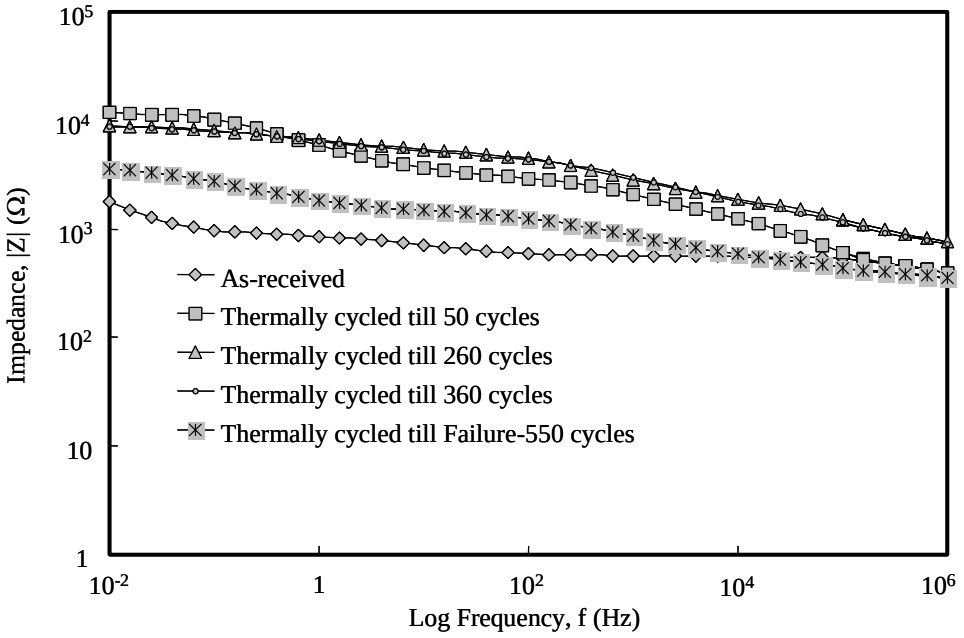

Figure 92. Typical impedance response from type-I APS TBCs as a function of 1-hour thermal cycling at 1121°C.

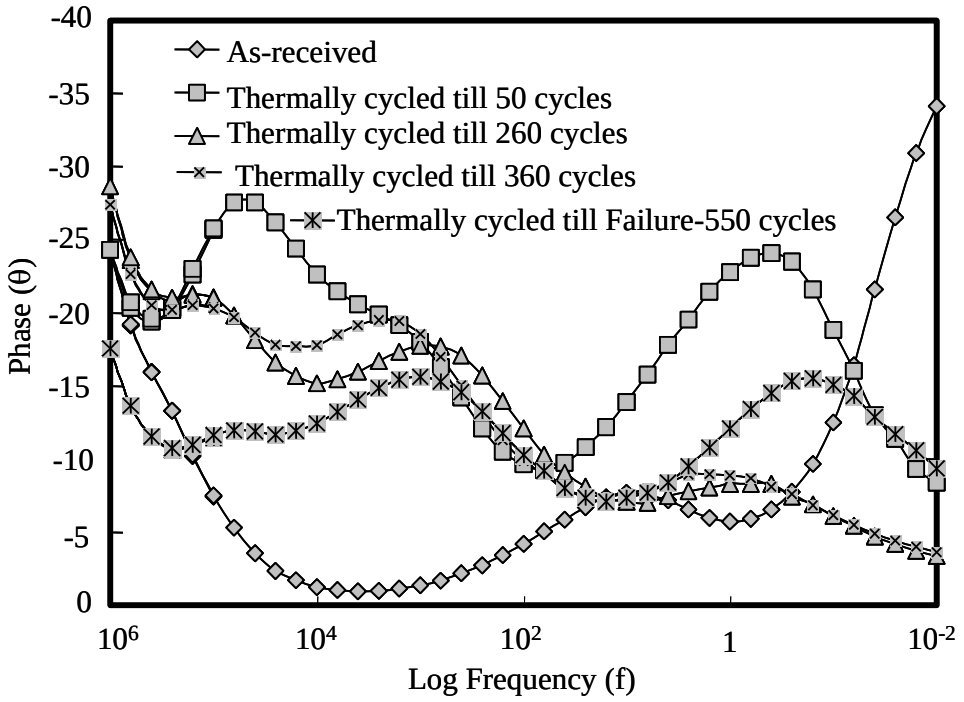

Figure 93. Typical phase angle plots from type-I APS TBCs as a function of 1-hour thermal cycling at 1121°C.

Table 12. Changes in resistance and capacitance of Type I APS TBC constituents as a function of 1-hour thermal cycling at 1121°C.

Thermal cycles	R_{YSZ} (kΩ)	C_{YSZ} (nF)	R_P (kΩ)	C_P (νF)	R_{TGO} (kΩ)	C_{TGO} (nF)	R_T (kΩ)	C_T (νF)
As-received	0.50 ± 0.4	2.2 ± 0.4	10.6 ± 4.2	377700 ± 21959	0	0	0.3 ± 0.1	16486 ± 2747
50 (10% lifetime)	2.72 ± 0.7	60.7 ± 21.9	13.55 ± 1.38	1574.3 ± 502.3	0.58 ± 0.4	42.9 ± 10.9	1.22 ±0.86	1347.3 ±192
260 (50% lifetime)	3.31 ± 0.09	49.6 ± 0.8	4.40 ± 0.03	1505 ± 18	1.05 ± 0.02	5.38 ± 0.2	1.06 ±0.05	571.9 ±2.8
360 (70% lifetime)	3.25 ± 0.10	45.8 ± 0.4	4.64 ± 0.07	1449 ± 45.7	0.96 ± 0.03	4.32 ± 0.3	0.80 ±0.03	33.6.3 ±1.9
550 (Failure)	0.59 ± 0.03	191.4 ± 5.9	2.96 ± 0.18	10789 ± 983.2	0.40 ± 0.01	3.5 ± 0.3	0.35 ±0.02	1321.6 ±40.2

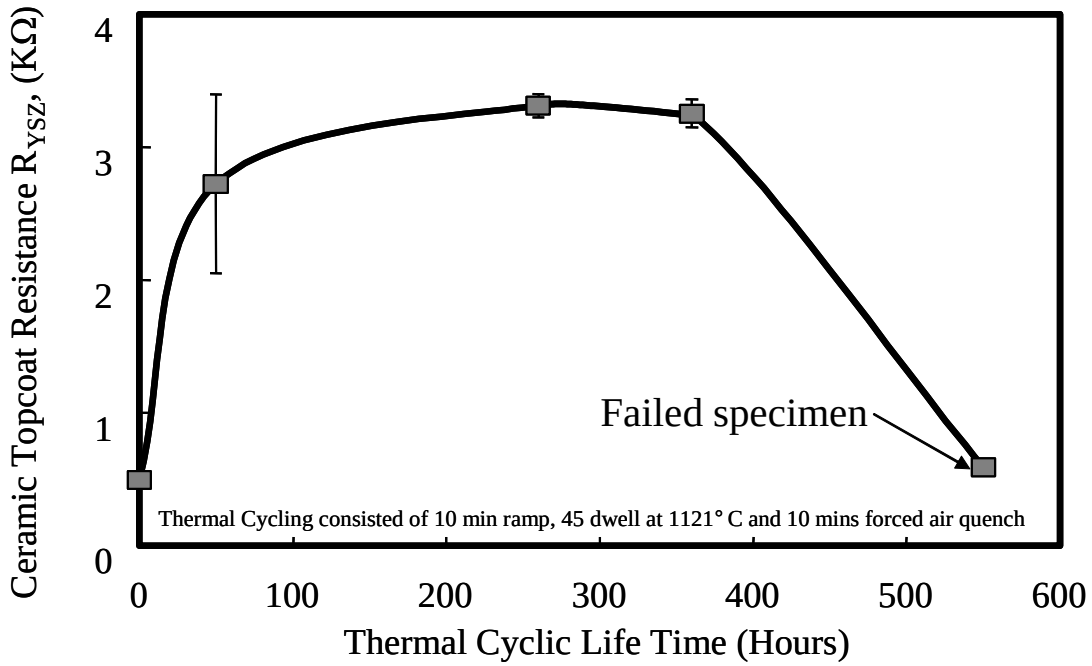

Figure 94. Evolution of ceramic topcoat resistance (R_{YSZ}) for type I APS TBCs as a function of 1-hour thermal cycling at 1121°C.

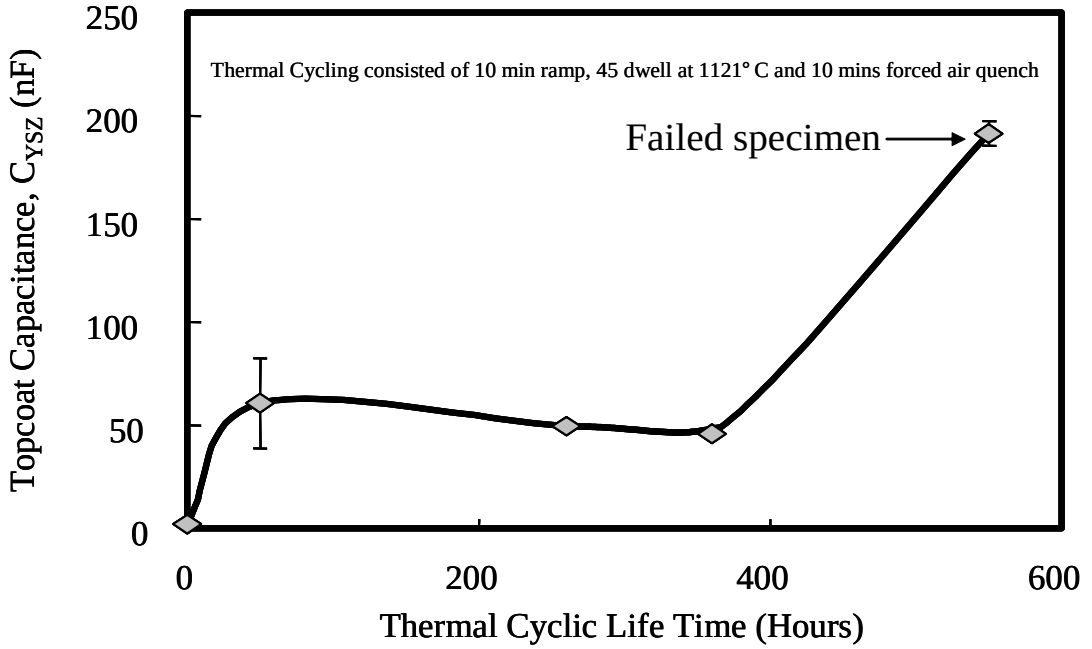

Figure 95. Evolution of ceramic topcoat capacitance (C_{YSZ}) for type I APS TBCs as a function of 1-hour thermal cycling at 1121°C.

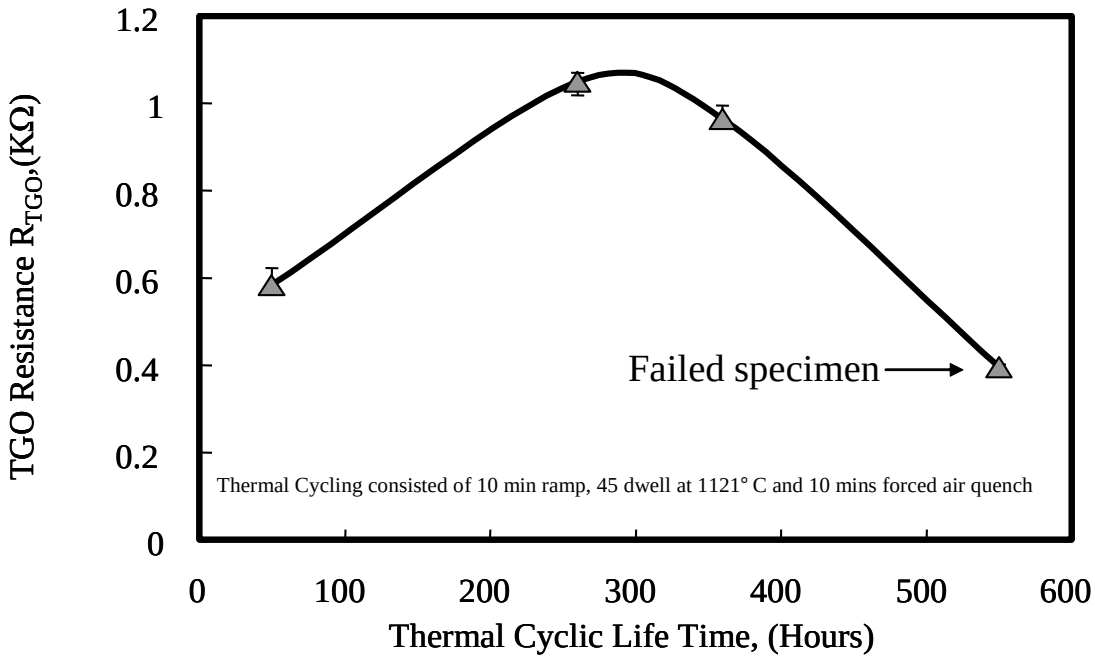

Figure 96. Evolution of TGO resistance R_{TGO} in type I APS TBCs as a function of thermal 1-hour cycling at 1121°C.

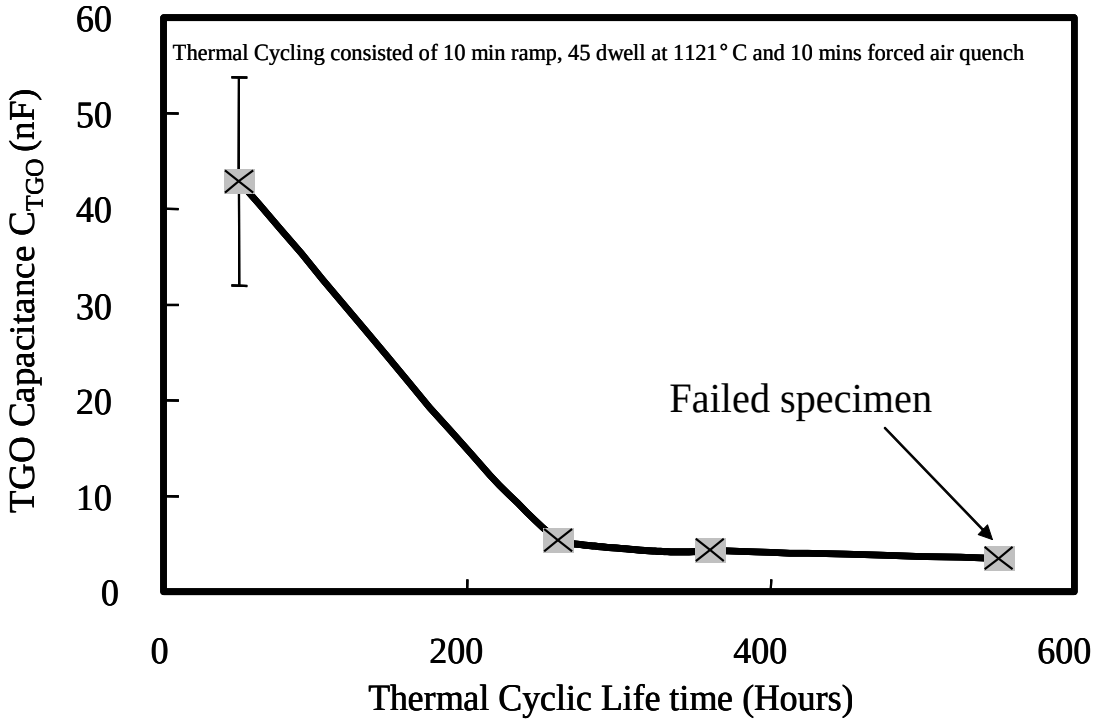

Figure 97. Evolution of TGO capacitance C_{TGO} in type I APS TBCs as a function of thermal 1-hour cycling at 1121°C.

For type II APS TBCs, EIS measurement was carried out 3 times on specimens at 10%, 50% and 70% of its thermal cyclic lifetime. The variation in the impedance and phase angle plot with respect to the thermal cycling is presented in Figure 98 and Figure 99, respectively. Table 13 also reports values of resistance and capacitance of the various TBC constituents. Resistance and capacitance of TBC constituents was determined as a function of thermal cycles as presented in Figure 100 through Figure 103.

Ceramic topcoat resistance R_{YSZ} initially increased then decreased with thermal cycling; this perhaps reflects two important microstructural changes, namely sintering and micro-cracking. While the growth of the TGO should intuitively increase the resistance and decrease the capacitance, the opposite results were observed for capacitance of the TGO as presented in Figure 102 and Figure 103. As seen in Figure 102 and Figure 103, the TGO resistance, R_{TGO} (not defined for as-coated condition) continuously decreases and the TGO capacitance, C_{TGO} continuously increases with thermal cycling. In addition, a sharp 2~5X increase in the C_{TGO} was observed as presented in Figure 103 for failed specimens. These trends were consistently observed and may reflect early initiation and growth of sub-critical damage in the TGO through which electrolyte can penetrate.

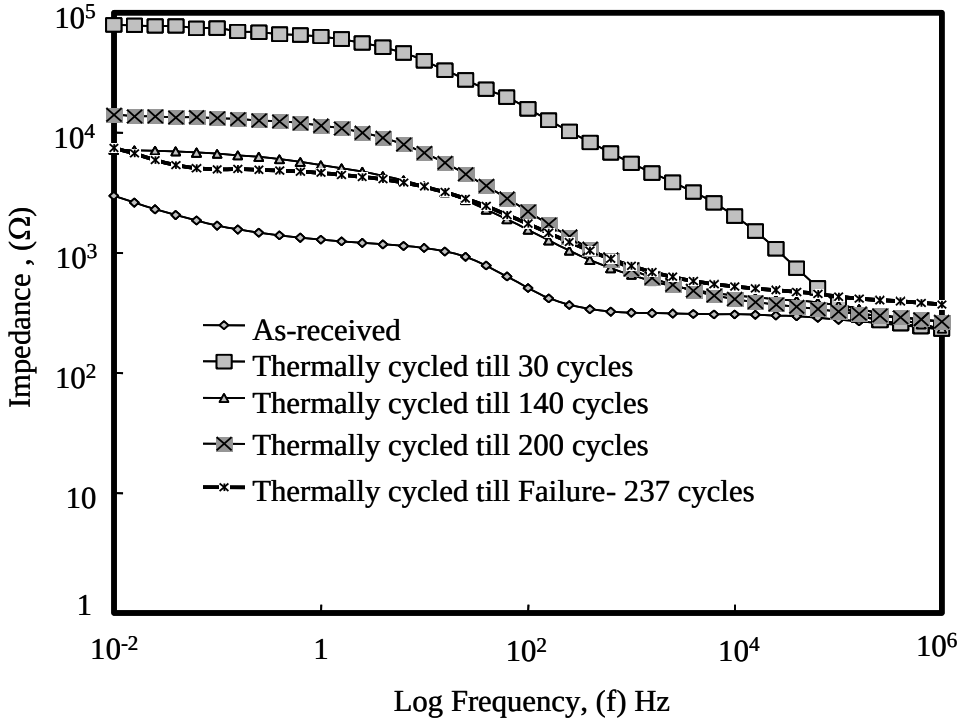

Figure 98. Typical Impedance plots from type-II APS TBCs as a function of 1-hour thermal cycling at 1121°C.

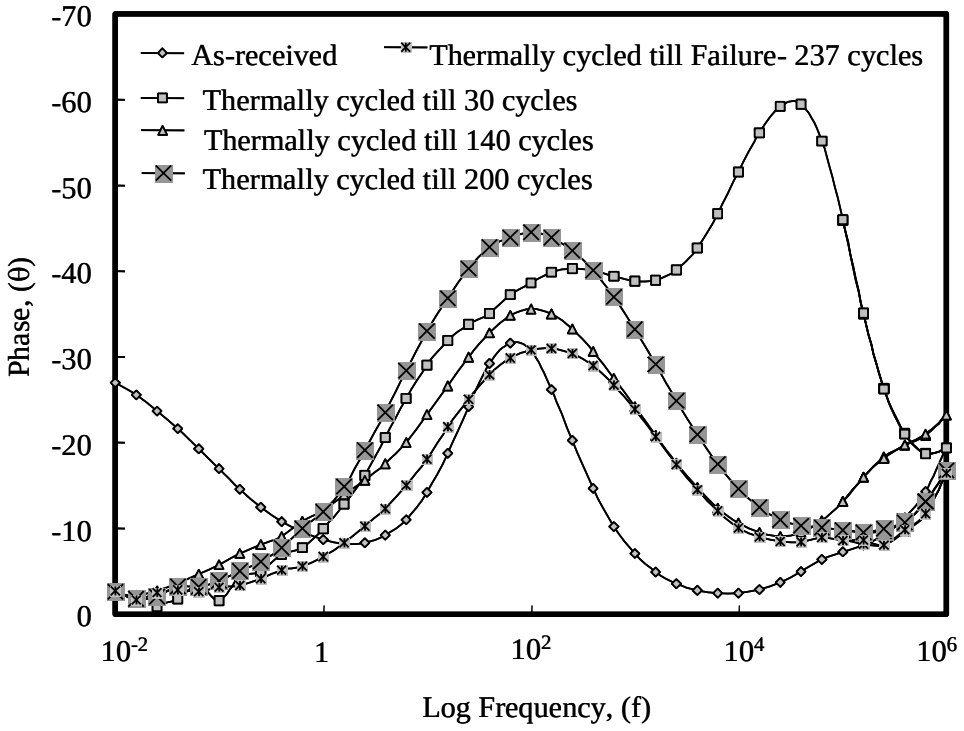

Figure 99. Typical phase angle plots from for type-II APS TBCs as function of 1-hour thermal cycling at 1121°C.

Table 13. Changes in resistance and capacitance of type-II APS TBC constituents as a function 1-hour of thermal cycling at 1121°C.

Thermal cycles	R_C (kΩ)	C_C (nF)	R_P (kΩ)	C_P (nF)	R_O (kΩ)	C_O (nF)	R_T (kΩ)	C_T (nF)
As-received	0.29 ± 0.02	4.8 ± 0.5	11.8 ± 1.4	38016.6 ± 9317	0	0	0.9 ± 0.1	3883 ± 219.2
35 (10% lifetime)	1 ± 0.06	13.9 ± 21.9	103.7 ± 3.3	33980 ± 1513	3.72 ± 0.2	9.42 ± 0.01	0.71 ±0.01	1228 ±39.6
140 (50% lifetime)	0.63 ± 0.03	4.6 ± 0.8	0.88 ± 0.8	351.3 ± 48.7	4.8 ± 0.1	517 ± 17.1	6.2 ±1.2	1534.7 ±131.4
200 (70% lifetime)	0.27 ± 0.01	3.3 ± 0.4	3.79 ± 0.3	941.1 ± 62.2	1.3 ± 0.07	32386.67 ± 644.7	9.7 ±0.6	454 ±3.3
Failure 237	0.37 ± 0.01	2.6 ± 5.9	1.04 ± 0.6	864.6 ± 182.1	1.3 ± 0.4	35635 ± 10981.4	5.2 ±1.8	623 ±164.1

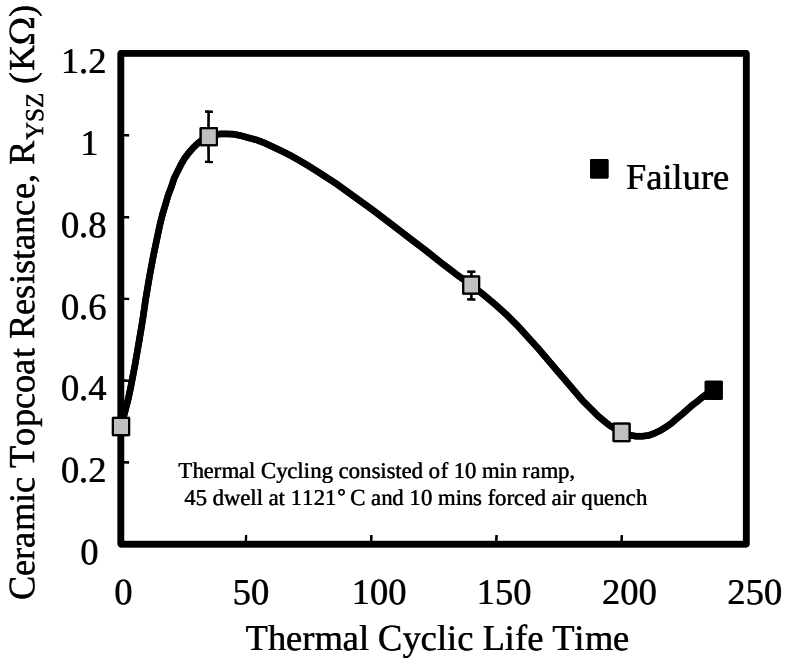

Figure 100. Evolution of ceramic top coat resistance (R_{YSZ}) for type II APS TBCs as a function of 1-hour thermal cycling at 1121°C.

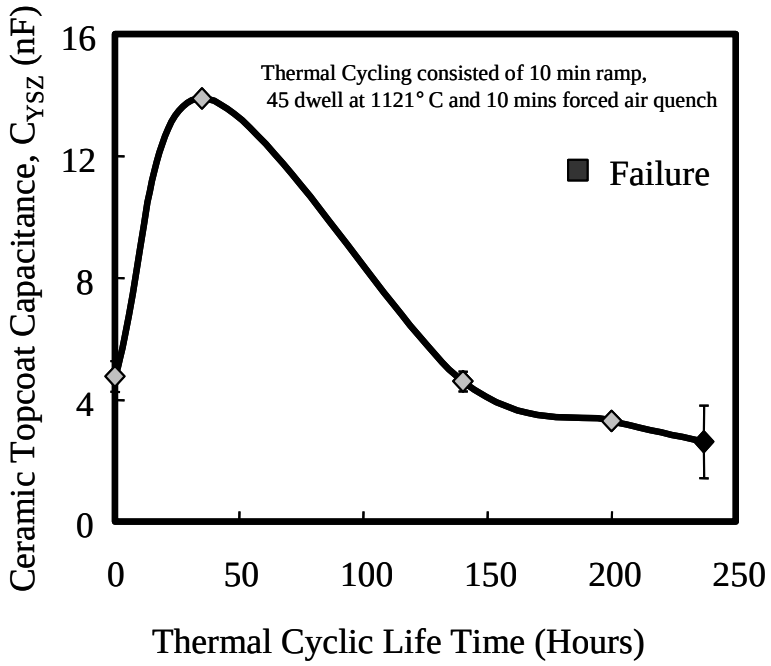

Figure 101. Evolution of ceramic top coat capacitance (C_{YSZ}) for type II APS TBCs as a function of 1-hour thermal cycling at 1121°C.

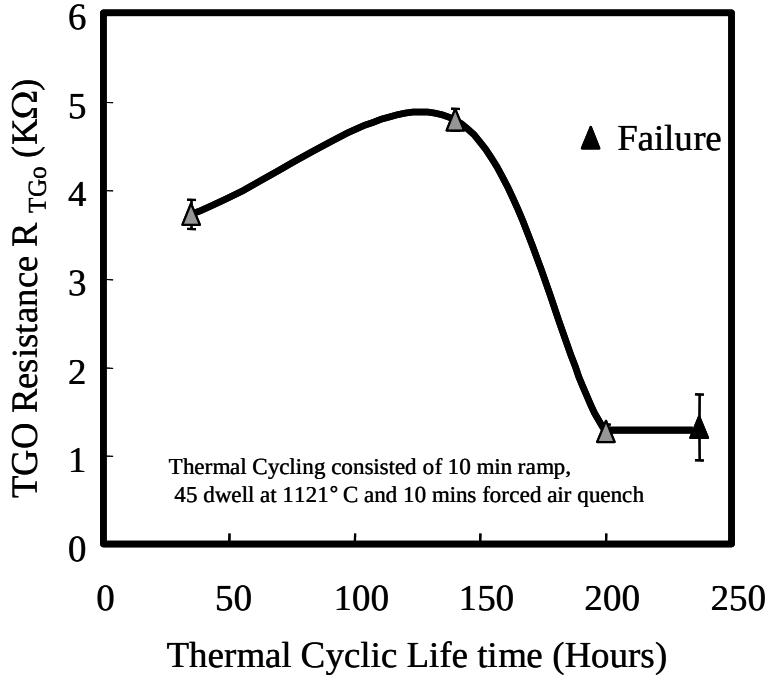

Figure 102. Evolution of TGO resistance (R_{TGO}) in type II APS TBCs as a function of 1-hour thermal cycling at 1121°C.

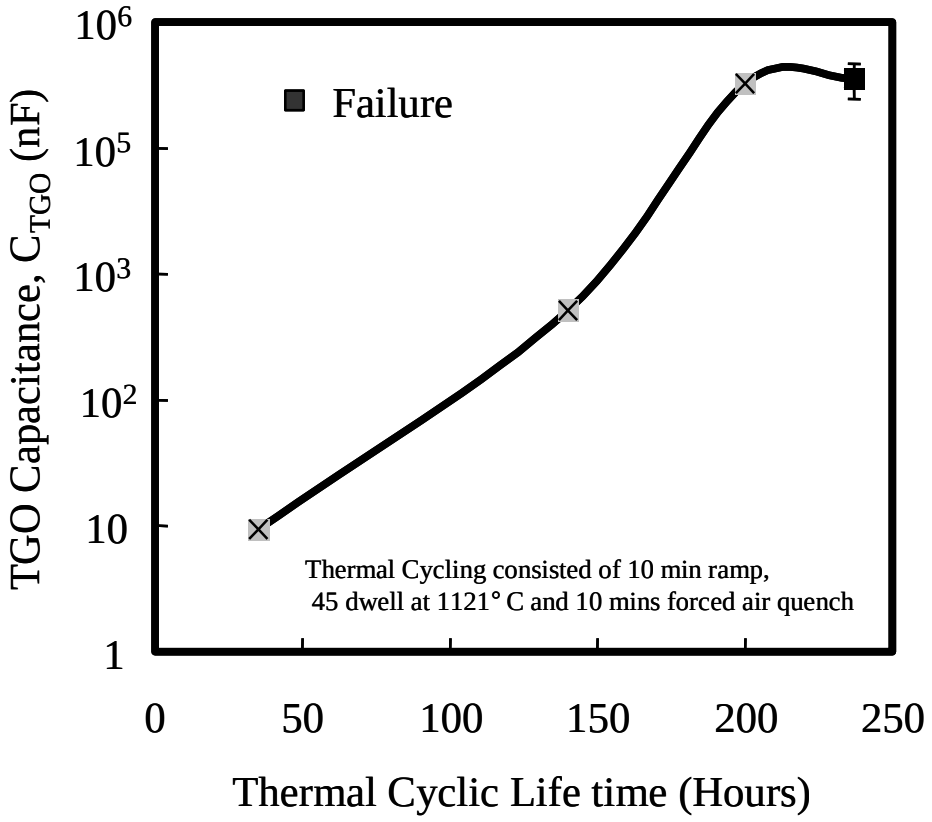

Figure 103. Evolution of TGO capacitance (C_{TGO}) in type II APS TBCs as a function of 1-hour thermal cycling at 1121°C.

4.6.2 Impedance response of APS TBCs during 10-hour and 50-hour thermal cycling

For type I APS TBCs, EIS measurement was carried out 3 times on specimens at 30% and 80% of its thermal cyclic lifetime. The variation in impedance with respect to the 10 and 50-hour thermal cycling is presented in Figure 104 and Figure 105, respectively. Table 14 also reports the values of resistance and capacitance of the various TBC constituents. The impedance plot presented in Figure 105 shows that the impedance response of the TBCs did not vary significantly with 10-hour thermal cycling. However, there are subtle changes in the values of

resistance and capacitance for the YSZ and TGO. These are reported in Table 15. This initial increase in the impedance response may be attributed to the sintering of the YSZ topcoat and growth of the TGO with high temperature exposure.

Comparing impedance response with furnace cycle dwell time shown in Figure 105. An increase in impedance for 1-hour thermal cycling is clear compared to compared 10-hour and 50-hour thermal cycling. This increase is in the lower frequency range, which depends on response from TGO layer and YSZ layer. With prolonged furnace cycle dwell time, YSZ sintering is more prominent but upon cooling, micro-cracks originate from sintered YSZ. Thus with longer dwell time, the impedance response decreases.

The resistance and capacitance of YSZ and TGO reported for type APS TBCs are presented as function of dwell time in Figure 106 through Figure 109. With an increase in the dwell time, the resistance of the topcoat and the TGO increased. With further prolonged dwell time the resistance of the topcoat and the TGO decreased. The capacitance of the topcoat increased at failure because of the large scale damage within the topcoat. The capacitance of the TGO did not increase abruptly at failure because the fracture path of the APS TBCs observed for type-I TBCs primarily occur at the YSZ\TGO interface.

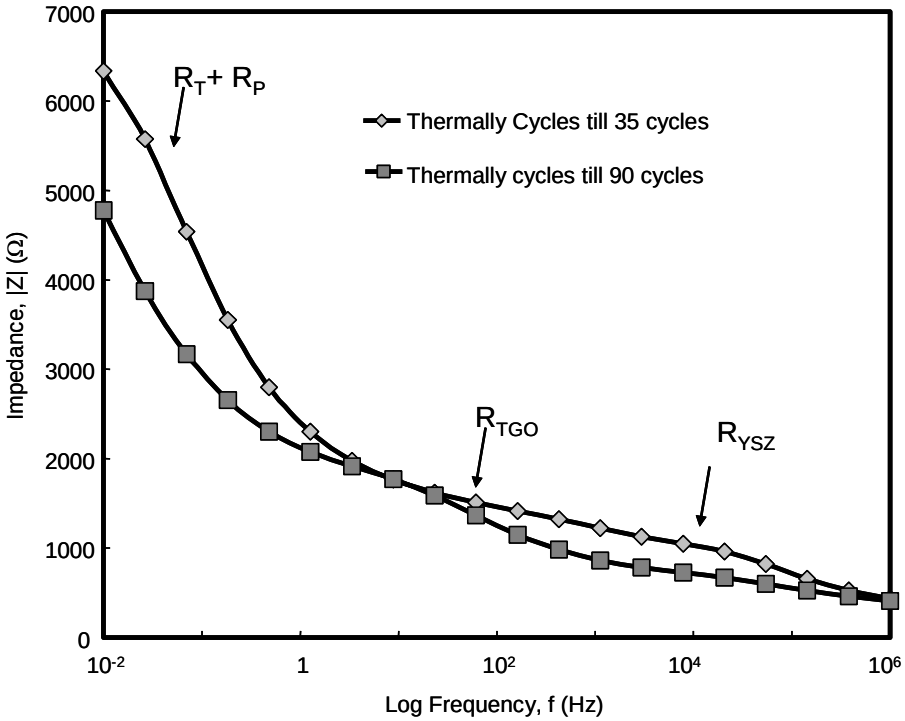

Figure 104. Typical Impedance plots from type-I APS TBCs as a function of 10-hour thermal cycling at 1121°C.

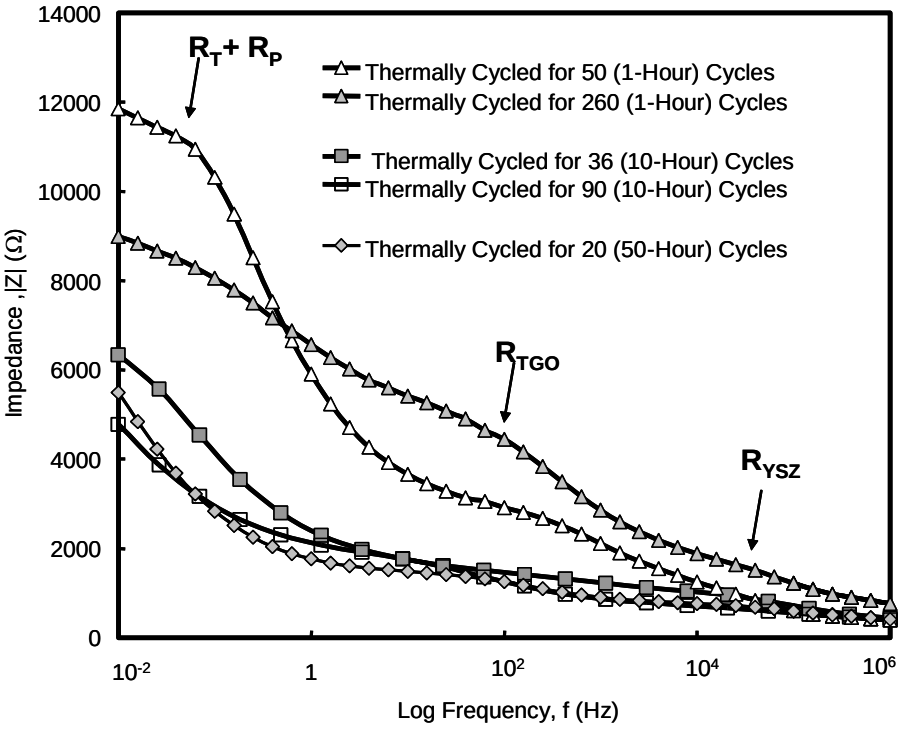

Figure 105. Typical Impedance plots from type-I APS TBCs as a function of 1, 10 and 50- hour thermal cycling at 1121°C.

Table 14. Changes in resistance and capacitance of type- I APS TBCs constituents as a function of 10-hour thermal cycling at 1121°C.

Thermal Cycles	R_{YSZ} (kΩ)	C_{YSZ} (nF)	R_P (kΩ)	C_P (uF)	R_{TGO} (kΩ)	C_{TGO} (nF)	R_T (kΩ)	C_T (nF)
As-received	0.50 ± 0.4	2.2 ± 0.4	10.6 ± 4.2	377700 ± 21959	0	0	0.3 ± 0.1	16486 ± 2747
36 cycles (30% lifetime)	.64 ±0.002	374.6 ±82.1	5.6 ±0.18	18.48 ±0.22	0.98 ±0.02	9.94 ±0.72	0.55 ±0.02	10531 ±996
90 cycles (80% lifetime)	0.88 ±0.09	431.95 ±0.0	6.58 ±4.87	11.34 ±0.02	0.58 ±0.10	6.14 ±0.01	0.51 ±0.13	3262 ±15.5

Table 15. Changes in resistance and capacitance of type- I APS TBCs constituents as a function of 50-hour thermal cycling at 1121°C.

Thermal Cycles	R_C (kΩ)	C_C (nF)	R_P (kΩ)	C_P (uF)	R_O (kΩ)	C_O (nF)	R_T (kΩ)	C_T (nF)
As-received	0.50 ± 0.4	2.2 ± 0.4	10.6 ± 4.2	377700 ± 21959	0	0	0.3 ± 0.1	16486 ± 2747
20 cycles (50% lifetime)	.60 ±0.01	892.3 ±21.7	4.03 ±0.08	7.3 ±0.32	0.78 ±0.02	8.5 ±0.16	9.6 ±0. 10	16085 ±148

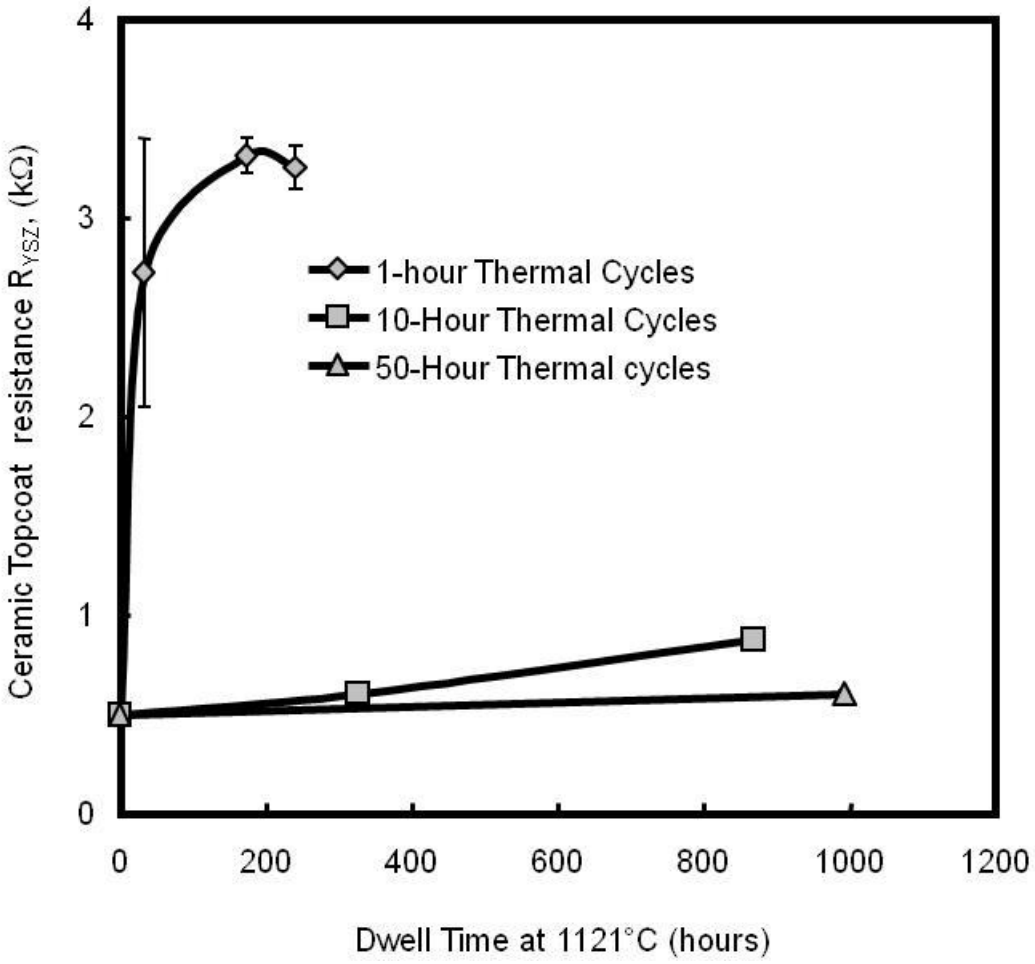

Figure 106. Evolution of ceramic topcoat resistance (R_{YSZ}) for type I APS TBCs as a function of dwell time at 1121°C.

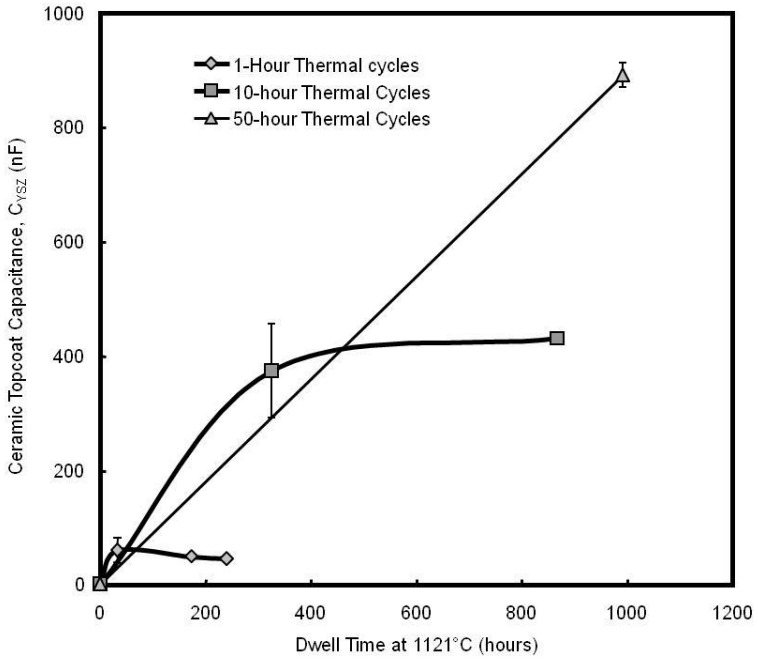

Figure 107. Evolution of ceramic topcoat capacitance (C_{YSZ}) for type I APS TBCs as a function of dwell time at 1121°C.

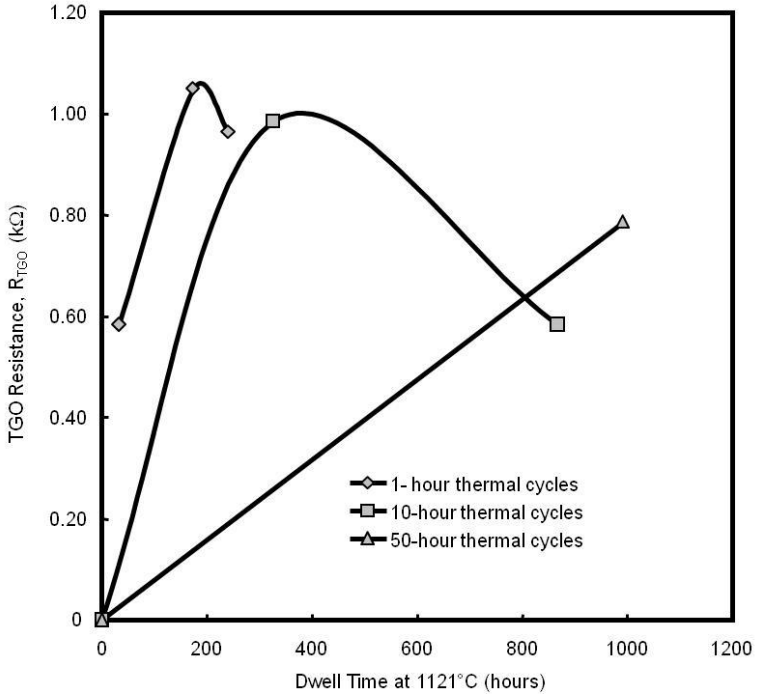

Figure 108. Evolution of TGO resistance (R_{TGO}) for type I APS TBCs as a function of dwell time at 1121°C.

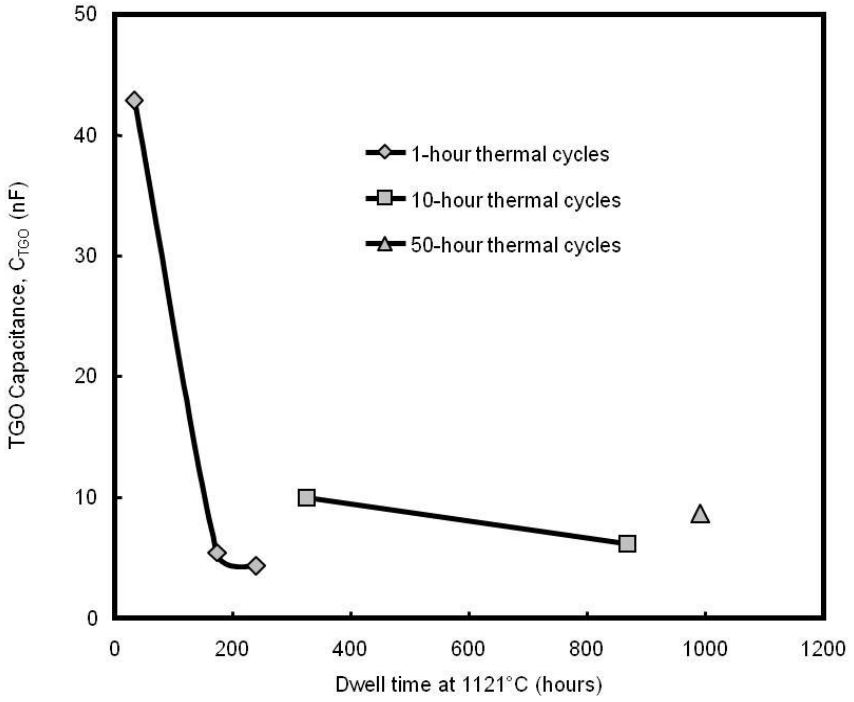

Figure 109. Evolution of TGO capacitance (C_{TGO}) for type I APS TBCs as a function of dwell time at 1121°C.

For type II APS TBCs, EIS measurement was carried out 3 times at 30% and 80% of thermal cyclic lifetime. Impedance response from 10-hour thermal cyclic lifetimes is presented in Figure 110. Table 16 also reports the values of resistance and capacitance of various TBC constituents. The initial increase in R_{YSZ} and R_{TGO} as presented in Figure 111 through Figure 114 is related to micro-cracks within YSZ because of high temperature exposure followed by cooling and growth of the TGO scale with thermal exposure.

Comparing to 1-hour thermal cycles the impedance response from 10-hour thermal cycles was significantly lower as presented in Figure 110. With increase in dwell time at high temperature, sintering of YSZ is more prominent and with subsequent cooling micro-cracks originates within the sintered YSZ and hence the impedance response is lower for longer dwells times.

The resistance and capacitance of the YSZ and TGO for type-II APS TBCs are presented as function of dwell time in Figure 111 through Figure 114. With an increase in the impedance, the resistance of the topcoat and the TGO increased. The capacitance of the TGO did not increase abruptly at failure because the fracture path of APS TBCs observed for type-I TBCs primarily occurs at the YSZ/TGO interface as shown in Figure 150.

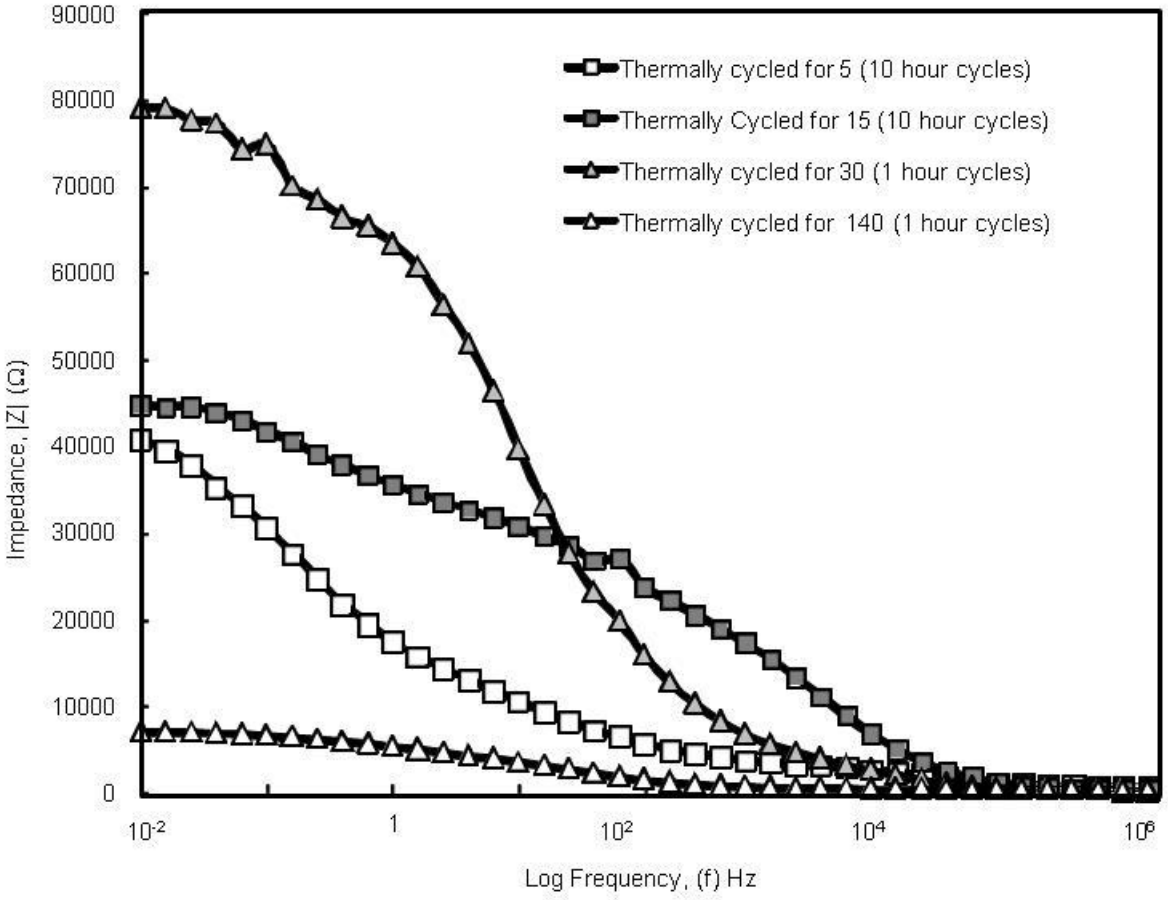

Figure 110. Typical impedance response from type-II APS TBCs as a function of 1 and 10-hour thermal cycle comparison.

Table 16. Changes in resistance and capacitance of type- I APS TBCs constituents as a function of 10-hour thermal cycling.

Thermal Cycles	R_C (kΩ)	C_C (nF)	R_P (kΩ)	C_P (nF)	R_O (kΩ)	C_O (nF)	R_T (kΩ)	C_T (nF)
As-received	0.29 ± 0.02	4.8 ± 0.5	11.8 ± 1.4	38.01 ± 9317	0	0	0.9 ± 0.1	3883 ± 219.2
5 cycles 30% LT	0.55 ±0.03	0.27 ±0.03	31.01 ±1.17	1586 ±76.63	2.07 ±0.08	8.9 ±0.28	11.71 ±0.50	165.5 ±10.1
15 cycles 80% LT	2.23 ±0.18	4.6 ±0.02	17.1 ±0.39	903 ±22.82	9.64 ±1.07	7.92 ±0.03	19.7 ±1.82	27.99 ±2.11

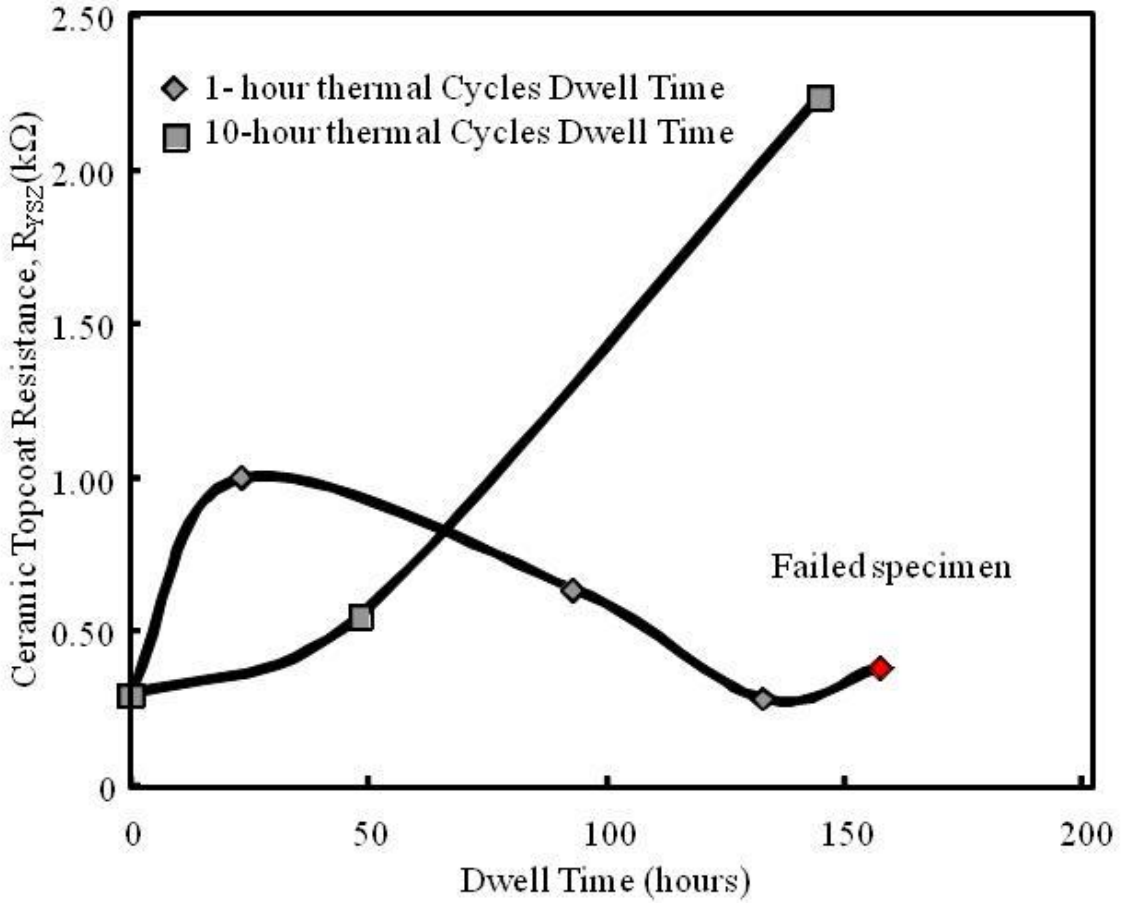

Figure 111. Evolution of ceramic topcoat resistance (R_{YSZ}) for type-II APS TBCs as a function of thermal cycling at 1121°C.

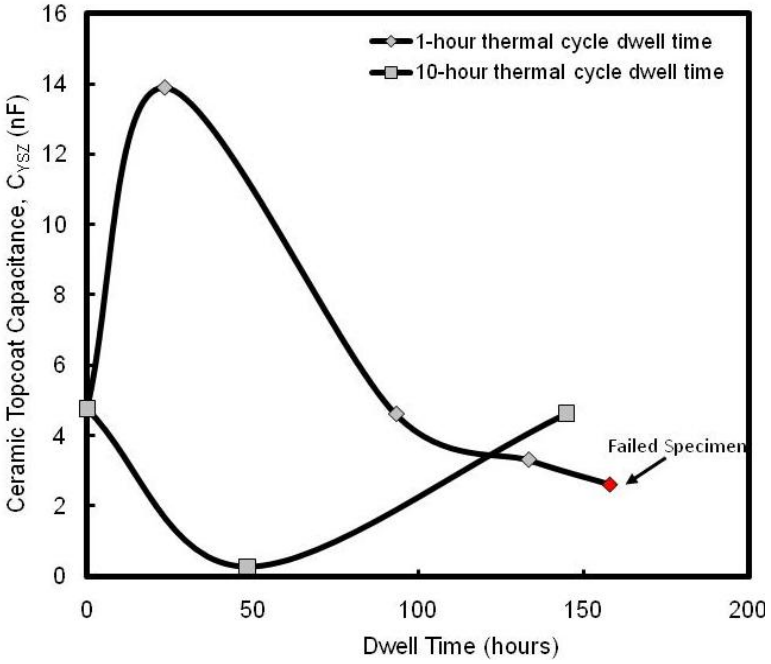

Figure 112. Evolution of ceramic topcoat capacitance (C_{YSZ}) for type-II APS TBCs as a function of thermal cycling at 1121°C.

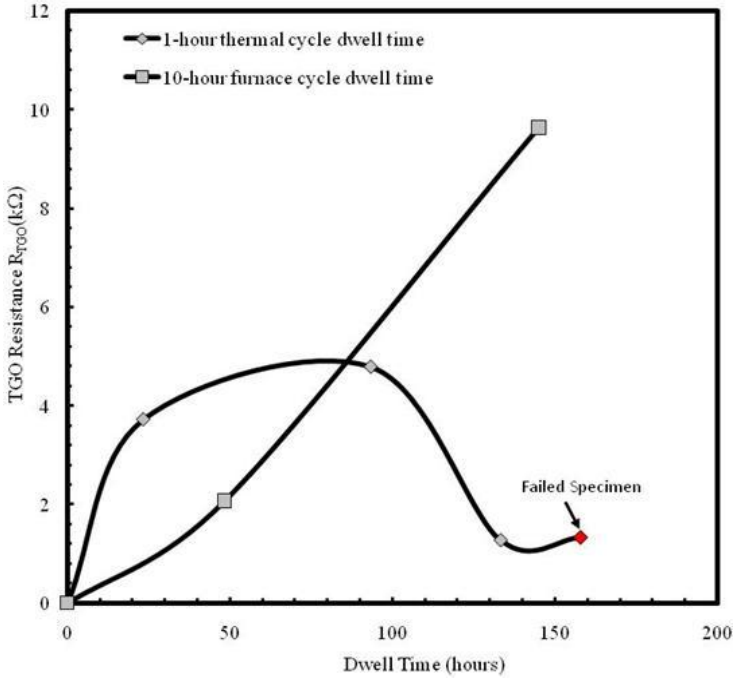

Figure 113. Evolution of TGO resistance (R_{TGO}) in type II APS TBCs as function of thermal cycling at 1121°C.

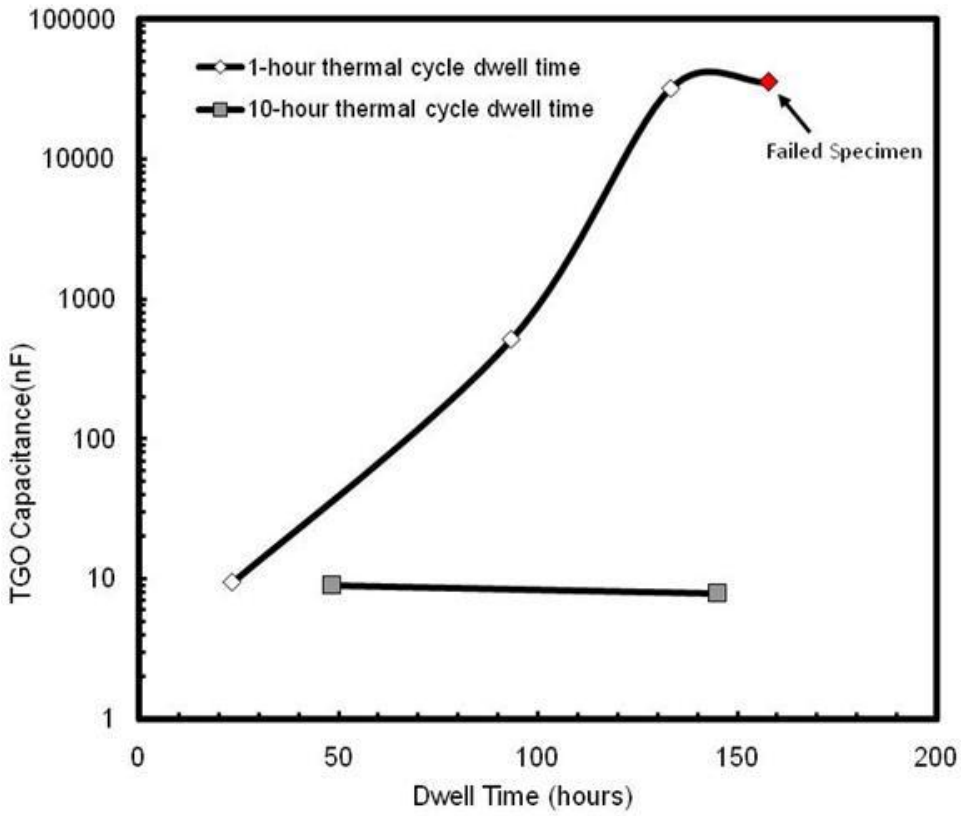

Figure 114. Evolution of TGO capacitance (C_{TGO}) in type-II APS TBCs as a function of thermal cycling at 1121°C.

4.7 EIS OF EB-PVD TBCs as a function of thermal cycling

For type III TBCs, EIS measurement was carried out 3 times for as-received, thermally cycled and failed specimen. Typical impedance and phase angle plots for these specimens are presented in Figure 115 and Figure 116, respectively. Table 17 reports the values of resistance and capacitance for various TBC constituents that were determined based on the ac-equivalent circuit presented in Figure 47. Evolution in the resistance and capacitance of TBC constituents as a function of thermal cycling are shown Figure 117 through Figure 120. The initial increase in the resistance of the YSZ and the TGO, shown in Figure 117 and Figure 118, may be due to the sintering of the YSZ and growth of the TGO with thermal exposure. After prolonged exposure

corresponding to the 70% of thermal cyclic lifetime, the resistance of the YSZ and TGO started to decrease, indicating the penetration of electrolyte through damages (e.g., cracks and voids) in the YSZ and the TGO. At failure for type-III TBCs the ceramic topcoat fragments into pieces leaving exposed of bondcoat surface with along with TGO scale resulting in a sharp increase in the capacitance of the YSZ and the TGO.

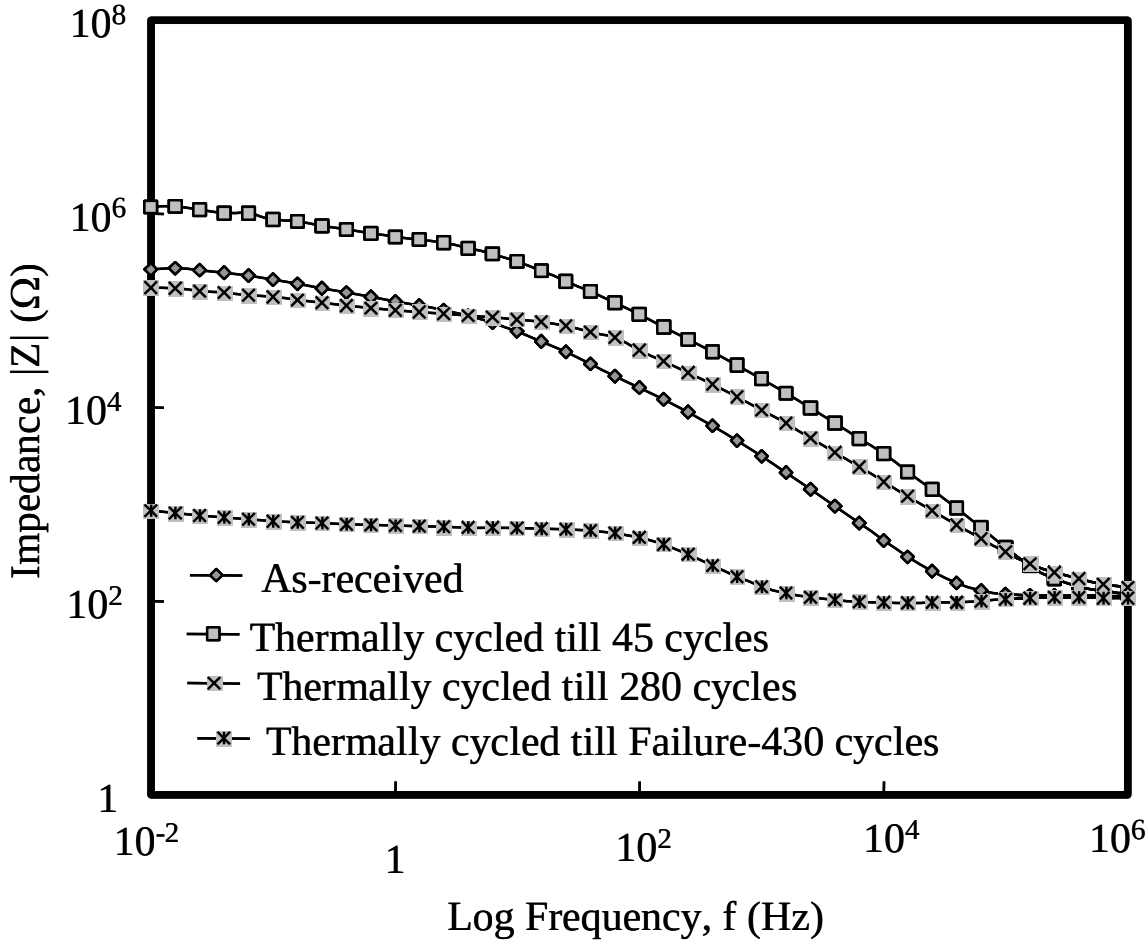

Figure 115. Impedance plots for type-III EB-PVD TBCs as function of 1-hour thermal cycle with 1-hour dwell time at 1121°C.

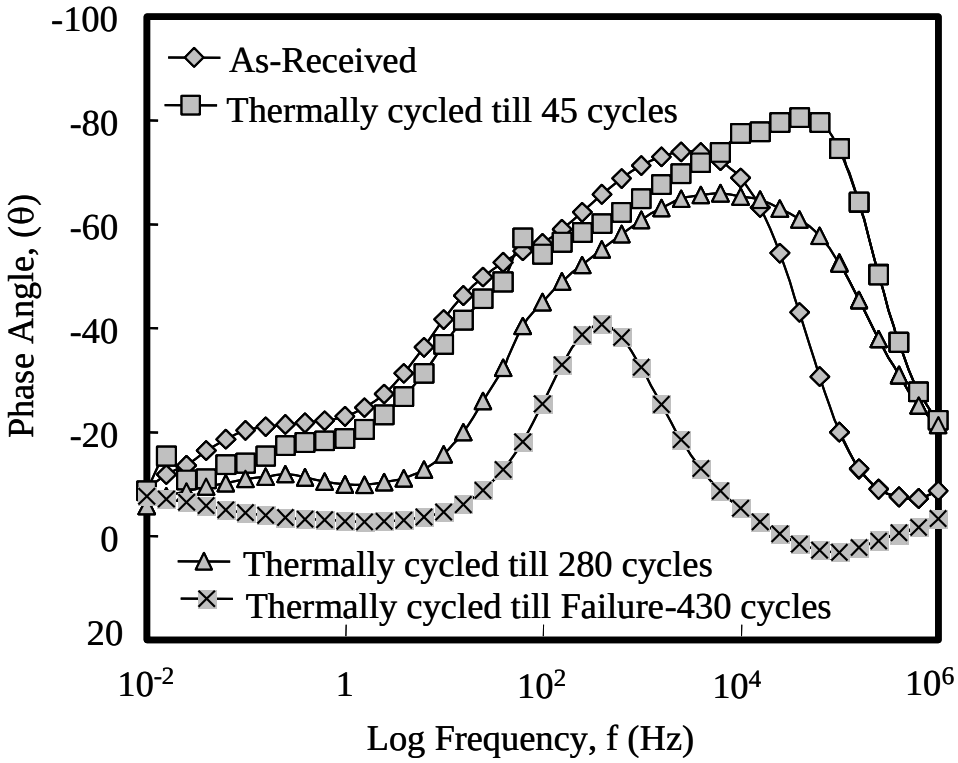

Figure 116. Phase angle plots for type-III EB-PVD TBCs as function of thermal cycle with 1-hour dwell time at 1121°C.

Table 17. Changes in resistance and capacitance of type-III EBPVD TBC constituents as a function of 1-hour thermal cycling.

Thermal Cycles	R_{YSZ} (kΩ)	C_{YSZ} (nF)	R_P (kΩ)	C_P (nF)	R_{TGO} (kΩ)	C_{TGO} (nF)	R_T (kΩ)	C_T (μF)
As-received	1.90 ± 0.45	46.9 ±2.3	309.8 ±81.7	24.46 ±0.03	0.05 ±0.01	283 ±19.4	28.3 ±4.9	447 ±135
45 (10% lifetime)	38.0 ±1.3	9.8 ±0.3	163.7 ±5.2	7.4 ±0.8	7.5 ±4.7	20 ±1.5	1.6 ±0.02	14.7 ±0.1
280 (70% lifetime)	22.8 ±7.2	26.6 ±0.6	262.4 ±74.2	7 ±1.9	4.8 ±0.2	17.03 ±0.07	0.28 ±0.01	8.9 ±0.12
430 (After Failure)	0.25 ±0.01	5015 ±61.5	0.75 ±0.1	63813 ±6542	0.17 ±0.01	9999 ±70.3	0.07 ±0.01	4193 ±145.5

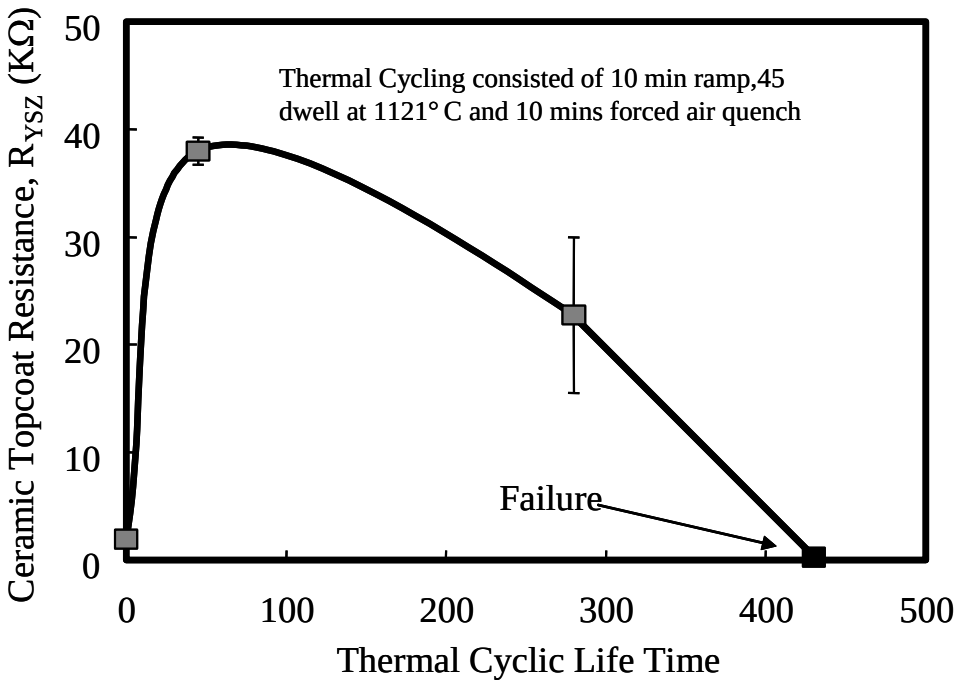

Figure 117. Evolution of the ceramic topcoat resistance (R_{YSZ}) for type III EB-PVD TBCs as a function of 1-hour thermal cycling at 1121°C.

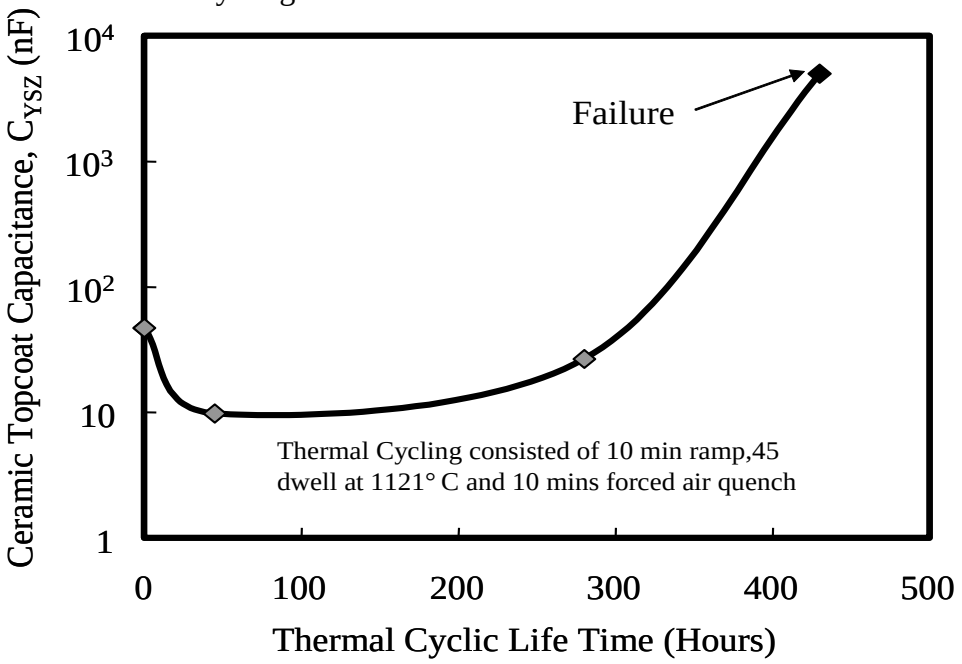

Figure 118. Evolution of the ceramic topcoat capacitance (C_{YSZ}) for type III EB-PVD TBCs as a function of 1-hour thermal cycling at 1121°C.

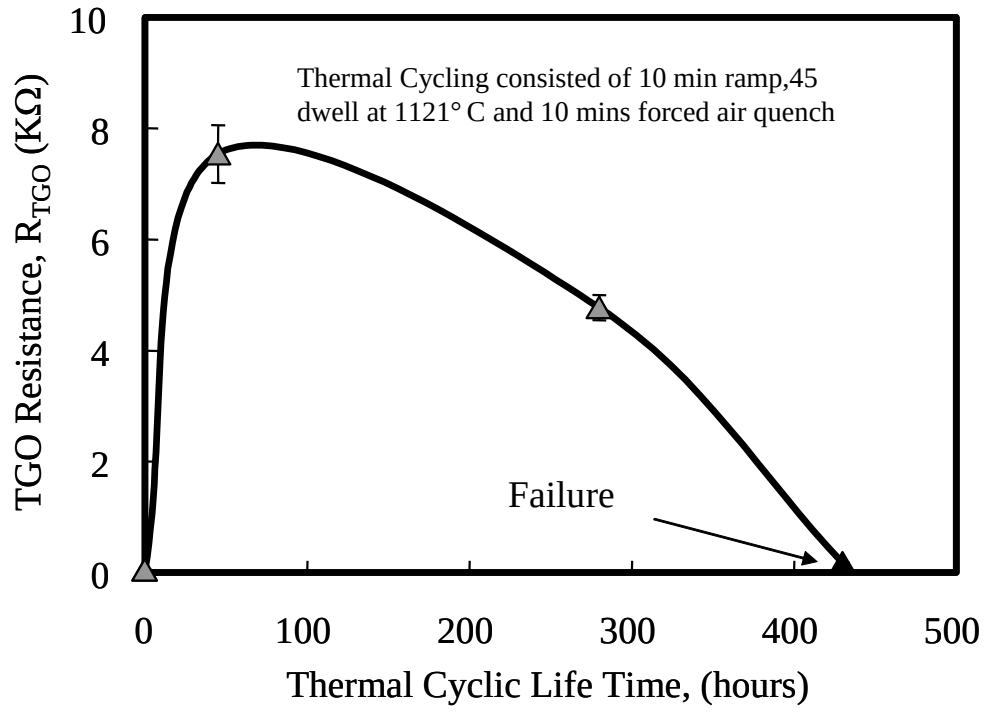

Figure 119. Evolution of the TGO resistance (R_{TGO}) for type III EB-PVD TBCs as a function of 1-hour thermal cycling at 1121°C.

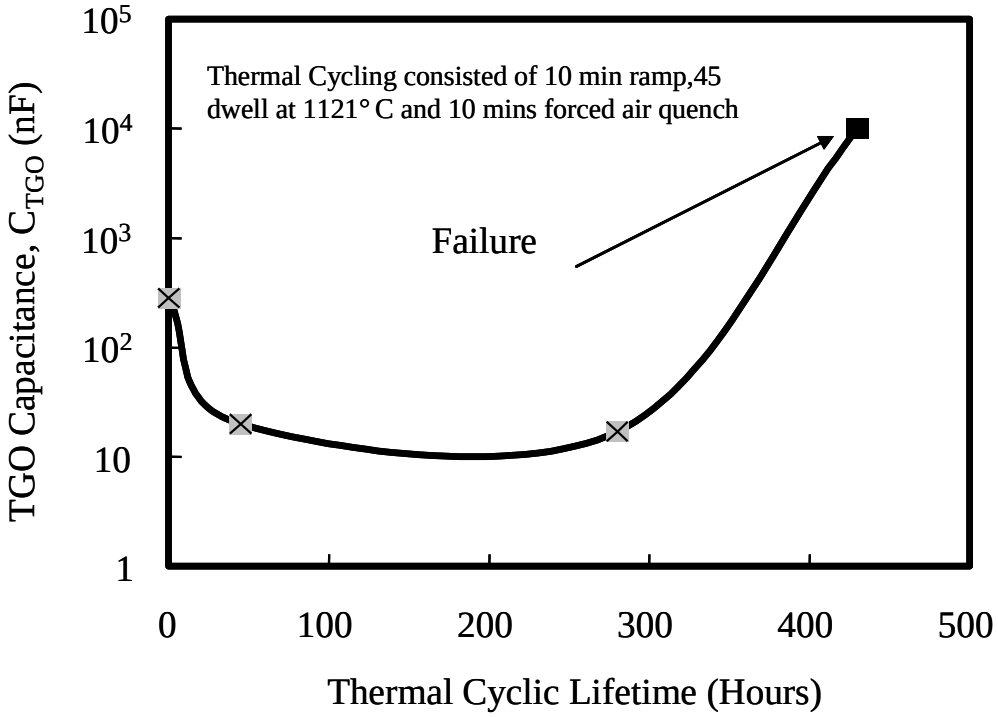

Figure 120. Evolution of the TGO capacitance C_{TGO} for type III EB-PVD TBCs as a function of 1-hour thermal cycling at 1121°C.

For type IV TBCs EIS measurement was carried out 3 times for as-received, thermally cycled and failed specimen. Typical impedance and phase angle plots for these specimens are presented in Figure 121 and Figure 122, respectively. Table 18 also reports the values of resistance and capacitance of the various TBC constituents that were calculated based on the ac-equivalent circuit in Figure 47. Evolution in resistance and capacitance of TBC constituents as a function of thermal cycling is presented in

Table 18, and Figure 123 through Figure 126. Figure 122 shows that the impedance of the type-IV TBCs increased with thermal cycling and decreased after prolonged exposure. This increase in the impedance is attributed to the growth of the TGO and the high temperature sintering of the YSZ. Aforementioned, this microstructural changes can be related to the electrical parameters such as the resistance and capacitance of the YSZ and the TGO. The resistance of the YSZ and TGO increased initially and decreased after prolonged exposure as shown in Figure 123 through Figure 125. Whereas the capacitance of the YSZ shown in the Figure 124, decreased initially and remained constant until failure where a sharp increase was observed. This is because the impedance of the failed specimen is lower than that of the as-received specimen due to the exposure of the bondcoat surface observed on the fracture surface. On the other hand, the capacitance of the TGO shown in Figure 126, decreased initially and increased with further thermal cycling related to the damages observed within the TGO scale.

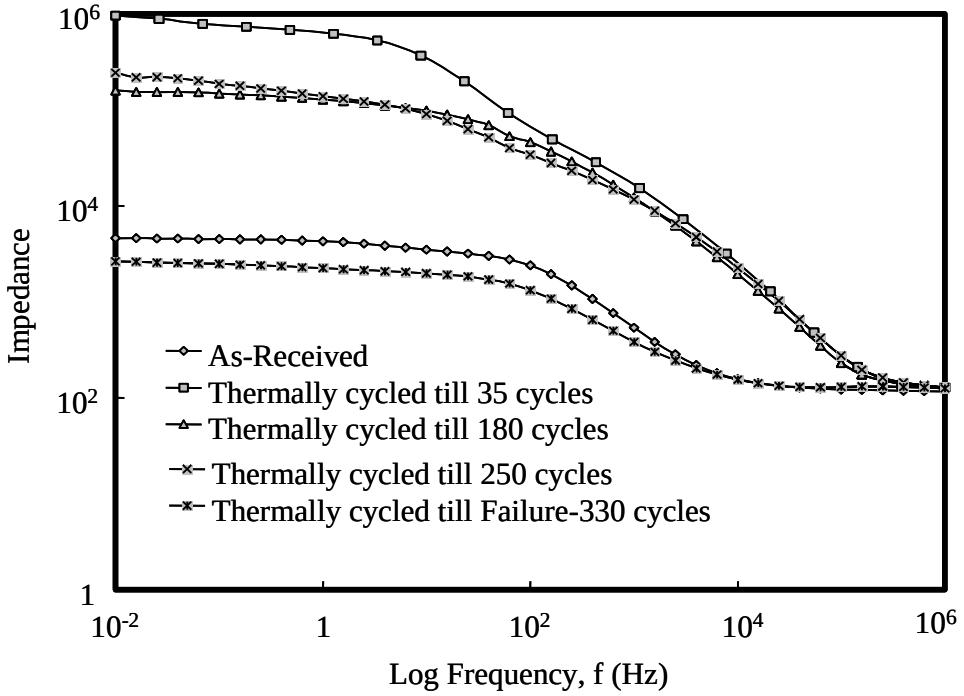

Figure 121. Typical impedance plots for type-IV EB-PVD TBCs as a function of 1-hour thermal cyclic lifetime at 1121°C.

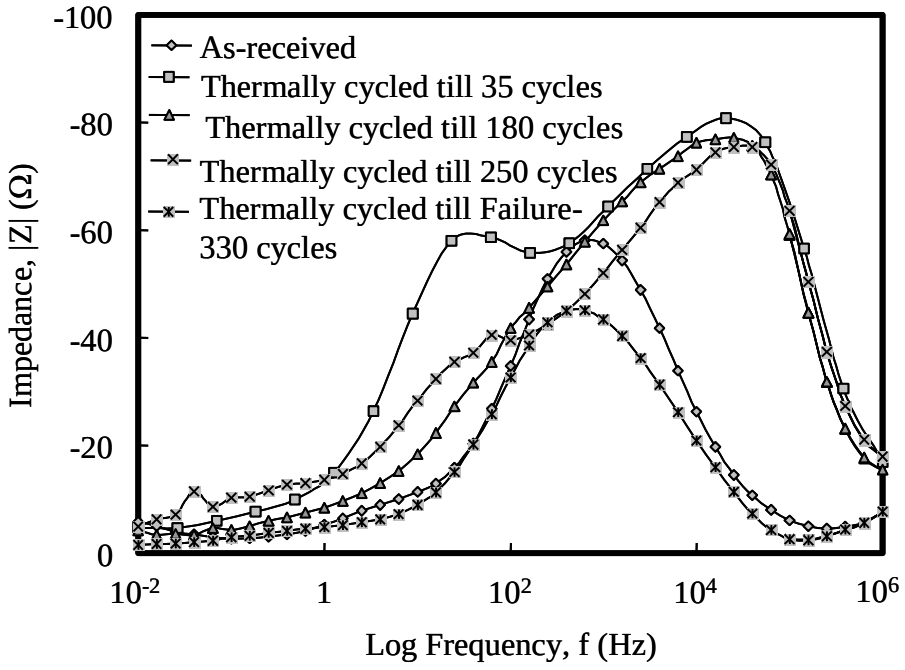

Figure 122. Typical phase angle plots for type-IV EB-PVD TBCs as a function of 1-hour thermal cyclic lifetime at 1121°C.

Table 18. Changes in resistance and capacitance of type-IV EB-PVD TBC constituents as a function of 1-hour thermal cycling.

Thermal Cycles	R_C (kΩ)	C_C (nF)	R_P (kΩ)	C_P (nF)	R_O (kΩ)	C_O (nF)	R_T (kΩ)	C_T (nF)
As-received	.01 ± 0	224 ±16.3	2.17 ±0.3	523.7 ±26.2	2.1 ±0.3	600 ±14.5	37.2 ±0.7	2 ±0.1
45 (10% lifetime)	6.2 ±2.2	6.8 ±0.2	735.5 ±175.6	8.6 ±0.8	431 ±6.6	50.1 ±2.3	23.8 ±0.9	2.4 ±0.3
180 (50% lifetime)	2.6 ±0.05	8.2 ±0.05	134.8 ±2.8	8.7 ±0.05	27.6 ±0.10	115 ±1.6	31.1 ±0.2	2.3 ±0.04
280 (70% lifetime)	0.44 ±0.05	6.5 ±0.04	140.2 ±26.8	9.72 ±0.15	31.43 ±0.8	182 ±15.8	35 ±0.3	1.9 ±0.01
330 (After) Failure	0.02 ±0	250 ±48.8	1.7 ±0.2	450.3 ±99.6	0.96 ±0.06	1203.2 ±365.4	40.8 ±0.9	1.7 ±0.1

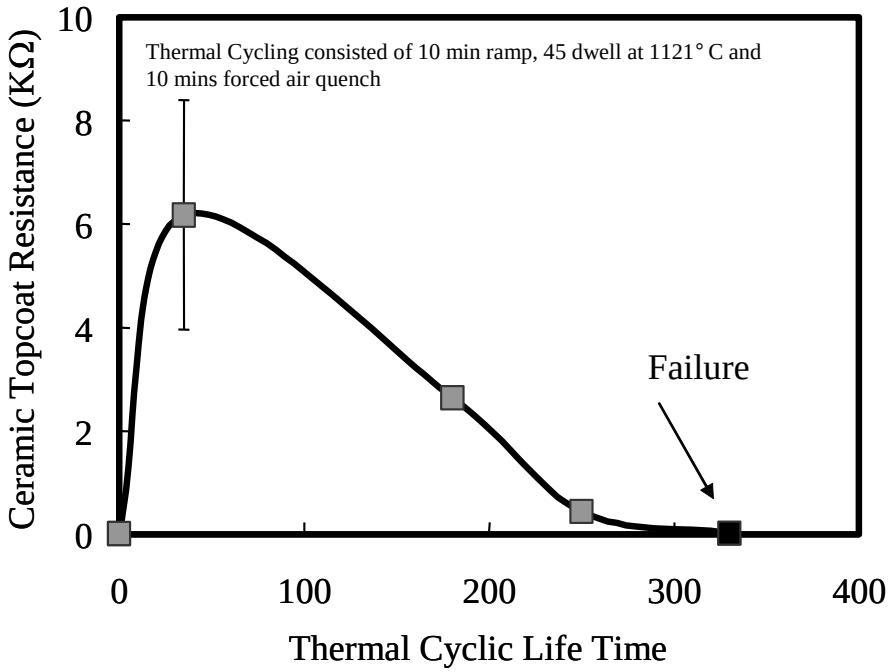

Figure 123. Evolution of the ceramic topcoat resistance (R_{YSZ}) for type IV EB-PVD TBCs as a function of 1-hour thermal cycling at 1121°C.

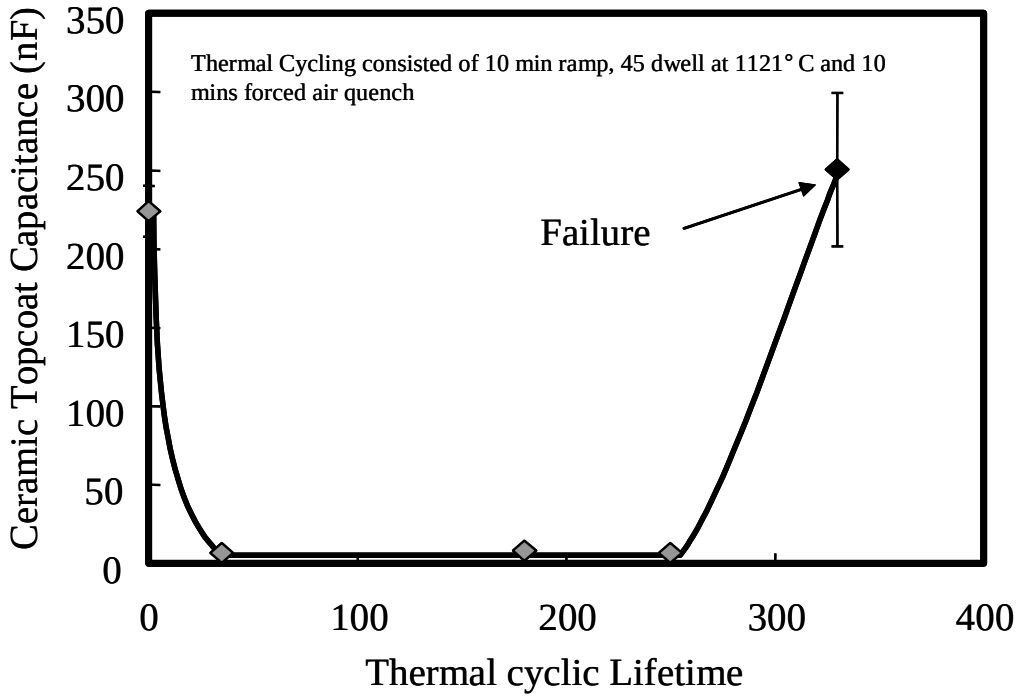

Figure 124. Evolution of the ceramic topcoat capacitance (C_{YSZ}) for type IV EB-PVD TBCs as a function of 1-hour thermal cycling at 1121°C.

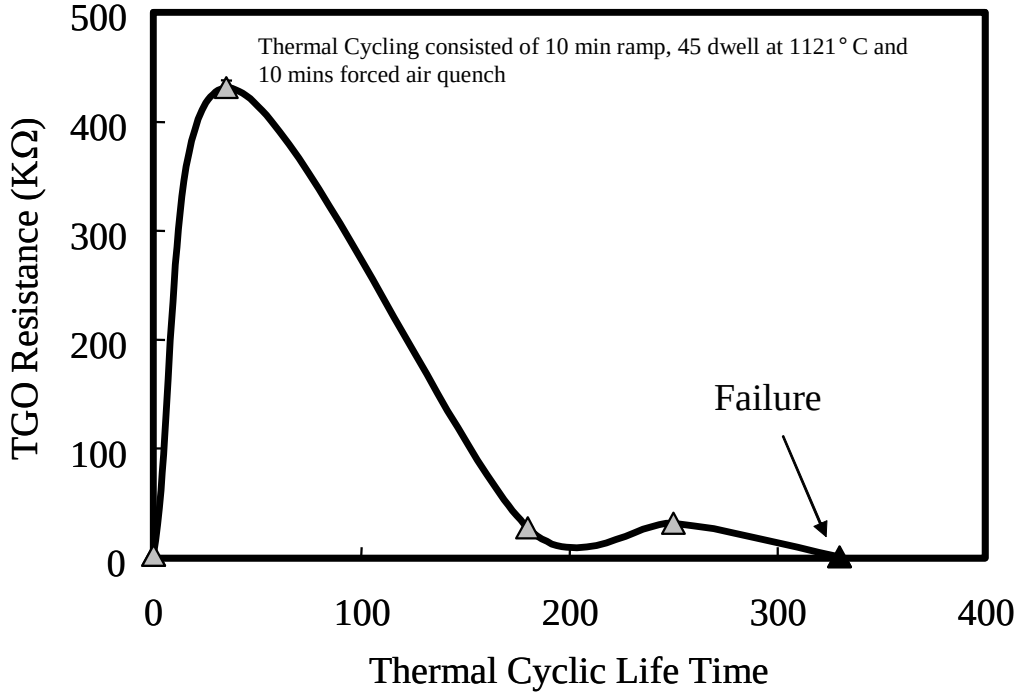

Figure 125. Evolution of the TGO resistance (R_{TGO}) for type IV EB-PVD TBCs as a function of 1-hour thermal cycling at 1121°C.

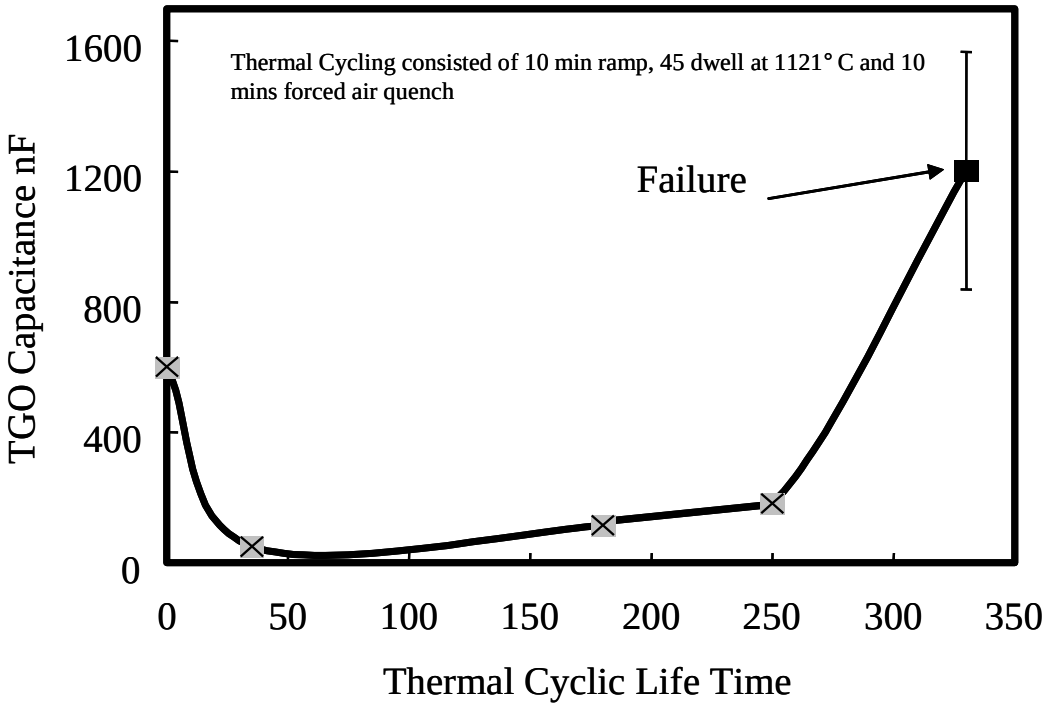

Figure 126. Evolution of the TGO capacitance (C_{TGO}) for type IV EB-PVD TBCs as a function of 1-hour thermal cycling at 1121°C.

4.8 Microstructural assessment of APS TBCs

4.8.1 Microstructural Assessment for APS TBCs after 1-hour Thermal Cycling

Typical backscatter electron micrographs for type-I APS TBCs as a function of thermal cycling is shown in Figure 127. In addition to the growth of the TGO scale, internal oxidation is observed to occur parallel to the YSZ/bondcoat interface, presumably following the splat boundaries of the APS NiCoCrAlY bondcoat. The internal oxides and mainly consisted of Al-rich oxides (presumably α-Al_2O_3) as presented in Figure 128. With progressive thermal cycling the YSZ topcoat showed densification and micro-cracking as shown in Figure 129.

The initial increase in impedance response as shown in Figure 92 is from the growth of the TGO and densification of ceramic topcoat. This correlation can be made from Figure 127 and Figure 129, respectively. The electrical component R_{YSZ} increased and decreased until failure as shown in Figure 94 . The initial increase is related to the high temperature sintering and after prolonged thermal cycles R_{YSZ} decreased due to micro-cracking within the YSZ. The electrical parameter C_{YSZ} did not vary significantly, because it depends on thickness of the coating and the dielectric layer thickness which varies with sintering and micro-cracking. In the case of TGO, R_{TGO} and C_{TGO} did increase and decrease, respectively even after failure because of the TGO growth. At failure an inverse trend reported earlier [89] was not observed for this particular type of TBCs, since bondcoat surface was not exposed after failure as shown in Figure 127 (e, f).

Cross-sectional backscatter micrograph from failed TBC is shown Figure 127(e,f), and bondcoat and YSZ fracture surface is shown in Figure 130. Fracture surface on the YSZ and bondcoat contained remnants of the TGO on both sides, fracture occurred primarily at the YSZ/TGO interface within YSZ.

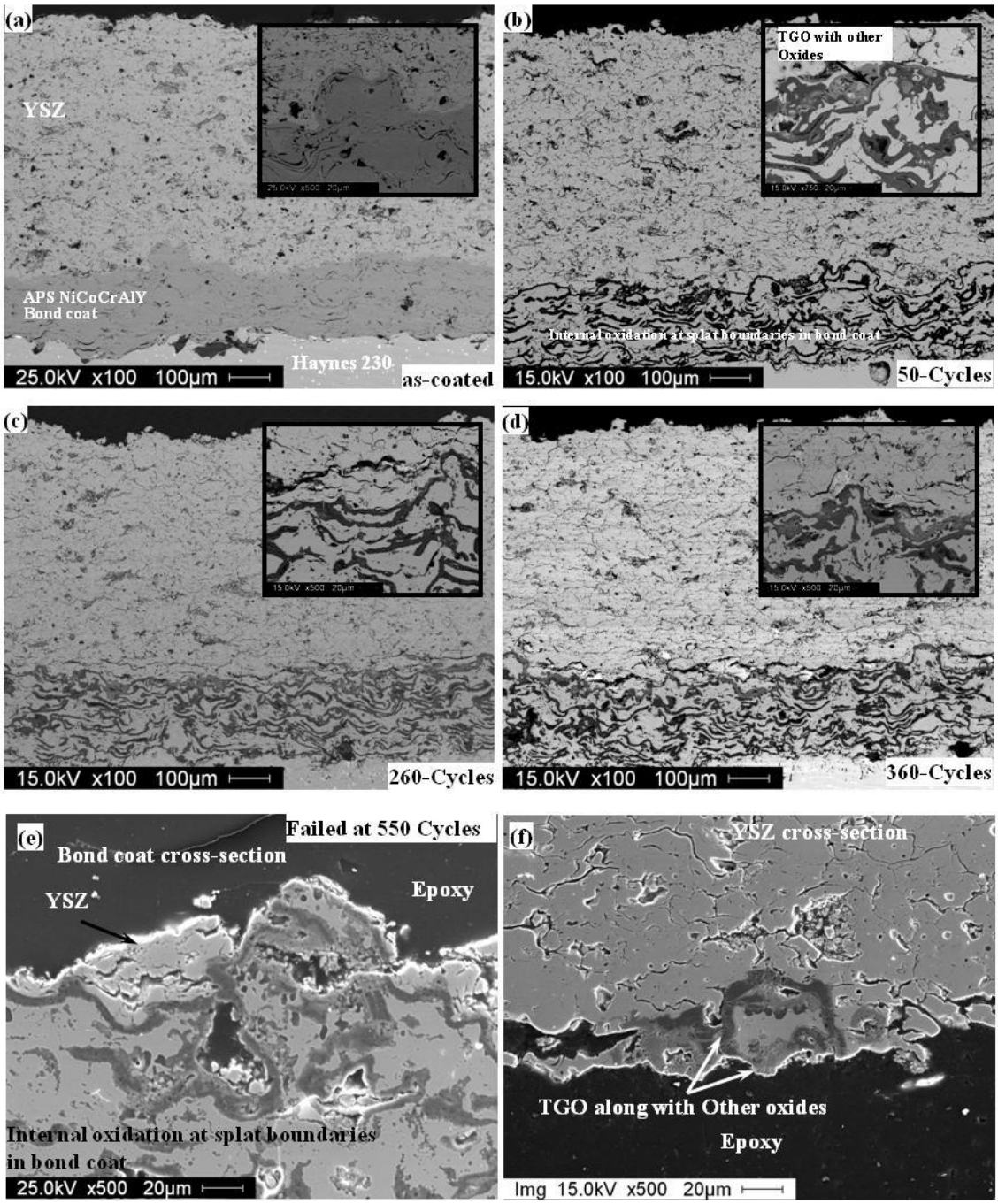

Figure 127. Typical backscatter electron micrographs of type-I APS TBCs with progressive 1-hour thermal cycling at 1121°C.

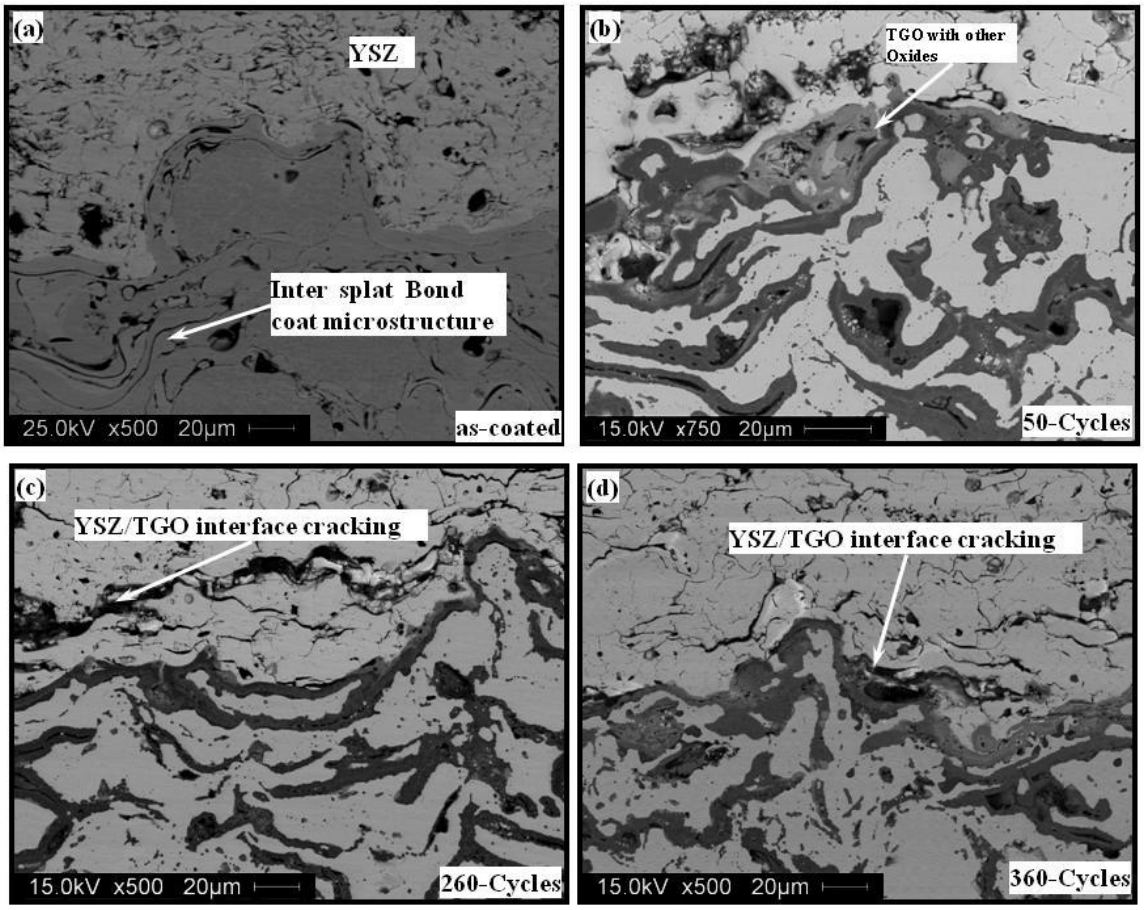

Figure 128. Typical backscatter electron micrographs of YSZ/bondcoat interface in type-I APS TBCs showing damage accumulation with progressive 1-hour thermal cycling at 1121°C.

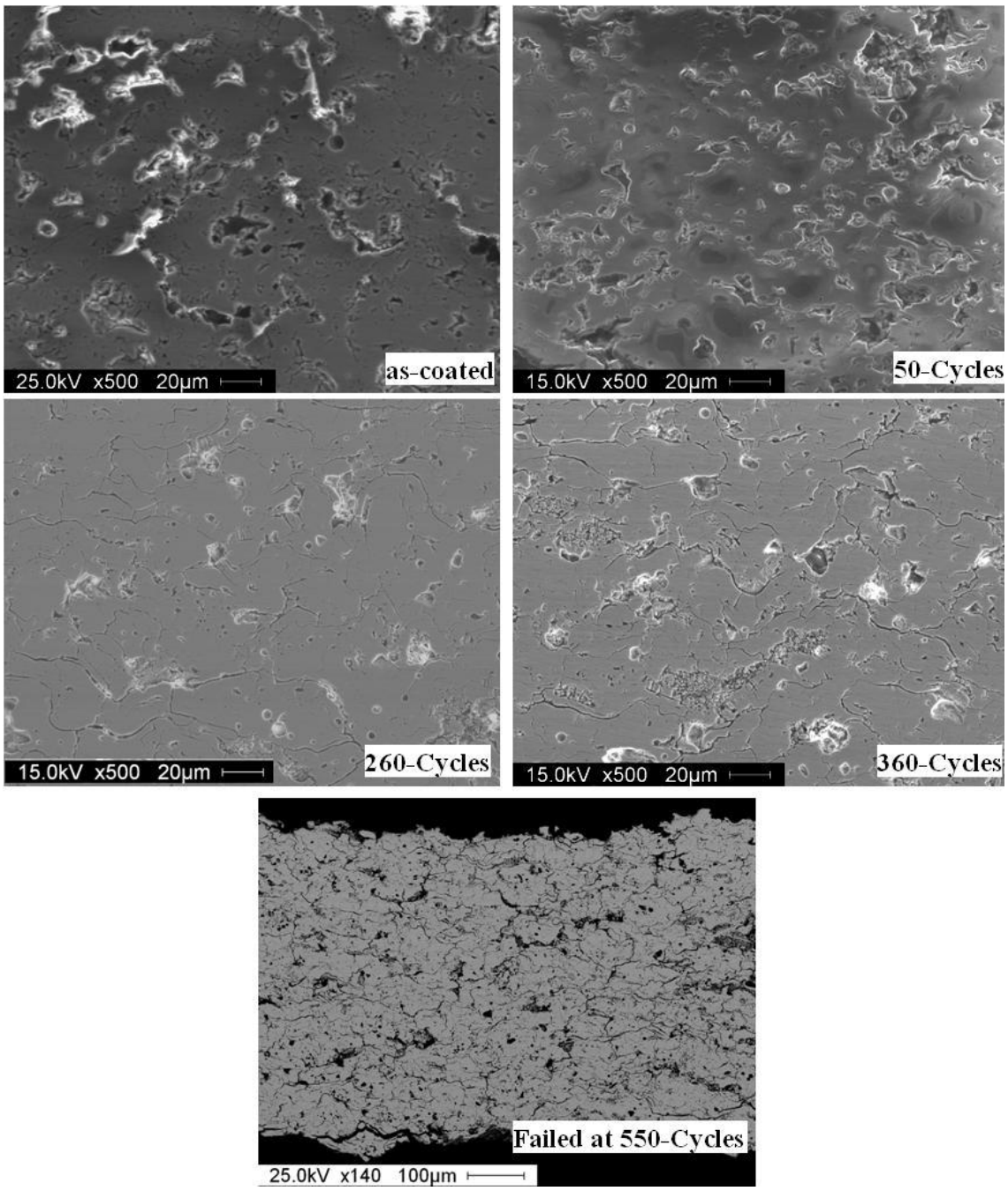

Figure 129. Microstructural observation of YSZ topcoat for type-I APS TBCs with progressive 1-hour thermal cycling at 1121°C.

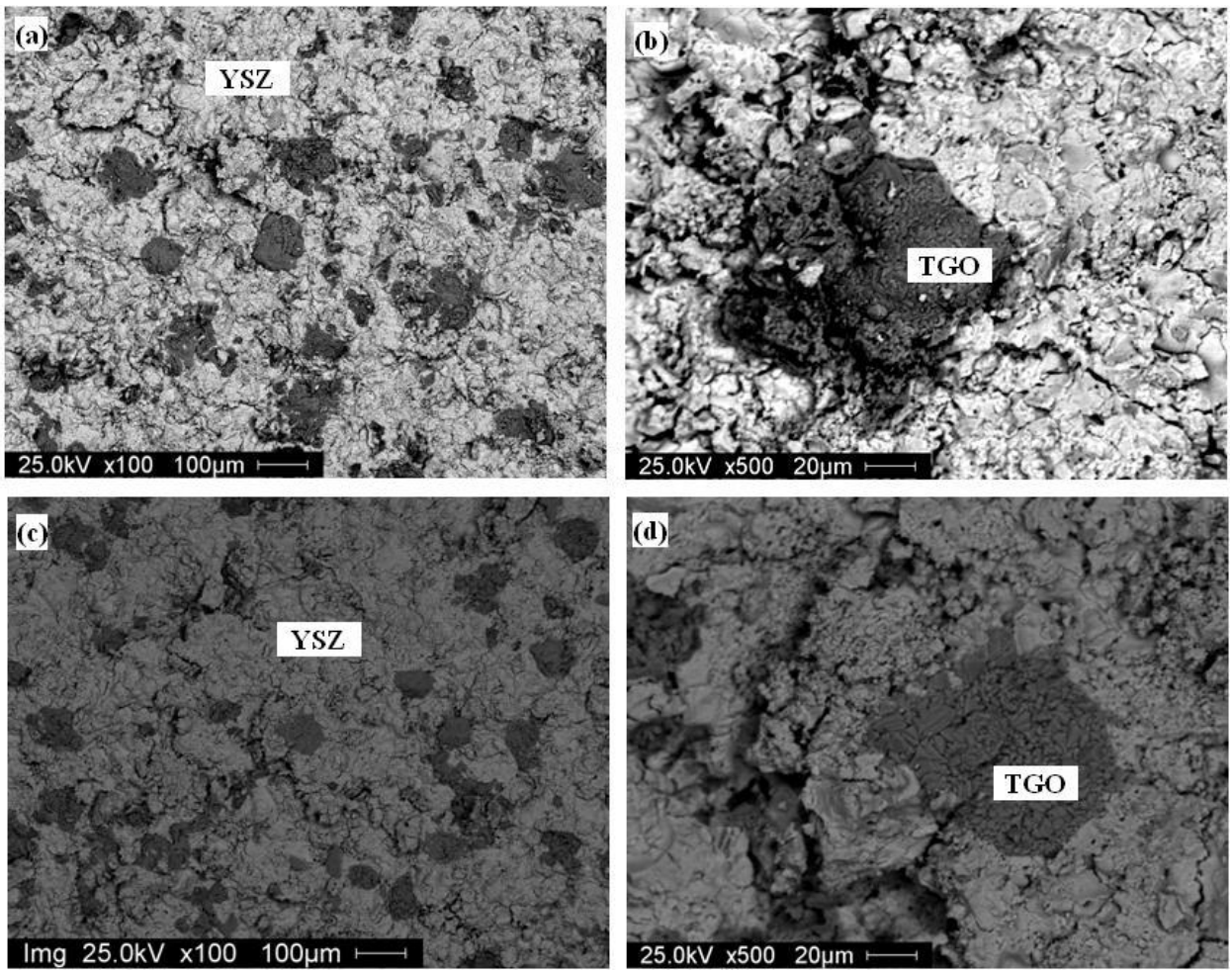

Figure 130. Fractographic observation of type-I APS TBCs with NiCoCrAlY APS bondcoat showing constituents on the coating spallation surface after 1-hour thermal cycles at 1121°C (a,b) YSZ bottom surface and (c, d) bondcoat surface.

Typical backscatter electron micrographs from type-II APS TBCs as a function of thermal cycling shown in Figure 131. In addition to the growth of the TGO, β-depletion of LPPS NiCoCrAlY bondcoat was observed and complete disappearance of the Al-rich β-phase was observed before failure as shown in Figure 132(c, d). With progressive thermal cycling the YSZ topcoat showed densification and micro-cracking as shown in Figure 133.

The initial increase in impedance response shown in Figure 98 is from the growth of the TGO and densification of the YSZ topcoat. This observation can be correlated to Figure 131 and

Figure 133. The electrical component R_{YSZ} did increase and decrease as shown in Figure 100. The initial increase is related to the sintering of the topcoat. With prolonged exposure and cooling causes micro-cracking within the YSZ resulting in the decrease of R_{YSZ}. The electrical parameter C_{YSZ} as shown in Figure 101 increased initially and decreased with thermal cycling until failure. The trend in C_{YSZ}, depends on the thickness of the coating and the dielectric layer thickness which varies with sintering and micro-cracking.

In case of TGO, R_{TGO} did increase initially until 50% lifetime and decreased even after failure with thermal cycling as shown in Figure 132. The increase in R_{TGO} is from the growth of TGO and the decrease is from the damage accumulation observed in the TGO scale. The C_{TGO} increased continuously with thermal cycling because of the TGO scale cracking was observed as early as 50% lifetime.

Cross-sectional observation after failure is shown in Figure 132(d). Micro-constituents on fracture surface of type-II APS TBCs are shown in Figure 134. The fracture surface consisted mostly of YSZ. The spalled surface of the YSZ consisted of YSZ with islands of the TGO and the bare bondcoat surface consisted mostly of YSZ with islands of TGO. The fracture for type-II APS TBCs occurred at the YSZ/TGO interface within the YSZ.

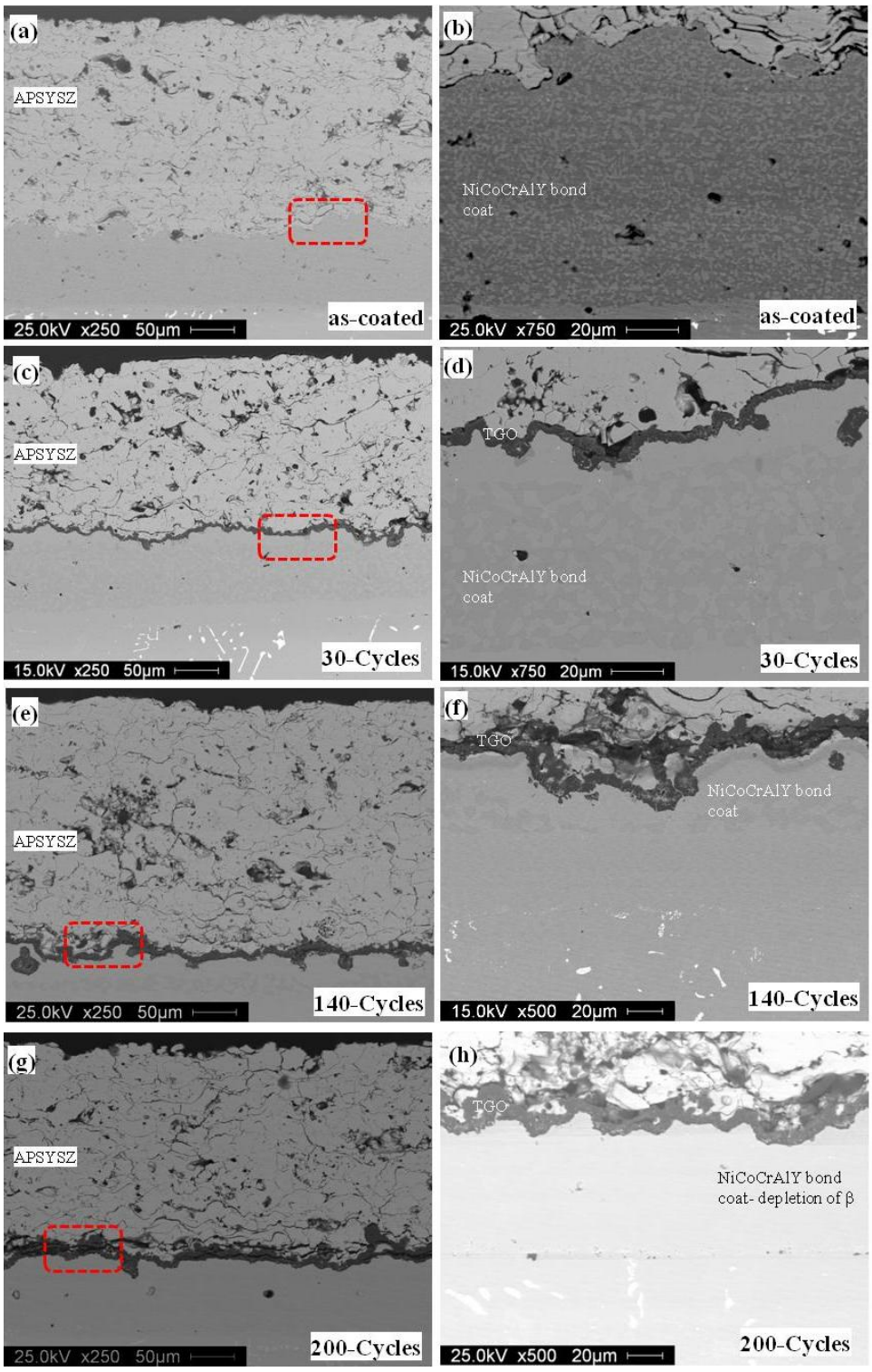

Figure 131. Typical backscatter electron micrograph of type-II APS TBCs with NiCoCrAlY LPPS bondcoat as a function of 1-hour thermal cycling at 1121°C.

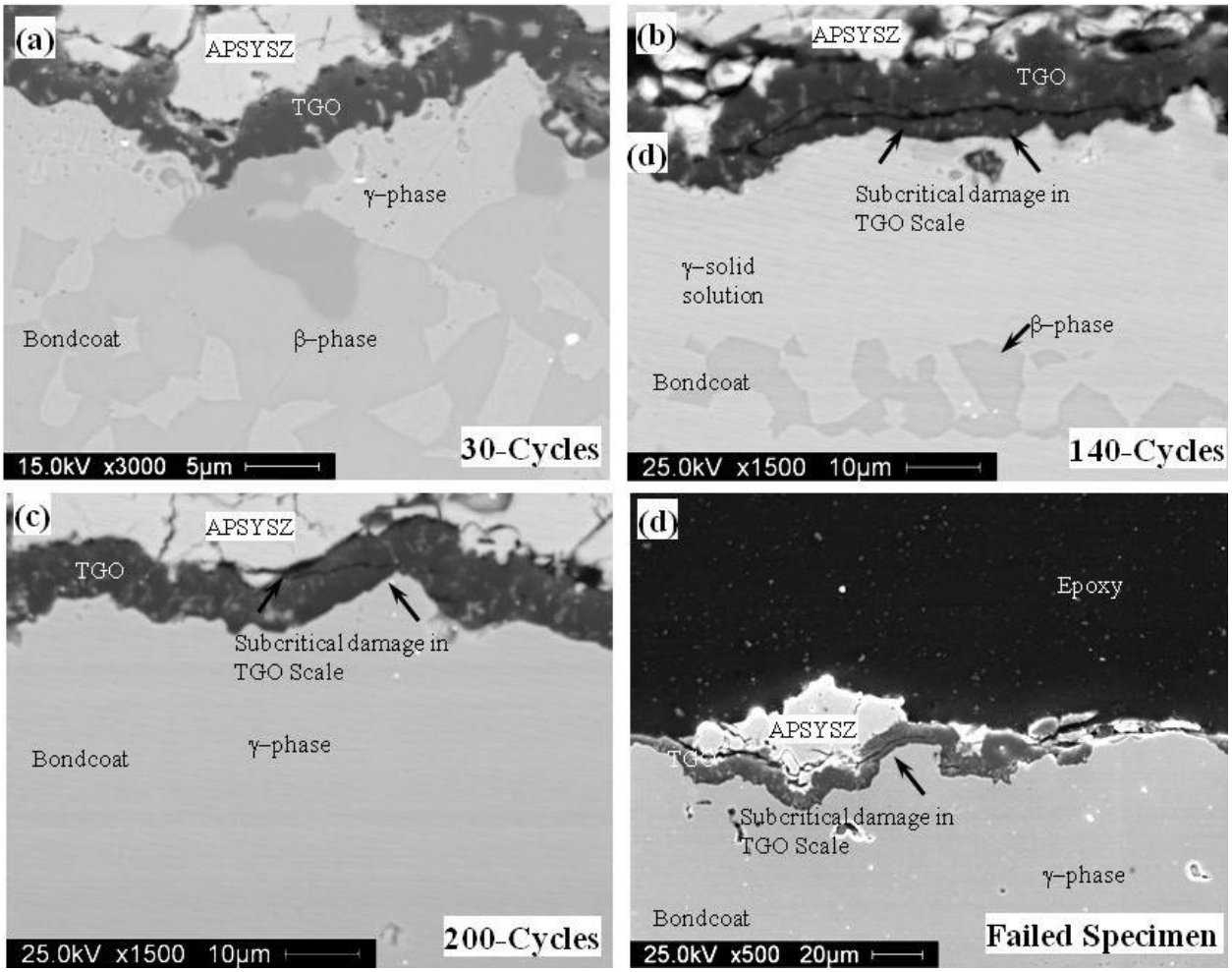

Figure 132. Microstructure evolution and damage accumulation in the TGO scale near the bondcoat surface with progressive 1-hour thermal cycles at 1121°C for type-II APS TBCs with LPPS NiCoCrAlY bondcoat.

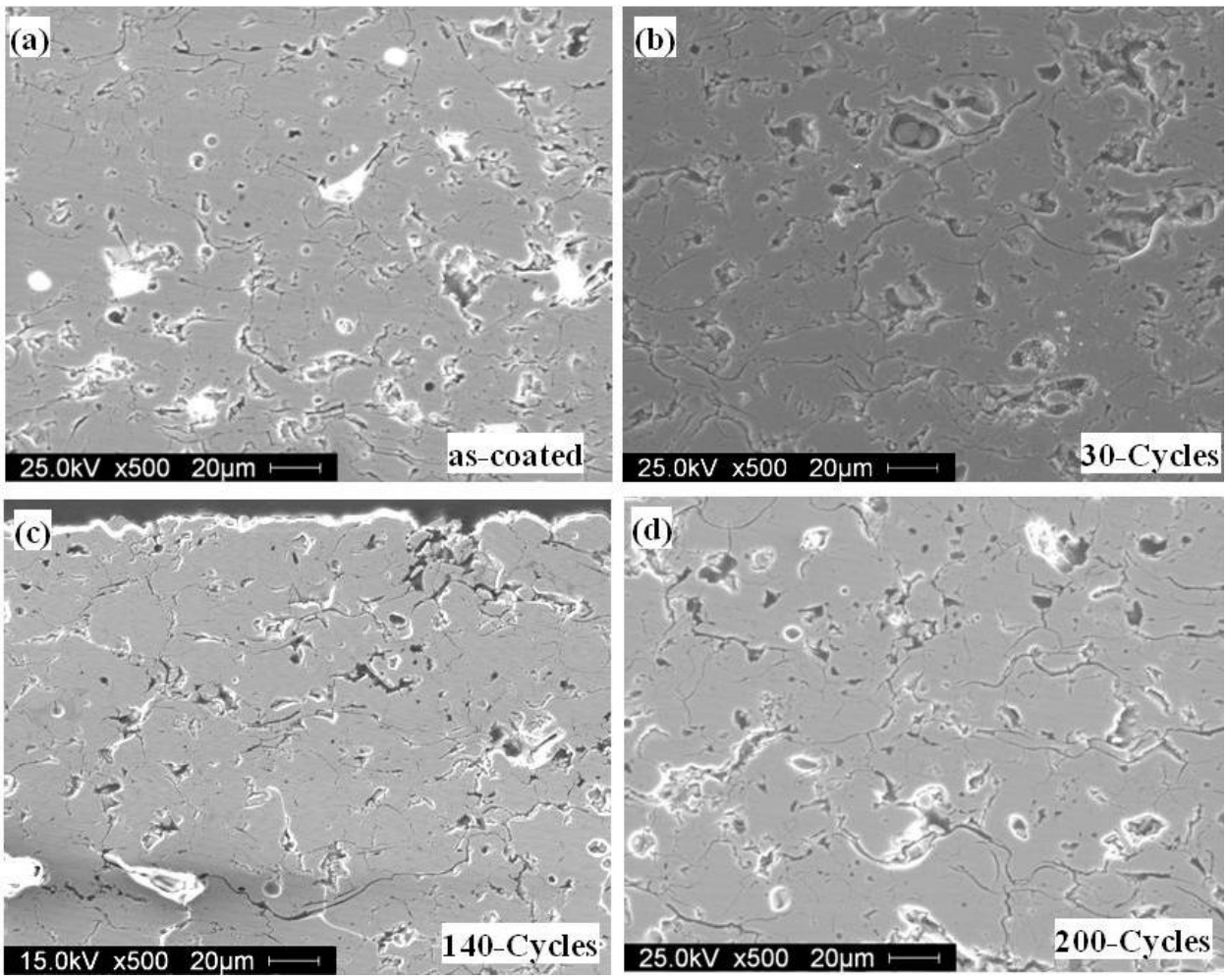

Figure 133. Microstructural observation of YSZ topcoat with progressive thermal cycles for type-II APS TBCs with LPPS NiCoCrAlY bondcoat with progressive 1-hour thermal cycling at 1121°C.

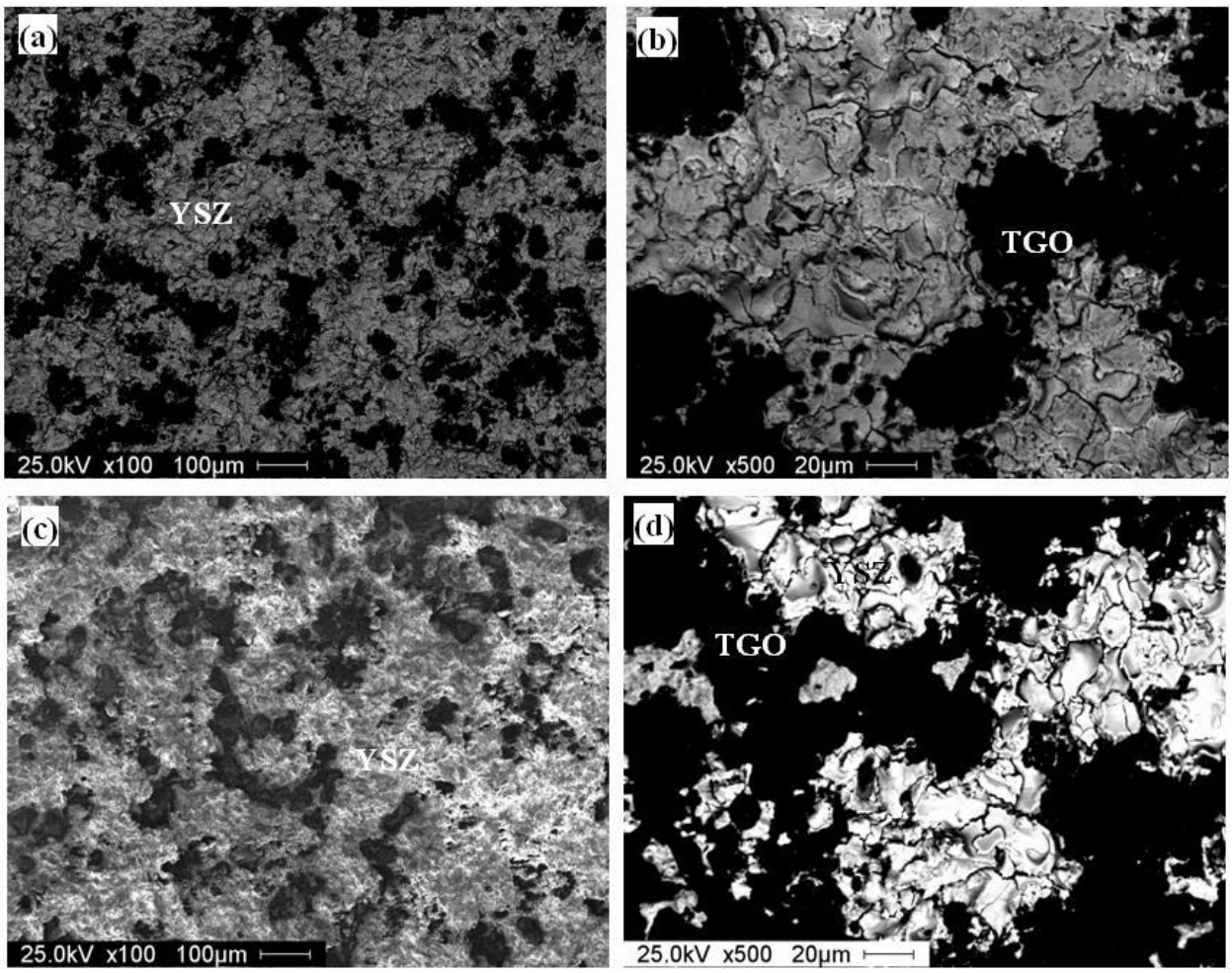

Figure 134. Fractographic observation of type-II APS TBCs with NiCoCrAlY LPPS bondcoat showing constituents on the coating spallation surface 1-hour thermal cycles at 1121°C (a,b) YSZ bottom surface and (c, d) bondcoat surface.

4.8.2 Microstructural Assessment for APS TBCs after 10-hour Thermal Cycling

Typical backscatter electron micrographs for type-I APS TBCs as a function of thermal cycling is shown in Figure 135. In addition to the growth of the TGO, internal parallel to the YSZ/bondcoat interface, as shown in Figure 135. With progressive thermal cycling the YSZ topcoat showed densification and micro-cracking as shown in Figure 136.

An initial increase in impedance response shown in Figure 104 is from the growth of the TGO shown in Figure 135 and densification of ceramic topcoat as shown in Figure 136. The electrical component R_{YSZ} did increase initially with sintering of the YSZ and then decreased due to the micro-cracking within the YSZ coating. The C_{YSZ} did not vary significantly with thermal cycling, and its dependent on dielectric layer capacitance will be discussed later in section 5.4.1.

In case of TGO, as shown in Figure 108 and Figure 109, R_{TGO} and C_{TGO} did increase and decrease even after failure respectively from as-coated condition because of the TGO growth. At failure inverse trend as reported earlier [89] was not observed for type-I APS TBCs because the failure occurred within the YSZ and at the YSZ/TGO interface without exposing the bondcoat. This can be seen in Figure 135 (e,f).

For type-I APS TBCs with 10-hour thermal cycling, the YSZ remained as one piece at failure and delaminated from the bondcoat surface. Cross-sectional micrograph from a failed sample after 10-hour thermal cycling is shown in Figure 135(e,f). The micro-constituents on the YSZ surface and bondcoat surface is shown in Figure 137. The back surface of the YSZ contained islands of the TGO, and the exposed bondcoat surface consisted of intact YSZ. The fracture for type-I APS TBCs with 10-hour thermal cycling occurred at the YSZ/TGO interface and within the YSZ.

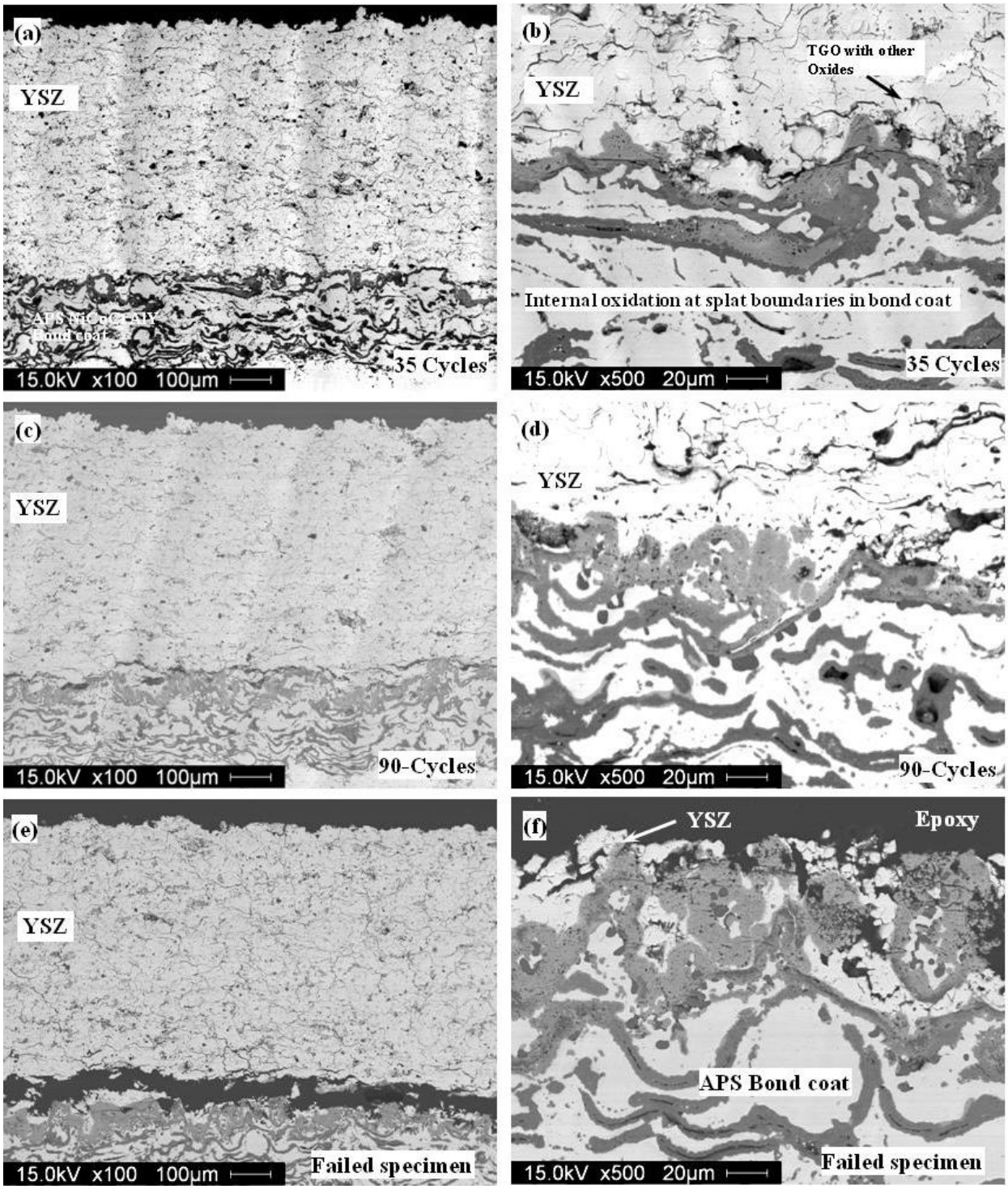

Figure 135. Typical backscatter electron micrographs of type-I APS TBCs with progressive 10-hour thermal cycling at 1121°C.

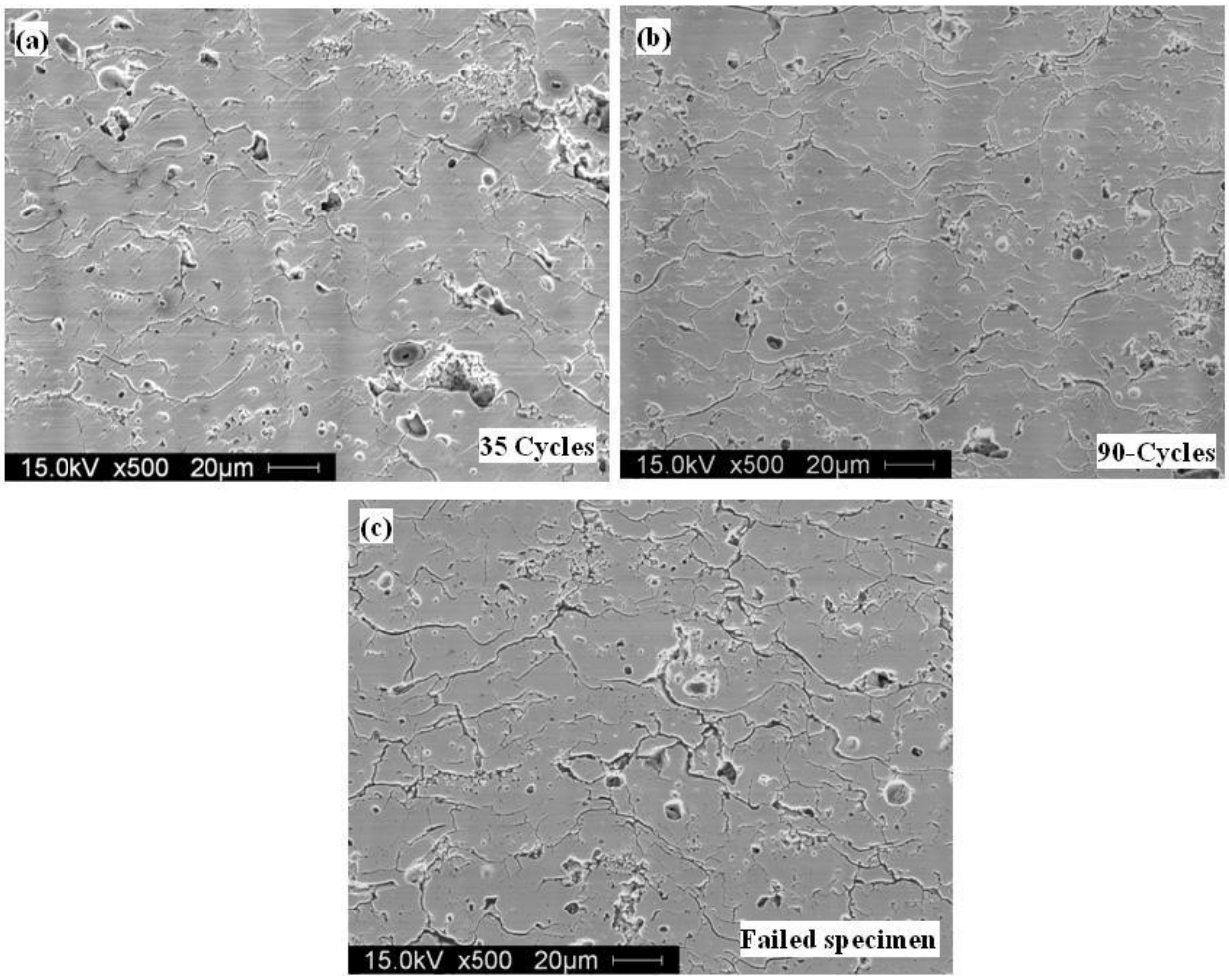

Figure 136. Microstructural observation of ceramic topcoat for type-I APS TBCs with progressive 10-hour thermal cycling at 1121°C.

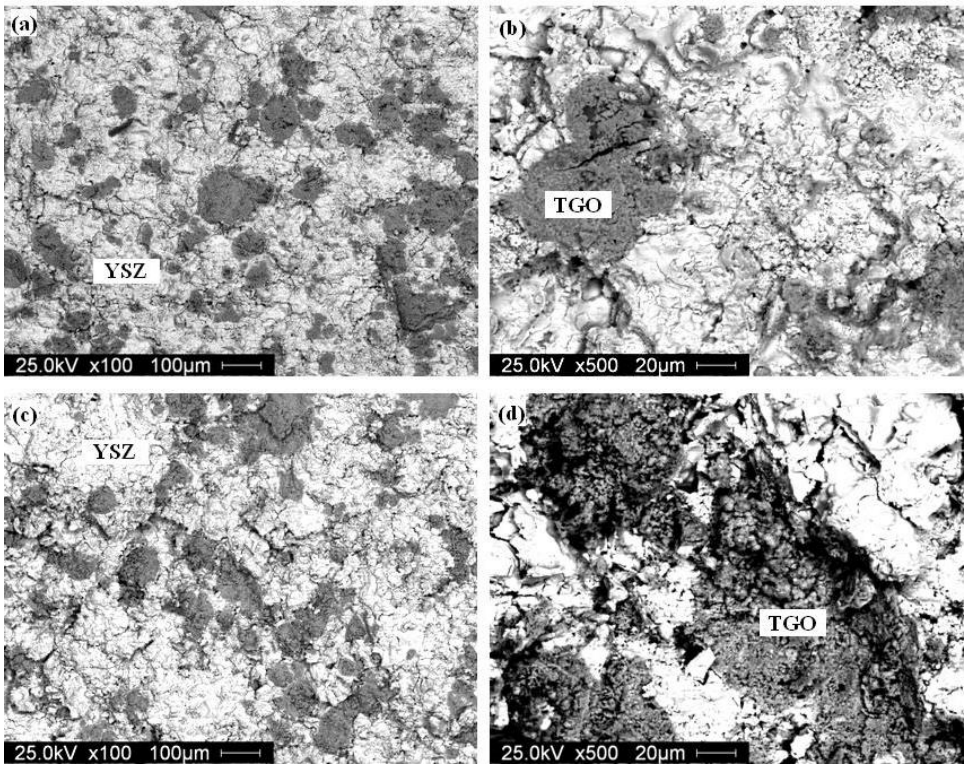

Figure 137. Fractographic observation of type-I APS TBCs with NiCoCrAlY APS bondcoat showing constituents on the coating spallation surface 10-hour thermal cycles at 1121°C (a,b) YSZ bottom surface and (c, d) bondcoat surface

Typical backscatter electron micrographs for type-II APS TBCs as a function of thermal cycling is shown in Figure 138. A uniform growth of the TGO scale at the interface between the bondcoat and ceramic topcoat is observed. With progressive thermal cycling, the YSZ topcoat showed densification and micro-cracking as shown in Figure 139.

An initial increase in impedance response during 10-hour thermal cycles as shown in Figure 110 is from the TGO growth as shown in Figure 138 and densification of ceramic topcoat as shown in Figure 139. The electrical component R_{YSZ} increased with thermal cycling due to sintering and then decreases due to micro-cracking. The R_{TGO} and C_{TGO} increased and decreased respectively even after failure and this is presumably due to the TGO growth.

At failure, for type-II APS TBCs after 10-hour thermal cycling, the YSZ remained as one piece and delaminated from the bondcoat surface. Cross-sectional micrograph after failure is shown in Figure 138(e,f). The micro-constituents on the fracture surface after failure is presented in Figure 140. The bottom surface of the spalled YSZ contained islands of the TGO, and the exposed surface was covered with the TGO and YSZ. Fracture for type-II APS TBCs with 10-hour thermal cycling occurred at the YSZ/TGO interface and within the YSZ.

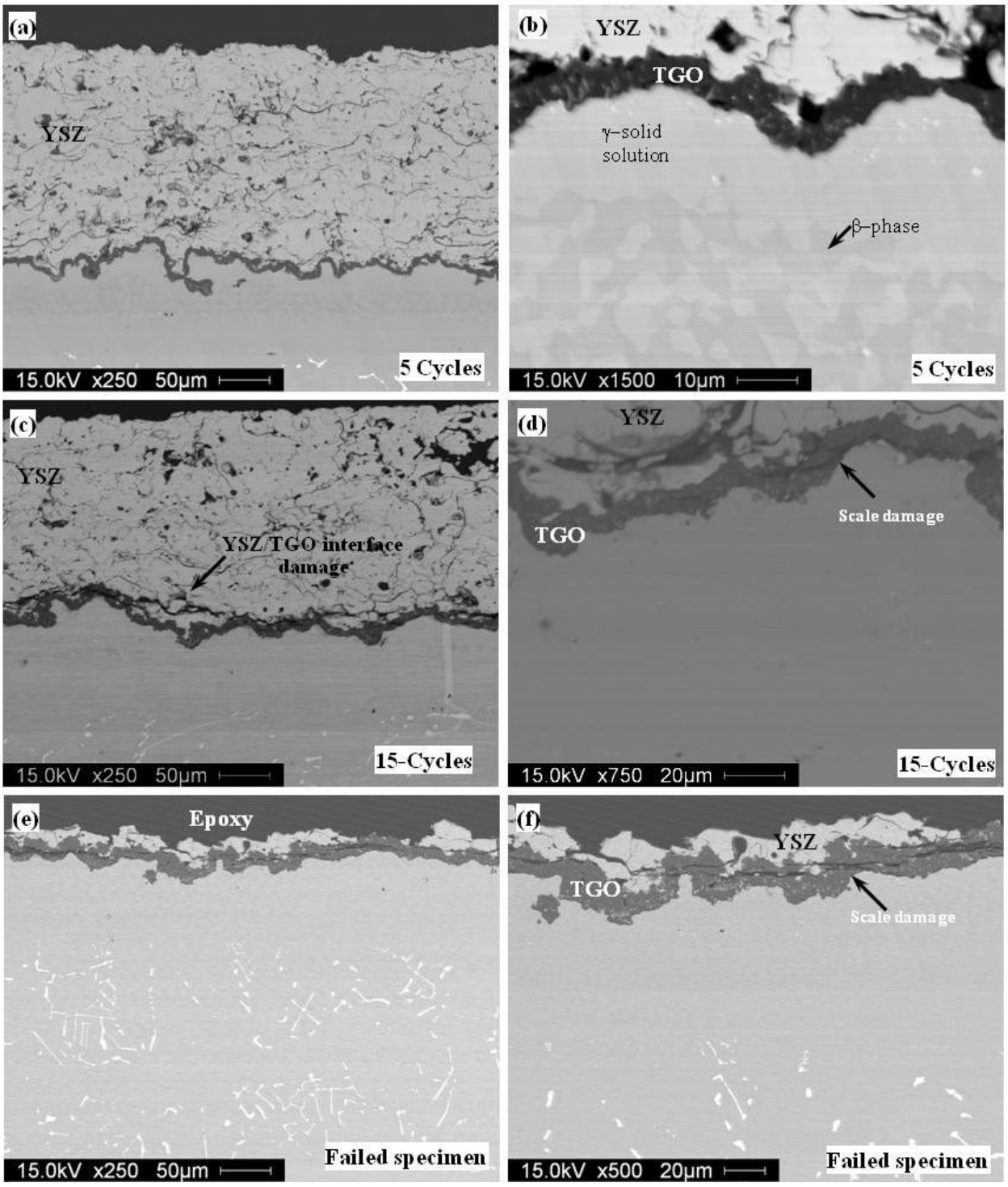

Figure 138. Backscatter electron micrograph of type-II APS TBCs with LPPS NiCoCrAlY bondcoat as function of 10-hour thermal cycling at 1121°C.

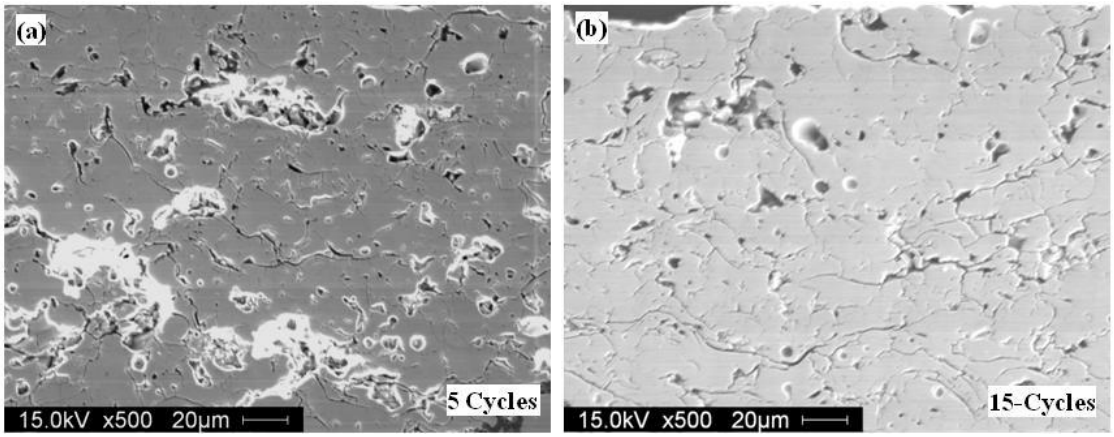

Figure 139. Ceramic topcoat microstructure development in type-I APS TBCs with LPPS NiCoCrAlY bondcoat during 10-hour thermal cycles 1121°C.

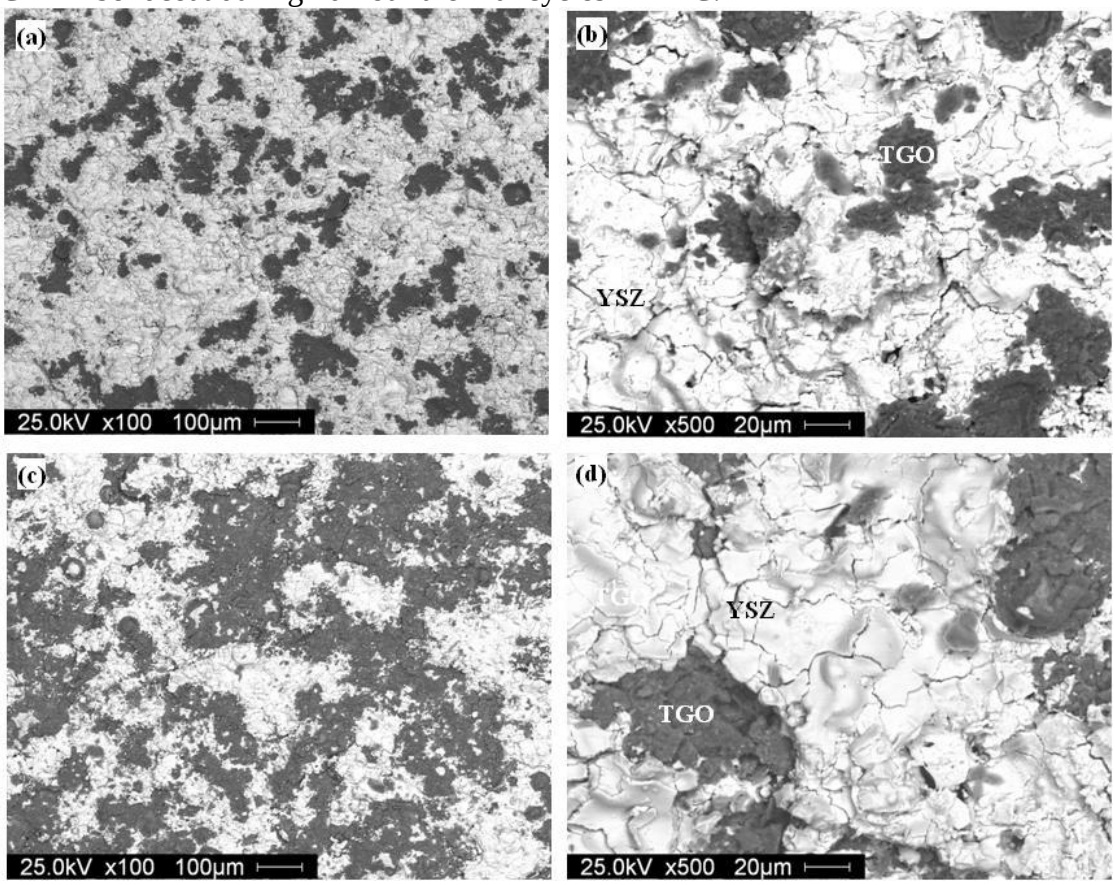

Figure 140. Fractographic observation of type-II APS TBCs with NiCoCrAlY LPPS bondcoat showing constituents on the coating spallation surface after 10-hour thermal cycles at 1121°C (a,b) YSZ bottom surface and (c, d) bondcoat surface.

4.8.3 Microstructural Assessment of APS TBCs after 50-hour Thermal Cycling

Typical backscatter electron micrograph from type-I APS TBCs at 50% lifetime is shown in Figure 141. In addition to the TGO growth, internal oxidation of bondcoat was observed. These observations are similar to those tested using 1 and 10-hour thermal cycles.

The impedance response overlapped the as-received condition as shown in Figure 105. Initially sintering takes place at high temperature but upon cooling micro-cracking from sintering YSZ along the splat boundaries is prominent. Hence, electrical component R_{YSZ} did not show a significant increase since micro-cracking may be more prominent than sintering. In the case of TGO, as shown in Figure 108 and Figure 109, R_{TGO} and C_{TGO} increased from as-coated condition because of the TGO growth with thermal cycling.

The APS YSZ delaminated in one piece from the bondcoat surface. Fracture surface investigation on the spalled YSZ surface and exposed surface is shown in Figure 142. Micro-constituents on the back surface of YSZ consisted of YSZ and islands of TGO, while bondcoat surface consisted of the TGO islands and of YSZ. For type-I APS TBCs after 50-hour thermal cycling, fracture occurred at the YSZ/TGO interface and within the YSZ.

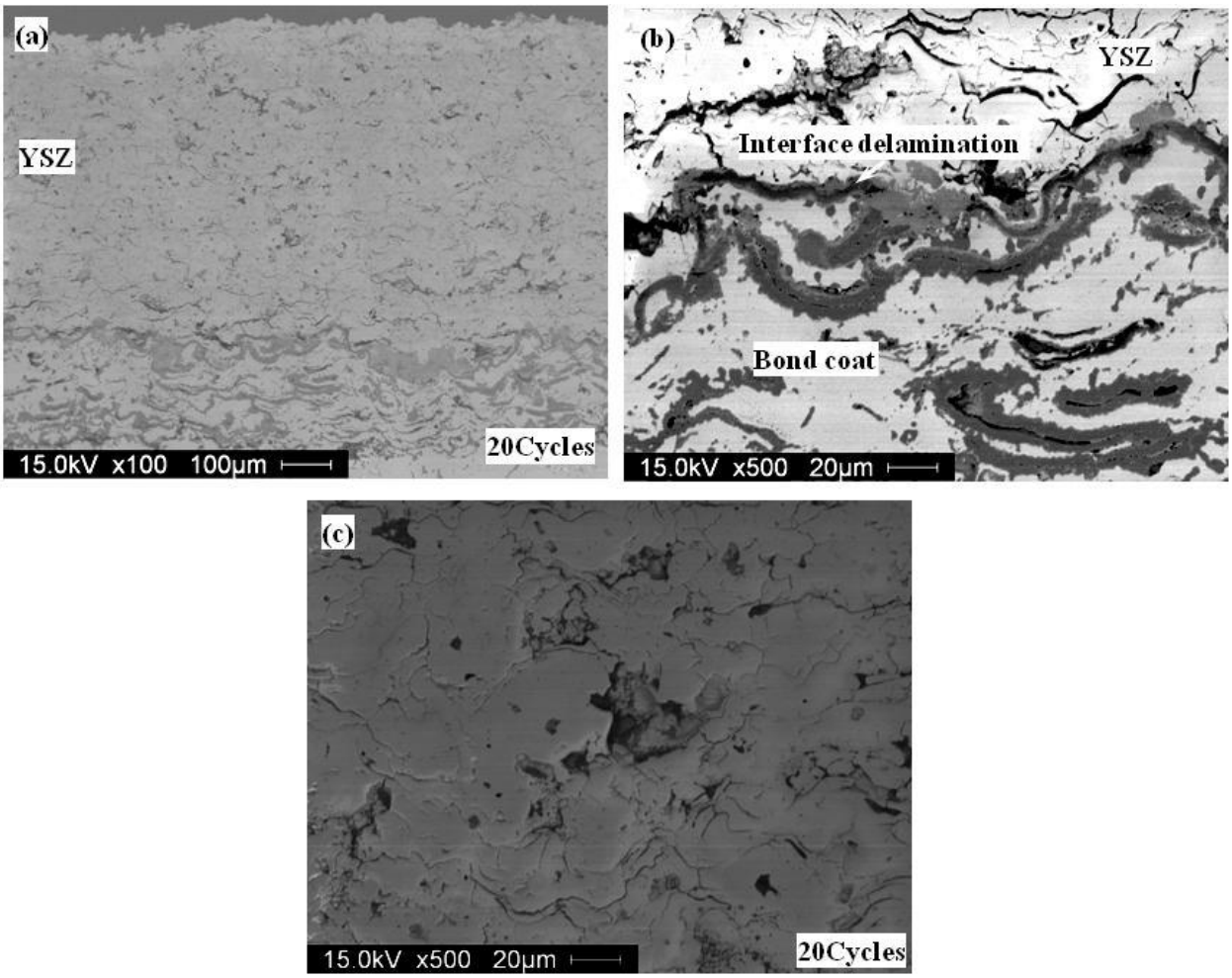

Figure 141. Typical backscatter electron micrographs for type-I APS TBCs after 50-hour thermal cycling at 1121°C (a,b) at 50% lifetime of TBCs (c) sintering of the YSZ at 50% lifetime.

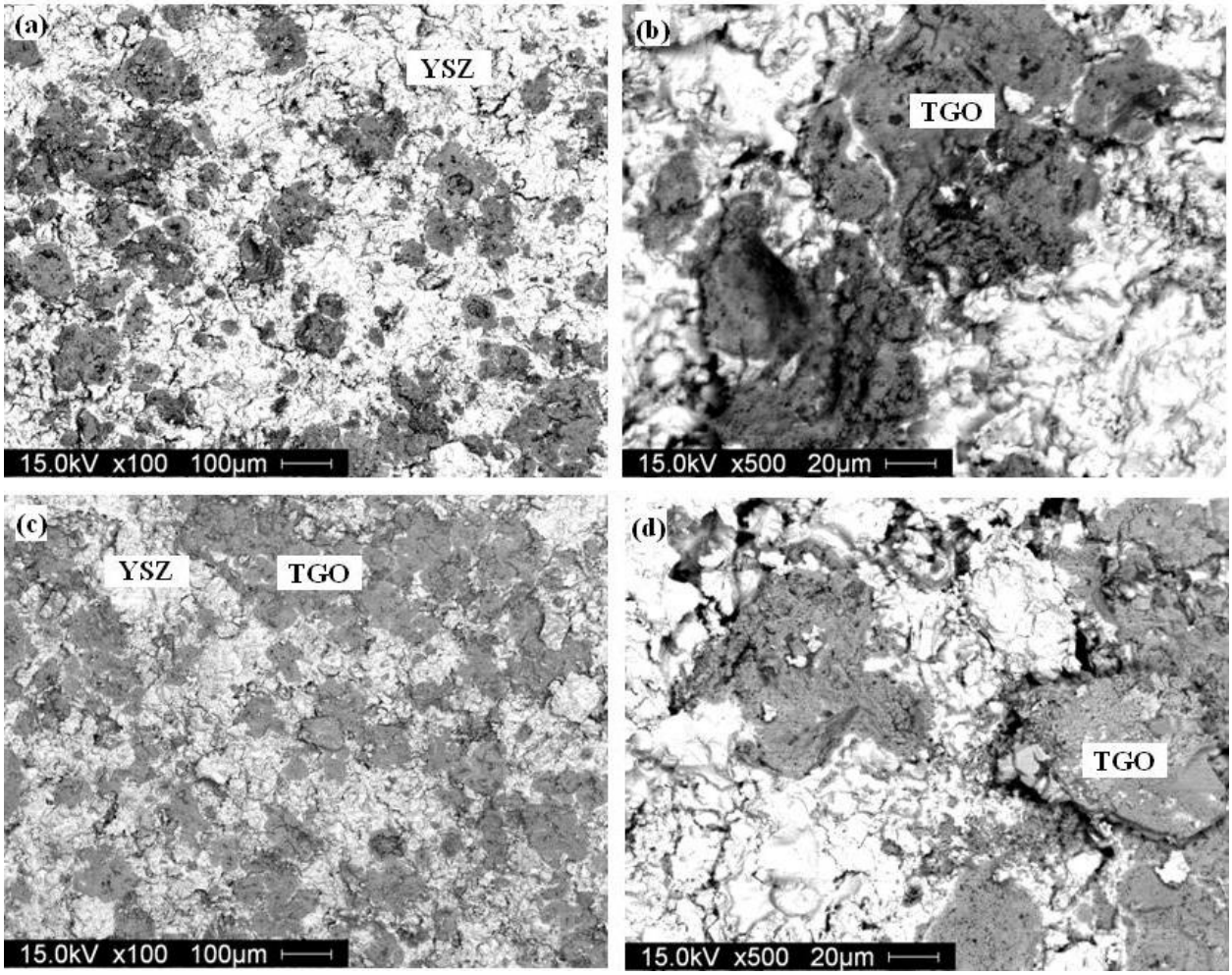

Figure 142. Fractographic observation of type-I APS TBCs with NiCoCrAlY APS bondcoat showing constituents on the coating spallation surface after 50-hour thermal cycles at 1121°C (a,b) YSZ bottom surface (c, d) and bondcoat surface.

4.9 Microstructural assessment of EB-PVD TBCS

4.9.1 Microstructural Assessment of EB-PVD TBCs after 1-hour Thermal Cycling

Microstructural development of type-III EB-PVD TBCs with respect to 1-hour furnace cycle lifetime at various stages of lifetime are shown in Figure 143. A uniform growth of TGO with progressive thermal cycling is clearly observed. With the development of TGO scale there was initial increase in compressive residual stress from PL (Figure 71 and Figure 72) and R_{TGO} increased and C_{TGO} decreased from EIS (Figure 117 through Figure 120). After 50% life time of the type-III as-coated (Ni,Pt)Al bondcoat EB-PVD TBCs, damages were observed within the TGO scale. With the damages within TGO scale there is a evolution of stress-free luminescence from PL (Figure 77), and R_{TGO} and C_{TGO} decreased and increased (Figure 119 and Figure 120) repectively.

With progressive 1-hour thermal cycling, the bondcoat surface showed progressive ratcheting/rumpling of the TGO, and damages were observed in the TGO scale at valleys and shoulders of the TGO in the ridge cavities as presented in Figure 144. Figure 144(d) also shows two layers within the TGO scale with the top layer consisting of Zr and Y particles mixed in Al_2O_3 scale. This layer is referred as the mixed oxide zone. At failure bondcoat surface consisted of TGO and bottom of YSZ surface consisted of TGO as presented in Figure 145. Facture occurred at the YSZ/TGO interface with little to no bondcoat surface exposed as seen in Figure 145.

Other observations like phase transformation of (Ni,Pt)Al bondcoat with thermal cycling localized to the ridge cavities is shown in Figure 143 (d,f).

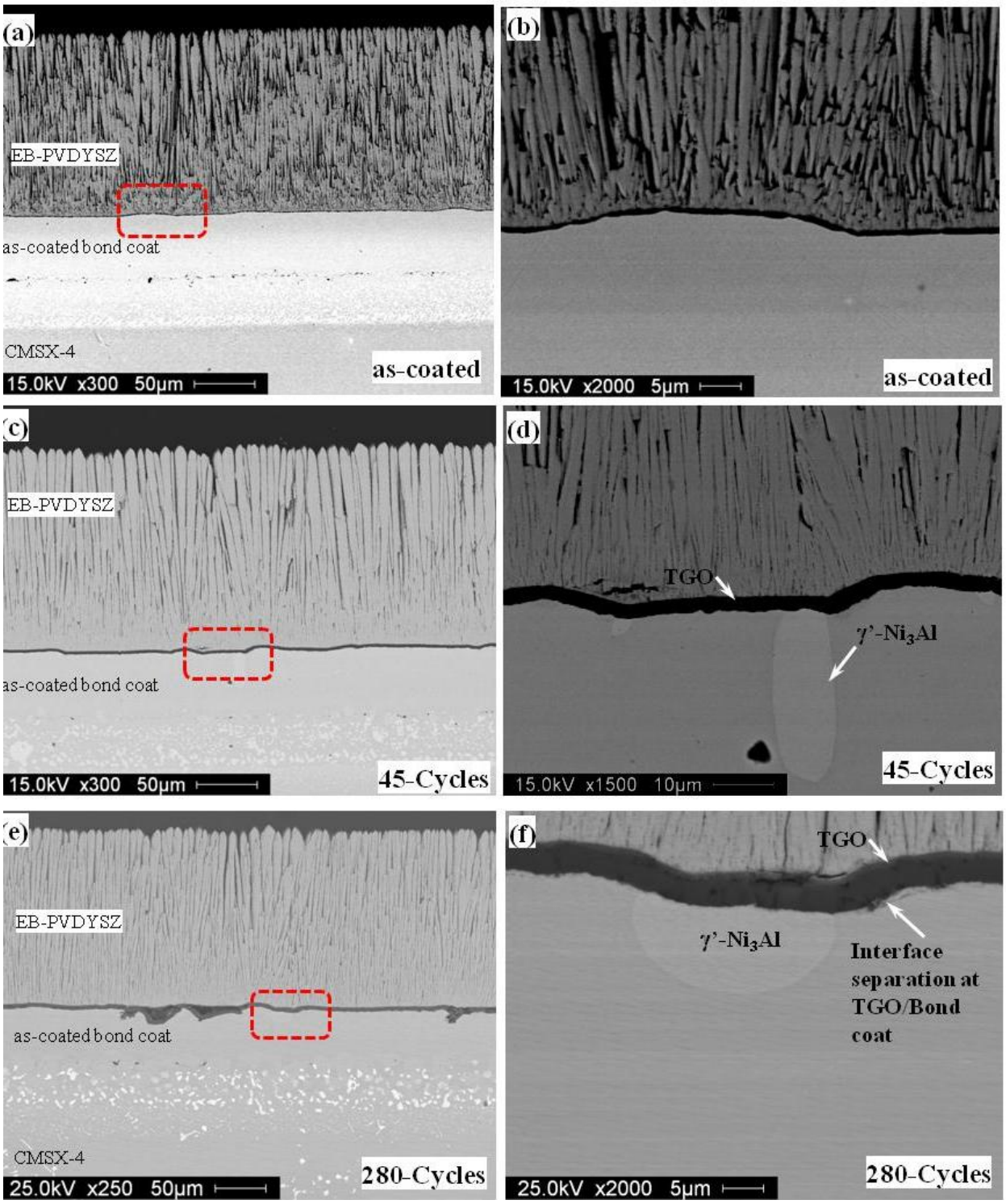

Figure 143. Typical backscatter electron micrographs of type-III TBCs with as-coated (Ni, Pt)Al bondcoat and CMSX-4 substrate as a function of 1-hour cycling at 1121°C.

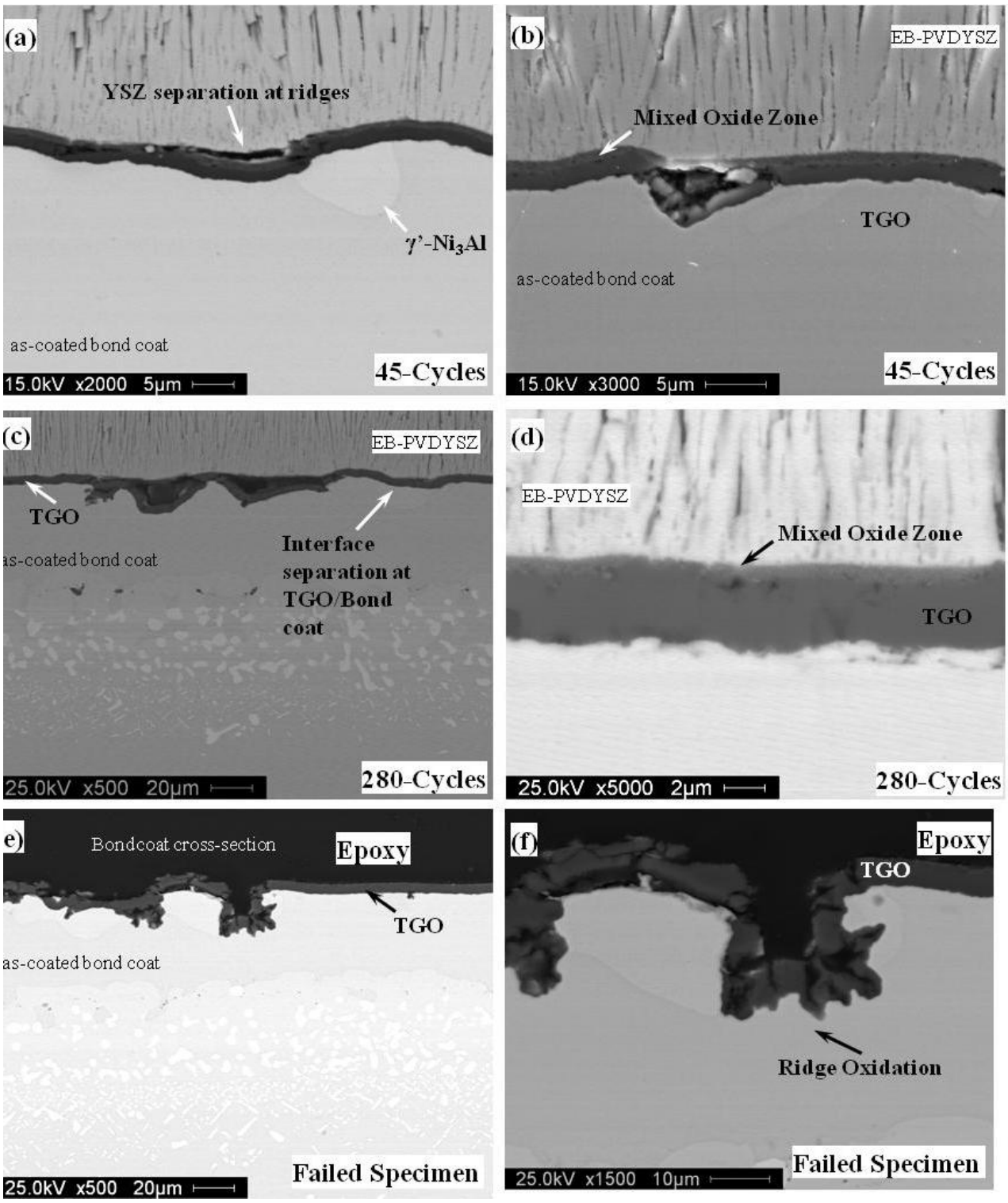

Figure 144. Sub-critical damages of the TGO/bondcoat interface observed by backscatter electron micrographs with progressive 1-hour thermal cycling for type-III TBCs with as-coated (Ni, Pt)Al bondcoat.

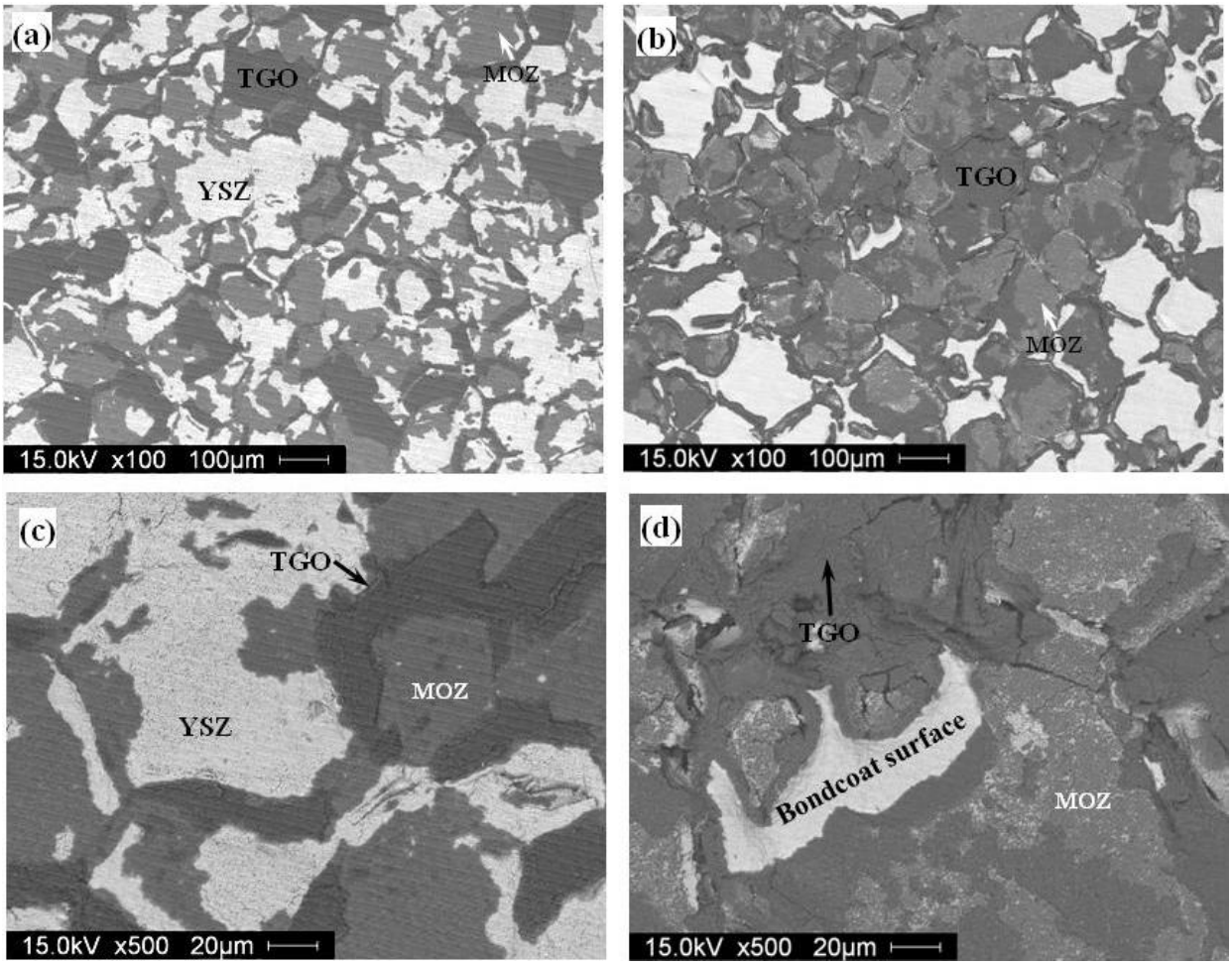

Figure 145. Microstructural observation of fracture surface for type-III TBCs with as-coated (Ni, Pt)Al bondcoat on CMSX-4 showing critical constituents for 1-hour thermal cycling at 1121°C and fracture propagation interface (a,c) YSZ bottom surface (b,d) bondcoat surface.

Microstructural development of type-IV EB-PVD TBCs as a function of 1-hour furnace cycle lifetime are shown in Figure 146. A uniform growth of the TGO with thermal cycling is clearly observed. The initial increase in the compressive residual scale reported in Figure 83, and increase in R_{TGO} and decrease in C_{TGO} is from the growth of TGO with cyclic oxidation. At 50% life time of the type-IV EB-PVD TBCs with grit blasted (Ni,Pt)Al bondcoat, damages were observed within the TGO scale. This is related to the gradual shift in luminescence as shown in

Figure 82 resulting in a decrease of compressive residual stress. From EIS these damages are seen as a change in the trend that R_{TGO} decreases and C_{TGO} increases.

With progressive 1-hour thermal cycling, Figure 147 shows the bondcoat surface ratcheting. The final fracture surface is presented in Figure 148. The micro-constituents consisted of the TGO on the backside of the YSZ surface and the TGO with specks of YSZ on the bondcoat surface. Fracture occurred at the YSZ/TGO interface with initial damages at the YSZ/TGO interface observed earlier in the thermal cycling. At failure, TGO resistance continued to decrease because the fracture surface showed intact TGO on bondcoat surface. The TGO capacitance showed an abrupt increase relating to the exposure of bare metal at failure.

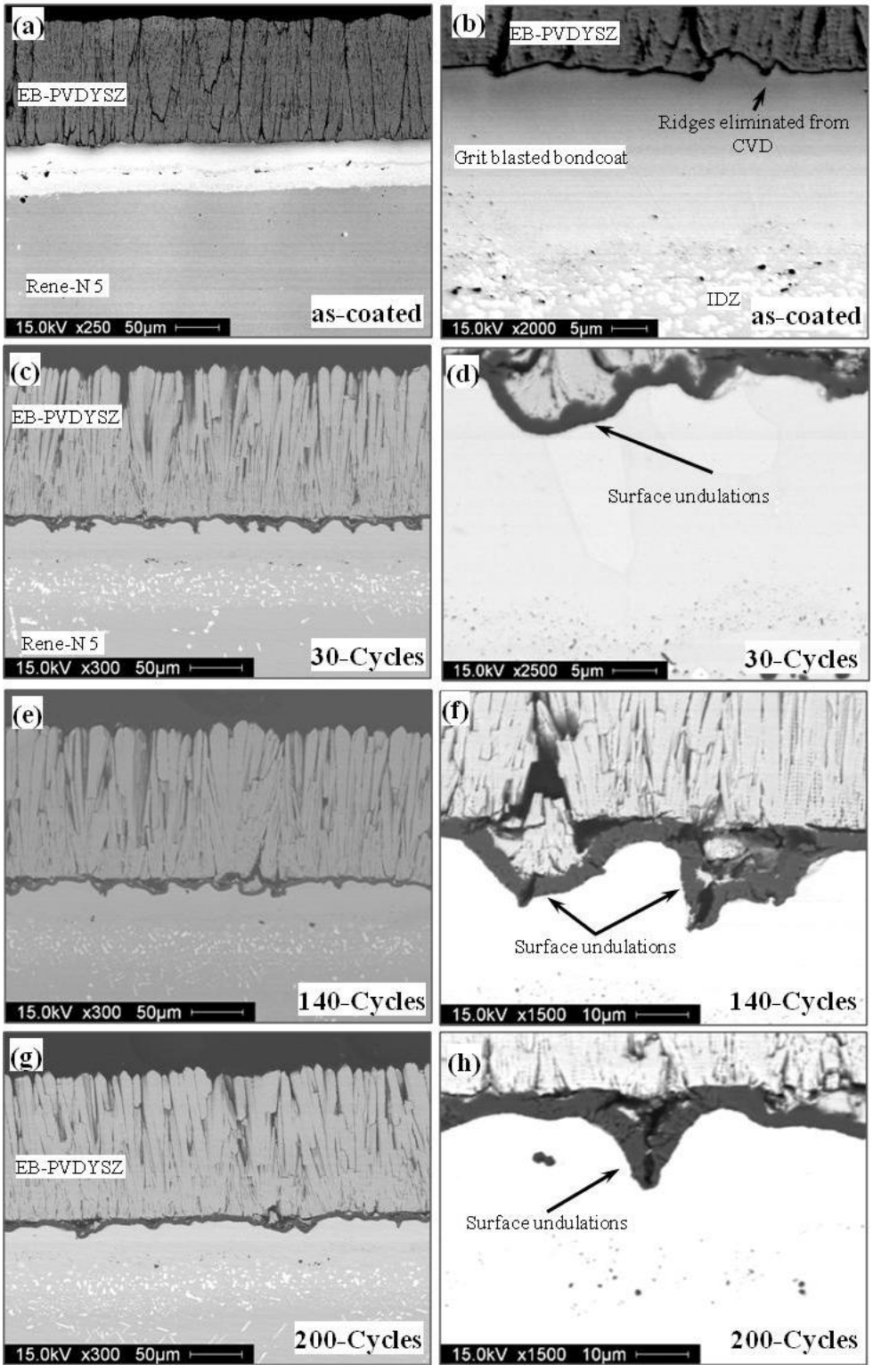

Figure 146. Typical backscatter electron micrographs of microstructure evolution in type-IV EB-PVDs with grit blasted (Ni, Pt)Al bondcoat as a function of 1-hour thermal cycling at 1121°C.

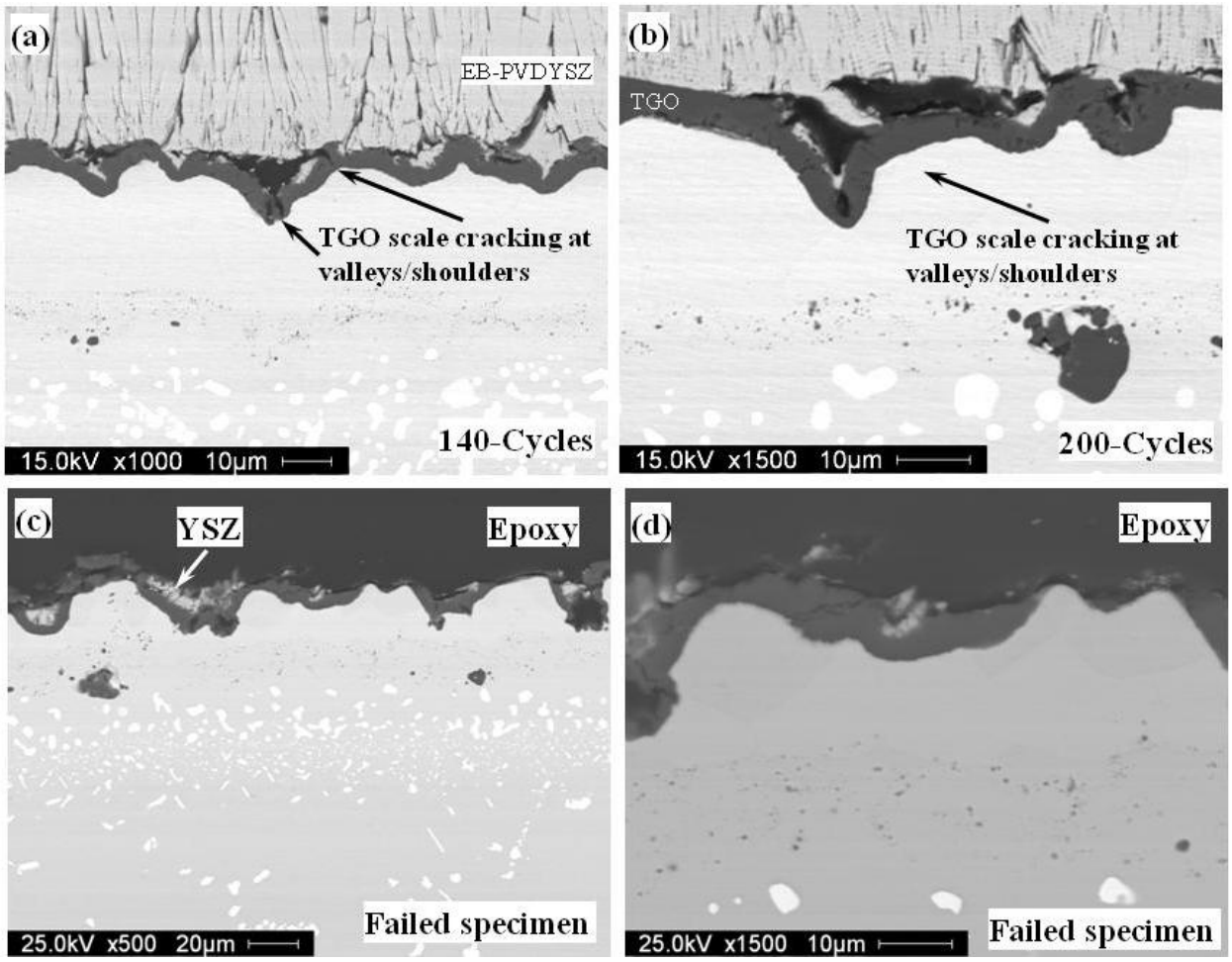

Figure 147. Sub-critical damages of the TGO/bondcoat interface observed by backscatter electron micrograph with progressive 1-hour thermal cycling for type-IV EB-PVD TBCs with grit blasted (Ni, Pt)Al bondcoat.

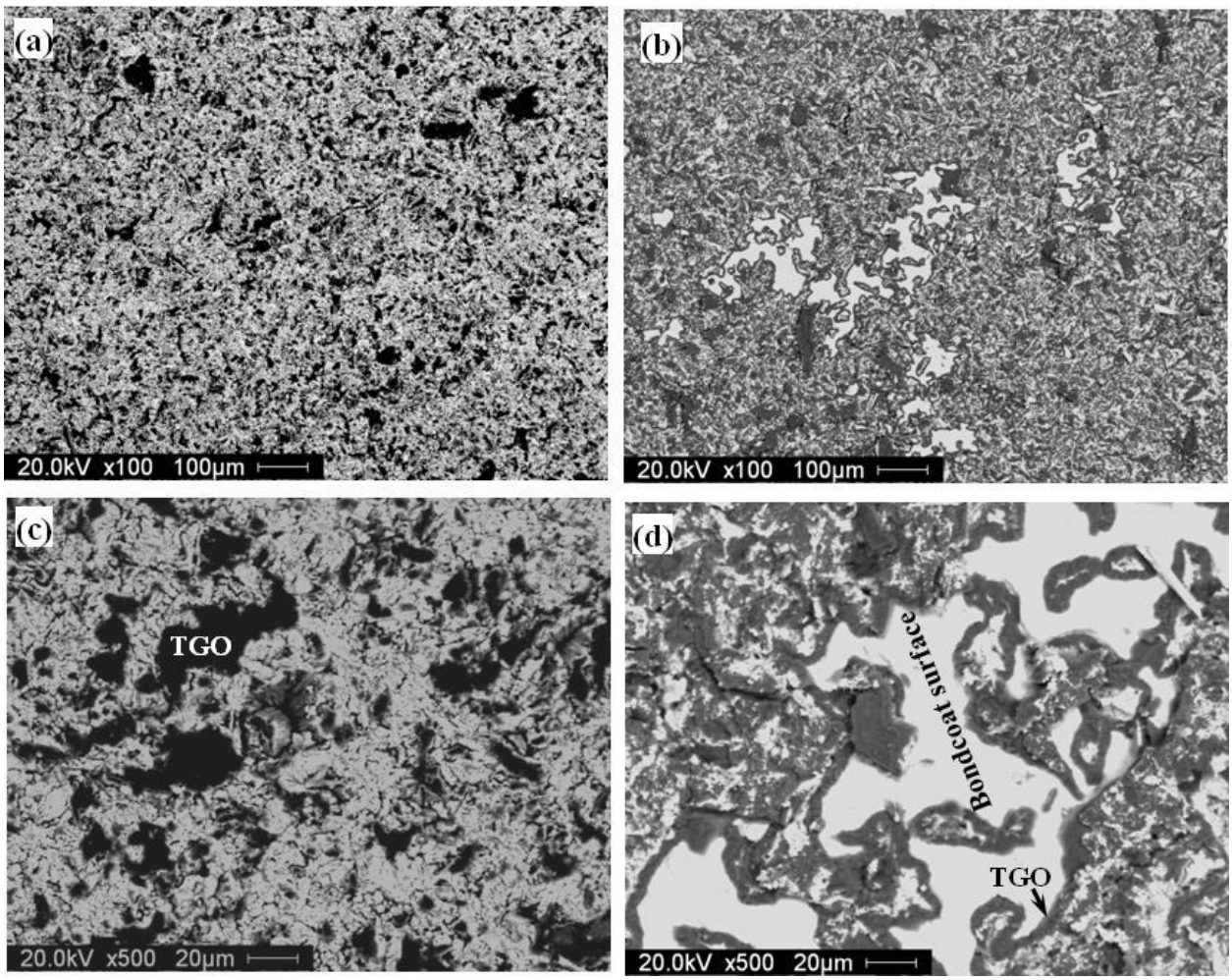

Figure 148. Microstructural observation of fracture surface for type-IV TBCs with grit blasted (Ni, Pt)Al bondcoat on Rene-N5 showing critical constituents for 1-hour thermal cycling at 1121°C and fracture propagation interface (a,c) YSZ bottom surface (b,d) bondcoat surface.

4.9.2 Microstructural Assessment of EB-PVD TBCs after 10-hour Thermal Cycling

Microstructural development of type-III EB-PVD TBCs as function of 10-hour furnace cycling are presented in Figure 149. A uniform growth of the TGO scale is presented. The initial increase in the compressive residual as reported in Figure 86 is from the growth of the TGO with cyclic oxidation. With progressive 10-hour thermal cycling, Figure 149 shows that the bondcoat surface rumples/ratchets along with the TGO. Damages were observed in the TGO scale at valleys and shoulders of the TGO in the ridge cavities. After 60% life time for type-III EB-PVD TBCs there is a sudden appearance of stress-free luminescence. This sudden appearance in luminescence may be correlated to the sub-critical damages seen at the TGO scale as presented in Figure 149(d).

The micro-constituents on the fractured bondcoat surface consisted of the TGO and exposed bondcoat surface. The YSZ fracture surface could not be examined since the coating fragmented into many small pieces at failure. Fracture occurred at the YSZ/TGO interface but with more bondcoat surface exposed compared to the 1-hour thermal cycling. In Figure 150, after failure the fracture surface showed TGO surface consisted of two layers with the top layer consisting of Zr and Y particles mixed in Al_2O_3 scale. This layer is referred as the mixed oxide zone (MOZ).

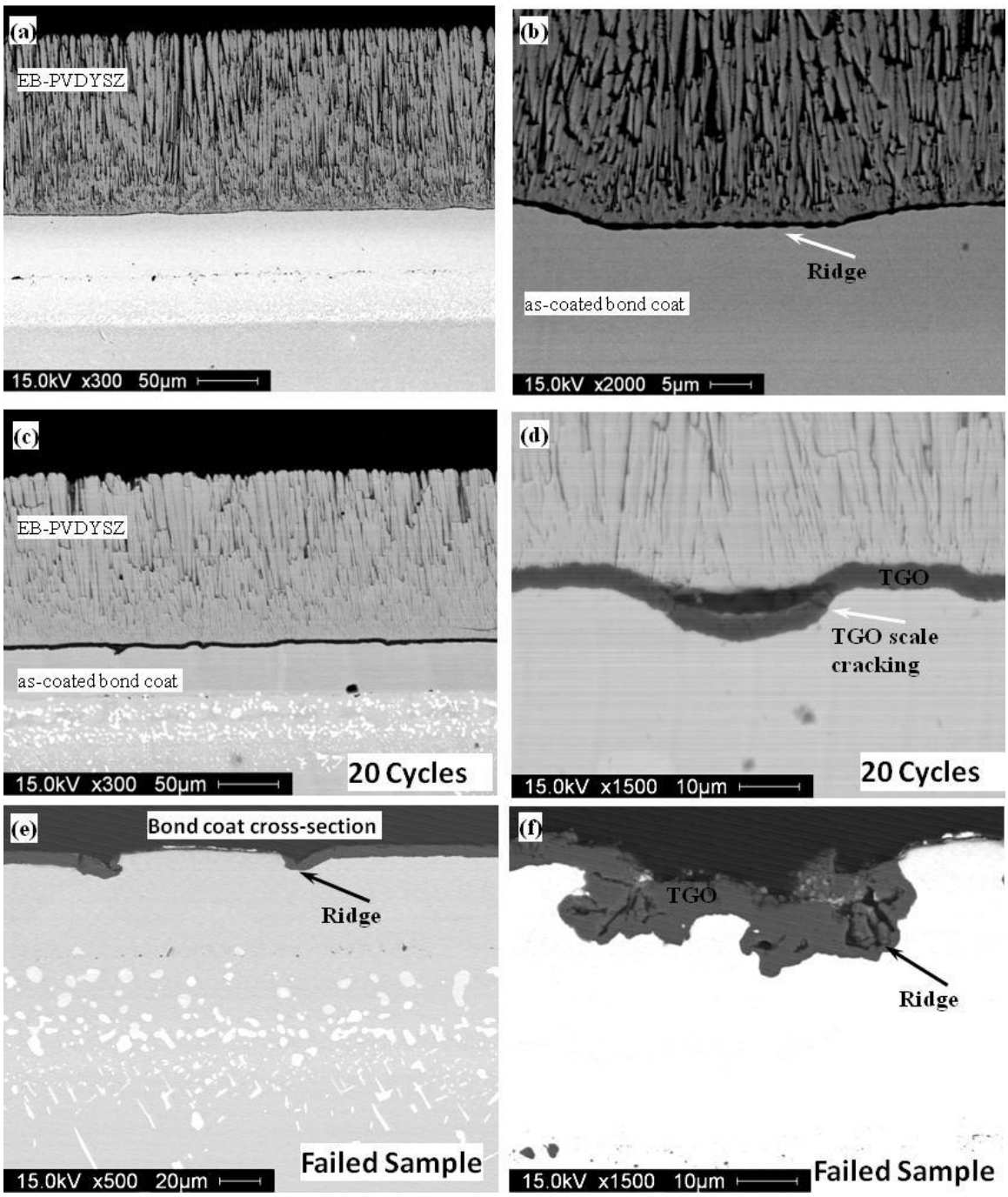

Figure 149. Typical backscatter electron micrograph of type-III TBCs with as-coated (Ni, Pt)Al bondcoat as function of 10-hour thermal cycling at 1121°C.

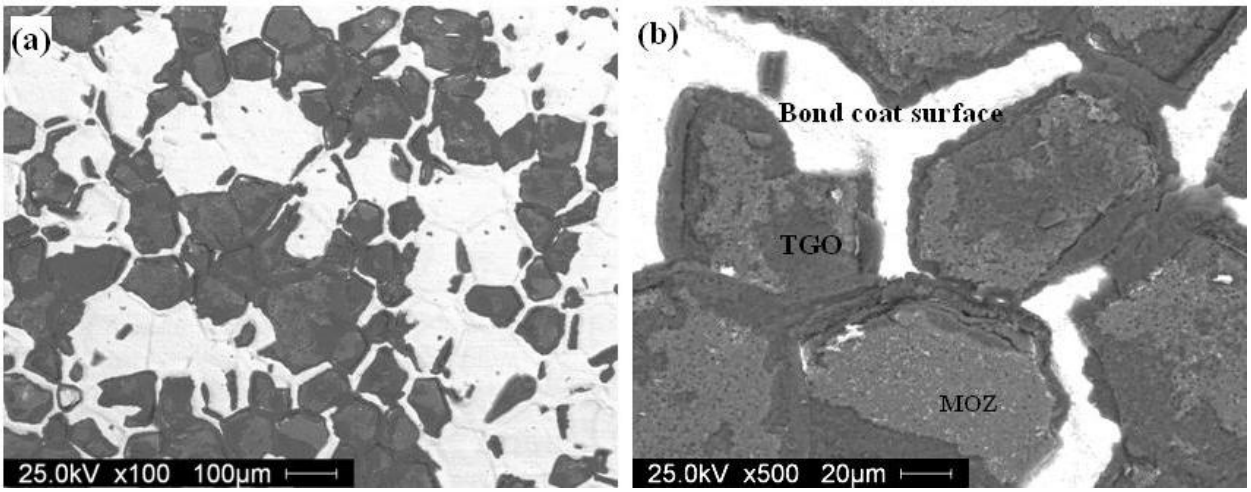

Figure 150. Microstructural observation of bondcoat surface for type-III TBCs with as-coated (Ni, Pt)Al bondcoat on CMSX-4 showing critical constituents after 10-hour thermal cycling at 1121°C.

Microstructural development of type-IV EB-PVD TBCs as a function of 10-hour furnace cycling at 1121°C is shown in Figure 151. A uniform growth of the TGO scale was observed. With progressive 10-hour thermal cycling, the bondcoat surface showed progressive increase in surface undulations along with TGO similar to 1-hour thermal cycling. However, damages as observed earlier with 1-hour thermal cycling were not observed during the 10-hour thermal cycling. The compressive residual stress remained constant throughout 10-hour thermal cycling without gradual shift in luminescence as observed for 1-hour thermal cycling.

Aforementioned, buckling of ceramic topcoat was observed on this type of TBCs and the final fracture surface is shown in Figure 152. Fracture path/plane was near vicinity of the TGO/bondcoat interface with some bondcoat surface exposure. Some residual YSZ coatings were also observed partly due to the presence of MOZ.

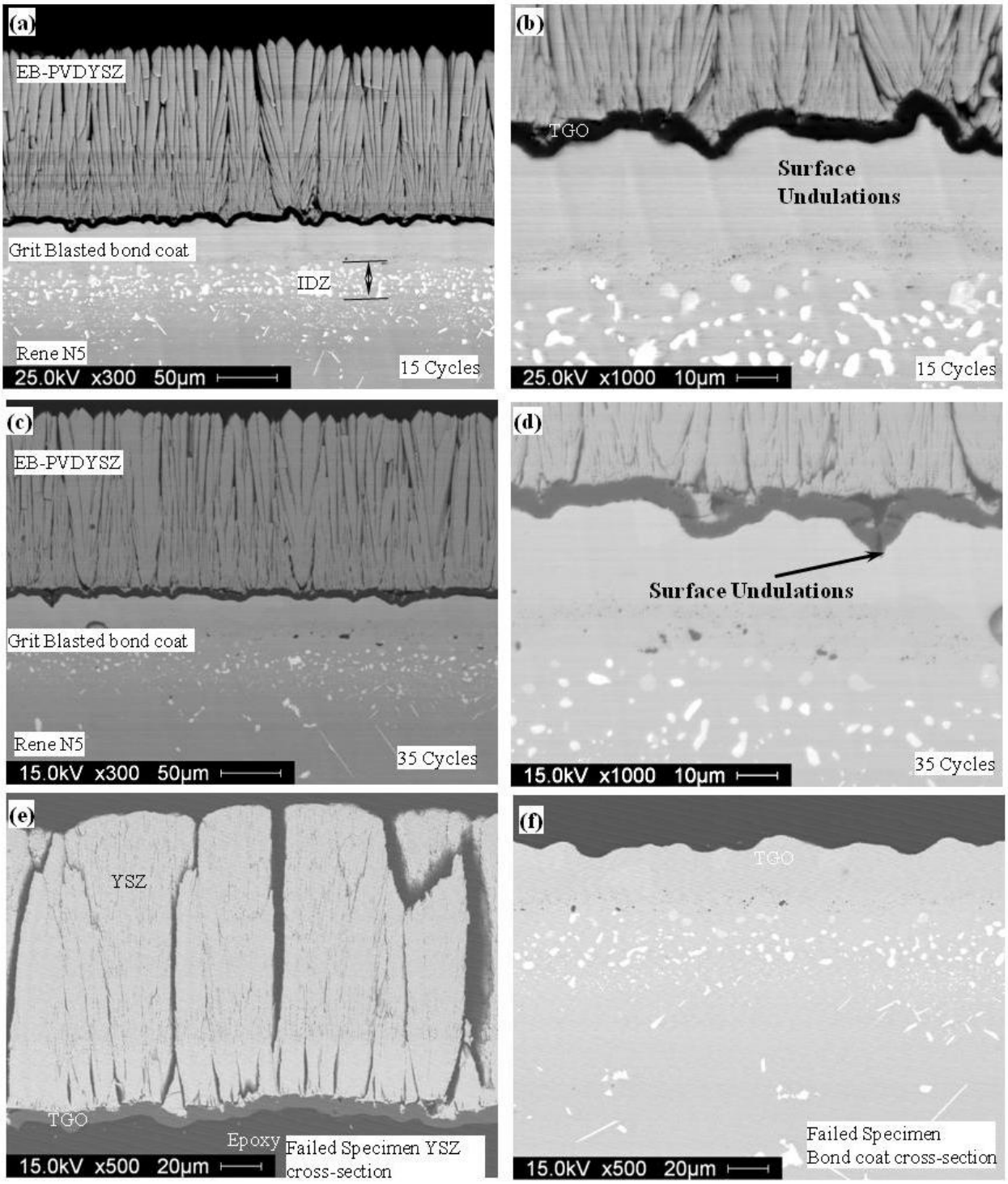

Figure 151. Typical backscatter electron micrograph of type-IV EB-PVD TBCs with grit blasted (Ni, Pt) Al bondcoat as a function of 10-hour thermal cycling at 1121°C.

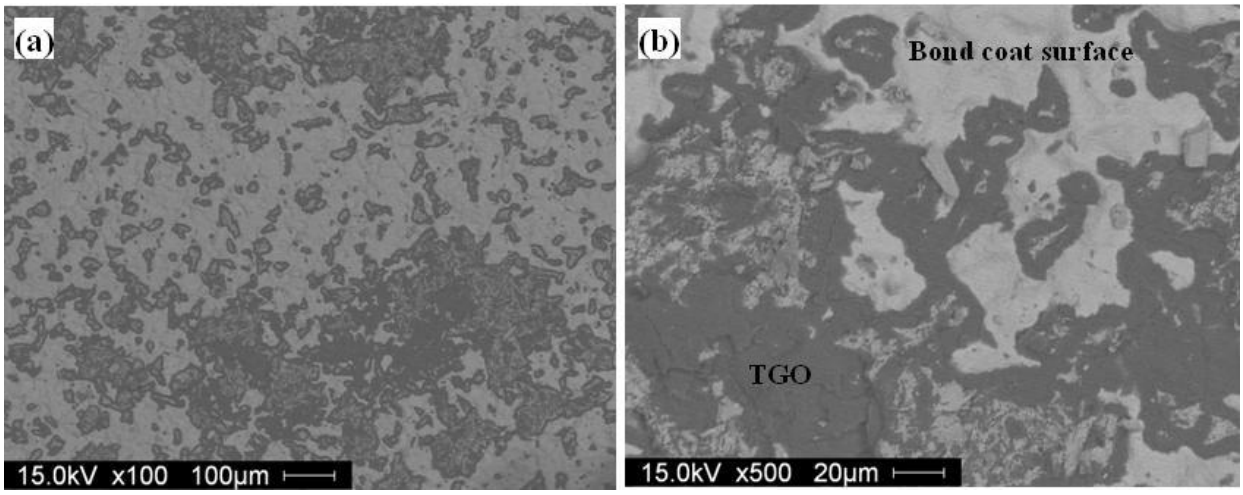

Figure 152. Microstructural observation on bondcoat surface for type-IV EB-PVD TBCs grit blasted (Ni, Pt)Al bondcoat showing critical constituents after 10-hour thermal cycling at 1121°C.

4.9.3 Microstructural Assessment of EB-PVD TBCs after 50-hour Thermal Cycling

Microstructural development of type-III EB-PVD TBCs as a function of 50-hour furnace cycling at 1121°C is shown in Figure 153. Development of the TGO with uniform growth until failure was observed. The magnitude of surface undulation in bondcoat was less prominent compared to 1 and 10-hour thermal cycle, but preferential ridge/grain boundary oxidation was still observed. Prominent damages observed during frequent thermal cycling in the TGO scale at valleys and shoulders of the TGO were not observed for 50-hour thermal cycles. From PL there was no emergence of stress-free luminescence and this may relate to the less progressive damage during cyclic oxidation with longer dwell times.

Microstructural observation of failed sample is shown in Figure 153 (e,f). The TGO did spall from the bondcoat surface with YSZ still attached to the TGO. Fracture occurred at the

TGO/bondcoat interface and exposed the bondcoat surface. MOZ was also observed on the bondcoat surface after failure.

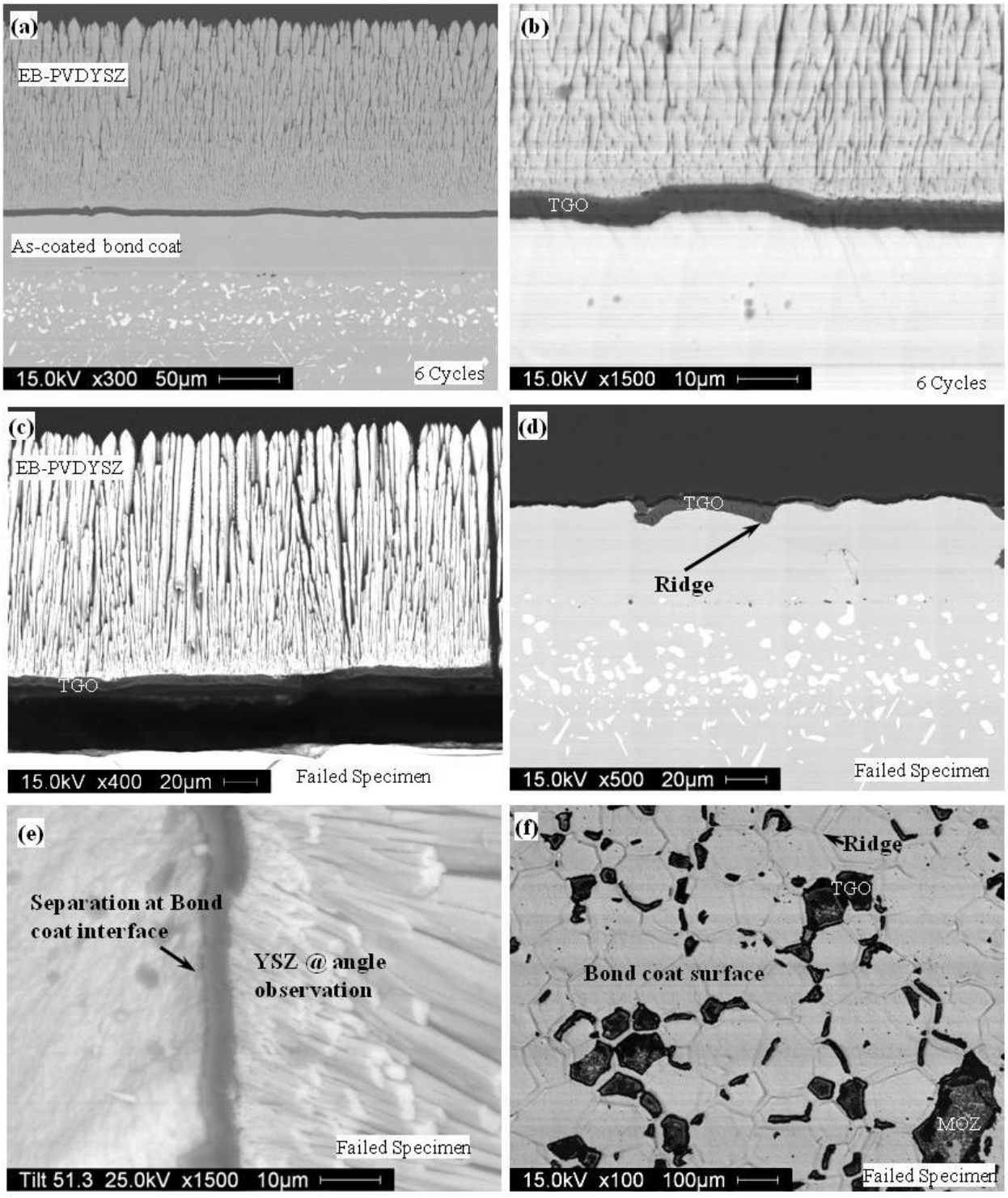

Figure 153. Backscatter electron micrographs for type-III EB-PVD TBCs from 50-hour thermal cycling at 1121°C (a,b) after 6 cycles (c,d) at failure (e) at failure with tilt angle observation showing delamination at the TGO/bondcoat interface and (f) bondcoat surface after failure.

Microstructural development of type-IV EB-PVD TBCs as a function of 50-hour furnace thermal cycling is shown in Figure 154. A uniform growth of the TGO scale with thermal cycling until failure was observed. Limited rumpling was observed. The compressive residual reported in Figure 91 remained constant until failure with initial increase from the growth of TGO with cyclic oxidation. Cross-sectional microstructure of failed specimen shown in Figure 154(c,d), shows that the TGO is still adherent to the YSZ surface and the bondcoat surface had little to no TGO attached as shown in Figure 154(e).

The final fracture mainly occurred at the TGO/bondcoat interface. Bondcoat surface was exposed, with small residual TGO and/or YSZ adhered.

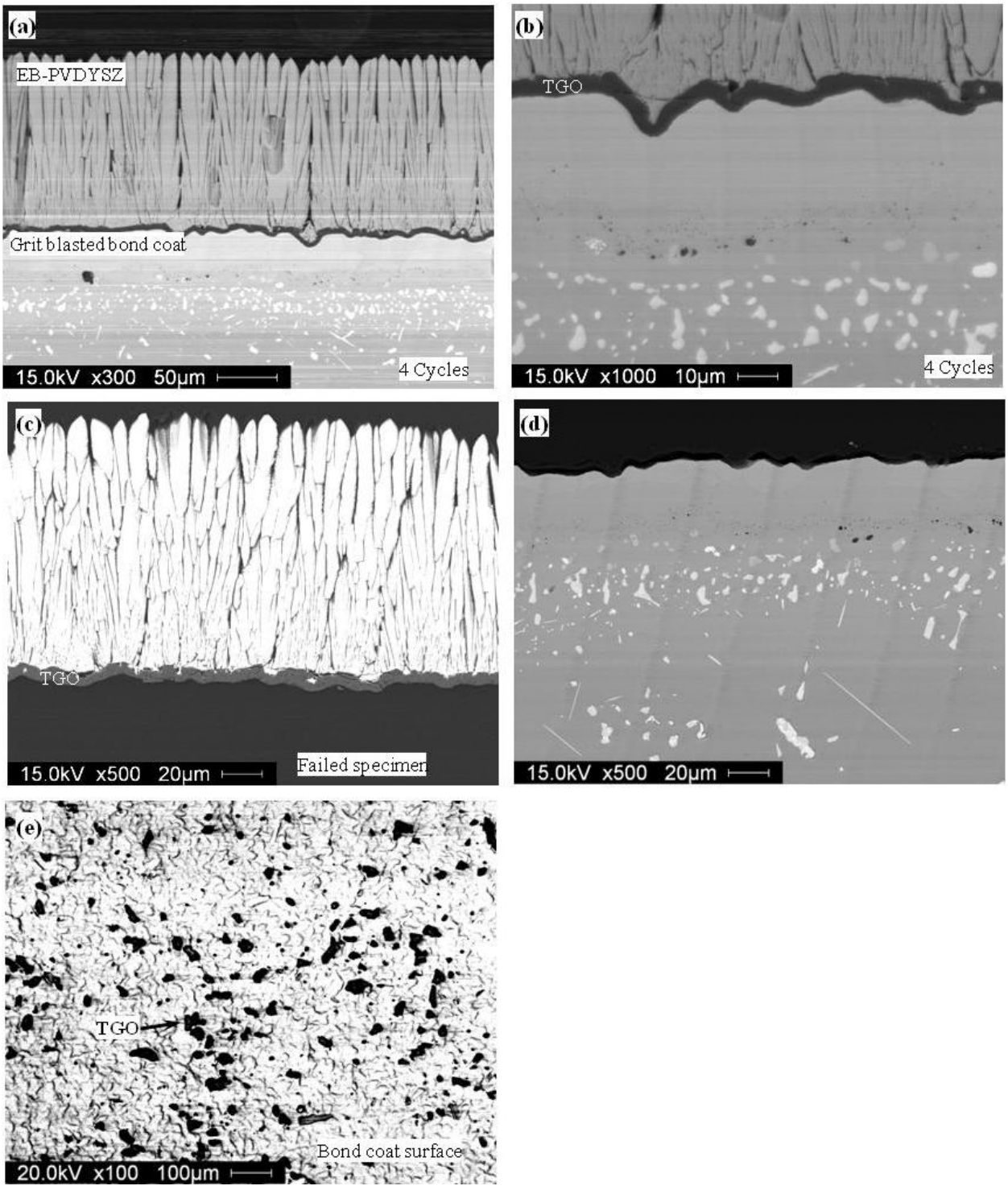

Figure 154. Backscatter electron micrographs for type-IV EB-PVD TBCs from 50-hour thermal cycling at 1121°C (a, b) after 4-cycles (c) cross-sectional observation of YSZ at failure (d) cross-sectional observation of bondcoat surface at failure (e) bondcoat surface at failure showing specks of TGO on the surface.

5 DISCUSSION

5.1 Damage Accumulation / Failure Mechanism for APS TBCs

For APS TBCs, irrespective of processing conditions and thermal cycling dwell time, the fracture path remained the same at the YSZ/TGO interface and within the YSZ not exposing the metallic bondcoat surface as shown in Figure 127, Figure 132, Figure 135, Figure 138, and Figure 142. The final failure for APS TBCs occurred by edge delamination with ceramic topcoat still intact as one-piece.

For type-I APS TBCs with APS bondcoat, internal oxidation of the bondcoat was observed. This is inherent to the APS bondcoat processing. During the deposition of bondcoat, the powder are injected into the plasma and melt (large particles may melt incompletely or may not melt at all), while transitioning through the plasma plume. The molten particles impact the substrate surface, which are flattened by the force of impact and solidify to form splats. Molten particles continue depositing on already solidified splats resulting in the microstructure as shown in Figure 127(a).

With thermal cycling internal oxidation of the bondcoat along with the TGO growth was observed for type-I APS TBCs. Type-I APS TBCs with APS bondcoat during 1, 10 and 50 hour thermal cycles developed other oxides rather than uniform α-Al_2O_3. A detail investigation on the oxide structure and composition based on TEM identified $(Ni,Co)(Al,Cr)_2O_4$, α-Al_2O_3 and α-$(Al,Cr)_2O_3$. [93]

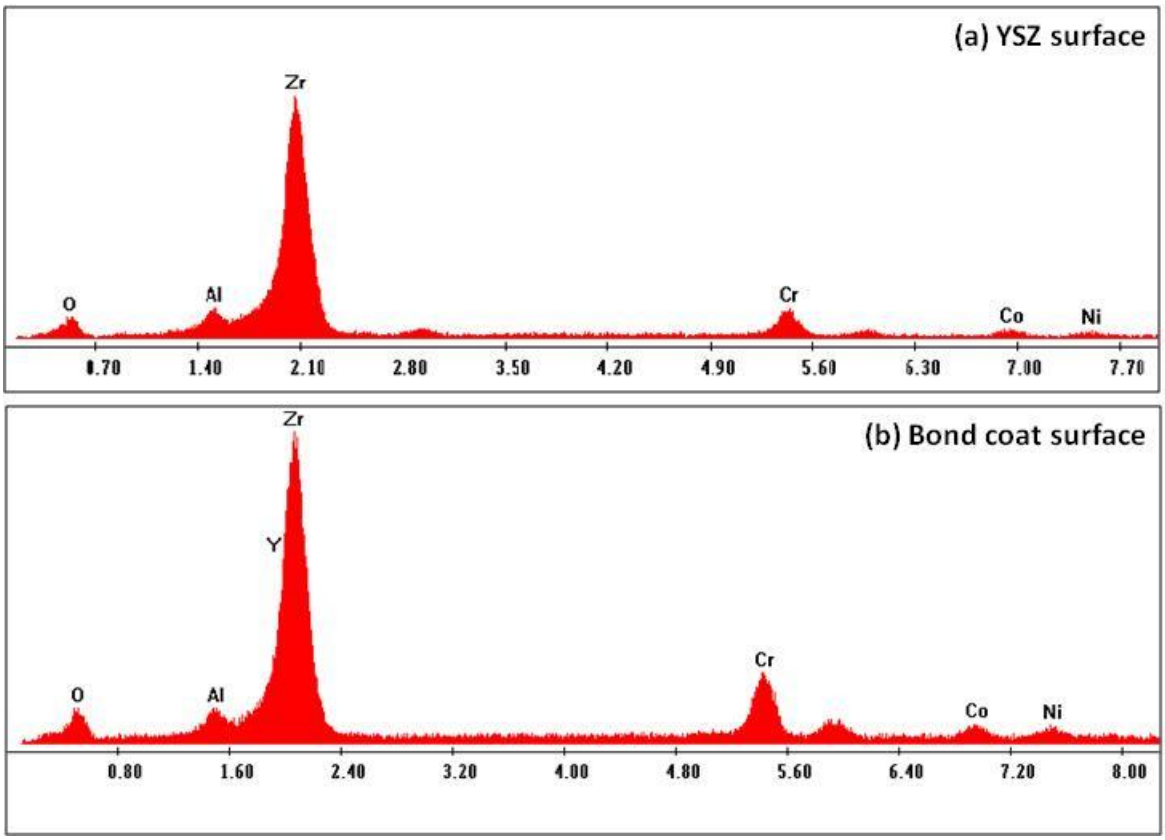

Figure 155. EDS data from the fracture surface from 1-hour thermal cycling at 1121°C after failure (a) EDS analysis on the YSZ bottom surface (b) EDS analysis on the bondcoat surface after YSZ detached.

For type-II APS TBCs with LPPS bondcoat the final failure occurred after the depletion of β-phase (NiAl) within the bondcoat. The fracture mechanism remained the same with various thermal cycling dwell times where the fracture occurred at the YSZ/TGO interface and within the YSZ. Failure of this particular TBC occurred at the vicinity of the TGO, within the YSZ, because of the thermal expansion mismatch stress between the topcoat/bondcoat along with the compressive residual stresses in the TGO.

When comparing type-I and type-II APS TBCs, type-I APS TBCs with APS bondcoat performed superior in terms of furnace cyclic lifetime. Although there are variations in the topcoat/bondcoat thickness and superalloy, composition but they could be playing a less

significant role in the furnace thermal cycling test. All the above parameters could play an important role in thermal cycling lifetime if the samples were internally cooled. APS TBCs failure depends on compressive residual stresses from thermal expansion mismatch between the YSZ and TGO, sintering of the YSZ and the growth of the TGO.

For internal oxidation of a bondcoat, the microstructure resembles a metal matrix composite with oxides originating from the splats parallel to the substrate/topcoat interfaces. With thermal cycling the volume fraction of the oxide can be qualitatively seen increasing and is uniformly distributed throughout the bondcoat matrix. The thermal expansion mismatch coefficient and thermal conductivity will change as a function of thermal exposure with thermal gradient. The thermal expansion mismatch can be calculated using upper and lower–bound properties of composites [95] to provide an approximate estimate on the changes in thermal expansion coefficient and thermal conductivity.

$$\alpha_{upper} = V_{metal}\alpha_{metal} + V_{oxide}\alpha_{oxide} \tag{25}$$

$$\alpha_{metal} = \frac{\alpha_{oxide}\alpha_{metal}}{V_{metal}\alpha_{oxide}+V_{oxide}\alpha_{metal}} \tag{26}$$

In the above equations it is assumed that the modulus of elasticity does not play a significant role in the thermal expansion mismatch. Similar expression can be written for thermal conductivity; but under thermal cycling conditions and no internal cooling this is also assumed not to vary significantly across the topcoat/TGO interfaces. In case of APS TBCs the intrinsic splat boundary along with micro-cracks and pores normal to the direction of the heat flow reduces the thermal conductivity from 2.3 $W.m^{-1}K^{-1}$ for a dense YSZ to 0.8 to 1.7 $W.m^{-1}.K^{-1}$. [96] Considering thermal expansion mismatch, the volume fraction of the oxides with respect to thermal cyclic lifetime is calculated from image analysis and reported in the Table 19.

Table 19. Internal oxidation area calculation based on image analysis for type-I APS TBCs with APS bondcoat after thermal cycling at 1121°C.

Thermal Cycling type	Thermal Cycles	Time at temperature 1121°C (hrs)	% Internal oxidation area
1-hour thermal cycles	0	0	13.1 ± 1.3
	50	33.5	41.7 ± 1.0
	260	174.2	43.8 ± 1.4
	360	241.2	43.9 ± 1.0
10-hour thermal cycles	0	0	13.1 ± 1.3
	35	343	47.3 ± 3.1
	90	882	48.0 ± 0.6
	120	1176	50.6 ± 1.7

Table 19 reports that the APS bondcoat internal oxidation can reach up to 50% in area. The reported values in literature for thermal expansion coefficient for NiCoCrAlY bondcoat and α-Al_2O_3 are 15×10^{-6} and 7×10^{-6} /°C respectively. The thermal expansion coefficient with internal oxidation based on Eqs. (25) and (26) should vary from $10\sim12\times10^{-6}$/°C which is a close to the value reported for YSZ coating 11×10^{-6}/°C. The smaller thermal expansion mismatch can attribute to the prolonged life for type-I APS TBCs. It should be noted that in both types of APS TBCs, the failure occurred at the YSZ/TGO interface and within the YSZ because of the compressive residual stresses arising from thermal expansion mismatch with prolonged cycling and sintering/densification of topcoat as discussed earlier in section 4.8.1. For APS TBCs, the accelerated 1-hour thermal cycling can produce similar failure mechanism for IGT engines.

5.2 Damage accumulation / Failure Mechanism for EB-PVD TBCs

With thermal cycling, for EB-PVD TBCs with diffusion aluminide bondcoats, failure occur at the YSZ/TGO and TGO/ bondcoat interface by phenomenon called rumpling or

ratcheting. For as-coated (Ni,Pt)Al bondcoat, TBC failed by preferential bondcoat ridge oxidation, and removal of these ridges prolong TBC lifetime by suppressing rumpling of bondcoat. This particular mechanism of 'rumpling' occurs with a characteristic wavelength of bondcoat along with TGO upon thermal cycling. From previous observations [97,98,99, 100] the wavelength of rumpling varied from 30-130 μm and amplitude varied from 10-15 μm depending on the furnace hold temperature and dwell time for diffusion aluminide bondcoats without TBCs.

For Type-III EB-PVD TBCs with as-coated (Ni,Pt)Al bondcoat, the failure mechanism changed with thermal cyclic dwell time at 1121°C. Comparing the fracture surface with thermal cycling it can be inferred that, with 1-hour thermal cycling, the fracture occurred at the YSZ/TGO interface with little to no bondcoat surface exposure while for 10- hour thermal cycling, the fracture occurred at the YSZ/TGO interface but with qualitatively more bondcoat surface exposed as seen in Figure 145 and Figure 150. With 50-hour thermal cycling, the fracture path was predominantly at the TGO/bondcoat surface. The amount of surface area for exposed bondcoat surface was determined based on image analysis along with amplitude of bondcoat undulation. These are reported in Table 20, and shown in Figure 156. Exposure of bondcoat surface increased and degree of rumpling/ratcheting decreased with an increase in dwell time of thermal cycling test.

Table 20. Amplitude of ridges measured at failure for 1, 10 and 50-hour thermal cycling.

Thermal cycling type	Life time (Cycles)	Dwell Time (Hours)	Amplitude (μm)	% Bondcoat area exposed
1-hour thermal cycles	406 ± 22	272	15.4 ± 6.96	27.6
10-hour thermal cycles	55 ± 3	539	14.3 ± 3.94	48.2
50-hour thermal cycles	12 ± 1.5	597	8.5 ± 3.90	80.5

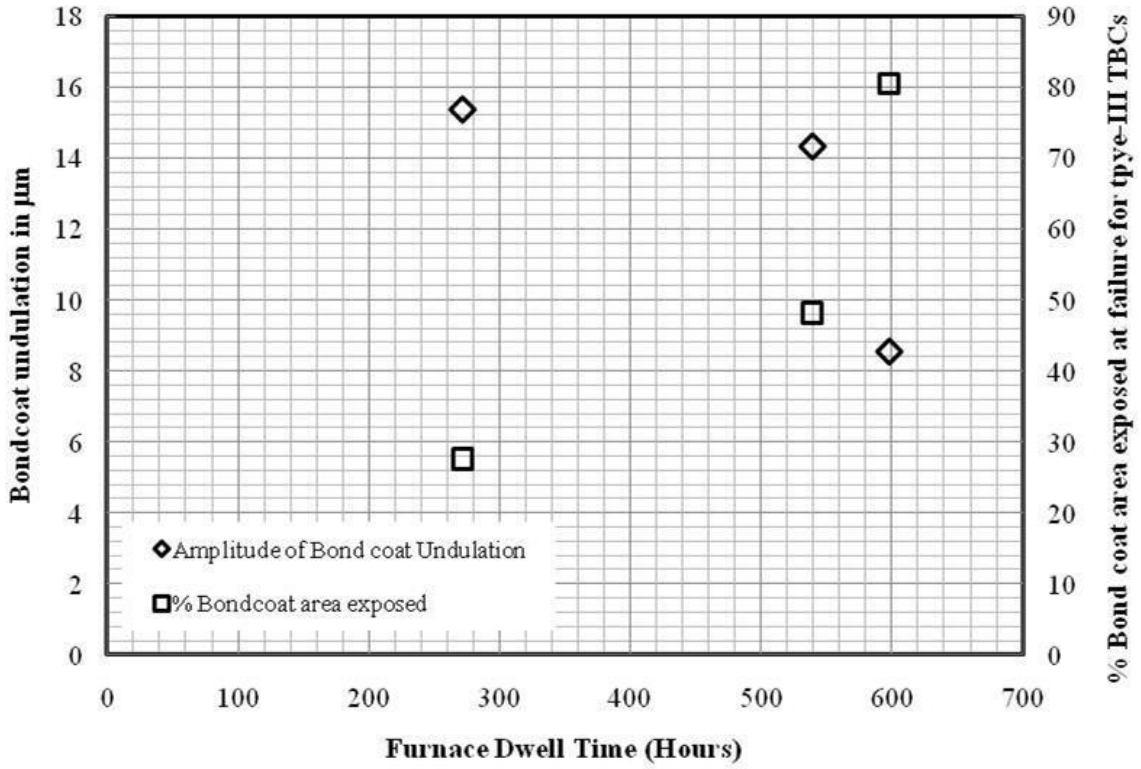

Figure 156. Bondcoat undulation and % area exposed at failure with respect to furnace cyclic dwell time for type-III TBCs with as-coated (Ni,Pt)Al bondcoat.

Plausible reason for the change in fracture path, from the YSZ/TGO interface to the TGO/bondcoat interface with longer dwell time may be due to thermal mechanical fatigue playing an important role in the former and less significant role in the latter. It has been reported that rumpling/ undulation of bondcoat, arising from the bondcoat ridges act as initial crack initiation site for TBC failure. This can be observed from Figure 144, Figure 149 and Figure 153. The bondcoat ridges play a significant role with frequent thermal cycling leading to cavity formation filled with oxide (α-Al_2O_3), with time at temperature that involve grain boundary oxidation, full thickness TGO cracking and widening of the grain boundary crack into a cavity by cyclic plasticity process in the bondcoat. Figure 144(b) shows that sub-critical damages

originated in/around ridges at the TGO interface as early as 10% of lifetime for type-III TBCs during 1-hour thermal cycling.

With thermal cycling, bondcoat strength decreases with an increase in the stress within the bondcoat and at the interface between the bondcoat and topcoat due to the development of TGO. [101] The damage initiation/progression in 1-hour thermal cycling occurred at the YSZ/TGO interface due to preferential oxidation around ridges causing bondcoat surface undulation. The YSZ, being shape-constrained, does not flow to the contour of undulations at the TGO/bondcoat interface, and this result in local defects as observed in Figure 143(d). During 10-hour thermal cycling, preferential oxidation is still observed around the vicinity of the ridges, but to a lesser extent. In addition, the rumpling amplitude in the bondcoat decreased, resulting in greater exposure of the bondcoat surface at failure after 10-hour thermal cycling when compared to 1-hour thermal cycling. This trend continued for 50-hour thermal cycling after which bondcoat surface exposure was up to 80% in area. With frequent thermal cycling, the fracture occurred at the YSZ/TGO interface initially, but changed to the TGO/bondcoat interface with longer dwell periods.

For type-IV TBCs with grit blasted bondcoat, similar TBC failure mechanism described for type-III TBCs was observed with respect to the variation in thermal cycling. The fracture path changed with increasing dwell time from the YSZ/TGO interface to the TGO/bondcoat interface as shown in Figure 148, Figure 152, and Figure 154. With the change in thermal cycling dwell time, the undulation amplitude of the bondcoat decreased and the bondcoat surface exposure increased as presented in Table 21 and shown in Figure 157. It is been reported in the literature [102,103] that type-IV TBCs with grit-blasted (Ni,Pt)Al bondcoat predominantly fail by ratcheting mechanism. This mechanism operates from (a) compressive residual stresses during

cooling from thermal expansion mismatch between the TBC/TGO interface and TGO/bondcoat interfaces and (b) elongation strain associated with new oxide formation on the bondcoat surface at high temperature.

The grit-blasting of (Ni,Pt)Al could have played an important role to the formation of rough bondcoat surface before and after cyclic oxidation. During 1-hour thermal cycling, heating expands the bondcoat significantly closer to that of the substrate (α for bondcoat 17.6×10^{-6}/°C and 18×10^{-6}/°C for substrate) and oxidation starts to occur. During cooling bondcoat shrinks much more compared to the TGO and/or YSZ due to the difference in thermal expansion coefficient. The excess oxide surface formed on bondcoat can only be accommodated with surface instabilities (i.e., bondcoat undulation or pegging of bondcoat by ratcheting). With the YSZ being shape-constrained during heating and cooling, sub-critical damages can occur at the YSZ/TGO interface as shown in Figure 146. Generally, the damages are observed at the geometrical valleys where the TGO is observed to be detached from the YSZ surface as shown in Figure 146(f, h). With progressive/frequent thermal cycling cracks originate and encounters the nearby stress fields which results in rapid crack link-up, and final failure predominantly occurring at the YSZ/TGO interface. During 10-hour thermal cycles, a similar observation of damage initiation at the YSZ/TGO interface was observed, but the final failure occurred at the TGO/bondcoat surface, exposing up to 50% of the bondcoat surface area. Furthermore, the amplitude of bondcoat surface undulation after 10-hour thermal cycling is reduced by a factor of 3 compared to the 1-hour thermal cycling. With a decrease in surface undulation amplitude, the fracture path follows the TGO/bondcoat interface because the thermal expansion coefficients for TGO at room temperature is 8.0×10-6/°C, for bondcoat is 13.6×10-6/°C and for the YSZ is 9×10-6/°C.

Table 21. Amplitude of bondcoat undulation measured at failure for 1, 10 and 50-hour thermal cycling.

Thermal cycling type	Life time (Cycles)	Dwell Time (Hours)	Amplitude (μm)	% Bondcoat area exposed
1-hour thermal cycles	360 ± 39	241	20 ± 3.66	5.9
10-hour thermal cycles	42 ± 2	411	6.34 ± 2.92	50.9
50-hour thermal cycles	9.5 ± 0.7	473	4.12 ± 0.78	88.7

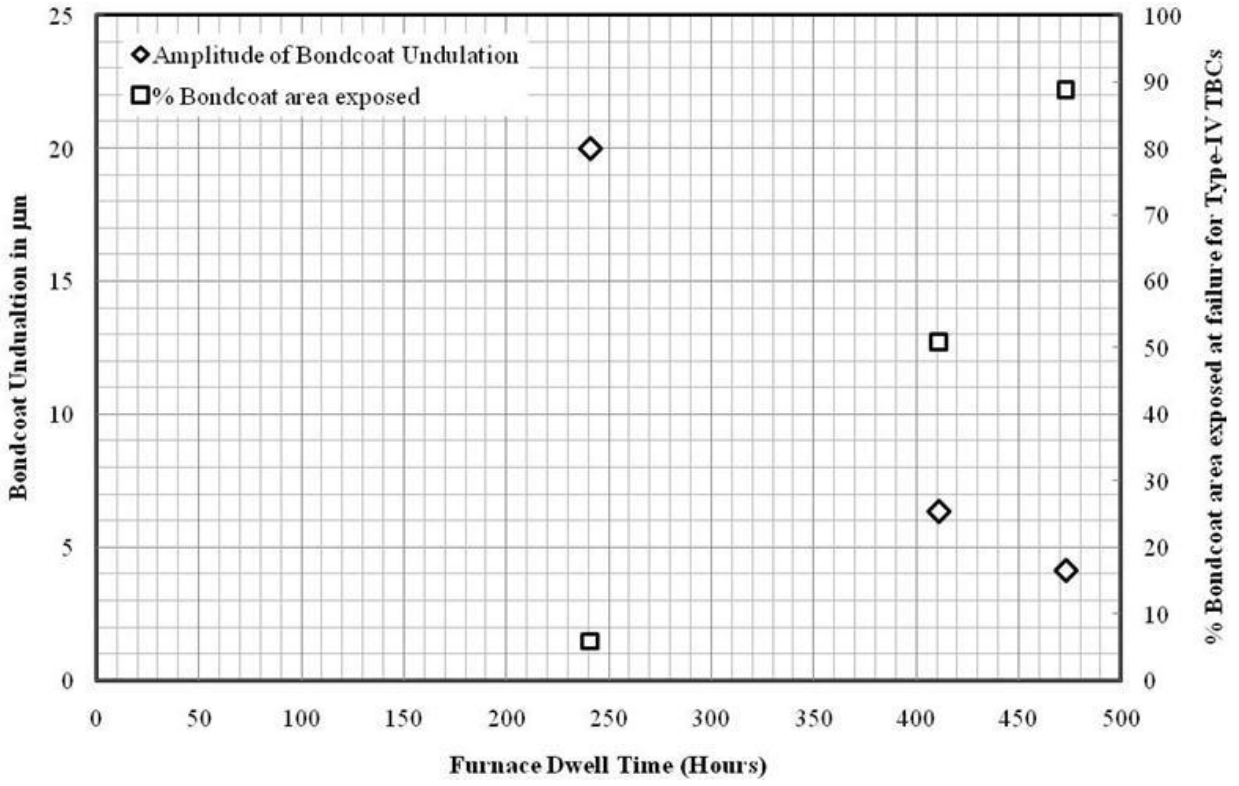

Figure 157. Bondcoat undulation and % area exposed at failure as a function of furnace cyclic dwell time for type-IV TBCs with grit-blasted (Ni,Pt)Al bondcoat.

5.3 Microstructure and Residual Stress Correlation with respect to Furnace Dwell time

During 1-hour thermal cycling, there is an initial increase in the compressive residual stress from the TGO growth and change in metastable phases within TGO (θ-α Al_2O_3) as reported in Figure 79. Luminescence from both 1-hour and 10-hour thermal cycling exhibited relief of the TGO scale as early as 50% of lifetime for type-III EB-PVD TBCs with as-coated (Ni,Pt)Al bondcoat. The stress relief was measured from a tri-modal luminescence from PL, which is related to the sub-critical damages associated with bondcoat ridge oxidation/scale damages as shown in Figure 144 and Figure 149(d).

With frequent thermal cycling, surface undulation of the bondcoat from the cavities associated with the bondcoat grain boundary ridges caused surface rumpling. With rumpling, damage beneath the EB-PVD TBC, was detected by PL after 50% lifetime. Before the final failure of TBCs, significant damages were observed at all interfaces: within the YSZ, between the YSZ/TGO interface and within the TGO, and stress free trimodal luminescence was observed in Figure 80 and Figure 86(a). Stress-free luminescence was observed during 1 and 10-hour thermal cycling but not during 50-hour thermal cycling. Also during 50-hour thermal cycling sub-critical damages within TGO that could give rise to a stress free luminescence with prolonged thermal cycling were not microstructurally identified for type-III EB-PVD TBCs.

The appearance of stress-free luminescence with frequent thermal cycling can be explained due to the fact there is thermal expansion mismatch between the bondcoat and theTGO during cycling that cause thermo-mechanical fatigue. During time at temperature 1121 °C the oxide grows at a relatively low stress on a yielding bondcoat with low residual stress. At cool down, the thermal expansion mismatch between the TGO (8×10^{-6}/°C), (Ni,Pt)Al bondcoat

(13.6×10^{-6}/°C) and substrate (14.8×10^{-6}/°C) causes the bondcoat to contract relatively faster inducing compressive stresses in TGO. [12,20,104,105] With frequent cycling the same thermal expansion mismatch at various interfaces causes strain within the each layer. Once a critical value of strain is reached within the layers damage initiation starts at the YSZ/TGO or TGO/bondcoat interface. These damages give rise to stress-free luminescence.

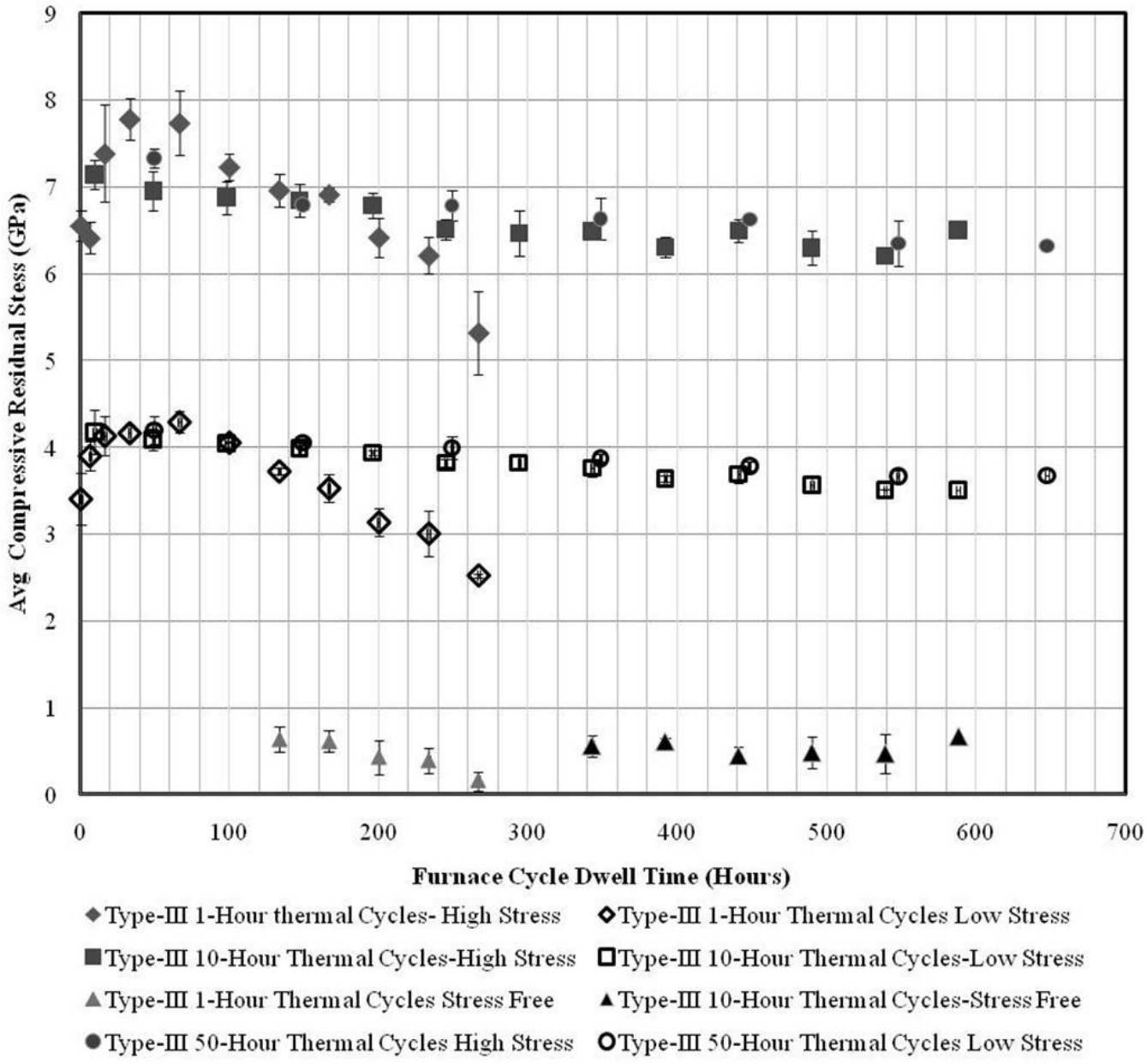

Figure 158. Compressive residual stress evolution and comparison with respect to 1, 10 and 50-hour thermal cycling for type-III TBCs with as-coated (Ni, Pt) Al bondcoat on CMSX-4 substrate.

For type-IV EB-PVD TBCs with grit-blasted (Ni,Pt)Al bondcoat, the evolution in compressive residual stress during 1-hour thermal cycling showed a gradual increase and a decrease with cyclic oxidation. An initial increase can be attributed to the formation of under developed TGO on the bondcoat surface. A decrease in the magnitude of compressive residual stress is reflected by the gradual shift in luminescence towards 14402 and 14432 cm^{-1} (stress-free luminescence for α-Al_2O_3) as observed in Figure 82. This gradual decrease can be attributed to the microstructural rumpling of the TGO scale. In this particular type of TBCs, as explained earlier, ratcheting was found as dominant failure mechanism with ceramic topcoat failure through large scale buckling. Ratcheting damages are observed within TGO scale on the peaks and valleys of the TGO scale as shown in Figure 146.

During 10-hour thermal cycling, a gradual shift in luminescence was not observed. Also the compressive residual stress did remained constant throughout the cycling with an initial increase from the development of the TGO. The frequency and amplitude of ratcheting observed for this particular cycling compared to 1-hour thermal cycling is lower and hence a significant sub-critical damage within TGO is not expected. For 50-hour thermal cycling similar trend was observed in the luminescence as well as in the compressive residual stress where the stress initially increased and remained constant until failure. The ratcheting amplitude with thermal cycling decreased with an increase in dwell time that would yield less cracking at the YSZ/TGO interface, and hence no relaxation of compressive residual stresses were observed.

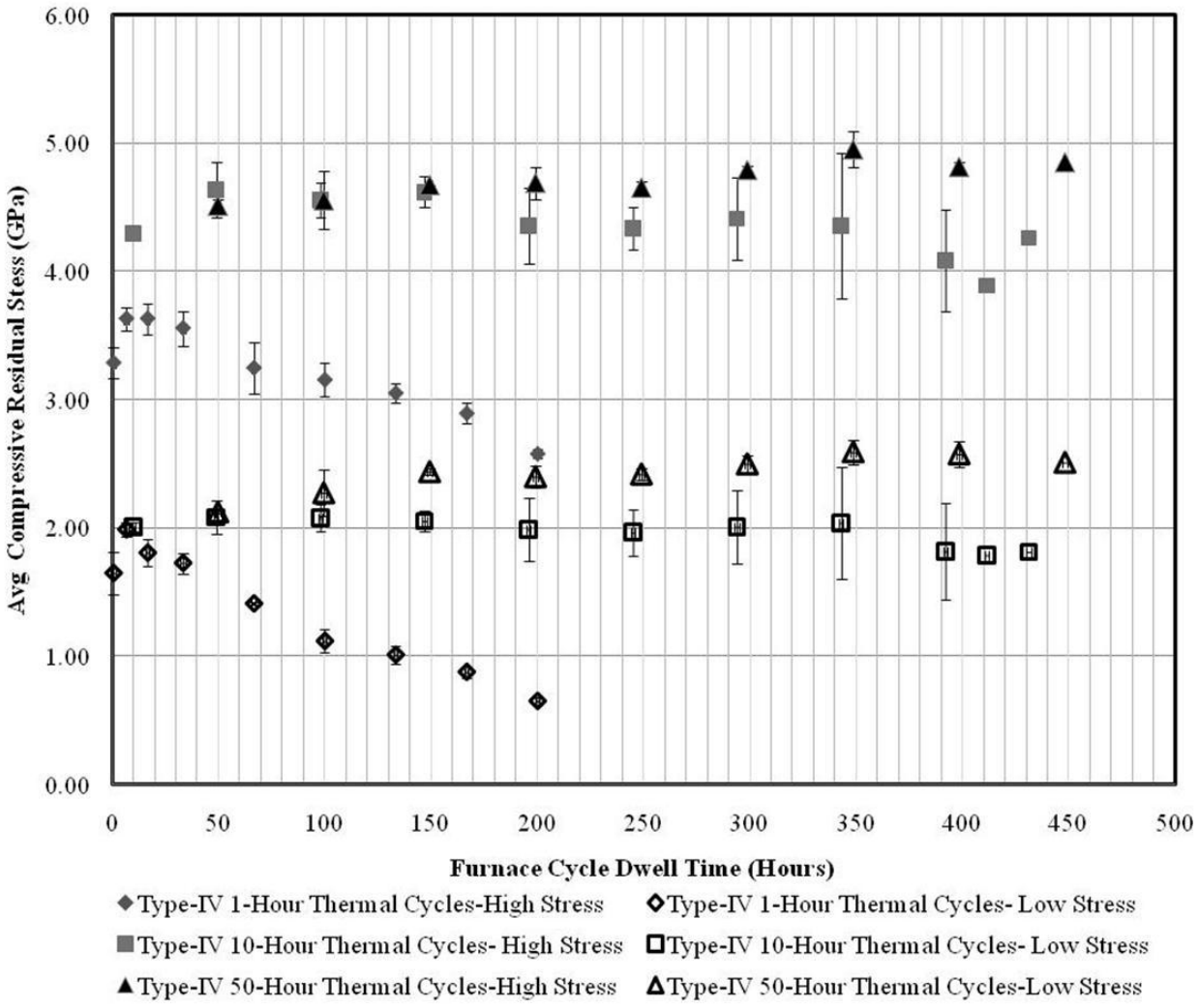

Figure 159. Compressive residual stress evolution and comparison for 1,10 and 50-hour thermal cycling for type-IV EB-PVD TBCs with grit blasted (Ni,Pt)Al bondcoat on Rene N5 substrate.

5.4 Sub-critical damages in TBCs and impedance correlation

5.4.1 Observation on APS TBCs

For APS TBCs, the impedance response increased from the initial as-coated condition to the thermally cycled condition as shown in Figure 105 and Figure 110. This impedance response was curve-fitted using the ac-equivalent circuit shown in Figure 45 and Figure 46 for APS TBCs with and without TGO, respectively. The individual parameters used in the ac-equivalent circuit namely resistance and capacitance of ceramic topcoat (R_{YSZ} and C_{YSZ}) and TGO (R_{TGO} and C_{TGO}) increased and decreased with thermal cycling based on the impedance response, respectively. The response depends on the microstructural characteristic such as pores/intersplat cracks within the YSZ and defects through which aqueous conductive electrolyte can penetrate. An increase in the resistance of YSZ and TGO can be explained by the expression:

$$R = \frac{\rho.t}{A} \tag{27}$$

Where the variables ρ, A and t refer to the electrical resistivity, measurement area and thickness of the material exposed. The resistivity depends on the volume fraction of the YSZ along with the volume fraction of the electrolyte inside the YSZ. Hence effective resistivity can be represented as follows:

$$\rho^{eff} = \rho_{YSZ}.V_{YSZ} + \rho_{electrolyte}.V_{electrolyte} \tag{28}$$

Substituting (28) in (27) the effective resistance of the YSZ will be represented as:

$$R = (\rho_{YSZ}.V_{YSZ} + \rho_{electrolyte}.V_{electrolyte})\frac{t}{A} \tag{29}$$

Within the two types of APS TBCs in this study, the R_{YSZ} for type-I APS TBCs was higher by ~2-3 times in magnitude than that for type-II APS TBCs, as reported in

Table 12 and Table 13. The larger R_{YSZ} based on the Eq. (29) is logical since the ceramic topcoat thickness for type-I APS was 600 μm while that of type-II APS TBCs was 200 μm. After prolonged heat treatment at high temperature irrespective of thermal cyclic dwell, R_{YSZ} for all types of APS TBCs increased and then decreased with thermal cycling. An initial increase in the R_{YSZ} is related to the sintering of the YSZ. With sintering, YSZ becomes denser, and contributes to the higher effective resistivity with an increase in the volume fraction of the YSZ according to Eq. (28).

With sintering, the YSZ is more prone to cracking because of the difference in thermal expansion coefficient between the topcoat and the underlying metal. Because of micro-cracking, the R_{YSZ} decreases due by the penetration of electrolyte. The resistivity according to Eq (28) should decrease since the volume fraction of electrolyte with lower resistivity, increases with cracking in the YSZ. For the two systems studied, this decrease can occur as early as 50% of lifetime.

The capacitance of the individual layers can be expressed by a simple equation:

$$C = \varepsilon_V . \varepsilon \frac{A}{t} \tag{30}$$

Where t, ε_V and ε refer to the thickness, dielectric constant of vacuum and dielectric constant of material, respectively. Based on Eq (30) the capacitance was larger for type-II APS TBCs in the as-coated condition. To understand the C_{YSZ} relation to thickness and microstructure of the coating, the porosity for as-coated condition was calculated based on image analysis and presented in Figure 160. Type-I APS TBCs showed less porosity and distribution of pores from image analysis based on gray contrast.

The C_{YSZ} is also dependent on the dielectric layer thickness; so as the porosity increases (type-II APS TBCs), the electrolyte effectively penetrates and hence the dielectric layer

decreases. The dielectric layer thickness for TBCs with more porosity is less compared to that with less porosity. This variation in the pore size and porosity as whole is incorporated in the actual value of C_{YSZ} and hence there is no significant magnitude difference to the C_{YSZ}. With prolonged heat treatment, irrespective of thermal cycling dwell time, there was no observable change in the C_{YSZ} values as a function of thermal cycling.

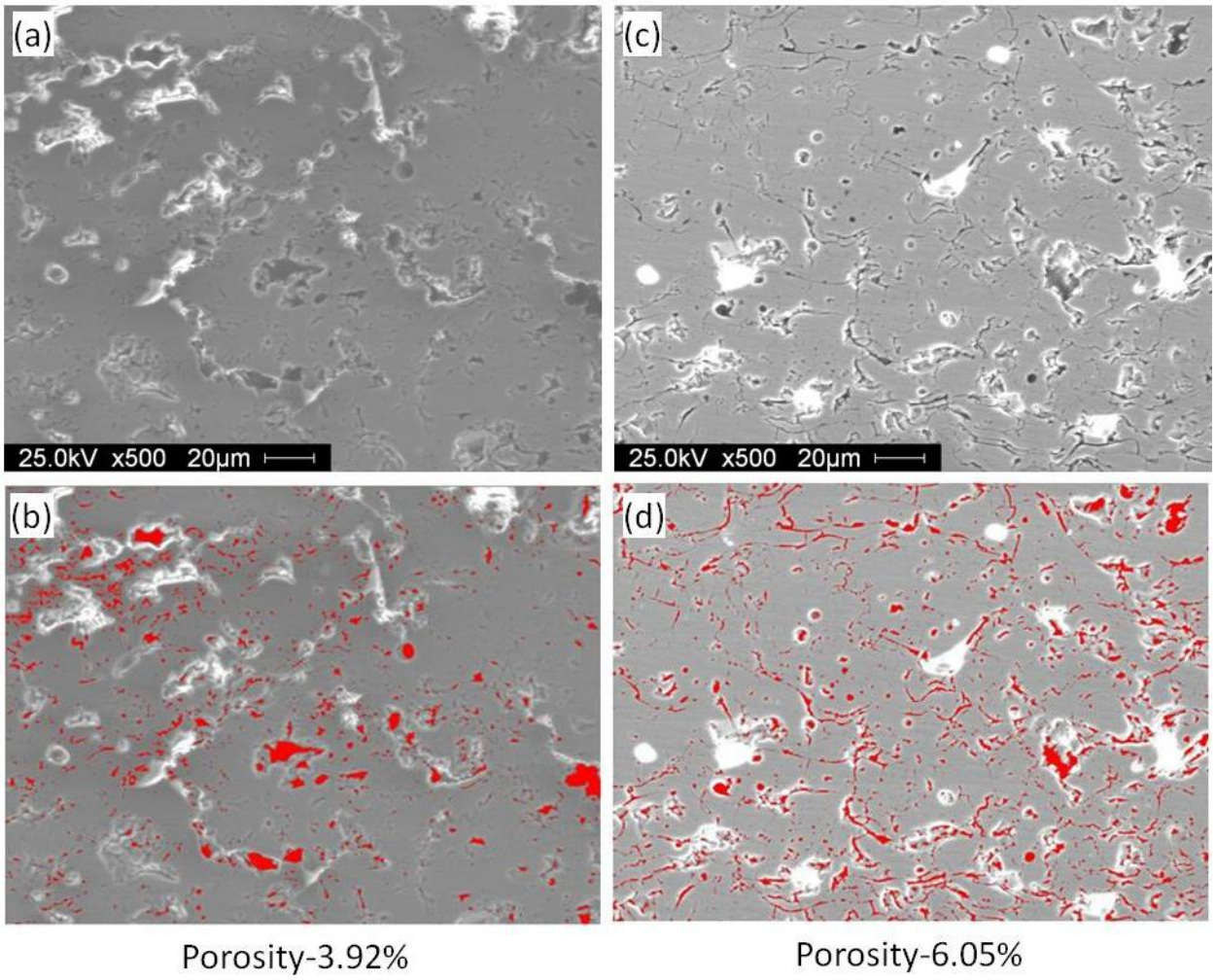

Figure 160. Porosity measurement for as-coated APS TBCs: (a) Type-I APS TBCs (b) Image analysis measurement for porosity type-I APS TBCs (b) Type-II APS TBCs (d) Image analysis measurement for porosity type-II APS TBCs.

For TGO electrical parameters (R_{TGO} and C_{TGO}) of APS TBCs, two different trends were observed. For type-I APS TBCs, R_{TGO} increased initially and then decreased around at 70% of lifetime with thermal cycling. Ideally if the TGO develops with a relatively dense microstructure and homogenous chemistry during thermal exposure, R_{TGO} will increase based on Eq.(27) and C_{TGO} will decrease based on Eq. (30). An initial increase and decrease in R_{TGO} and C_{TGO} is related to the initial growth of the TGO as shown in Figure 108 and Figure 109. As reported earlier [89] C_{TGO} increases abruptly at failure, due to the exposure of metallic bondcoat, which increases effective number of cations from electrolyte and anions from metal surface for a free conduction. For type-I APS TBCs, C_{TGO} does show an inverse trend and decreases until failure which is related to the fracture path of type-I TBCs. The fracture occurs near the YSZ/TGO interface and within the YSZ, hence there is no exposure of the bondcoat surface, and an abrupt increase in C_{TGO} was not observed. For type-II APS TBCs, R_{TGO} and C_{TGO} did increase and decrease respectively from an under-developed TGO, but after 50% of lifetime, an inverse trend was observed. This inverse in trend can be explained from microstructural observation shown in Figure 161 where the TGO scale has subcritical damages where the electrolyte can penetrate easily and contact the bondcoat surface and increase the C_{TGO} abruptly explained earlier.

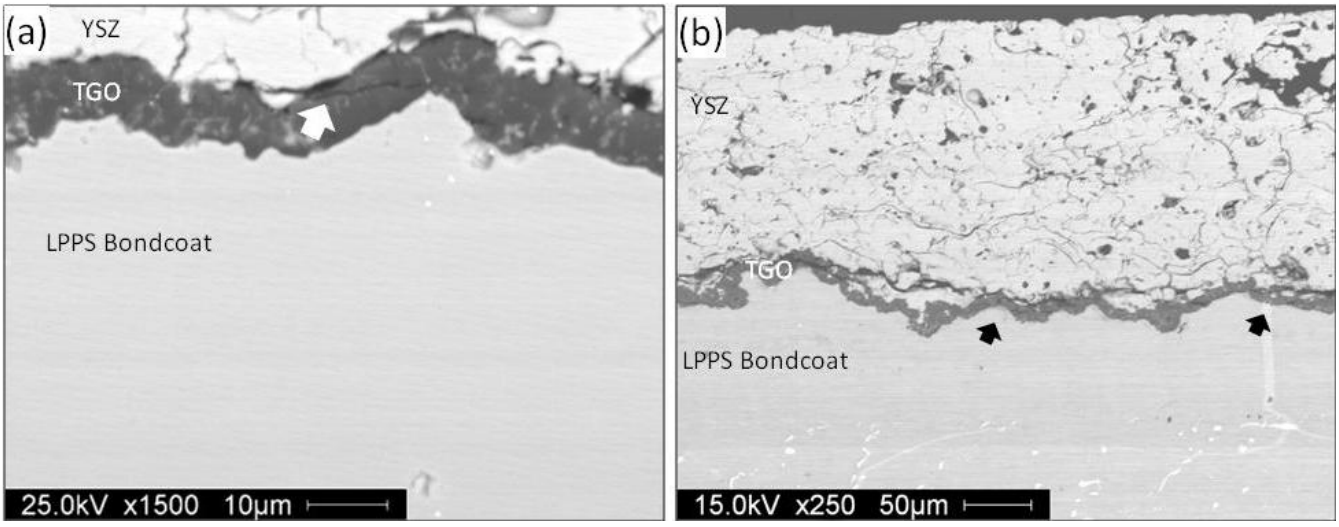

Figure 161.The TGO scale damages observed in type-II APS TBCs at (a) 70% of lifetime during 1-hour thermal cycling and (b) 80% of lifetime during 10-hour thermal cycling at 1121°C.

5.4.2 Observation on EB-PVD TBCs

Similar to APS TBCs, the impedance response from both EB-PVD TBCs increased initially and then decreased with thermal cycling. The impedance response is curve fitted based on the ac equivalent circuit shown in Figure 47. The ceramic topcoat resistance R_{YSZ} increased and then decreased with thermal cycling, the initial increase being related to the sintering observed at high temperature. During sintering, in case of EB-PVD TBCs, the intercolumnar porosity decreases and the YSZ becomes denser, and therefore contributes to the higher effective resistivity with an increase in the volume fraction of the YSZ according to Eq.(29). With continued thermal cycling, the R_{YSZ} decreased due to the intercolumnar cracks that nucleate due to sintering. The resistivity should decrease since the volume fraction of electrolyte with lower resistivity increases with cracking in the YSZ. The C_{YSZ} did not change with thermal cycling until failure because capacitance is a function of thickness and dielectric constant according to Eq.(30). With thermal cycling, the thickness of YSZ remains the same and dielectric constant of

electrolyte is effectively zero. Therefore, C_{YSZ} did not vary significantly since the ε_{YSZ} remains constant.

For EB-PVD TBCs, the TGO grows with relatively dense microstructure and homogenous chemistry (Al_2O_3), The relative value of C_{TGO} according to Eq.(30) then depends only on the thickness of TGO; specifically an inverse relation. With the increase in scale thickness, the C_{TGO} decreased initially but the sub-critical damages within the TGO scale, as shown in Figure 144 and Figure 146 resulted in an increase in C_{TGO}. These sub-critical damages were detected by the C_{TGO} parameters before the actual failure demonstrating that EIS could be a potential technique for damage detection beneath the TBC layer.

5.4.3 Master Plot for C_{TGO} and TGO scale thickness

From the EIS results, a master plot is generated for the C_{TGO} and thickness of the TGO. This is shown in Figure 162. For a comparison, results from previous study [92,89] were included. Without any damages, there is an inverse linear trend between the C_{TGO} and the thickness of TGO, since capacitance varies inversely to the thickness. A deviation from this trend was observed for one particular type-IV TBCs with grit-blasted (Ni,Pt)Al bondcoat. This may be due to significant damages in the TGO that can expose the metallic surface.

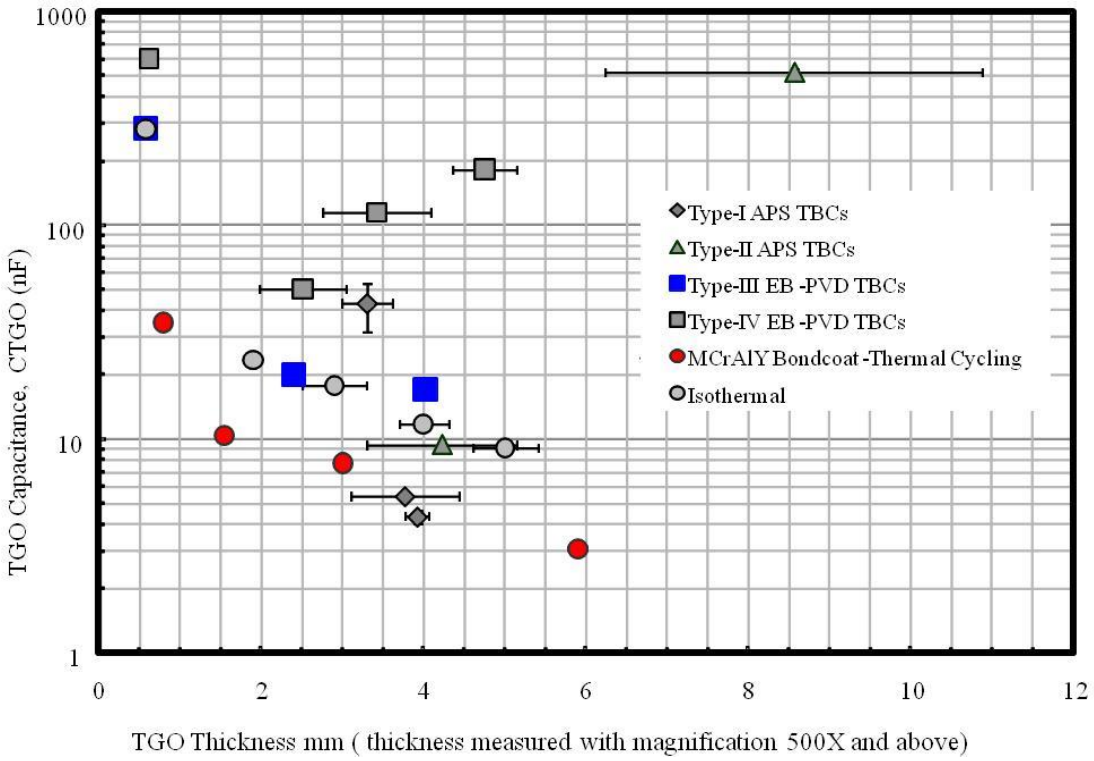

Figure 162. Master plot showing the inverse linear relation between the C_{TGO} and thickness of the TGO prior to spallation

6 CONCLUSION

Characteristics and mechanisms of failure in TBCs were examined by two complimentary NDE techniques, namely PSLS and EIS, and correlated to microstructural degradation and failure analyses carried out by SEM/EDS. Both APS and EB-PVD TBCs were examined using furnace thermal cyclic oxidation at 1121°C with a variation in high temperature dwell time. Using PSLS, the TGO scale on as-coated EB-PVD TBC specimens (both Type III and Type IV) was observed to contain some metastable Al_2O_3 phases in addition to the equilibrium α-Al_2O_3. With high temperature exposure, the transformation towards the equilibrium α-Al_2O_3 was observed. The magnitude of compressive residual stress in the TGO scale (i.e., α-Al_2O_3) increased initially with the initial development of the TGO scale. During 1-hour thermal cycling, the magnitude of compressive residual stress in the TGO scale decrease due to either stress relief (e.g., emergence of luminescence from stress-relieved TGO) or stress relaxation (e.g., gradual shift in luminescence). This change in PSLS was correlated to the damage initiation/progression involving the TGO scale and relevant interfaces (e.g., TGO/bond coat interface or YSZ/TGO interface). However, during 10- and 50-hour thermal cycling, changes in luminescence were not observed, and the magnitude of compressive residual stress remained relatively constant until failure. This observation suggests that the TGO scale damage is more progressive for thermal cycling oxidation with shorter dwell time.

Overall, electrochemical impedance increased with thermal exposure for TBCs. This is attributed to the sintering of the YSZ topcoat and oxidation of bond coat (i.e., growth of the TGO scale). With the growth of the TGO, resistance of TGO (R_{TGO}) increased and capacitance of TGO (C_{TGO}) decreased. Before failure, the R_{TGO} exhibited a gradual decrease, and at failure, C_{TGO} showed an abrupt increase. These changes are correlated to the exposure of conductive

bond coat surface due to the spallation of the TGO scale, particularly for EB-PVD TBCs. Similar trends were observed for APS TBCs but smaller in magnitude. A linear relationship between the capacitance of TGO (C_{TGO}) and thickness of the TGO scale was observed provided that there is no significant damage to the TGO scale and relevant interfaces.

While failure characteristics of APS TBCs remained the same regardless of composition and dwell time, a significant variation was observed for EB-PVD TBCs, particularly as a function of dwell time. During 1-hour thermal cycling, a significant undulation of the TGO/bond coat interface (e.g., rumpling and ratcheting) was observed, which lead to fracture at the YSZ/TGO interface, since the YSZ topcoat does not conform to the changes in interfacial curvature. This interfacial undulation is also correlated to changes in PSLS. However during 10- and 50-hour thermal cycling, the TGO/bond coat interface exhibited limited rumpling, further supported by relatively unchanging PSLS, and the failure occurred mostly at the TGO/bond coat interface.

7 LIST OF PUBLICATIONS

Journal Publications

1. T. Patterson, A. Leon, B. Jayaraj, J. Liu, Y.H. Sohn, "Oxidation Behavior of Air Plasma Sprayed NiCoCrAlY Bond Coats in Air Plasma Sprayed Thermal Barrier Coatings," *Surface and Coatings Technology,* Vol. 203 (2008) pp. 437-441.
2. B. Jayaraj, S. Vishweswaraiah, V.H. Desai, Y.H. Sohn, "Changes in Electrochemical Impedance with Microstructural Development in Thermal Barrier Coatings," *Journal of Metals,* vol. 57 (2006) pp. 61-64.
3. J. Byeon, B. Jayaraj, S. Vishweswaraiah, V.H. Desai, Y.H. Sohn, "Non-Destructive Evaluation of Degradation in Multi-Layered Thermal Barrier Coatings by Electrochemical Impedance Spectroscopy," *Materials Science and Engineering A,* Vol. 407 (2005) pp. 213-225.
4. J.W. Byeon, B. Jayaraj, Y.H. Sohn, "Characterization of Isothermally Oxidized ZrO_2-8wt.%Y_2O_3 Thermal Barrier Coatings by Electrochemical Impedance Spectroscopy," *Materials Science Forum,* Vol. 486-487 (2005) pp. 145-148.
5. Y.H. Sohn, B. Jayaraj, S. Laxman, B. Franke, J.W. Byeon, A.M. Karlsson, "Non-Destructive and Microstructural Characterization of Thermal Barrier Coatings," *Journal of Metals,* Vol. 56 (2004) 53-56.
6. B. Jayaraj, V.H. Desai, C.K. Lee, Y.H. Sohn, "Electrochemical Impedance Spectroscopy of Porous ZrO_2 – 8 wt.% Y_2O_3 and Thermally Grown Oxide on Nickel Aluminide," *Materials Science and Engineering A,* Vol. A372 (2004) pp. 278-286.

Conference Proceedings:

1. J. Liu, B. Jayaraj, Y.H. Sohn, "Selected Microstructural Observations in Thermal Barrier Coatings by Transmission Electron Microscopy," Proceedings of the Materials Science and Technology 2006 Conference: Symposium on Surface Protection for Enhanced Materials Performances, October 15-19, 2006, Cincinnati, Ohio, USA, pp. 523-534 (2006)
2. B. Jayaraj, Y.H. Sohn, B. Franke, D. Miranda, S. Laxman, J. Liu, J.W. Byeon, "Evolution of Photostimulated Luminescence During Thermal Cycling of Electron Beam Physical Vapor Deposited Thermal Barrier Coatings," Proceedings of the ASME Turbo Expo 2005 Sponsored by International Gas Turbine Institute, June 6-9, 2005, Reno-Tahoe, Nevada, USA, GT2005-69121.
3. B. Jayaraj, S. Vishweswaraiah, V.H. Desai, Y.H. Sohn, "Damage Detection of Thermal Barrier Coatings by Electrochemical Impedance Spectroscopy," Proceedings of the 29th Annual International Conference on Advanced Ceramics and Composites, pp. 129-136 (2005).

Invited Presentations:

1. Y.H. Sohn, B. Jayaraj, B. Franke, S. Laxman, J.W. Byeon, "Evolution in Photoluminescence and Electrochemical Impedance with Microstructural Changes in Thermal Barrier Coatings," Invited Presentation at the 2006 International Conference on Metallurgical Coatings and Thin Films - ICMCTF, May 1 – May 5, 2006, San Diego, California, USA.

Presentations:

1. T. Patterson, B. Jayaraj, J. Liu, A. Leon, Y.H. Sohn, "Oxidation Behavior of Air Plasma Sprayed NiCoCrAlY Bond Coats in Air Plasma Sprayed Thermal Barrier Coatings," Presented at 7th International Symposium on High-Temperature Corrosion and Protection of Materials, May 18-23, 2008, Lez Embiez, France.
2. T. Patterson, A. Leon, B. Jayaraj, J. Liu, Y.H. Sohn, "Oxidation Behavior of Air Plasma Sprayed NiCoCrAlY Bond Coats in Air Plasma Sprayed Thermal Barrier Coatings," Presented at 2008 International Conference on Metallurgical Coatings and Thin Films, April 28 – May 2, 2008, San Diego, California, USA.
3. B. Jayaraj, J. Liu, Y.H. Sohn, "Microstructural Development of Thermal Barrier Coatings with Air Plasma Sprayed NiCoCrAlY Bond Coats," Presented at International Thermal Spray Conference and Exposition, May 14-16, 2007, Beijing, China.
4. J. Liu, B. Jayaraj, Y.H. Sohn, "Selected Microstructural Observations in Thermal Barrier Coatings by Transmission Electron Microscopy," Presented at Materials Science & Technology (MS&T) 2006: Symposium on Surface Protection for Enhanced Materials Performances, October 15-19, 2006, Cincinnati, Ohio.
5. B. Jayaraj, Y.H. Sohn, "Thermal Cycling Lifetime and Microstructural Development of Thermal Barrier Coatings with Air Plasma Sprayed NiCoCrAlY Bond Coats," Presented at the 2006 International Conference on Metallurgical Coatings and Thin Films - ICMCTF, May 1 – May 5, 2006, San Diego, California, USA.
6. B. Jayaraj, D. Miranda, Y.H. Sohn, "Photostimulated Luminescence Spectroscopy of Various Electron Beam Physical Vapor Deposited Thermal Barrier Coatings," Presented at the 30th

Annual International Conference on Advanced Ceramics and Structures, January 22-27, 2006, Cocoa Beach, Florida, USA.

7. Y.H. Sohn, E. Perez, S. Laxman, J. Liu, B. Jayaraj, J.W. Byeon, "Interdiffusion and High Temperature Coatings," Presented at First International Conference on Diffusion in Solids and Liquids, July 6-8, 2005, Aveiro, Portugal.
8. Y.H. Sohn, B. Franke, B. Jayaraj, D. Miranda, S. Laxman, J. Liu, J.W. Byeon, "Evolution of Photostimulated Luminescence During Thermal Cycling of Electron Beam Physical Vapor Deposited Thermal Barrier Coatings," Presented at ASME Turbo Expo 2005 Sponsored by International Gas Turbine Institute, June 6-9, 2005, Reno-Tahoe, Nevada, USA.
9. Y.H. Sohn, B. Jayaraj, S. Laxman, B. Franke, J.W. Byeon, "Non-Destructive and Microstructural Characterization of Thermal Barrier Coatings," Presented at the TMS 2005: 134th Annual Meeting and Exposition, February 13-17, 2005, San Francisco, California, USA.
10. J. Liu, A. Puccio, N. Garimella, B. Jayaraj, S. Laxman, J.W. Byeon, Y.H. Sohn, "Selected Observations of Multicomponent-Multiphase Diffusion in High Temperature Coatings," Presented at the TMS 2005: 134th Annual Meeting and Exposition, February 13-17, 2005, San Francisco, California, USA.
11. B. Jayaraj, S. Vishweswaraiah, C.K. Lee, V.H. Desai, Y.H. Sohn, "Damage Detection of Thermal Barrier Coatings by Electrochemical Impedance Spectroscopy," Presented at the 29th Annual International Conference on Advanced Ceramics and Structures, January 23-28, 2005, Cocoa Beach, Florida, USA.
12. B. Franke, B. Jayaraj, S. Laxman, C. O'Toole, Y.H. Sohn, "Non-Destructive Evaluation of Electron Beam Physical Vapor Deposited Thermal Barrier Coatings as a Function of

Furnace Thermal Cycling by Photostimulated Luminescence Spectroscopy," Presented at The 2004 International Surface Engineering Congress and Exhibition, August 2-4, Orlando, Florida, USA.

13. B. Jayaraj, S. Vishweswaraiah, V. Desai, Y.H. Sohn, "Non-Destructive Lifetime Monitoring of Thermal Barrier Coatings Using Electrochemical Impedance Spectroscopy," Presented at The 2004 International Surface Engineering Congress and Exhibition, August 2-4, Orlando, Florida, USA.

14. S. Vishweswaraiah, B. Jayaraj, V.H. Desai, Y.H. Sohn, "Non-Destructive Evaluation of ZrO_2-7wt.%Y_2O_3 by Electrochemical Impedance Spectroscopy for Thermal Barrier Coatings Applications," Presented at The 106^{th} American Ceramic Society Annual Meeting, Symposium on Thermal and Environmental Barrier Coatings, April 18-21, 2004, Indianapolis, Indiana, USA.

15. S. Vishweswaraiah, B. Jayaraj, T. Du, V.H. Desai, Y.H. Sohn, "Non-Destructive Evaluation of Thermal Barrier Coatings by Electrochemical Impedance Spectroscopy," Presented at the 2004 TMS Annual Meeting and Exposition: Symposium on Electrochemical Processing and Measurement, March 14-18, 2004, Charlotte, North Carolina, USA.

8 LIST OF REFERENCES

[1] R. L. Jones, *Metallargical. and Ceramic Protective Coatings.* K. H. Stern, Ed. (Chapman & Hall, London, 1996) 194.
[2] R.A. Miller, *J. Am. Ceram. Soc*., 67 (1984) 517.
[3] H.Herman, *Plasma Spray deposition process, M R S Bull.,* 13, 60-7, (1988).
[4] E. Demaray, *Thermal barrier coatings by electron beam physical vapor deposition, DOE contract,* DE-AC06-76 *RL01830,* 1982.
[5] E. Muehlberger, Method of forming uniform thin coatings on large substrates, U. S. Patent No. 5,853,815.
[6] B. Irving and R. Knight and R. W. Smith, The HVOF process, the hottest topic in the thermal spray industry, *Journ. Welding.,* July 1993, pp. 25-30.
[7] A. J. Sturgeon, M. D.F. Harvey, F. J. Blunt, and S. B. Dunkerton, in *Conference Proceedings: Thermal Spraying- Current and Future Trends,* pp. 101-106, Ed. A. Ohmori, High Temperature Society of Japan, Osaka, 1995.
[8] P. Kofstad, *High Temperature Corrosion* (Elsevier Applied Science, New York, 1988).
[9] Q. Wen, D. M.Lipkin, D. R. Clarke, *J. Am. Ceram. Soc.,*81(1998) 3345.
[10] E. Y. Lee, R.R. Biederman, R. D. Sisson, Jr., *Micro. Sci.,* 7(1991) 505.
[11] E. Schumann, C. Sarioglu, J. R. Blachere, F. S. Pettit, G. H. Meier, *Oxid. Met.,* 53 (2000) 259.
[12] D. M. Lipkin, D. R. Clarke, *Oxid. Met.,* 45 (1996) 267-280.
[13] K. W. Schlichting et al., *Mater. Sci. Eng. A,* 291 (2000) 68.
[14] S. M. Meier, D. M. Nissley, K. D. Sheffler, T. A. Cruse, *J. Eng. Gas Turbines Powers,* 112 (1990) 521.
[15] D. R. Clarke, V. Sergo and M. Y. He, Elevated Temperature Coatings: Science and Technology III, ed. J. M. Hampikian and N. B. Dahotre, TMS, Warrendale, PA, pp. 67, 1999.
[16] J. A. Haynes, M. K. Ferber, W. D. Porter and E.D. Rigney, *Oxid. Of. Metals.,*Vol 52, 112. 1999.
[17] Q. Ma, D.R. Clarke, *J. Am. Ceram. Soc*., 76 (1993) 1433.
[18] Q. Ma, D.R. Clarke, *J. Am. Ceram. Soc*., 77 (1994) 298.
[19] J.R. Christensen, D.M. Lipkin, D.R. Clarke, K. Murphy, *Appl. Phys. Lett*., 69 (1996) 3745.
[20] V. Sergo, D.R. Clarke, *J. Am. Ceram. Soc.,* 81 (1998) 3237.
[21] D.R. Clarke, J.R. Christensen, V. Tolpygo, *Surf. Coat. Technol.,* 94/95 (1997) 89.
[22] Y.H. Sohn, K. Vaidyanathan, M. Ronski, E.H. Jordan, M. Gell, *Surf. Coat. Technol.,* 146/147 (2001) 102.

[23] Y.H. Sohn, K. Schlichting, K. Vaidyanathan, E.H. Jordan, M. Gell, *Metall. Mater. Trans. A*, 31A (2000) 2388.
[24] M. Gell, E. Jordan, K. Vaidyanathan, *Surf. Coat. Technol*., 120/121 (1999) 53.
[25] Y. H. Sohn,E. Y. Lee, B. A. Nagaraj, R. R. Biederman and R. D. Sisson Jr, *Surf. Coat. Technol.*,2001, 146-147, 132-149.
[26] Q. Wen, D.M. Lipkin, D.R. Clarke, *J. Am. Ceram. Soc*., 81 (1998) 3345.
[27] K.W. Schlitchting, K. Vaidyanathan, Y.H. Sohn, E.H. Jordan, M. Gell, N.P. Padture, *Mater. Sci. Eng. A*, A291 (2000) 68.
[28] J. R.MacDonald, Impedance Spectroscopy. John Wiley & Sons, Chichester, 1987.
[29] V.H. Desai, Final Report for AGTSR No. 98-01-SR067, 2001.
[30] J. Zhang, "Development of Electrochemical Impedance Spectroscopy for Non-Destructive Evaluation of Thermal Barrier Coatings," Ph.D. Dissertation, The University of Central Florida, 2001.
[31] K. H. Stern, Ed (Chapman & Hall, 1996), Metallurgical and ceramic protective coatings.
[32] Advances in Ceramics, Vol 3 Science and Technology of Zirconia, Ed. A. H. Heuer and L. W. Hobbs.
[33] H. C. Scott. J. Mater. Sci, 1975, 10, 1527-1535
[34] I. Nettleship and R. Stevens, *Int. J. High Tech. Ceram.*,3 (1987) 1.
[35] S. Stecura, "Optimization of the NiCrAl- Y/ZrO2-Y2O3 thermal barrier system" NASA *Tech. Memo. 86905*, NASA, Cleveland OH.
[36] S. Stecura, *Thin Solid Films.*, 150 (1987) 15.
[37] P. A. Siemers and D. W. Mckee (1982) U.S. Patent 4, 328, 285.
[38] English, L.K., Coatings technology for wear protection, Mater. Eng., September 1985, pp. 53-56.
[39] Herman, H., Plasma-sprayed coatings, Sci, Am., 1988, 259 (3),112-117.
[40] D. V. Rigney, T. E. Mantkowski and M. J. Froning, "Influence of raw materials on the performance characteristics of ceramic coatings, in *Proceedings of the 1987 Coatings for Advanced Heat Engines Workshop*, Ed. J. W. Fairbanks, Castine ME, Dept. of Energy, Washington D. C., 45 (1987) 60.
[41] Strangman, T. E., Thermal barrier coatings for turbine airfoils, Thin Solid Films, 1985, 127, 93-105.
[42] Ulion, N.E. and Ruckle, D. L. (1982) U.S. Patent 4,321,310.
[43] S. M. Meier, D. M. Nissley and K. D. Sheffler, Thermal barrier coating life prediction model development. *NASA Contractor Report 189111*, NASA Lewis Research Center, Cleveland OH.
[44] Sivakumar, R., An evaluation study of aluminide and chromoaluminide coatings on IN-100, Oxid.Metals, 1982, pp. 17, 27-41.

[45] J. R. Nicholls, P. Hancock, Advanced high temperature coatings for gas turbines, Ind. Corros., 1987, pp. 5(4), 8-18.
[46] J. R. Nicholls, Designing oxidation resistant coatings, JOM, 2000, pp. 52(1), 28-35.
[47] B. K. Gupta, T.E. Mantkowski., (1997) U. S. Patent 5,817,371.
[48] J. A. Haynes, M.K. Ferber, and W.D. Porter, J.of Thermal Spray Technology, 38, vol 9(1) March 2000.
[49] H-D.Steffens, Spray and detonation gun technologies, Laser assisted technologies in *Coatings for high Temperature Application*, pp. 121-138, Ed. E.Lang, Applied Science, 1983.
[50] M. R. Jackson, J. R. Rairden, J. S. Smith and R. W. Smith. (1981) Production of metallurgical structures by rapid solidification plasma deposition. Jour. Metals, 33, 23-7.
[51] G. W. Goward, L. L. Seigle, Diffusion coatings for gas turbine engine hot section parts, *ASM Handbook*, Vol 5, *Surface Engineering*, pp. 611-620, ASM, 1994.
[52] G. W. Goward., Progress in coatings for gas turbine airfoils, *Surf. Coat. Technol.*, 1998, 108-109,pp. 73-79.
[53] M. W. Bruce and P. C. David, Clean diffusion coatings by chemical vapor deposition, *Surf. Coat. Technol.*, 1997, 94-95, 1-6.
[54] D.R. Clarke and W. Pompe, *Acta Materialia*, 47 (6) (1999) 1749.
[55] A. Rabiei and A.G. Evans, *Acta Materialia* 48 (2000) 3963
[56] P. Xiao, D. R. Clarke, *Journ. Am. Ceram. Soc.*, 83(5), (2000), 1165-1170.
[57] M. Gell, K. Vaidyanathan, B. Barber, J. Cheng, E. Jordan, *Met. Mater. Trans. A*, 30,(1999) 427.
[58] K. Vaidyanathan, M. Gell, E.H. Jordan, *Surf. Coat. Technol.*, 133-134, (2000), 28-34.
[59] K. Vaidyanathan, E. H. Jordon and M. Gell, *Acta Mater.*, 52, (2004), 1107.
[60] J. Cheng, E. H. Jordan, B. Barber, and M. Gell, *Acta Mater.*, 46 (1998) 5839.
[61] P. Deb, D. H. Boone and T. F. Manley, *J. Vac. Sci. Technol.*, A5, (1987) 3366.
[62] J.W. Holmes, F.A. McClintock, *Metall. Trans. A*, 21 (1990) 1209.
[63] Y. H. Zhang, P. J. Withers, M. D. Fox, and D. M. Knowels, *Mater. Sci. Technol.*,(1999), 15, 1031.
[64] R. Panat, K. J. Hsia and J.Oldham, *Philo. Mag.*, 85 (1), (2005), 45-64.
[65] R. Panat, S. Zhang, K.J. Hisa, *Acta Mater.*, 51 (2003) 239-249.
[66] A. G. Evans, G. B. Crumley, R. E. Demaray, *Oxid. Met.*, 20 (1983) 193.
[67] Y. H. Sohn, J.H Kim, E.H. Jordan and M. Gell, *Surf. Coat. Technol.*, 70-78, (2001), 146-147.
[68] B.W. Kempshall, Y.H. Sohn, S.K. Jha, S. Laxman, R.R. Vanfleet, J. Kimmel, *Thin Solid Films*, 466 (2004) 128-136.
[69] Y.H. Sohn, V.H. Desai, L.A. Giannuzzi, *UTSR Semi-Annual Report*, No.1, 2002.
[70] K. Vaidtanathan, M. Gell, E. Jordan, *Surf. Coat. Technol.*, 133-134 (2000) 28.

[71] Y. H. Sohn, B. Jayaraj, S. Laxman, B. Franke, J. Byeon, and A.M. Karlsson, *Journal of Metals*, 56 (10) (2004) 53
[72] S. R. Choi, J. W. Hutchinson, A. G. Evans, *Mech. of materials.*, 31 (1999) 431.
[73] Gardiner, D.J. (1989). *Practical Raman spectroscopy*. Springer-Verlag. ISBN 978-0387502540.
[74] L. Grabner, *Journal of Applied Physics* 49 (2) (580) 1978.
[75] J. He and D. R. Clarke, *Journ. Am. Ceram. Soc.,* 78(1995)1347.
[76] J. Yu, D.R. Clarke, *J. Am. Ceram. Soc*., 85 (2002) 1966-70.
[77] G. W. Walter, *Corros. Sci.,* 26 (1986) 681.
[78] G. W. Walter, *J. electroanal. Chem., 118* (1981) 259.
[79] J. Epelboin, P. Morel and H. Takenouti, *J. Electrochem. Soc.,* 118 (1971) 1282.
[80] U. Rammelt and G. Reinhard, *Electrochimica. Acta.,* 35 (1990) 1045.
[81] U. Rammelt, G. Reinhard and K. Rammelt, *J. Electroanal. Chem.,* 180 (1984) 327.
[82] M. Kendig, F. Mansfeld and S. Tsai, *Corros. Sci.,* 23 (1983) 317.
[83] J. E. Bauerle, *J. Phys. Chem. Solids.*, 30 (1969) 2657.
[84] A. K. Jonscher, *Phys. St. Sol.,* A32, (1975) 665.
[85] J. F. Mc Cann and S. P. S. Badwal, *J. Electrochem. Soc.,* 129 (1982) 551.
[86] R. de Levie, *Electrochim. Acta,* 10, Issue 4, (1965) 395.
[87] A. Conde, J.J. de Damborenea, *Corr. Sci.* 44 (2002) 1555.
[88] J. R.MacDonald, Impedance Spectroscopy. John Wiley & Sons, Chichester, 1987.
[89] B.Jayaraj, *M.S. Thesis.*, (2003), University of Central Florida.
[90] J.A. Nychka and D.R. Clarke, *Surf. and Coat. Technol.,* 146-147 (2001) 110.
[91] B. Jayaraj, S.Vishweswaraiah, V. H. Desai and Y. H. Sohn, *Surf. Coat. Technol.,* 177-178, (2004) 140-151.
[92] B. Jayaraj, V. H. Desai, C. K. Lee and Y. H. Sohn, *Mat.Sci. Engr.*,A372, (2004), 278-286.
[93] Y. H. Sohn, V. H. Desai, UTSR project 02-01-SR103, DOE- DE-FC26-02NT41431.
[94] B. Franke, *M.S.Thesis*,(2005), University of central florida.
[95] W.D. Callister, Materials Science and Engineering an Introduction, John Wiley & Sons, Inc. 7th Ed 2007.
[96] H. E. Eaton, J. R. Linsey, R. B. Dinwiddle, In Thermal Conductivity 22, T. W. Tong, Ed. (Technomic , Lancaster, PS, 1994), p.289.
[97] R. C. Pennfather, D. H. Boone, *Surf. Coat. Technol.,* 76-77 (1995) 47.
[98] P. Deb, D. H. Boone, T. F. Manley, *J. of Vac. Sci. Technol.,* 5(6), (1987), 3366.
[99] V. K. Tolpygo, D. R. Clarke, *Acta. Mater.,* 48, (2000), 3283.
[100] J. W. Holmes,

[101] M. Gell, E. Jordan, Bond strength and Stress measurements in thermal barrier coatings, DE-FC21-92MC29061.
[102] T.Xu, M.Y.He, A.G.Evans, *Acta.Mater.*, 51,(2003),3803-3820.
[103] D.R. Mumm, A.G. Evans, I.T.Spitsberg, *Acta. Mater.*, 49,(2001),2329-2340.
[104] V.K. Tolpygo and D.R. Clarke, *Oxidation of Metals*, 49 (1998) 187.
[105] R. J. Christensen, V.K. Tolpygo, and D.R.Clarke, *Acta Materialia*, 45 (1997) 1761.